Structural and Optical Properties of Plasmonic Core-Shell Microgels and their 2D Assemblies

Inaugural-Dissertation

zur Erlangung des Doktorgrades
der Mathematischen-Naturwissenschaftlichen Fakultät
der Heinrich-Heine-Universität Düsseldorf

vorgelegt von

Déborah Feller
aus Luxemburg

Düsseldorf, April 2025

aus dem Institut für Physikalische Chemie I – Kolloide und Nanooptik
der Heinrich-Heine-Universität Düsseldorf

Gedruckt mit der Genehmigung der
Mathematisch-Naturwissenschaftlichen Fakultät der
Heinrich-Heine-Universität Düsseldorf

Berichterstatter:

1. Prof. Dr. Matthias Karg

2. Prof. Dr. Jérôme Crassous

Tag der mündlichen Prüfung: 17.07.2025

Eidesstattliche Erklärung

Die vorliegende Arbeit wurde in der Zeit von März 2021 bis April 2025 am Lehrstuhl für Physikalische Chemie I an der Heinrich-Heine-Universität Düsseldorf unter Betreuung von Herrn Prof. Dr. Matthias Karg angefertigt.

Ich, Déborah Feller, versichere an Eides statt, dass die Dissertation von mir selbständig und ohne unzulässige fremde Hilfe unter Beachtung der „Grundsätze zur Sicherung guter wissenschaftlicher Praxis an der Heinrich-Heine-Universität Düsseldorf“ erstellt worden ist. Alle verwendeten Quellen und Hilfsmittel sind als solche gekennzeichnet und im Literaturverzeichnis aufgelistet.

Ort, Datum	*Unterschrift*

Table of Contents

Danksagung

Bevor wir zu dem wissenschaftlichen Teil dieser Arbeit kommen, will ich kurz den Moment nutzen, um einigen Menschen zu danken, ohne die diese Arbeit so nicht hätte zustande kommen können.

Zuerst will ich mich bei Prof. Dr. Matthias Karg bedanken. Danke, dass du mich vor nun mehr als 6 Jahren bei dir im Arbeitskreis damals für die Bachelorarbeit aufgenommen hast. Ich konnte über die ganzen Jahren hinweg so viel Verschiedenes lernen und durfte viele spannende Themen behandeln während meiner Bachelorarbeit, meines HiWi-Jobs, der Masterarbeit und nun meiner Promotion. Des Weiteren möchte ich mich für die vielen unzähligen Gespräche, meist wissenschaftlich, aber manchmal auch über das Backen oder Festivals, bedanken und für das offene Ohr bei jeglichen Fragen meinerseits, egal wie klein die Frage auch war. Ich schätze es sehr, dass du mir die Möglichkeit geboten hast mich weiterzubilden, ob es die unzähligen Konferenzbesuche waren oder die verschiedensten Forschungsaufenthalte in anderen Arbeitsgruppen und Länder. Hier konnte ich sehr viel mehr als nur über meine eigenen Themen lernen.

Außerdem würde ich mich gerne bei Prof. Dr. Jérôme Crassous bedanken, dass Sie sich die Zeit für die Übernahme des Zweitgutachtens dieser Arbeit nehmen. Danke außerdem für die ganzen Messungen am Synchrotron, die einen Teil zu dieser Arbeit beigetragen haben.

An dieser Stelle würde ich mich auch gerne bei meinen unzähligen Kooperationspartnern bedanken, die einerseits einen Teil zu dieser Arbeit beigetragen haben und andererseits mir viele neue Themen und Bereiche der Wissenschaft gezeigt haben. Hier zu nennen sind: Dr. Julian Oberdisse, Dr. Olaf Soltwedel, Dr. Andrea Scotti, Dr. Yuri Gerelli, Dr. Sylvain Prévost, Filip Bandelewicz, Jiakai Wang und Prof. Dr. Paul Mulvaney.

Ein weiterer Dank gilt meinen Abschlussarbeiten, die ich über die Jahre hinweg betreuen durfte. Es war mir eine Freude, gepaart mit manchmal ein bisschen Verzweiflung und ich konnte sehr viel durch die Betreuungsarbeit lernen. Danke an Max Beffort, Julian Kippenberger, Philipp Hammers, Christian Washeim, Elena Vanselow und Amélie Habermann. Hierbei möchte ich Julian Kippenberger

hervorheben, der mir unteranderem tatkräftig mit Fusion-Abbildungen zur Seite stand und durch den ich mich dann auch getraut habe, selbst Abbildungen in Fusion zu erstellen. Des Weiteren möchte ich auch kurz Elena Vanselow danken für die unzähligen privaten Gespräche neben der Arbeit und dem stätigen Kontakt auch nach deiner Bachelorarbeit. Auch Philipp Hammers würde ich gerne nochmals explizit danken, da über die Zeit hinweg als mein HiWi über die Masterarbeit eine wirkliche Freundschaft entstanden ist.

Ein großer Dank gilt auch dem gesamten Arbeitskreis Karg. Über die letzten Jahre sind viele Leute gekommen und dann auch wieder gegangen, allerdings möchte ich jedem einzelnen davon danken, da jeder auf seine Art und Weise meinen Weg geprägt hat. Ich möchte allerdings kurz einige Leute hervorheben, die zum Beispiel die letzte Zeit für sehr viele interessante Gespräche gesorgt haben: Vahan Abgarjan, Julian Ringling und Jonas Schmitz. Es waren immer wieder sehr witzige Mittagspausen und interessante Fachgespräche. Außerdem will ich noch Jacob Nachtwey kurz erwähnen, der ja dann doch irgendwie Teil des Arbeitskreises geworden ist. Schön, dass du für Kaffeepausen hochkommst.

Außerdem möchte ich mich bei den Leuten bedanken die anfangs nur Kollegen waren und dann zu Freunden geworden sind. Allem voran ist hier Büro 27 mit Marco Hildebrandt und Marius Otten zu nennen. Es war eine unfassbar tolle Zeit mit euch gemeinsam in einem Büro mit vielen tollen Gesprächen, guter Musik und sehr viel Lachen. Marco ich schätze es sehr und bin dir unendlich dankbar für deine Geduld und Zeit, die du aufgebracht hast, um mir immer wieder auch fachlich weiter zu helfen. Ich durfte sehr viel von dir lernen, von SANS-Auswertung bis hin zum Löten. Marius, dir danke ich für die tollen Momente in denen wir zur Musik abgetanzt haben, die witzigen Spieleabende (nur mit BigBox wohlverstanden) und die viele Fachsimpelei über Rezepte und das Kochen. Außerdem für dein offenes Ohr, deine ehrlichen Ratschläge und die tiefgründigen Gespräche zwischendurch. Außerdem bedanke ich mich bei Caspar Croonenbrock, Philipp Hammers und Jonathan Garthe. Danke Philipp und Jonathan, dass ich immer in euer Büro kommen kann, ob es zum Reden ist, Kaffee oder Bier trinken. Gute Laune, Memes und zum Teil gute Musik sind hier vorprogrammiert. Die kurze gemeinsame Zeit im Labor hat unfassbar viel Spaß gemacht.

Bei euch Marco und Meli, Marius, Caspar und Jenni, Philipp und Valeria, Jonathan will ich mich wirklich bedanken für die gemeinsame Zeit in den letzten Jahren. Die unzähligen Treffen ob beim Brunchen, in Restaurants, gemeinsame Geburtstagsfeiern, auf Konzerten und Festivals, zuhause für Spieleabende und vieles mehr, haben Düsseldorf wirklich zu einem Zuhause für mich gemacht und ich blicke sehr gerne auf die Zeit zurück! Ich freue mich auf alle zukünftigen Erlebnisse mit euch!

Des Weiteren würde ich mich gerne bei meinen Kommilitonen, aka Labor LK, bedanken für die gemeinsame Zeit über das ganze Studium und die Promotion hinweg: Larissa Hinz, Sven Daniel, David Wolf und Jeremy Kaminski. Dir Jeremy danke für die ganzen Kaffeetreffen, es war immer wieder schön mal kurz über alles zu quatschen.

Bevor ich so langsam zum Ende komme, möchte ich einer Person ganz besonders danken, meinem Freund Jonathan. Danke, dass du mir immer mit Rat und Tat zur Seite standest und immer zur Stelle warst um jegliche fachlichen Fragestellungen mit mir auszudiskutieren, auch wenn ich am Ende nur entgegnete, dass ich das ja so aus der Literatur habe. Außerdem danke ich dir für die Motivation in unseren Late-Night Schreibsessions. Ich danke dir für deine bedingungslose Unterstützung und dass du immer für mich da bist. Vor allem für deine Geduld und dein Verständnis, besonders aber nicht nur in den letzten Wochen, kann ich dir nicht oft genug danken. Es ist schön dich an meiner Seite zu wissen!

Zum Schluss will ich mich noch bei meinen Eltern Maggy und Gilbert bedanken für die Unterstützung die letzten Jahre hinweg. Merci, dass ihr es mir ermöglicht habt im Ausland zu studieren und dann auch zu promovieren. Auch dass ihr mir immer wieder zugehört habt, wenn ich über die Arbeit geredet habe und meine Begeisterung für meine wissenschaftliche Arbeit unterstützt habt. Merci, dass ihr für mich da seid. Außerdem gilt auch meiner Schwester Yana ein großer Dank. Merci auch dir für die Unterstützung die letzten Jahre und immer wieder die gute Ablenkung und Erholung, ob bei einem kurzen Urlaub oder im Wellness. Een riesen Merci un ierch drei, ouni ierch wier daat net meiglech gewierscht!

Merci!

List of Publications

1. **Déborah Feller**, Marius Otten, Marco Hildebrandt, Marcel Krüsmann, Gary Bryant and Matthias Karg

   Translational and rotational diffusion coefficients of gold nanorods functionalized with a high molecular weight, thermoresponsive ligand: a depolarized dynamic light scattering study

   Published in *Soft Matter,* **2021**, 17, 4019-4026

2. Kirsten Volk, Tobias Honold, **Déborah Feller** and Matthias Karg

   Surface Lattice Resonances in Self-Templated Plasmonic Honeycomb and Moiré Lattices

   Published in *Advanced Materials Interfaces*, **2021**, 8, 210031

3. **Déborah Feller** and Matthias Karg

   Fluid interface-assisted assembly of soft microgels: recent developments for structures beyond hexagonal packing

   Published in *Soft Matter*, **2022**, 18, 6301-6312

4. Eric Sidney Aaron Goerlitzer, Mario Zapata-Herrera, Ekaterina Ponomareva, **Déborah Feller**, Aitzol Garcia-Etxarri, Matthias Karg, Javier Aizpurua, and Nicolas Vogel

   Molecular-Induced Chirality Transfer to Plasmonic Lattice Modes

   Published in *ACS Photonics*, **2023**, 10, 1821-1831

5. Adolfo Sepúlveda, **Déborah Feller**, Matthias Karg, and Denis Boudreau

   A Simple and Fast Compression-Based Method to Fabricate Responsive Gold-pNIPAM Hybrid Materials: From Thin Films to Anisotropic Microgels

   Published in *Advanced Materials Interfaces*, **2023**, 10, 2300453

6. **Déborah Feller**, Marius Otten, Michael S. Dimitriyev and Matthias Karg

   Non-close-packed plasmonic Bravais lattices through a fluid interface-assisted colloidal assembly and transfer process

   Published in *Colloid and Polymer Science*, **2024**, 302, n/a

7. **Déborah Feller**, Jiakai Wang, Julian Kippenberger, Chrisitan Washeim, Jan Meissner, Jan Meisner, Paul Mulvaney and Matthias Karg

   Following plasmon resonance coupling in soft, confined colloidal films during continuous compression

   Manuscript in preparation for submission

8. **Déborah Feller**, Julian Oberdisse, Sylvain Prévost and Matthias Karg

   In situ core overgrowth of gold core-shell microgels: Resolving changes in the polymer shell

   Manuscript in preparation for submission

Presentations at Scientific Conferences

1. **Déborah Feller**, Marius Otten, Marco Hildebrandt, Marcel Krüsmann, Gary Bryant and Matthias Karg

   Poster presentation (online participation):
   A depolarized dynamic light scattering study on gold nanorods functionalized with thermoresponsive ligands

   35th Conference of the European Colloid and Interface Society (**2021**), Athens, Greece

2. **Déborah Feller** and Matthias Karg

   Poster presentation:
   Non-close packed Bravais lattices via self-assembly of core-shell microgels

   36th Conference of the European Colloid and Interface Society (**2022**), Crete, Greece

3. **Déborah Feller** and Matthias Karg

   Poster presentation:
   Non-close packed Bravais lattices via self-assembly of core-shell microgels

   7th International Conference on Multifunctional, Hybrid and Nanomaterials (**2022**), Genoa, Italy

4. **Déborah Feller**, Christian Washeim, Sylvain Prévost and Matthias Karg

   Poster presentation:
   Form factor analysis of core-shell microgels at different states of core growth

   37th European Colloid and Interface Society Conference (**2023**), Naples, Italy

5. **Déborah Feller**, Christian Washeim, Sylvain Prévost and Matthias Karg

   Poster presentation:
   Form factor analysis of core-shell microgels at different states of core growth

   Bayreuth Polymer Symposium BPS ´23 (**2023**), Bayreuth, Germany

6. **Déborah Feller**, Elena Vanselow, Julian Oberdisse, Sylvain Prévost and Matthias Karg

   Poster presentation:
   Plasmonic core-shell microgels: The role of the core size

   Microgels 2024 (**2024**), Montabaur, Germany

7. **Déborah Feller**, Elena Vanselow, Julian Oberdisse, Sylvain Prévost and Matthias Karg

   Oral presentation:
   Plasmonic core-shell microgels: The role of the core size

   19th Zsigmondy Colloquium 2024 (**2024**), Düsseldorf, Germany

8. **Déborah Feller**, Elena Vanselow, Julian Oberdisse, Sylvain Prévost and Matthias Karg

   Oral presentation:
   Plasmonic core-shell microgels: The role of the core size

   Particle-Based Materials Symposium 2024 (**2024**), Bremen, Germany

9. **Déborah Feller**, Julian Oberdisse, Sylvain Prévost and Matthias Karg

   Poster presentation:
   Plasmonic core-shell microgels: The role of the core size

   Ostwald Colloquium (**2025**), Bielefeld, Germany

List of Abbreviations and Symbols

a	Lattice constant
A_{121}	Hamaker constant
a.u.	Arbitrary units
A_{AFM}	Area depicted in the AFM image
$A_{available}$	Available area at interface for one microgel
A_{hex}	Area of a hexagon
A_{tri}	Area of equilateral triangle
A_{trough}	Area of the trough
AFM	Atomic force microscopy
Ag	Silver
Au	Gold
AuNP	Gold nanoparticle
Au-PNIPAM	Gold-poly(*N*-isopropylacrylamide)
BIS	*N*,*N*´-methylenebisacrylamide
c	Speed of light in vaccum
c_0	Concentration
C_1	Boundary conditions
C_2	Boundary conditions
C_{abs}	Absorption cross section
C_{ext}	Extinction cross section
C_{scat}	Scattering cross section
cryo-SEM	Cryo-scanning electron microscopy
CS	Core-shell
D	Diameter
$d_{spacing}$	Interplanar spacing
$d_{c\text{-}c}$	Nearest neighbor center-to-center distance
d_{ia}	Distance of two interacting bodies
d_{path}	Pathlength of the cuvette
D_{core}	Diameter of the core
D_h	Hydrodynamic diameter
D_i	Interfacial diameter

$D_{\text{scat obj}}$	Diameter of scattering object
DLS	Dynamic light scattering
DLVO theory	Derjaguin, Landau, Verwey and Overbeek theory
e_c	Elementary charge
EM	Electromagnetic
E_0	Amplitude of the electric field
E_λ	Extinction of sample at a specific wavelength of light
FDTD	Finite difference time domain
FreSCa	Freeze-fracture shadow casting
h_M	Miller index
I	Intensity of transmitted light
I_0	Intensity of incident light
I_B	Scattering intensity of the background
I_{ExpShell}	Scattering intensity of the exponential shell form factor model
$I_{\text{fluct}}(0)$	Lorenzian intensity
I_{OZ}	Ornstein-Zernike scattering intensity
$I(q)$	Scattering intensity
k	Wave vector
k_B	Boltzmann constant
k_M	Miller index
KPS	Potassium peroxydisulfate
LBT	Langmuir-Blodgett trough
LCST	Lower critical solution temperature
LSPR	Localized surface plasmon resonance
LT	Langmuir trough
m	Diffraction order
m_0	Effective mass of the conduction electrons
m_e	Mass of the free electron
$m_{\text{scat obj}}$	Average mass of scattering object
$M_{\text{scat obj}}$	Molecular weight of scattering object
N	Number of particles
N_A	Avogadro constant
N_{AFM}	Number of microgels in the AFM image
N_{total}	Total number of microgels at the air/water interface

n	Diffraction order
n_c	Number density of charged carriers
NIPAM	*N*-isopropylacrylamide
NP	Nanoparticle
p	Dipole moment
P(q)	Form factor
PMMA	Polymethylmethacrylate
PNIPAM	Poly(*N*-isopropylacrylamide)
PS	Polystyrene
q	Magnitude of the scattering vector
Q	Quality factor
r	Distance
R	Radius
R_{circle}	Radius of circle
R_{core}	Radius of the core
R_g	Radius of gyration
R_h	Hydrodynamic radius
R_{sphere}	Radius of sphere
RA	Rayleigh anomaly
RDG	Rayleigh-Debye-Gans
RI	Refractive index
RI	Refractive index
RMC	Reverse Monte-Carlo
S(q)	Structure factor
SALS	Small-angle light scattering
SANS	Small-angle neutron scattering
SAXS	Small-angle X-ray scattering
SLD	Scattering length density
SLD_{core}	Scattering length density of the core
SLD_{Exp}	Scattering length density of the shell
$SLD_{ExpShell}$	Scattering length density of the microgel
SLD_{shell}	Scattering length density of the pure shell material
$SLD_{solvent}$	Scattering length density of the solvent
SLR	Surface lattice resonance

t_{shell}	Thickness of the shell
T	Temperature
TEM	Transmission electron microscopy
V	Volume
V_h	Hydrodynamic volume
$V_{h,swollen}$	Hydrodynamic volume at the swollen state
$V_{scat\ obj}$	Volume of the scattering object
VPT	Volume phase transition
VPTT	Volume phase transition temperature
W_{DL}	Double-layer interaction
W_{DLVO}	Net interaction of DLVO theory
W_{vdW}	Van der Waals interaction
2D	Two-dimensional
3D	Three-dimensional
α	Parameter for the exponential diffuse profile of the shell
$\alpha_{deswell}$	Deswelling ratio
α_{pol}	Polarizability
γ	Collision frequency
$\varepsilon(\omega)$	Frequency-dependent dielectric function of the free electron gas
ε_m	Dielectric constant of the surrounding medium
ε_0	Dielectric permittivity of vacuum
ε_λ	Molar attenuation coefficient of particles at a certain wavelength
ε_∞	Dielectric constant
θ	Scattering angle
θ_c	Contact angle
κ	Debye length
λ	Wavelength
λ_{Bragg}	Wavelength of the Bragg mode
λ_D	Debye length
μ_m	Permeability of the medium
ξ	Correlation length
$\rho_{scat\ obj}$	Density of the scattering object
σ	Surface charge density

σ_{SD}	Standard deviation
τ	Relaxation time
ϕ_{in}	Amount of solvent at R_{core}
ϕ_{out}	Amount of solvent at R_{core} + t_{shell}
ϕ_{polymer}	Polymer volume fraction
ω	Angular frequency
ω_{LSPR}	Frequency of LSPR
ω_{p}	Plasma frequency of the free electron gas
ψ	Electrostatic potential
ψ_0	Surface potential
°C	Degree Celsius
ΔSLD	Difference in scattering length density
$\Delta\lambda$	Resonance linewidth
$\vec{k}_{\mathrm{in}}$	Wave vector of incident radiation
$\vec{k}_{\mathrm{out}}$	Wave vector of scattered radiation
$\vec{q}$	Scattering vector

Abstract

Hybrid microgels with a rigid, inorganic core and a soft, polymeric shell are highly interesting for fundamental and applied science due to their - often synergistic - properties originating from both the core and the shell. A prominent example is gold nanoparticle core-poly(*N*-isopropylacrylamide) (PNIPAM) shell microgels. These microgels exhibit an optical response which arises from two primary contributions: the localized surface plasmon resonance (LSPR) of the gold nanoparticle and the strong scattering from the PNIPAM shell. To enhance the plasmonic properties, the gold cores are overgrown *in situ* within the shell, increasing their size and absorbance. This results in a stronger plasmonic signal that can outweigh the scattering contribution of the shell. At the same time, the crosslinked PNIPAM shell renders such colloids with thermoresponsive properties due to the lower critical solution temperature behavior of PNIPAM in water. The polymeric shell further enables adsorption of the microgels at fluid interfaces and promotes their self-assembly into hexagonally ordered arrangements with interparticle distances in the range of the wavelength of visible light. Here, the shell acts as stabilizer and spacer for the gold cores. These arrangements can be transferred onto substrates to form periodic coatings that feature pronounced plasmonic properties. Even though they find application in the field of, e.g., sensing, only little is known about the interplay of the structural properties and the interface-assisted assembly behavior of such microgels.

This thesis investigates the structural and optical properties of plasmonic core-shell microgels and their suitability as colloidal building blocks for the preparation of plasmonic monolayers through interface-assisted assembly. One objective is to investigate the microgels before and after the overgrowth of the core *in situ* within the shell. Small-angle scattering techniques are used to follow the core growth, but more importantly to investigate the resulting change in the local morphology of the microgel shells – a change that has not been addressed so far. Crucial for the clarification of the structural changes are the pronounced differences in contrast of the cores and the shells for neutrons and X-rays. While the cores primarily contribute to the scattering signal in X-ray scattering experiments, the polymeric shells provide excellent contrast in neutron scattering. Prior to core overgrowth, the scattering profiles of the microgels are described by an exponential shell form factor model, whereas the scattering

profiles of the microgels after the core overgrowth significantly deviate from the common form factor models. Consequently, reverse Monte-Carlo simulations are employed to reveal structural changes within the polymer shell induced by the overgrowth of the core. While the overall dimensions of the microgels do not significantly change, as revealed by, e.g., dynamic light scattering, analysis by transmission electron microscopy and reverse Monte Carlo simulations point to a densification of the polymer shell in the close vicinity of the gold nanoparticle cores upon *in situ* overgrowth of those.

The thesis further explores the fabrication of non-hexagonal, plasmonic monolayers using fluid interface-assisted assembly. Typically, the microgels assemble at fluid interfaces and are then transferred to a substrate resulting in a hexagonally ordered monolayer. By adjusting parameters such as transfer direction, speed and substrate contact angle, 2D non-close-packed Bravais lattices of gold nanoparticles are obtained. All five lattices exhibit pronounced LSPR peaks as shown by extinction spectroscopy and supported by finite difference time domain simulations. The lattices show surface lattice resonance, if the RI environment around the gold nanoparticle cores is adjusted to enable plasmonic-diffractive coupling. Further it is proven that the transfer process is applied to microgels with different dimensions resulting in the same lattices with other periodicities.

A novel aspect of this research is the *in situ* measurements of monolayers of plasmonic core-shell microgels at the air/water interface. This is achieved by using a Langmuir trough combined with an optical fiber-based extinction spectrometer. *In situ* spectroscopy is performed on plasmonic monolayers with interparticle distances in the range of the wavelength of visible light. At the interface, resonance coupling with in-plane diffractive modes is enabled. This is followed in dependence of interparticle distance, controlled through uniaxial compression of the monolayer. A shift of the resonance peak is observed during the reduction of the total interfacial area. These findings are validated by COMSOL simulations which support that at large interparticle distances plasmonic-diffractive coupling is enabled providing a sharp narrow surface lattice resonance peak. This study provides a deeper understanding of not only the plasmonic response, but also of the interfacial behavior of assembled microgels in dependence of their packing fraction.

1. Introduction

Microgels represent a prominent subgroup in colloidal science and were intensively studied as model system for soft colloidal particles in the last years.[1-7] These crosslinked polymer networks that are highly swollen by a large amount of solvent, exhibit dimension in the range of 100 nm up to several micrometers.[5, 8-10] Microgels present characteristics associated to surfactants, macromolecules and colloids.[5, 11] Based on their composition, microgels can be triggered by external stimuli, such as pH and temperature.[12-17] Most often their response leads to expulsion of solvent from the three-dimensional network, resulting in a reduction of its effective size. In 1986, Pelton and Chibante introduced the thermoresponsive microgel based on poly(*N*-isopropylacrylamide) (PNIPAM), which has become the most studied microgel.[18] PNIPAM microgels internally crosslinked with *N*,*N´*-methylenebisacrylamide (BIS) were synthesized via a free-radical precipitation polymerization above the lower critical solution temperature (LCST) of the PNIPAM homopolymer at around 32 °C.[19, 20] Via this synthesis route monodisperse, spherical microgels in the size range of submicron to microns could be obtained. At low temperatures, PNIPAM microgels are highly swollen with solvent and exhibit a large volume. As soon as the temperature is increased above the volume phase transition temperature (VPTT), the microgels undergo a volume phase transition (VPT) by expelling solvent and thereby decreasing in size. At this stage PNIPAM microgels still host a large amount of solvent, maintaining their soft and deformable character. This characteristic differentiates them from more rigid polymeric colloids such as polystyrene- (PS) or polymethylmethacrylate-based (PMMA) microgels.[21, 22] The physicochemical properties, e.g., swelling and responsive behavior, of these microgels could be further tuned by implementing different crosslinker concentrations or comonomers.[13, 23-25] The soft character and the VPT behavior of PNIPAM microgels lead to their usage as model system to study interactions of soft particles.[26-29] Here, the microgel volume fraction at a given number density can be tuned only by varying the temperature.[30, 31] Furthermore, they are interesting for applications such as sensing or drug delivery systems.[32-34]

In 1999, Zhang and Pelton observed that PNIPAM microgels spontaneously adsorb to the air/water interface leading to a significant reduction in interfacial tension.[35]

Because of this, microgels can also stabilize emulsions, which has been intensely studied during the last decades.[36-39] In contrast to hard colloids, microgels can interconnect and stretch laterally at interfaces, as shown by various studies employing cryo-scanning electron microscopy (cryo-SEM)[40] and freeze-fracture shadow casting (FreSCa) cryo-SEM.[41, 42] FreSCa cryo-SEM measurements of the three-dimensional interfacial structure revealed that the microgels are predominantly immersed in the aqueous phase and only slightly in the oil or air phase. Furthermore, microgels reach interfacial diameters D_i, which are considerably larger than their hydrodynamic diameters D_h in bulk.[41] At interfaces, microgels can spontaneously self-assemble into hexagonally ordered monolayers, representing their equilibrium structure. Their interfacial dimensions can be reduced below their dimensions in dilute dispersion by compressing the monolayer. Due to their soft nature, microgels maintain their hexagonal arrangement at the interface up to a certain level of compression. This unique behavior led to various studies analyzing the phase behavior of microgels at flat interfaces by reducing the available surface area.[43-47] The microstructure of the monolayers at different surface areas are mostly studied after the transfer from the interface to a solid substrate. These coated substrates were then found to be interesting for applications such as masks for nanolithography.[47, 48]

The functionalities of microgels can be extended by incorporating inorganic nanoparticles (NP), such as silica or gold nanoparticles. Karg *et al*. demonstrated that gold core–PNIPAM shell microgels exhibit distinct optical properties due to the plasmonic gold nanoparticle (AuNP) core featuring a localized surface plasmon resonance (LSPR).[49, 50] Such core-shell (CS) microgels also adsorb to the interface and spontaneously self-assemble into highly ordered plasmonic monolayers. The PNIPAM shell enables the adsorption to the interface and acts as a spacer in the crystal lattice, while the AuNP cores contribute to the optical response to the monolayer. The response can be tuned by altering the size, shape and composition of the core[51-53] or by changing the interfacial dimensions of the microgel, thereby influencing the interparticle distance.[54, 55] The advantage of AuNP cores in respect to, e.g., silica cores is that they can be overgrown with Au or silver (Ag) ions *in situ* in the PNIPAM shell, as demonstrated by various works.[51, 52, 54] This post modification can be performed without damaging the PNIPAM shell. The increase in size shifts the LSPR to higher wavelengths and enhances its intensity. For CS microgels with small AuNP cores (diameter < 16 nm), the Rayleigh-Debye-Gans scattering of the PNIPAM

shell dominates and outweighs the absorption of the AuNP cores.[49, 56] When the cores are overgrown (diameter > 50 nm), the scattering of the shell remains constant, but the extinction of the individual AuNP increases. Thus, the optical response of Au-PNIPAM microgels is dominated by the LSPR of the individual AuNP. The plasmonic characteristic of such arrays can be tuned by varying the interparticle distance between the CS microgels. A common approach to do so, is by applying CS microgels at the interface in a Langmuir trough equipped with movable barriers to reduce or extend the surface area available for the microgels.[48] When the interparticle distance is in the order of the wavelength of visible light, plasmonic-diffractive coupling can occur. This coupling process results in a surface lattice resonance (SLR) which exhibits a narrower peak at higher wavelengths compared to the LSPR of the individual AuNP cores.[55, 57] Because of this phenomenon, such arrangements are interesting as plasmonic coatings.[58-61]

Most often such monolayers present a hexagonal order, but in the last years, the interest for non-hexagonal structures prepared *via* interface-assisted assembly has grown significantly.[62] Various fabrication techniques have been developed, such as controlling the assembly by adjusting the surface pressure,[63] assembly of binary mixtures[48, 64, 65] and multi-deposition onto a single substrate.[66-68] The latter is a typical approach to obtain non-hexagonal structures of Au-PNIPAM and Ag-PNIPAM microgels. Honold *et al*. first introduced this preparation method.[53] The authors transferred a first monolayer of one microgel type onto the substrate. After drying, a subsequent monolayer of another microgel type was deposited onto the same substrate. This led to the formation of honeycomb or Moiré lattices in dependence of the drying speed, as later shown by Volk *et al*.[67]

A commonality of these techniques is that microgels are transferred from the fluid interface to a solid substrate and analyzed *ex situ* by various microscopy techniques. It was assumed that the interfacial structure of the monolayer was maintained during the transfer. In the literature, several groups reported observing a transition during the compression of the monolayer and assumed that it occurs at the interface. This transition was assigned to an ´isostructural solid-solid phase transition´ where two hexagonal ordered phases coexist, with one phase of swollen microgels and one denser phase with collapsed microgels.[44, 46, 69-71] Recently, Kuk *et al*. showed that the microstructure at the interface is not necessarily retained on the substrate, if dried slowly.[72] The authors analyzed microgels *in situ* at the air/water interface by

small-angle light scattering (SALS). During compression of the monolayer, they observed a continuous decrease of the distance between the microgels and concluded that the structure of the monolayer can be altered by the transfer method, resulting in clusters of microgels. These findings underline the importance of *in situ* measurements to elucidate the microstructure at interfaces. However, *in situ* measurements remain challenging due to the movement of both, interface and microgels, as well as the small size of microgels. Kuk *et al*. circumvented the size limitations by synthesizing micron-sized microgels. Consequently, the authors were not only able to detect the microgels using their SALS setup, but also to track them using a light microscope.[72] Rubio-Andrés *et al*. investigated monolayers of PNIPAM microgels at the interface during compression by using an *in situ* microscope.[73] The microscopy images showed hexagonally ordered monolayers at the interface regardless of the compression. Thus, similar to Kuk *et al*. they found a continuous decrease of the interparticle distance with increasing compression. The authors further investigated the drying of a transferred monolayer on a substrate and found that clustering only occurs during the drying of the colloidal monolayer, as soon as the capillary forces become stronger than the adhesion force of the microgels. Recently, new insights in the interplay between the compression behavior of microgels and the structure of the corresponding monolayers were given by Kawamoto *et al*.[74] The authors visualized PNIPAM-based microgels at the interface in a Langmuir trough by a fluorescence microscope. They found that independent of the crosslinker density, the microgels deformed and assembled into hexagonally ordered structures at the air/water interface. Upon compression, the hexagonal arrangement of the microgels was maintained. These results could help to better understand the deformation and compression of microgels at fluid interfaces. Vialetto *et al*. extended the understanding of microgels at fluid interfaces by studying single PNIPAM microgels at the oil/water interface.[75] The authors recorded *in situ* atomic force microscopy *(*AFM) images of single microgels from the side of the oil and aqueous phase to reconstruct the 3D shape of the microgel at the interface. They confirmed findings of previous works and concluded that most of the volume of the microgel was located in the aqueous phase and that the microgel deformed and stretched into the classical ´fried-egg´ like shape at the interface. The authors further found that the volume of the microgel located in the aqueous phase deswelled upon increase of the temperature above the VPTT. The volume located in the oil phase remained

unchanged, as this part is always collapsed due to the bad solvent conditions of the oil for PNIPAM.

The main objective of this thesis was to resolve the structural and optical properties of plasmonic CS microgels to develop functional colloidal building blocks for the preparation of plasmonic monolayers *via* interface-assisted assembly. These microgels were used to exploit transfer methods from the interface to a substrate for the fabrication of non-close-packed periodic monolayers of AuNP covering all two-dimensional (2D) Bravais lattices. Furthermore, the enhanced plasmonic response of the CS microgels allowed spectroscopic measurements of plasmonic monolayers at the interface. This enabled, for the first time *in situ* measurements of assembled microgels exhibiting smaller dimensions than those used in previous studies for interfacial measurements.

Chapter 4 addresses the synthesis and characterization of plasmonic CS microgels that serve as building blocks throughout this thesis. Following an established protocol,[76] CS microgels with monodisperse, spherical AuNP as core were synthesized using seeded precipitation polymerization. Subsequently, the cores were overgrown *in situ* within the polymer shell. As proven by dynamic light scattering (DLS), the overall hydrodynamic diameter, D_h, of the microgel was not affected by the growth of the core. The CS microgels before and after the overgrowth of the core are schematically shown in **Figure 1.1**.

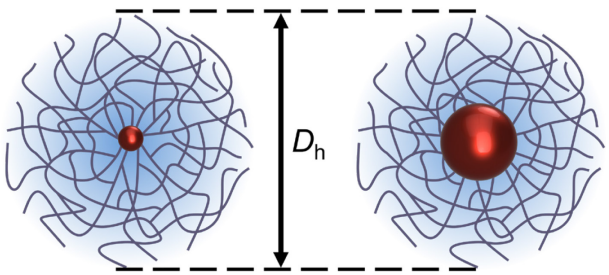

Figure 1.1. Schematical illustration of the cross-section of Au-PNIPAM microgels before (left) and after (right) core overgrowth. Their hydrodynamic diameter D_h is marked. The shown dimensions are schematically and do not depict the scaling in reality.

The core growth was followed by small-angle X-ray scattering to extract core sizes and by extinction spectroscopy to track the optical behavior of the CS microgels. Small-angle neutron scattering (SANS) was used to identify changes in the internal morphology of the shell caused by the overgrowth of the core, as these changes have not been addressed yet. The comparison between scattering profiles of the microgels before and after overgrowth of the core revealed differences in the internal structure of the shell. Density profiles of the microgels before the overgrowth were extracted from the scattering curves and supported by reverse Monte-Carlo (RMC) simulations. For CS microgels with overgrown cores, the scattering curves could not be described by common form factor models and polymer density profiles were only accessible *via* RMC simulations. Temperature-dependent DLS measurement confirmed that neither the overall dimension nor the thermoresponsive behavior of the microgels were influenced by the overgrown cores.

Due to the pronounced optical properties, such microgels are suitable building blocks for plasmonic superstructures such as self-assembled plasmonic monolayers. These monolayers can be prepared by different techniques while fluid interface-assisted assembly has emerged as main method. Typically, the microgels assemble into a hexagonal order upon contact of their shells at the interface. These arrangements can be transferred from the interface to a substrate resulting in periodic plasmonic coatings of non-close-packed AuNP. Recently, Hummel *et al*. presented an interface-assisted method to prepare non-hexagonal arrangements of non-deformable, rigid particles on substrates.[77] Thereby, the authors managed to obtain all 2D Bravais lattices of non-close packed particles.

In this thesis, the preparation method of Hummel *et al*. was adapted to the CS microgels with large cores (**Chapter 5**). The PNIPAM shell enabled adsorption of the microgels to the air/water interface. Here, the shell acted as spacer between AuNP cores. The five Bravais lattices could be prepared on substrates by varying parameters, such as transfer direction and speed, as well as contact angle of the substrates. This resulted in different non-close-packed plasmonic arrangements. The microstructures were visualized by AFM. The optical response of the ordered monolayers was studied by extinction spectroscopy and the findings were supported by finite difference time domain (FDTD) simulations. Furthermore, the plasmonic response of the ordered Au cores on substrates was investigated for different refractive index (RI) environments.

While the microstructure of such monolayers is typically studied *ex situ*, i.e., after monolayer transfer onto solid supports, studies that address the structural arrangement at the fluid interfaces are scarce. Only recently, optical microscopy and SALS were employed to study microgel monolayers *in situ*.[72-74] Both methods can only be applied, if the size of the microgels exceed a certain limit to overcome the optical resolution. Thus, the visualization of the microstructure at the air/water interface remains a challenge for smaller microgels.

In this thesis, a self-built setup was used to measure *in situ* extinction spectra of the plasmonic CS microgels at the air/water interface in a Langmuir trough (**Chapter 6**). The analyzed microgels exhibited sizes below the optical resolution. The high absorption of the AuNP cores compared to the low scattering of the PNIPAM shell in microgels with overgrown cores was utilized to visualize the optical response of a monolayer at the interface. The optical response was investigated in dependence of the surface pressure. The *ex situ* microstructure at low surface pressure was taken as reference to determine the interparticle distance at the interface. Thus, the interparticle distance could be linked to peak positions of *ex situ* and *in situ* extinction spectra. The experimental findings were validated by COMSOL simulations to clarify the physical processes underlying the optical response.

2. Theoretical Background

2.1. Microgels

Microgels are three-dimensional crosslinked polymer networks, which possess sizes in the micron and submicron range.[5, 8, 10] The network of the microgel exhibits an internal gel-like structure due to physical and/or chemical crosslinking between polymer chains. Physical crosslinking refers either to entanglements and loops between individual polymer chains, to hydrogen bonds between polymer chains or to ionic crosslinking. The latter occurs when polymer chains exhibit a polyelectrolyte-like character and function as macroions.[78] Oppositely charged bifunctional molecules or even ions can serve as linking point between individual polymer chains. Chemical crosslinking is equivalent to covalent bonding between polymers. Typically, crosslinkers are added as comonomers during the microgel synthesis to achieve the bonding of individual polymer chains. Comonomers for chemical crosslinking present at least two functional groups with the ability to react intermolecularly, such as double bonds or thiols, which serve as bridging points within the polymer network. In the following work, predominantly chemically crosslinked microgels will be addressed.

Microgels can host a high amount of solvent, giving them a soft character.[5, 8, 10, 11] For this reason, microgels are often employed as model system to study soft particle interactions.[27, 79] The focus is mainly on microgels containing water as solvent. These are also called hydrogels.[8] However, internal solvent content, size and soft, polymeric nature of microgels makes it difficult to designate them into a specific material class, so they range between surfactants, colloids and macromolecules.[5, 11, 80]

The properties of microgels can be tuned by varying type and amount of crosslinker or by incorporating responsive polymers. Thus, depending on the composition microgels can be responsive to external stimuli, such as pH[17, 81, 82], ionic strength[83, 84] or temperature.[12, 13, 85-87] Triggered by external stimuli, microgels can release or take up solvent and thereby collapse or swell resulting in a decrease or increase of their effective volume. Before and even after the collapse, microgels still contain a large

amount of solvent.[21] This distinguishes them from rigid, non-deformable colloids, such as silica-, polystyrene- (PS) or polymethylmethacrylate- (PMMA) based colloids.

In the following part, thermoresponsive poly(*N*-isopropylacrylamide) (PNIPAM) microgels will be discussed in detail in terms of their internal structure and responsive behavior.

2.1.1. Thermoresponsive microgels

PNIPAM microgels were intensively studied since their introduction in 1986 by Pelton and Chibante.[18] They are most commonly synthesized *via* free-radical precipitation polymerization in dispersion resulting in monodisperse, spherical microgels. Typically, *N*,*N´*-methylenebisacrylamide (BIS) is used as chemical crosslinker, due to its chemical similarity to *N*-isopropylacrylamide (NIPAM). BIS features a higher reactivity than the monomer NIPAM, which leads to a faster consumption of BIS during the initial part of the synthesis.[88] Consequently, microgels exhibit a gradient in the crosslinker density with a much higher crosslinker and polymer density in the inner than the outer part.[21, 88-91] This results in a core-shell like structure, often referred to as fuzzy sphere which is schematically depicted in **Figure 2.1 top left**. The inner part is stiffer, which can influence interactions between microgels in bulk and the loose polymer chains in the periphery of microgels sterically stabilize them. Similar to the lower critical solution temperature (LCST) at around 32 °C of linear PNIPAM,[19, 20] the corresponding microgels exhibit a volume phase transition (VPT) at a specific temperature depending on, e.g., the crosslinker density. Their volume and morphology can be adjusted by changing temperature above or below the volume phase transition temperature (VPTT), as shown in **Figure 2.1**. At temperature below the VPTT, microgels are highly swollen with a water content of up to 80 %,[21] as polymer-solvent interactions are highly favorable. Here, microgels display their largest volume and the polymer volume fraction (ϕ_{Polymer}) is constant in the inner part. At a certain radius it decreases to the outside, as shown by simulated radial density profile in **Figure 2.1 bottom left**. The profiles were calculated based on the exponential shell model.[56, 92] When the temperature increases, the microgels expel water which results in a collapse of the network.[21] The size of the microgels decreases and they exhibit a hard sphere-like structure, as shown in **Figure 2.1 right**. The border of the microgel

become more defined and the polymer density is homogeneously distributed in the polymer network, which is presented as a constant ϕ_{Polymer} in the radial profile. The network still contains up to 50 % of solvent which classify these microgels as soft colloids even at high temperatures.

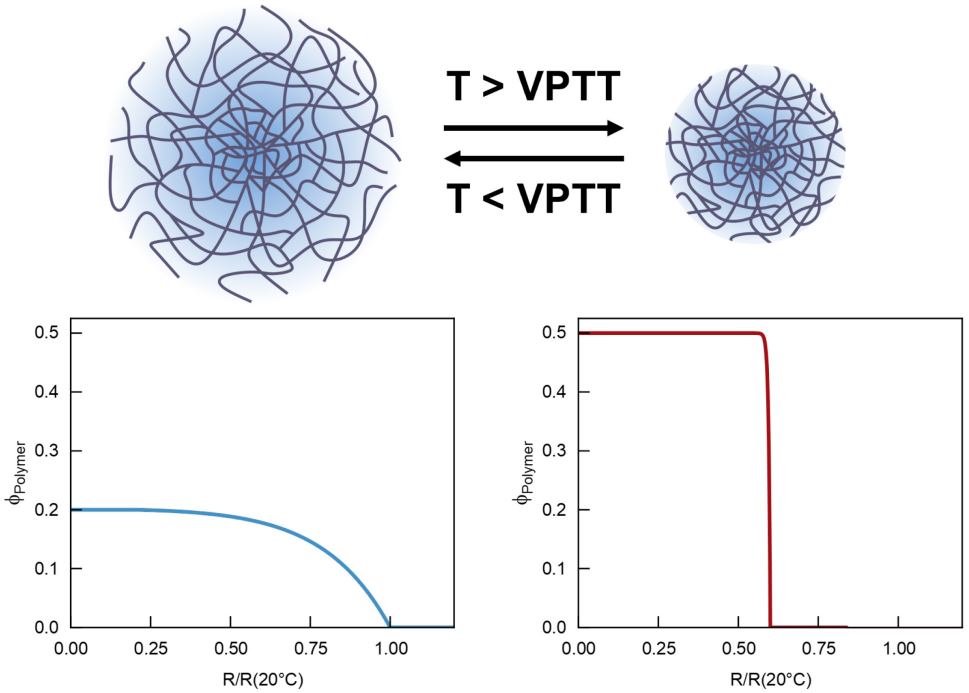

Figure 2.1. Schematic depiction of a thermoresponsive microgel (top) and the corresponding radial density profiles of the polymer volume fraction (ϕ_{Polymer}) (bottom). Below the VPTT, the microgel features a core-shell like structure with a fuzzy shell and the polymer volume fraction decreases to the outside (left). Above the VPTT, the microgel exhibits a hard sphere-like structure with a homogenously distributed polymer volume fraction (right). The profiles were calculated based on the exponential shell model[56, 92] with estimated values in accordance with the literature.[21]

The thermoresponsive behavior of PNIPAM based microgels can be tuned by, e.g., changing the crosslinker content added during the synthesis. BIS shows a more hydrophilic character than the monomer NIPAM due to two amid groups compared to one. For this reason, an increased amount of BIS increases the hydrophilicity of the corresponding microgels and thereby shifts the VPTT to higher temperatures.[89, 93] Furthermore, a higher crosslinker content renders the microgels stiffer and thereby

decreases its swelling capacity.[89] The latter is characterized by the deswelling ratio $\alpha_{\mathrm{deswell}}$, the inverse of which is also known as the swelling ratio. $\alpha_{\mathrm{deswell}}$ refers to the relation between the hydrodynamic volume V_{h} at a specific temperature T and the hydrodynamic volume in the swollen state $V_{\mathrm{h,swollen}}$ as shown in **equation 2.1**.[94]

$$\alpha_{\mathrm{deswell}}(T) = \frac{V_{\mathrm{h}}(T)}{V_{\mathrm{h,swollen}}} \tag{2.1}$$

For PNIPAM microgels, the swollen state often correlates to the state at 20 °C. Values for $\alpha_{\mathrm{deswell}}$ range from 0 to 1 and the larger the value the stiffer the microgel. The deswelling ratio is often used to compare microgels in terms of their swelling capacity over a broad range of temperatures.

2.1.2. Core-shell microgels

Core-shell (CS) microgels with a rigid core and a soft polymer shell present a unique subgroup of hybrid material featuring properties of the individual building blocks. In literature, PS is often used as polymeric, hard core, which is neither swellable nor responsive in water and PNIPAM as shell material. Such PS core-PNIPAM shell microgels are polymerized *via* a one-step or two-step synthesis[95, 96] and then employed as, e.g., model colloids to study particle assemblies and rheological properties of the corresponding dispersions.[97, 98] Further, inorganic cores can be implemented and most often consist of iron oxide, silica, gold or silver.[49, 99-102] They attribute magnetic, optical or catalytic characteristics to these hybrid microgels. Silica core-PNIPAM shell microgels present an interesting hybrid material, because the core can be removed without damaging the shell. Thus, it is possible to prepare hollow microgels to study their behavior in crowded environments.[103, 104]

Au core-PNIPAM shell microgels are a prominent example of CS microgels, as they are interesting for their potential use in applications in, e.g., sensors and optics.[105-107] These CS microgels are synthesized *via* seeded precipitation polymerization with AuNPs acting as seeds. Via this synthesis route it is possible to obtain monodisperse CS microgels, each with a single core. The final microgels still exhibit the thermoresponsive behavior of PNIPAM, but the VPTT is slightly shifted to higher

temperature, i.e., around 34 °C.[21] Additionally, the CS microgels present the optical properties of single AuNPs, which will be discussed in the following.

2.2. Optical properties of gold nanoparticles

Core-shell microgels with plasmonic AuNP cores represent the main colloidal building blocks in this thesis. For this reason, this chapter addresses the optical properties of AuNPs. The first part focuses on the optical response of AuNPs in dispersion and the influence of various parameters. The second part addresses the optical response of lattices formed by AuNPs.

2.2.1. Gold nanoparticles in dispersion

The optical properties of metals can be described by a plasma model introduced by Paul Drude in 1900,[108] which considers the behavior of free conduction electrons in metals in response to external electromagnetic fields. In the model, the metal is defined as positively charged background ion cores at fixed positions with a gas of free, negatively charged electrons. Even though electron-electron interactions and details of the lattice potential are neglected, the Drude model is widely used. The classical Drude model describes the frequency-dependent dielectric function of the free electron gas $\varepsilon(\omega)$ as given in **equation 2.2**.[109]

$$\varepsilon(\omega) = 1 - \frac{\omega_p^2}{\omega^2 + i\gamma\omega} = \varepsilon_1(\omega) + i\varepsilon_2(\omega) \tag{2.2}$$

With $\varepsilon_1(\omega)$ and $i\varepsilon_2(\omega)$ as real and imaginary components as given by **equations 2.3 and 2.4**, respectively.

$$\varepsilon_1(\omega) = 1 - \frac{\omega_\mathrm{p}^2\tau^2}{1 + \omega^2\tau^2} \tag{2.3}$$

$$\varepsilon_2(\omega) = \frac{\omega_p^2 \tau}{\omega(1+\omega^2\tau^2)} \tag{2.4}$$

Here, $\omega = 2\pi\frac{c}{\lambda}$ represents the angular frequency of the incident light with c corresponding to the speed of light in vacuum with $3 \cdot 10^8$ m/s and λ to the wavelength of light. γ refers to the characteristic collision frequency at which the oscillating motion of electrons in response to the electromagnetic (EM) field is damped. The collision frequency is given by $\gamma = \frac{1}{\tau}$ with τ as the relaxation time of the free electron gas. ω_p corresponds to the plasma frequency of the free electron gas and is given by **equation 2.5**.

$$\omega_p^2 = \frac{n_c e_c^2}{\varepsilon_0 m_0} \tag{2.5}$$

With n_c referring to the number density of charged carriers and e_c to the elementary charge. ε_0 corresponds to the dielectric permittivity of vacuum with a value of $8.854 \cdot 10^{-12}$ F/m and m_0 corresponds to the effective mass of the conduction electrons which is different from the mass of the free electron m_e.

For noble metals, such as gold and silver, the Drude model needs to be extended for the region of $\omega > \omega_p$. Here, the optical response is governed by the behavior of the free electrons. The extended Drude model considers the effect of positive background cores by implementing a dielectric constant ε_∞ as given by **equation 2.6**.

$$\varepsilon(\omega) = \varepsilon_\infty - \frac{\omega_p^2}{\omega^2 + i\gamma\omega} \tag{2.6}$$

If metal NPs are employed, for instance AuNPs in this work, the collective oscillation of the free electrons in response to the EM field of light leads to localized surface plasmon resonance (LSPR), a non-propagating excitation.[109] The curved surface of the NPs exercise an effective restoring force on the free electrons, leading to their oscillations in-phase and forming quasi-particles, called plasmons. Thus, the resonance leads to enhanced electromagnetic fields near the surface of the NPs. The interaction of the EM field with the NPs can be investigated by using the quasi-static

approximation which is valid for NPs displaying diameters *D* much smaller than the wavelength λ of light, i.e., *D* << λ.[109] The approximation considers the EM field as uniform across the entire volume of the NP. The NP can then be modeled as oscillating dipole. The approximation is valid for all AuNPs used in this work, as the diameters are smaller than 100 nm.

The dipole moment p induced to spherical NPs with radius R_{sphere} by the EM field is given by **equation 2.7**.

$$p = 4\pi\varepsilon_0\varepsilon_{\text{m}}R_{\text{sphere}}^3\frac{\varepsilon(\omega)-\varepsilon_{\text{m}}}{\varepsilon(\omega)+2\varepsilon_{\text{m}}}E_0 \tag{2.7}$$

ε_{m} refers to the dielectric constant of the surrounding medium, which is isotropic and non-absorbing and E_0 is the amplitude of the electric field of the incident light. As the polarizability α_{pol} is directly related to p via $p = \varepsilon_0\varepsilon_{\text{m}}E_0\alpha_{\text{pol}}$, the polarizability can be given by **equation 2.8**.[110]

$$\alpha_{\text{pol}} = 4\pi R_{\text{sphere}}^3\frac{\varepsilon(\omega)-\varepsilon_{\text{m}}}{\varepsilon(\omega)+2\varepsilon_{\text{m}}} \tag{2.8}$$

Under the condition, that $\varepsilon(\omega)+2\varepsilon_{\text{m}}$ is a minimum, the polarizability is resonantly amplified leading to a simplified resonance given by the Fröhlich condition. The latter is depicted by **equation 2.9**.[109]

$$Re[\varepsilon(\omega)] = -2\varepsilon_{\text{m}} \tag{2.9}$$

If this condition is met, the dipole oscillation of the NP is in resonance with the EM field, leading to the enhancement of the local electromagnetic field, as well as increased absorption and scattering cross sections of the NPs which will be discussed later in this chapter. This resonant mode presents the dipolar surface plasmon which is only valid for metallic NPs with *D* << λ. Such a dipolar LSPR is schematically shown for two AuNPs with *D* << λ in **Figure 2.2**.

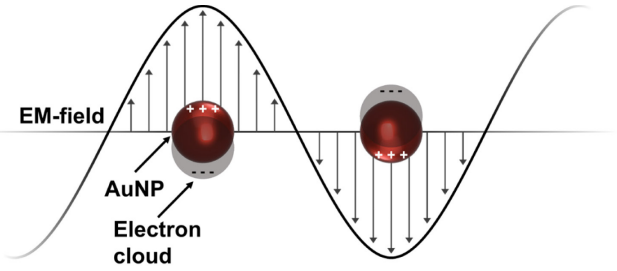

Figure 2.2. Schematic illustration of dipolar LSPR for two AuNPs excited by an EM-field of incoming light.

By implementing the Drude model (**equation 2.6**) into the Fröhlich condition, the frequency of the LSPR ω_{LSPR} for small spherical NPs can be approximated by **equation 2.10**.

$$\omega_{\mathrm{LSPR}} = \frac{\omega_{\mathrm{p}}}{\sqrt{\varepsilon_{\infty} + 2\varepsilon_{\mathrm{m}}}} \tag{2.10}$$

For a spherical NP consisting of a Drude metal in air ($\varepsilon_{\mathrm{m}} = 1$), the Fröhlich criterium is fulfilled at a frequency $\omega_{\mathrm{LSPR}} = \frac{\omega_{\mathrm{p}}}{\sqrt{3}}$. **Equations 2.9 and 2.10** show the strong dependence of the frequency on the dielectric permittivity of the surrounding environment, which itself is linked to the refractive index *RI* through **equation 2.11**.[111]

$$RI = \sqrt{\varepsilon_{\mathrm{m}}\mu_{\mathrm{m}}} \tag{2.11}$$

With μ_{m} representing the permeability of the medium. μ_{m} is approximated to 1 and therefore *RI* can be simplified to $RI = \sqrt{\varepsilon_{\mathrm{m}}}$. Thus, the resonance is shifted to lower frequency, i.e., to higher wavelengths, if the refractive index of the medium is increased.[109]

Metal NP absorb and scatter light and the efficiency is expressed by the absorption and scattering cross section C_{abs} and C_{scat} dependent on the polarizability α_{pol} as depicted by **equations 2.12 and 2.13**.[109, 112]

$$C_{\mathrm{abs}} = k\mathrm{Im}\left[\alpha_{\mathrm{pol}}\right] = 4\pi k R_{\mathrm{sphere}}^{3}\mathrm{Im}\left[\frac{\varepsilon(\omega) - \varepsilon_{\mathrm{m}}}{\varepsilon(\omega) + 2\varepsilon_{\mathrm{m}}}\right] \tag{2.12}$$

$$C_{\mathrm{scat}} = \frac{k^4}{6\pi}\left|\alpha_{\mathrm{pol}}\right|^2 = \frac{8\pi}{3}k^4 R_{\mathrm{sphere}}^6 \left|\frac{\varepsilon(\omega)-\varepsilon_{\mathrm{m}}}{\varepsilon(\omega)+2\varepsilon_{\mathrm{m}}}\right|^2 \quad (2.13)$$

With k referring to the wave vector as $k = \frac{\omega}{c} = \frac{2\pi}{\lambda}$. For small particles with diameters below 100 nm, the efficiency of absorption scales with R_{sphere}^3 and dominates over the efficiency of scattering which scales with R_{sphere}^6.[109] If the Fröhlich condition is met, absorption and scattering and thus extinction overall is resonantly strengthened at the dipole plasmon resonance. In the quasi-static approximation, a spherical nanoparticle with a volume *V* and a dielectric function as given in **equation 2.2** exhibit an extinction cross section C_{ext} which is the sum of absorption and scattering as shown by **equation 2.14**.

$$C_{\mathrm{ext}} = C_{\mathrm{abs}} + C_{\mathrm{scat}} = 9\frac{\omega}{c}\varepsilon_{\mathrm{m}}^{3/2} V \frac{\varepsilon_2(\omega)}{[\varepsilon_1(\omega)+2\varepsilon_{\mathrm{m}}]^2+\varepsilon_2(\omega)^2} \quad (2.14)$$

Thus, the intensity of the extinction is highly influenced by the size of the NP, such as the larger the NP, the higher the value of C_{ext}. The extinction cross section of a single particle decreases the intensity of light detected in an extinction spectroscopy experiment. When AuNPs dispersed in a medium are illuminated with light of an intensity I_0, the intensity of the transmitted light I is weakened due to absorption and scattering processes as given by **equation 2.12** to **2.14**. The attenuation of the light therefore depends on the extinction cross section of a single particle, the number of particles *N* and the pathlength of the cuvette d_{path} containing the sample. The Beer-Lambert law expressed the relation of the loss in intensity with these parameters in **equation 2.15**.

$$E_\lambda = log_{10}\left(\frac{I_0}{I}\right) = \frac{C_{\mathrm{ext}} N d_{\mathrm{path}}}{2.303} \quad (2.15)$$

With E_λ representing the extinction of the sample at a specific wavelength of light. Further details on extinction spectroscopy experiments, as well as a schematic setup are discussed in more detail later in **Chapter 2.6**.

The LSPR phenomenon can be detected as well-pronounced peak in an extinction spectrum. The position and intensity of the peak can be tuned by different parameters

such as shape,[113, 114] composition,[115] size[116, 117] and RI environment of the NP.[116, 118] The effects of some of these parameters on the peak are shown in **Figure 2.3**.

Experimental extinction spectra of AuNPs with different sizes in aqueous dispersion are depicted in **Figure 2.3 a**. The AuNPs were grown from approximately 15 nm (dark blue) to approximately 45 nm (dark brown) in diameter in four steps. The enhancement of the extinction, according to **equation 2.14**, and the shift of the resonance peak to higher wavelengths can be clearly identified in the spectra. An increase of 30 nm in diameter results in a shift of 14 nm, which can attributed to retardation effects.[109] When the size of NPs increases, the distance between charges located at opposite interfaces increases as well and thus reduces the restoring force in between. Less energy is then required to induce the oscillation of the free electrons, resulting in a decrease in the resonance frequency, i.e., an increase in wavelength.

The effect of the RI on the LSPR of AuNPs with a diameter of 15 nm is illustrated by simulated extinction spectra in **Figure 2.3 b**. Here, the RI increases from 1 to 1.3, 1.4 and 1.5 (from dark blue to brown) leading to an enhancement of the resonance peak and a shift to higher wavelengths (see **equations 2.9 and 2.10**). The total shift of the LSPR equals 30 nm.

The surrounding environment of AuNPs can not only be tuned by the dispersion medium, but also by encapsulation of AuNPs into a polymeric shell, e.g., PNIPAM shell. An experimental extinction spectrum of CS microgels (dark blue) is shown in respect to one of bare AuNPs with a diameter of approximately 15 nm (red) in **Figure 2.3 c**. The LSPR peak for bare AuNPs can be clearly identified at λ = 518 nm, whereby the peak for encapsulated AuNPs can just be identified as a small shoulder. Here, the Rayleigh-Debye-Gans (RDG) scattering of the PNIPAM shell dominates the spectrum and overweighs the LSPR of the AuNP core.[49, 56] By overgrowing the AuNP core to increase its size to 100 nm, the intensity of the LSPR peak is enhanced, as shown in **Figure 2.3 d**. This enhancement was predicted by **equation 2.14**. The dark blue spectrum corresponds to the CS microgels before the overgrowth and the brown spectrum corresponds to the CS microgels after core overgrowth with core diameter D_{core} of approximately 50 nm. Here, the LSPR overweighs the scattering of the shell, dominating the optical response of such CS microgels.

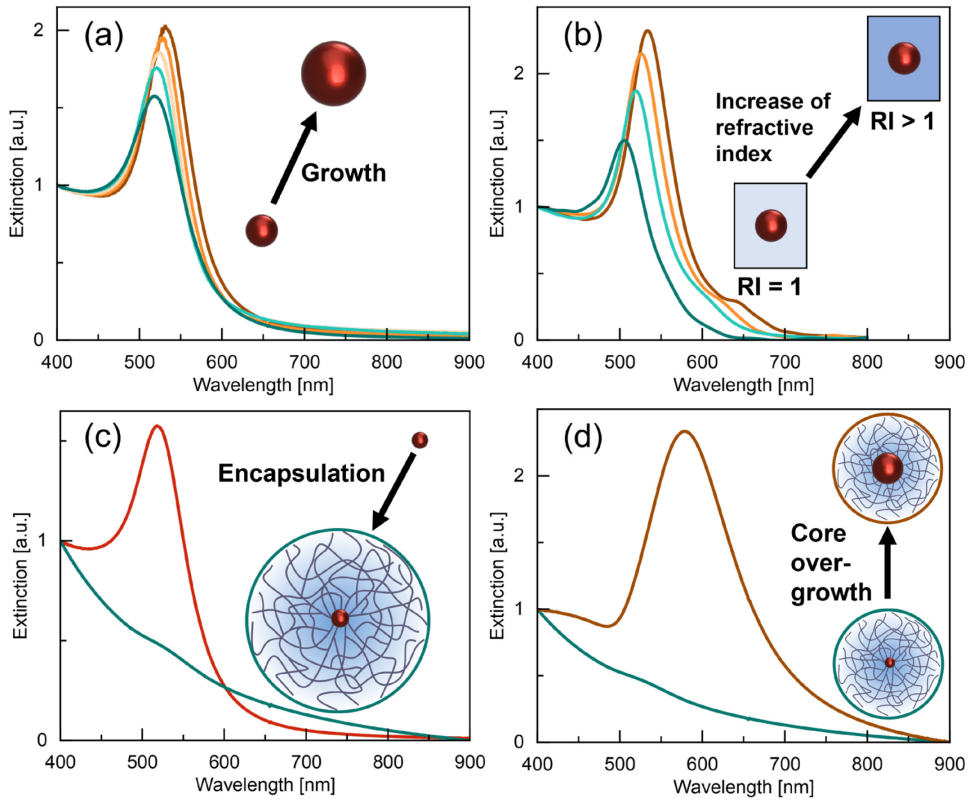

Figure 2.3. Changes in the LSPR peak influenced by different parameters. (a) Experimental extinction spectra of AuNPs with different sizes in aqueous dispersion. The size increases from dark blue to brown from 15 nm to 45 nm in diameter in four steps. Data was provided by Jonathan Garthe. (b) Simulated extinction spectra of AuNPs in environments with different refractive indices (RI). The dark blue spectrum is simulated with a RI of 1. Then RI is increased from 1.3 to 1.5 in 0.1 steps from light blue to brown. (c) Experimental extinction spectra of AuNP in aqueous dispersion before (red) and after (dark blue) encapsulation into a PNIPAM shell. (d) Experimental extinction spectra of Au-PNIPAM in aqueous dispersion before (dark blue) and after (brown) overgrowth of the core. All extinction spectra are normalized to the extinction at a wavelength of 400 nm.

2.2.2. Gold nanoparticles in two-dimensional periodic arrays

AuNPs can be assembled into two-dimensional (2D) periodic lattices exhibiting crystalline characteristics similar to common crystals. In such crystals, Bragg diffraction can occur when the incident light of a wavelength λ is coherently scattered by crystalline planes of the periodically assembled AuNPs. This leads to constructive interference at specific angles as given by the Bragg condition in **equation 2.16**.[119]

$$n\lambda = 2d_{\text{spacing}}\sin(\theta) \tag{2.16}$$

Here, *n* corresponds to the diffraction order, d_{spacing} to the interplanar spacing and θ refers to the angle of the incident light at which constructive interference occurs.

If the lattice spacing is in the order of the wavelength of visible light, the diffractive mode exhibits a photonic character. Such diffractive modes known as Bragg modes show an enhanced transmission at specific wavelengths in the transmission geometry. The spectral position of the Bragg modes λ_{Bragg} can be calculated by multiplying the refractive index and the interplanar spacing d_{spacing}, see **equation 2.17**.[120, 121]

$$\lambda_{\text{Bragg}} = RI \cdot d_{\text{spacing}} \tag{2.17}$$

The interplanar spacing d_{spacing} in a lattice can be calculated according to **equation 2.18** with h_{M} and k_{M} corresponding to Miller indices for a 2D system and *a* to the lattice constant.

$$\frac{1}{d_{\text{spacing}}^2} = \frac{4}{3}\left(\frac{h_{\text{M}}^2 + h_{\text{M}}k_{\text{M}} + k_{\text{M}}^2}{a^2}\right) \tag{2.18}$$

In a hexagonally ordered lattice, *a* equals to the nearest neighbor center-to-center distance $d_{\text{c-c}}$, see **Figure 2.4 a**. In a square lattice, *a* equals to $d_{\text{c-c}}$ and d_{spacing}, as shown by **Figure 2.4 b**. If the diffractive mode is oriented in-plane to the lattice, the spectral position at which it arises is referred to as Rayleigh anomaly (RA).[122]

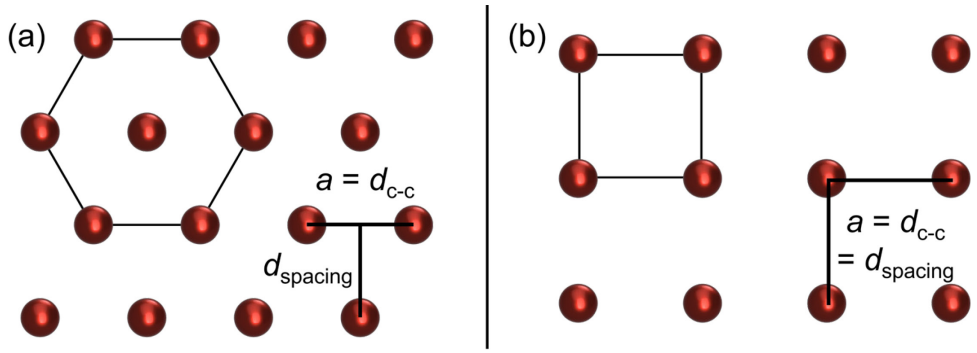

Figure 2.4. Schematic depiction of a 2D hexagonal (a) and square (b) lattice. A hexagon and a square are illustrated to clarify the periodic structure. The lattice constant *a*, the nearest neighbor center-to-center distance $d_{c\text{-}c}$ and the interparticle spacing $d_{spacing}$ are marked for both lattices. For the hexagonal lattice, *a* equals $d_{c\text{-}c}$, but differ from $d_{spacing}$. For the square lattice, *a* equals $d_{c\text{-}c}$ and $d_{spacing}$.

Collective radiative coupling between single particle LSPRs and photonic diffractive modes is enabled when interparticle distances are in the order of the wavelength of visible light. Here the spectral position of the diffraction mode and the single LSPR strongly overlap.[110, 123] This coupling phenomenon is referred to as surface lattice resonance (SLR). SLRs are spectrally narrower and exhibit a longer plasmon lifetime compared to LSPRs.[124] The lifetime of the SLR ranges in the picoseconds, whereby the lifetime of the LSPR ranges in the femtoseconds.[109, 125] The LSPR is shortened due to radiative losses and nonradiative decays such as metallic intra- and interband absorption losses.[126] In the SLR phenomenon, the scattered light of a single particle remains in phase with the plasmon resonance from the particles in its periphery. Thus, the scattered fields can effectively counterbalance the radiative damping experienced by individual NPs.

Furthermore, a homogeneous RI environment is mandatory to support SLR, as the LSPR then couples with in-plane diffraction modes.[57, 110, 120, 123, 127] The homogenous RI environment allows long-range interactions between NPs while these are quenched in an asymmetric environment due to scattering losses. SLR modes feature a plasmonic and a photonic character as a result of the coupling. The plasmonic character becomes more dominant with decreasing overlap between LSPR and in-plane diffractive mode. This results in the coexistence of a SLR and LSPR contribution to the optical response of the monolayer.

Exemplarily extinction spectra of 2D periodic, hexagonally ordered lattices formed by AuNPs (48 nm radius) in an asymmetric (dark blue) and a symmetric (brown) environment are presented in **Figure 2.5**. Both cases are schematically illustrated in the graph by the schemes of AuNPs assembled on a glass substrate with air (asymmetric RI) or coating with *RI* = 1.49 (symmetric RI) as superstrate. The dashed light blue line corresponds to the {1,0} Bragg mode for this lattice with a $d_{c\text{-}c}$ of 448 nm calculated with **equations 2.17 and 2.18**. The LSPR peak at 525 nm couples with the Bragg mode at 578 nm, resulting in the SLR peak in a homogenous environment. The SLR exhibits a redshifted and narrower peak compared to the LSPR.

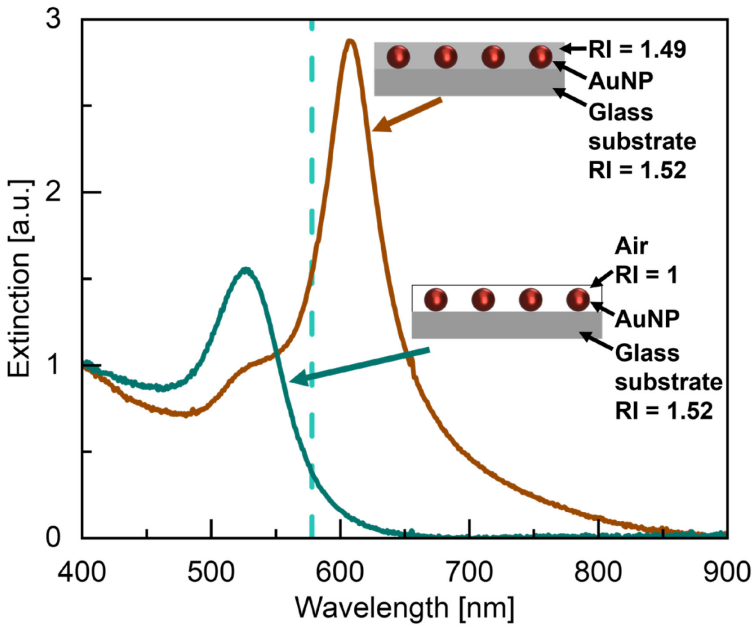

Figure 2.5. Extinction spectrum of a hexagonally ordered monolayer of AuNPs on a glass substrate in an asymmetric (dark blue) and a symmetric (brown) RI environment. The dashed light blue line corresponds to the calculated {1,0} Bragg mode for this lattice. The monolayer presents a $d_{c\text{-}c}$ of 448 nm and the RI for the symmetric environment corresponds to 1.49. Data was provided by Philipp Hammers.

The quality of the SLR is often expressed by the quality factor *Q* given as $Q = \frac{\lambda}{\Delta\lambda}$, which represents the relation between the spectral position λ and the resonance linewidth $\Delta\lambda$. Various parameters such as number and size distribution of particles forming the lattice or structural defects in the lattice can strongly affect the quality.[128-

[130] Furthermore, when the overlap of the LSPR and the diffractive mode decreases, the SLR mode is broadened.[123]

2.3. Microgels in dispersion: Colloidal stability and soft interactions

The following part deals with microgels in aqueous dispersion. First, parameters describing the colloidal stability of microgels are discussed. Second, the multi-Hertzian model according to Bergman *et al*. to describe the soft interactions between microgels is introduced.[27] The aspects mentioned in this chapter are also valid for CS microgels and more specifically Au-PNIPAM microgels.

Colloidal stability of microgels is ensured by repulsive interactions, such as electrostatic forces and steric repulsion. PNIPAM microgels synthesized with ionic initiators such as potassium peroxydisulfate (KPS) present negative charges. This results in these electrostatic forces or Coulomb interactions. Thus, the solvated shell attracts counter ions forming an electrostatic double layer around the microgel. Helmholtz initially described this effect for flat surfaces and Gouy and Chapman extended this model by implementing the thermal motion of ions.[131, 132] They considered the layer around the microgel as a diffuse and not a defined layer. The distribution of the electrostatic potential ψ around charged flat surfaces is modelled by the Poisson-Boltzmann equation in **equation 2.19**, which accounts for the ions in solution and their response to the surface charge.[132, 133] The equation describes the repulsive forces within the electrostatic double layer between the charged flat surface and counterions due to electrostatic interactions.

$$\frac{d^2\psi(x)}{dx^2} = \frac{c_0 e_c}{\varepsilon_m \varepsilon_0} \cdot \left(e^{\frac{e_c \psi(x)}{k_B T}} - e^{-\frac{e_c \psi(x)}{k_B T}} \right) \tag{2.19}$$

In the equation, c_0 is the concentration of salt in bulk *a*nd k_B represents the Boltzmann constant.

If the charge is screened in electrolyte solutions, the Debye approximation is applied by providing a linearized version of the Poisson-Boltzmann equation.[132] By the approximation, it is assumed that ψ is small compared to the thermal energy $k_B T$ and decays exponentially with increasing distance from the charged surface due to the presence of mobile ions in the surrounding medium. The linearized form of the Poisson-Boltzmann equation can be expressed by expanding the exponential function into a series and neglecting all terms expect the first one, see **equation 2.20**.

$$\frac{d^2\psi(x)}{dx^2} = \frac{c_0 e_c}{\varepsilon_m \varepsilon_0} \cdot \left(1 + \frac{e_c \psi(x)}{k_B T} - 1 + \frac{e_c \psi(x)}{k_B T} \pm \cdots\right) \approx \frac{2 c_0 e_c^2}{\varepsilon_m \varepsilon_0 k_B T} \cdot \psi \qquad (2.20)$$

The general solution is shown in **equation 2.21**.

$$\psi(x) = C_1 \cdot e^{-\kappa x} + C_2 \cdot e^{\kappa x} \qquad (2.21)$$

with κ representing the inverse Debye length:

$$\kappa = \sqrt{\frac{2 c_0 e_c^2}{\varepsilon_m \varepsilon_0 k_B T}} \qquad (2.22)$$

C_1 and C_2 are constants defined by boundary conditions. The first condition specifies that the potential equals the surface potential at the surface, meaning that $\psi(x = 0) = \psi_0$. This leads to $C_1 = \psi_0$. The second condition ensures that the potential asymptotically approaches zero and vanishes at large distances from the surface, meaning that $\psi(x \to \infty) = 0$. This implies that $C_2 = 0$. With these conditions, the potential can be simplified to the **equation 2.23**.[133]

$$\psi(x) = \psi_0 \cdot e^{-\kappa x} \qquad (2.23)$$

The electrostatic repulsion of the electrostatic double layer decreases exponentially with a decay length of $\lambda_D = \kappa^{-1}$, called Debye length.

To extend the use of the Poisson-Boltzmann equation into colloidal science, the Derjaguin approximation needs to be considered.[134] It is used to estimate the interaction energy between curved surfaces, such as spheres based on the interaction

energy between flat surfaces calculated by the Poisson-Boltzmann equation. Considering the Derjaguin approximation, the electrostatic double-layer interaction per unit area W_{DL} is given in **equation 2.24**.[133]

$$W_{\mathrm{DL}}(d_{\mathrm{ia}}) = \frac{2\pi R_{\mathrm{sphere}}\sigma^2}{\kappa^2 \varepsilon_{\mathrm{m}}\varepsilon_0} e^{-\kappa d_{\mathrm{ia}}} \tag{2.24}$$

Here, d_{ia} gives the distance between two interacting spheres, R_{sphere} the radius of the interacting spheres and σ the surface charge density.

The interaction of the electrostatic double layer is encountered by van der Waals forces which are weak, but attractive due to fluctuations in electron density of colloids. The van der Waals interaction potential is dependent on the shape and distance d_{ia} between two interacting bodies. If two spherical bodies, such as microgels, interact, the Derjaguin approximation can also be applied here. The interaction energy between two curved surfaces scales with the energy between planar surfaces, but only if d_{ia} is smaller than the radius of the spheres R_{sphere}.[133] The van der Waals interaction per unit area W_{vdW} in dependence of d_{ia} is given by **equation 2.25** with A_{121} representing the Hamaker constant. A_{121} represents the intensity of the van-der-Waals interaction between two materials assuming that the surrounding medium exhibits bulk properties and surface-induced phenomena can be neglected.[135, 136]

$$W_{\mathrm{vdW}}(d_{\mathrm{ia}}) = -\frac{A_{121} \cdot R_{\mathrm{sphere}}}{12 d_{\mathrm{ia}}} \tag{2.25}$$

The net interaction W_{DLVO} of the interplay between W_{DL} and W_{vdW} is given as a function of the distance in **equation 2.26**. This net interaction is part of the DLVO theory named after its developers Derjaguin, Landau, Verwey and Overbeek.[134, 137]

$$\begin{aligned} W_{\mathrm{DLVO}}(d_{\mathrm{ia}}) &= W_{\mathrm{DL}}(d_{\mathrm{ia}}) + W_{\mathrm{vdW}}(d_{\mathrm{ia}}) \\ &= -\frac{A_{121} \cdot R_{\mathrm{sphere}}}{12 d_{\mathrm{ia}}} + \frac{2\pi R_{\mathrm{sphere}}\sigma^2}{\kappa^2 \varepsilon_{\mathrm{m}}\varepsilon_0} e^{-\kappa d_{\mathrm{ia}}} \end{aligned} \tag{2.26}$$

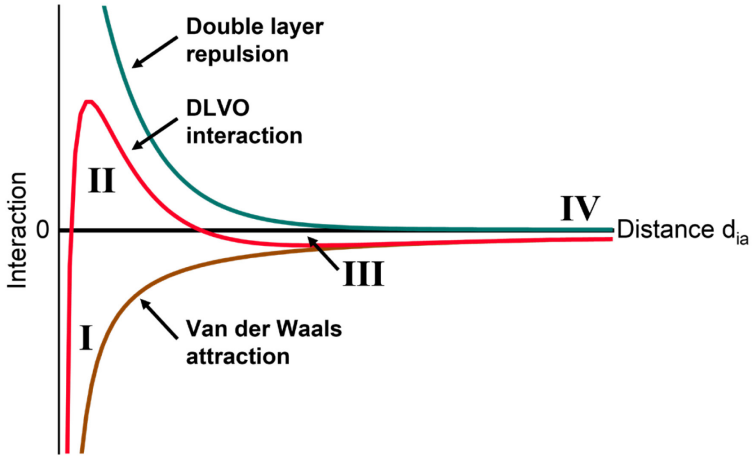

Figure 2.6. DLVO interaction (red) for two spherical particles in dependence of the distance d_{ia} between the two interacting spheres. The double layer repulsion and the van der Waals attraction are shown in blue and brown, respectively. Different distinct interaction regions are marked with roman numerals. I: Irreversible aggregation. II: Colloidal stability defined by the height of the energy barrier. III: Reversible aggregation. IV: Balance between interactions.

The different interactions as a function of d_{ia} are shown in **Figure 2.6**. In regime I, the van der Waals attraction dominates the net interaction and particles aggregate irreversible. In regime II, the repulsive interactions dominate and define the colloidal stability by the height of the energy barrier. In regime III, reversible aggregation occurs due to a slight dominance of the van der Waals interaction. In regime IV, both interactions are completely balanced to maintain the distance between particles.

The DLVO interaction can be influenced by the size or shape of the interacting bodies or by the ionic strength, pH, charge distribution and density.[132] Furthermore, the DLVO theory can predict long-ranged interactions important for colloidal stability, but reaches its limits in the region of short distances between the interacting bodies. Different factors, such as hydrogen bonds or capillary forces determine the interaction in this regime.[133, 138]

The colloidal stability of PNIPAM microgels at low temperatures is further enhanced by steric repulsion. The shell is solvated and exhibits a fuzzy structure with loosely crosslinked outer polymer chains, the so-called dangling ends. When the distance between two microgels decreases, the polymer chains start to overlap. Thereby, the chains will get compressed and their mobility decreases, resulting in an unfavorable

decrease of the entropy. Furthermore, the polymer concentration increases in the overlap region leading to an increased osmotic pressure. Thus, solvent flows into the high concentrated region and prevents aggregation.[139] However, if the temperature rises above the VPTT of the microgels, the shell collapses and the microgels aggregate. The van der Waals forces dominate due to a lower distance between the microgels.

Additionally, as the DLVO theory presents limitations, some models, such as a soft Hertzian model were elaborated to describe the interactions between soft microgels in dispersion.[29] However, for fuzzy core-shell like microgels, this simple model also reaches its limits, as there exist interactions of different length scales. At large distances, where only the dangling ends interact, the soft Hertzian model is appropriate. When the microgels approach each other and the shell or also called corona of two microgels start to interact, shell-shell or also called corona-corona interactions become dominant and the model becomes inadequate. By further reducing the distance, the stiffer highly crosslinked core of the microgel interacts with the shell of the other microgel represented by core-corona interactions until core-core interactions are reached. Here, the model (dashed blue line) highly deviates from reality (depicted as the colored area), as shown in **Figure 2.7**. Therefore, Bergman *et al*. introduced a multi-Hertzian model as a function of temperature and volume fraction, as shown in **Figure 2.7** by the red dashed line.[27] The authors considered the inner part of the microgel as a series of shells with decreasing density as the distance from the center increases. By this approach, it is possible to create a combined potential and thereby to describe the interactions between microgels at different length scales.

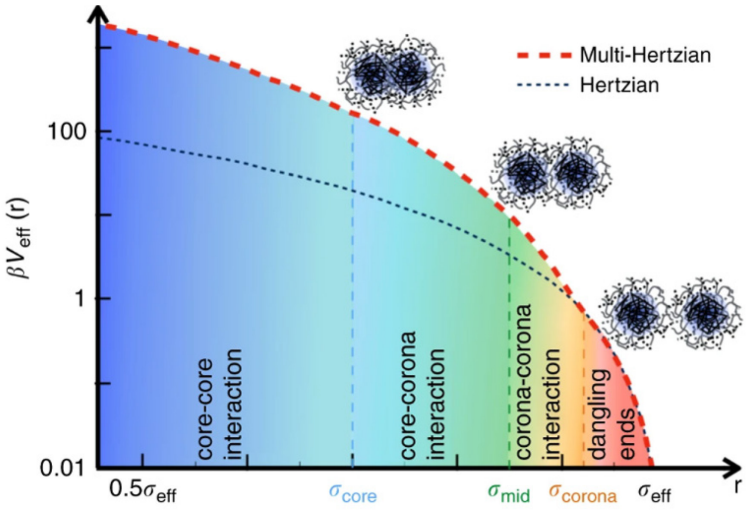

Figure 2.7. Hertzian (dashed blue line) and multi-Hertzian (dashed red line) model. The multi-Hertzian model describes the experimental data by taking into account the length scales at σ_{corona} for the heterogeneity of the shell, below σ_{mid} for the core-corona interaction and below at σ_{core} for core-core interactions. *r* represents the distance between two microgels and βV_{eff} represents the interaction potential. Reproduced with permission from reference[27]. Copyright 2018 Nature Communications.

Core-shell microgels with a rigid inorganic core and a soft deformable shell, such as Au-PNIPAM microgels, show interactions which are influenced by the size ratio between shell and core. For microgels with small cores in respect to the total size of the microgel, there is no difference in the behavior as for microgels without core.[140] If the shell to core ratio is small, the core-core interaction weighs more for the total interaction especially for high volume fraction of the CS microgels.

2.4. Fluid interface-assisted assembly

The comprehension and control of fluid interface-assisted assembly presents a main part of this thesis. Therefore, this chapter first focusses on the forces and interactions between colloids at the interface, before different techniques to prepare 2D lattices *via* self-assembly are covered. The following part puts the focus on the air/water interface while the oil/water interface is neglected here.

2.4.1. Colloidal particles at the interface

Colloidal particles show a high tendency to adsorb to interfaces.[35] The presence of colloidal particles at the interface strongly reduces the interfacial tension, as the contact area between air and water is minimized. The reduction of the interfacial energy is strong enough that the adsorption is irreversible according to Pieranski, who first described this effect in 1990.[141] The vertical position of particles in respect to the interface depends on different parameters, such as size, composition weight, deformability and wetting properties. The latter are influenced by the surface chemistry of the particle. The contact angle θ_c between the particle and the water surface presents a possibility to quantify the wettability. There are three possible vertical positions of the particle depicted in **Figure 2.8 a**. For hydrophilic particles, θ_c is below 90 ° and they are mainly located in the aqueous phase (i). If θ_c is 90 °, the particles are located exactly at the interface, as they do not have an affinity towards one of the phases (ii). For θ_c above 90 °, the particles show hydrophobic characteristics and are mainly located in the air (iii).

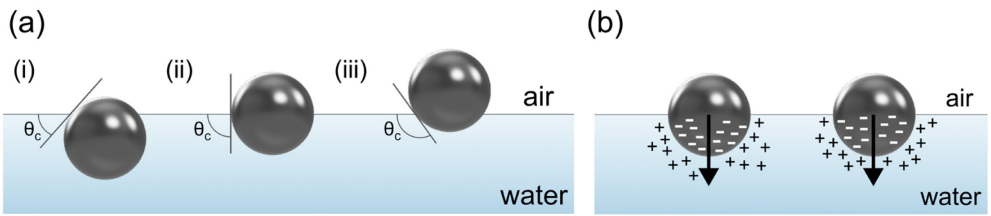

Figure 2.8. (a) Schematic depiction of wetting properties of a colloidal particle at the air/water interface. The contact angle θ_c in respect to the water surface is below (i), at (ii) and above (iii) 90 °. (b) Dipolar interactions due to dissociation of ionic groups at the surface of the colloid located in the water.

During the assembly of colloids at the interface, repulsive and attractive interactions play a key role. At the interface, the part of the colloid immersed in water is highly stabilized due to electrostatic repulsion, as the water, with a high dielectric constant of 78.5 at 20 °C, causes the ionic groups at the surface of the colloid.[132, 142, 143] In contrast, air, with a low dielectric constant of around 1 at 20 °C, presents an environment, which does not allow the dissociation of the ionic groups. Thus, the

surface located in the air stays uncharged leading to a dipole in the colloid, as shown in **Figure 2.8 b**. Dipoles of neighboring colloids align parallel and perpendicular to the interface, resulting in repulsive dipolar interactions.[142, 144] Competing attractive forces, like lateral capillary forces, bring the colloids together. According to Kralchevsky and Nagayama, these forces are mandatory for 2D assemblies of colloids.[145, 146] Identical colloids symmetrically deform the interface and approach each other to decrease the curvature of the interface. The capillary forces increase if the deformation of the surface is increased. One has to distinguish between flotation and immersion capillary forces, see **Figure 2.9**. The first ones occur between colloids at the air/water interface due to gravitational forces **(a)**. These forces vanish, if the colloids are smaller than 5 µm in radius, as they cannot deform the surface.[147] Immersion forces appear when colloids, immersed in a thin liquid film, are present on a substrate **(b)**. For these forces to occur, the film needs to be thinner than the diameter of the colloids. This effect is driven by the wettability properties of the colloids which results in a deformation of the interface. This effect can also be seen for very small particles (< 10 nm).

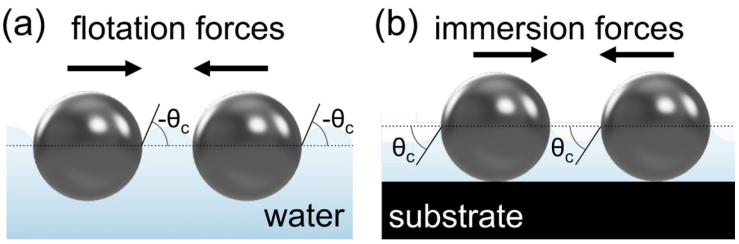

Figure 2.9. Schematic depiction of lateral capillary forces. (a) The flotation forces of freely floating colloids and (b) the immersion forces of colloids immersed in a thin film on a substrate. θ_c represents the contact angle of the water in respect to the lot of the surface.

When soft, deformable colloids, e.g., microgels, assemble at the air/water interface, further effects have to be considered. They can spread at the interface into a ´fried-egg´ like shape (see **Figure 2.10** for a CS microgel) to minimize the contact area between air and water phase to reduce the interfacial tension.[38, 148, 149] This morphology is due to the fuzzy sphere structure of the microgels. The loosely crosslinked shell can spread more at the interface than the highly crosslinked core. Microgels can stretch to larger interfacial dimensions D_i compared to their dimensions

in bulk D_h. Here, the limiting factor is the bulk elasticity, which is also a good indicator for the softness of microgels.[150, 151] Furthermore, the crosslinker content influences the deformation. If the content increases, microgels become more rigid and less deformable. The microgels can behave more or less like hard spheres, if their rigidity is further increased in the extreme case.

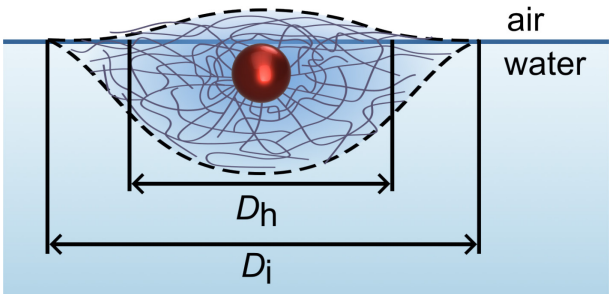

Figure 2.10. Schematic illustration of the ´fried-egg´ like shape of a CS microgel at the air/water interface. D_h and D_i of the CS microgel are marked.

If microgels are deposited at the interface, different stages of microgel deformation can be achieved, as depicted in **Figure 2.11** with decreasing interparticle distance from **(a)** to **(d)**. The decrease in interparticle distance can be achieved either by decreasing the available surface area or by increasing the surface coverage. When the surface coverage is low, microgels stretch to their maximum, as the gain of energy due to the minimization of the interface between water and air is larger than the energy required to deform the microgels **(a)**. Due to a larger wetting radius and a rougher surface of microgels compared to hard colloids of similar sizes, stronger capillary forces can reign at the interface.[152, 153] Therefore, islands consisting of multiple microgels can be formed at this stage of surface coverage. This effect is even more pronounced for hard core-soft shell microgels. If the surface area is reduced, microgels can come into shell-shell contact **(b)** with interparticle distances in the range of the interfacial dimension of the microgels. When the surface coverage is further increased, the deformation and hence the elastic energy will decrease. This leads to an increase in interfacial pressure. The surface will remain covered by microgels to prevent air/water contact. At this stage, microgels will reduce their deformation and their shells will interpenetrate until core-shell contact is reached **(c)**. Upon further

compression, the deformation will be reduced until interfacial dimensions smaller than dimensions in bulk, core-core contact, are reached **(d)**. If the surface area is further compressed, microgels will desorb from the interface, as this becomes energetically more favorable. The interactions between the microgels at the interface can be described by a simple Hertzian-like potential.[66, 154]

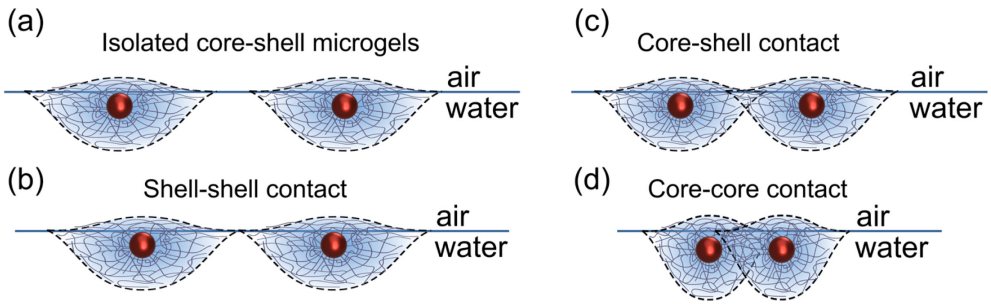

Figure 2.11. Core-shell microgels at the air/water interface at different stages of surface coverage. (a) Freely floating CS microgels at low surface coverage. Surface coverage is increased until shell-shell contact (b), then core-shell contact (c) and finally core-core contact (d) is reached. For reasons of clarity, coloring of the water was omitted and only two CS microgels out of a monolayer are depicted.

Vasudevan *et al*. analyzed the position of CS microgels at oil/water interfaces, but this behavior can also be translated to air/water interfaces, as for both cases microgels adsorb to the interface to reduce the interfacial tension.[155] The authors claimed that the vertical position of the core in CS microgels in respect to the interface is dependent on core size and shell thickness, see **Figure 2.12**. The left side shows the regime where the position of the core is only dependent on the core size and independent on the shell thickness. If the shell thickness reaches a critical value (dashed blue line), the position becomes dependent on the shell thickness and independent on the core size.

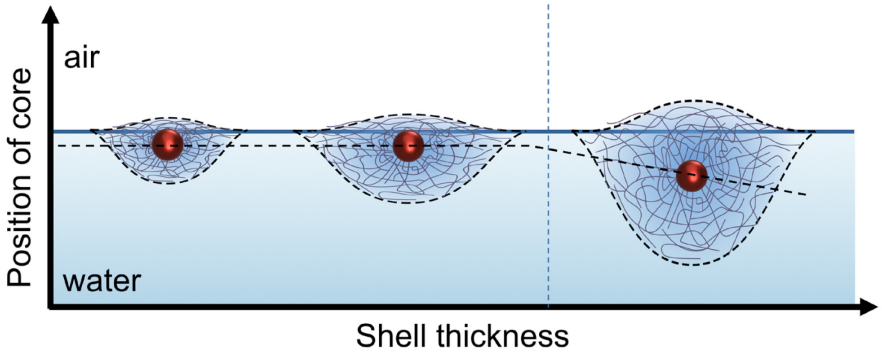

Figure 2.12. Schematic illustration of the position of CS microgels at the air/water interface dependent on the shell thickness. The black dashed line represents the vertical position of the center of the core. The vertical blue dashed line represents the shell thickness from which on the position of the core is dependent on the shell thickness.

The understanding of the behavior of microgels in dispersion and at the interface are elementary to control the assembly of such particles either in 3D or 2D. The next chapter gives an overview of some preparation methods for 2D assemblies resulting in hexagonally and non-hexagonally ordered monolayers.

2.4.2. 2D assembly methods

Self-assembly of microgels at the air/water interface is a spontaneous process, where microgels typically assemble into a 2D hexagonal order under the condition that the microgel shells come into contact.[149] The hexagonal order is the equilibrium structure for soft microgels as well as for hard colloids. In the following, different techniques are presented to fabricate such 2D colloidal assemblies. The preparation methods can be divided into two main groups, the direct assembly and the fluid interface-assisted assembly. Both categories lead to mostly hexagonal ordered lattices and include solvent evaporation and convective assembly by immersion capillary forces. These methods can be applied to almost all colloidal particles, including but not limited to soft microgels and hard colloids. Additionally, as the interest for non-hexagonal structures increased in the last years, approaches to prepare non-hexagonal structures are discussed at the end of this chapter.[62] As these methods are less

common and not transferable to all sort of colloids, some specific examples are presented in this thesis.

Hexagonally ordered monolayers

Some selective direct assembly methods are depicted in **Figure 2.13** for CS microgels, but they can be applied to any other colloidal particle. The methods will be shortly described in the following.[144] These methods are relatively easy to perform, but they exhibit some disadvantages. Spin-coating is the fastest method and employs mechanical shear forces **(a)**. Here, a droplet of particles dispersed in a volatile solvent is added onto a substrate. The substrate is then spined to evaporate the solvent.[156-159] Due to high lateral shear forces and fast solvent evaporation, long-range order is difficult to achieve and multilayers may form.[160] For drop-casting, also a droplet of particles dispersed in solvent is added onto a substrate and the solvent is then left to evaporate **(b)**.[161-163] This method is hard to control and the formation of multilayers presents a high risk. Furthermore, the order can be destroyed due to the coffee stain effect or meniscus pinning.[164, 165] The effect of meniscus pinning can be minimized by controlling and slowing down the movement of the meniscus. Such methods are, e.g., vertical[69, 166, 167] **(c)** and horizontal[157, 168, 169] **(e)** deposition. For the vertical deposition also known as dip-coating, a substrate is vertically retracted from a dispersion of particles. A convective particle flux caused by the evaporation of water leads to the absorption of the particles from the water. The monolayer is then formed at the drying front where the particles are nucleating. The horizontal deposition also known as doctor blading consists of a substrate and a blade where a dispersion is trapped in between. A meniscus is built between the blade and the substrate by slowly retracting the blade. Thereby, particles will move towards the three-phase-contact line and deposit onto the substrate to form a monolayer. The last assembly method is the electrostatic deposition **(d)**, which cannot be applied for every sort of microgels, as functionalized substrates and particles have to present a relatively high charge.[170, 171]

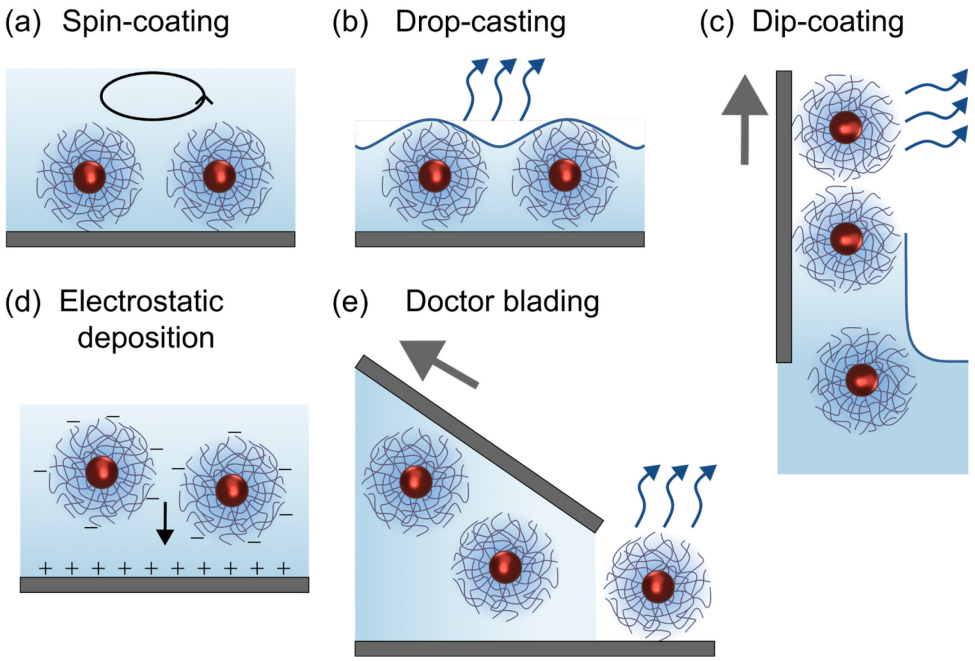

Figure 2.13. Different direct self-assembly methods to prepare 2D monolayers. The methods are spin-coating (a), drop-casting (b), dip-coating (c), electrostatic deposition (d) and doctor blading (e). The grey arrows show the direction of movement, the blue arrows show the evaporation of solvent. The black arrows show the spinning direction and the movement of the microgels for spin-coating and electrostatic deposition, respectively.

An experimentally simple and fast method to prepare colloidal monolayers presents the interface-assisted assembly resulting in 2D hexagonally ordered monolayers at the air/water interface.[144, 172] These monolayers show a high degree of order and can be transferred from the interface to a substrate. A method to prepare such assemblies is the interface-assisted assembly in a conventional crystallizing dish with subsequent transfer onto a solid substrate.[54, 55] The process is schematically shown in **Figure 2.14** for different methods of particle deposition onto the interface. Note, the scheme presents CS microgels, but the process can also be applied to any other colloidal particle. Typically, an ethanolic dispersion of particles is applied to the interface with a needle **(a)**. The needle comes into contact with the interface, where a meniscus is formed alongside the needle tip wall. During the application, the particles will move to the edges of the crystallizing dish, where the monolayer starts to form until the whole surface is covered. This movement occurs due to a gradient in surface tension, the Marangoni effect. Particles move from the region with a low surface tension to a higher

surface tension.[173] Zhang *et al*. demonstrated this method to fabricate close-packed hexagonally monolayers of PS particles with different sizes.[173] Volk *et al*. adapted this method to CS microgels and thereby prepared highly ordered monolayers of Au-PNIPAM microgels with different interparticle distances.[54, 57, 121] The authors formed freely floating monolayers at the interface with interparticle distances close to the dimensions of the microgels in dispersion. As the shell of the microgels energetically stretches to a maximum to cover more surface and reduce the interfacial tension, they achieved larger interparticle distances by waiting. Another method to apply the particles at the interface is by spin-coating them onto a substrate which is then immersed into the aqueous phase **(b)**. During the immersion, the particles detach from the substrate and assemble into a close-packed monolayer at the interface because of capillary immersion and flotation forces. This method was introduced by Retsch *et al*. with PS particles.[174] A third possibility introduced by Vogel *et al*. is the use of a substrate as a slide.[175] The particles are applied with a needle onto a substrate which is half immersed into the aqueous phase at an angle of 45 ° angle **(c)**. The particles slide down the substrate and assemble at the interface. The close-packed monolayer will form as soon as the particle flow front reaches the contact line between substrate, water and air. This method reduces defects in the monolayer due to reduced particle flow into the aqueous phase. After the assembly of the particles at the air/water interface **(d)**, the monolayers can be transferred to a solid substrate. For this, the substrate is immersed into the aqueous phase **(e)** and then withdrawn at a shallow angle from underneath the monolayer **(f)**.[54] The monolayer then attaches onto the substrate exhibiting the same arrangement as at the interface. The substrate can be either dried at ambient conditions or by evaporating the solvent with heat from underneath the substrate. The effects of the drying process on the monolayer will be discussed later.

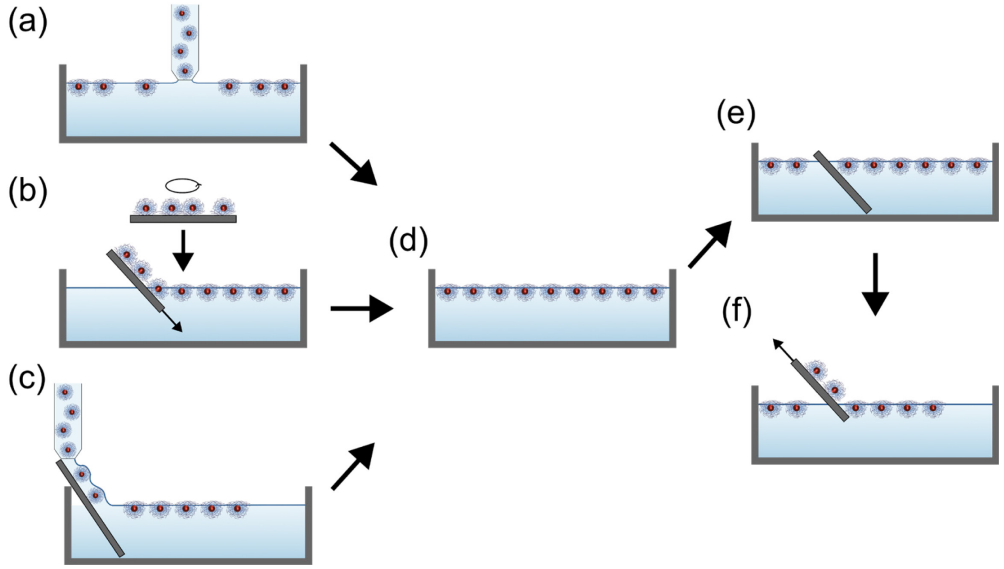

Figure 2.14. Schematical depiction of interface-assisted assembly of CS microgels. (a) Application of microgels at the air/water interface with a needle. (b) Spin-coating and subsequent immersion of the coated glass substrate in the aqueous phase. (c) Application of microgels with a needle over a glass substrate at the air/water interface. (d) Assembled CS microgels at the air/water interface. (e) Immersion of glass substrate in the aqueous phase under the monolayer. (f) Retraction of glass substrate at a shallow angle through the monolayer to transfer the CS microgels from the interface to the substrate.

A more controllable method to prepare such assemblies is the deposition of particles at the air/water interface in a Langmuir trough. The principle of a Langmuir trough will be discussed in detail in the following chapter. Briefly, the surface coverage can be controlled in a Langmuir trough by precise change of the surface area while the surface pressure can be monitored simultaneously. Particles will form a loose monolayer at the beginning and upon compression a close-packed monolayer will form. The monolayer can be transferred from the interface to a solid substrate during the compression by the Langmuir-Blodgett deposition or the Langmuir-Schäfer method, which both will also be discussed later.[46, 176] The advantage of the Langmuir trough is the high reproducibility, as the assembly can be monitored through changes in surface pressure.

Non-hexagonally ordered monolayers

Besides colloidal hexagonal lattices, the demand for other more complex patterns has risen over the last years.[62] In the following, different approaches to achieve such non-hexagonal lattices will be discussed. First, a method to prepare lattices with hard PS particles will be presented. Second, different process types to fabricate non-hexagonal arrangements with microgels are described.

Usually, the transfer of the particles is performed with glass substrates from the aqueous phase through the monolayer into the air. Hummel *et al.* introduced the formation of any of the five Bravais lattices by simply changing the wettability of the substrate and submerging the substrate through the monolayer into the aqueous phase, as depicted in **Figure 2.15**.[77] The authors deposited PS particles at the air/water interface to prepare a close-packed hexagonal monolayer. The latter is then one-dimensionally stretched into a non-close-packed monolayer of any Bravais symmetry by using hydrophobic substrates during the transfer **(a)**. Here, the degree of stretching and thereby the resulting symmetry was influenced by the hydrophobicity of the substrate, as the authors used substrates of different material. The capillary forces upon drying were inhibited by thermal annealing of the monolayer in the subphase near the glass transition temperature of either the particles or the substrate **(b)**. Thereby, the particles were immobilized on the substrate and the symmetry was retained during retraction from the subphase. The resulting non-close-packed monolayer **(c)** featured one of the following five Bravais lattices: hexagonal **(i)**, square **(ii)**, oblique **(iii)**, rectangular **(iv)** or centered rectangular **(v)**.

In this work, the presented method is adapted to produce Bravais lattices of CS microgels.[177] The soft shell acts as spacer between the cores and Bravais lattices with different interparticle distances could be obtained by changing the dimensions of the shell.

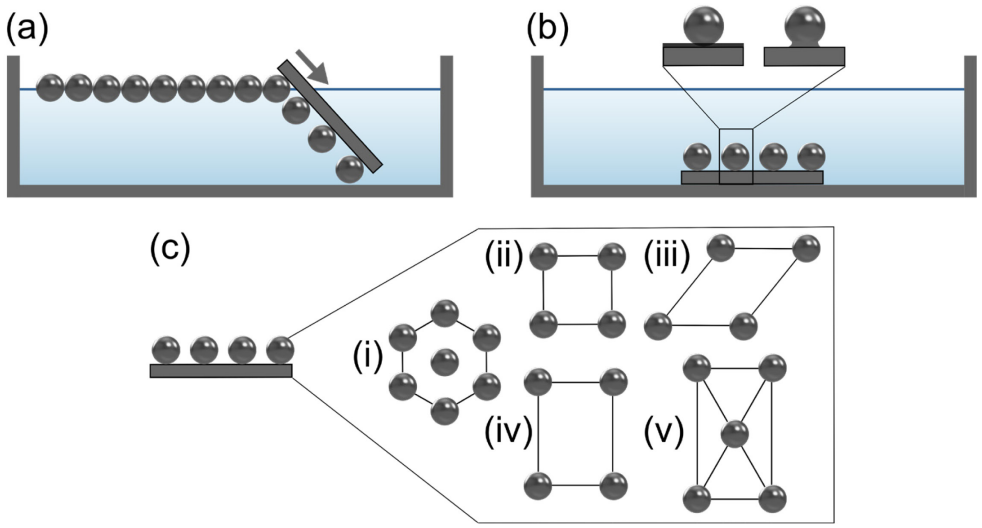

Figure 2.15. Schematic illustration of preparation method to fabricate Bravais lattices of PS particles. (a) Particles are transferred to the hydrophobic substrate by immersing the substrate through the monolayer into the aqueous phase. (b) Thermal annealing near glass transition temperature of substrate or particle to immobilize particles on the substrate. (c) Final dried non-close-packed monolayer featuring a hexagonal (i), square (ii), oblique (iii), rectangular (iv) or centered rectangular (v) arrangement.

The key challenge of preparing rectangular arrangements of microgels at interfaces is bringing steric repulsion of microgels and attractive quadrupolar capillary forces at the interface in an equilibrium. Fernandez-Rodriguez *et al.* applied PNIPAM microgels at the oil/water interface and produced rectangular arrangements *via* control of the surface pressure to be near zero.[63] At this surface pressure, the repulsive and attractive forces were balanced. The authors showed the applicability of their technique for different PNIPAM microgels varying in hydrodynamic dimensions in bulk, as well as crosslinker content. All microgels assembled into a rectangular lattice exhibiting a long-ranging order. These arrangements were then used as soft masks in soft colloidal lithography. However, when the surface pressure was increased above 1 mN m^{-1}, the rectangular arrangement changed to the typical hexagonal lattice.

Further non-hexagonal structures can be prepared by using binary mixtures of colloids, as shown by different works.[48, 64, 65] The binary mixtures consist of colloids that differ in size, softness or even both. In the following, different methods are presented.

Rey *et al.* used the attraction forces between soft microgels and hard PS particles.[64] The authors obtained PS particles covered with soft, deformable microgels by mixing small PNIPAM microgels (D = 145 nm) and large PS particles (D = 1.5 µm) in bulk. The covered PS particles experienced less attraction in bulk which resulted in less clustering due to weakened capillary forces at the interface. Applied at the air/water interface, the particles formed non-close-packed hexagonal structures at low surface pressures, as shown in **Figure 2.16 a (i)**. The PS particles covered with microgels are represented as grey spheres with a light blue shell. As soon as the surface pressure increased due to reduction of surface area, the shells of the microgels started to overlap leading to chain like structures **(ii)** followed by square like arrangements **(iii)**. When the shells of the microgels fully overlapped, the PS particles came into contact leading to the formation of close-packed hexagonally ordered arrangements **(iv)**. These structures could also be simulated by minimum energy calculations and finite temperature Monte Carlo simulations of hard core-soft shell particles. For this, an interaction potential of particles exhibiting two different length scales was used. One length scale was represented by the PS particles acting as core and the other length scale was determined by the PNIPAM microgels acting as shell. The hard core was implemented with a hard sphere potential and the soft shell with a longer ranged soft repulsion shoulder. All these different structures were also theoretically predicted by Jagla in the late 1990.[178, 179]

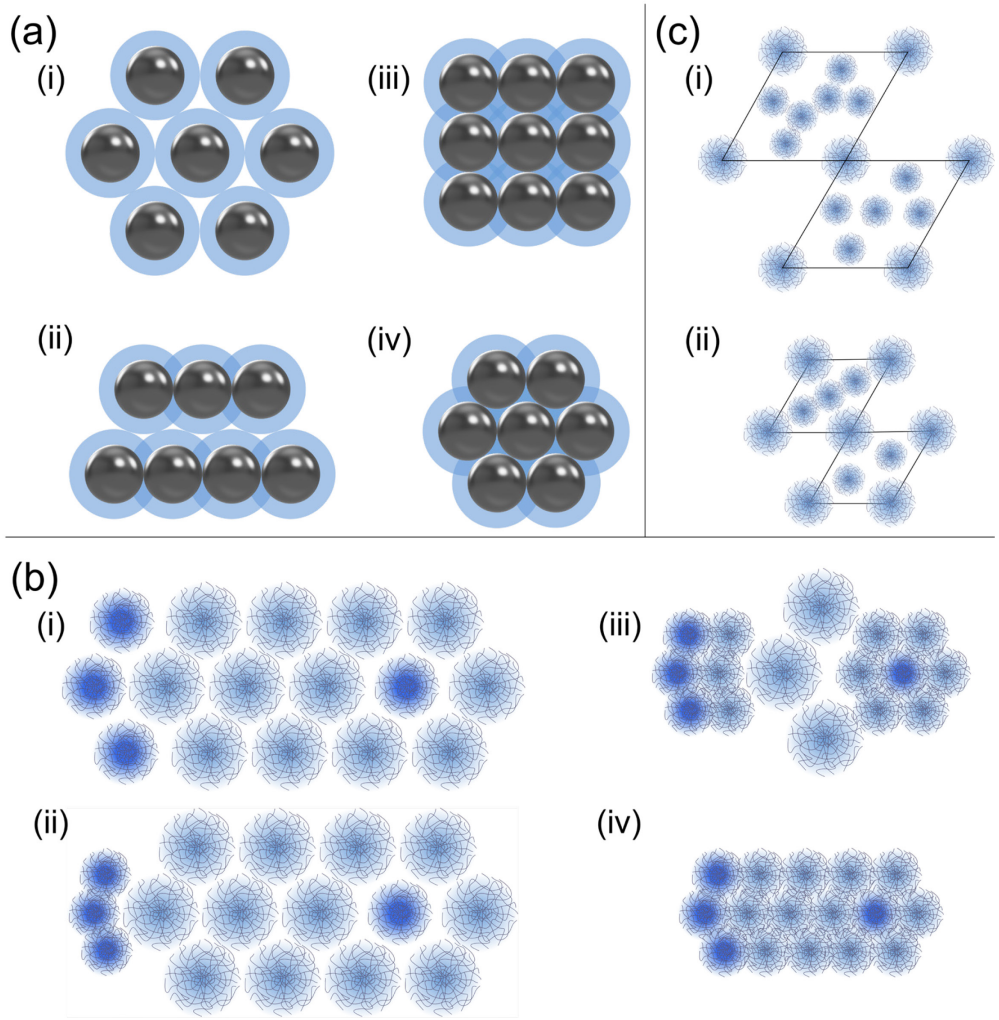

Figure 2.16. Schematic depiction of binary arrangements. (a) Non-close-packed hexagonal (i), chain like (ii), square like (iii) and close-packed hexagonal structures received during reduction of surface area where a mixture of large PS particles covered with small microgels (grey sphere with light blue shell) was assembled. (b) Interfacial phase transitions of a mixture from soft PNIPAM microgels (light blue) and stiffer PNIPAM microgels (dark blue) at different compressions. The compression increased from (i) to (iv). (c) Arrangements obtained *via* first deposition of large microgels followed by second deposition of small microgels onto the same substrate. The structures at low (i) and high (ii) surface pressures are shown.

Flower-like arrangements at the interface can be produced by mixing different microgels of similar dimensions in bulk, but with different softnesses, as shown by Harrer *et al.*[65] Soft PNIPAM microgels were mixed in excess with stiffer PNIPAM microgels. At low surface pressure, the softer microgels (light blue microgels) showed

larger interfacial dimensions than the stiffer microgels (dark blue microgels), but nonetheless all microgels were in shell-shell contact as shown in **Figure 2.16 b (i)**. Above 19 mN m^{-1}, neighboring stiffer microgels collapsed and interpenetrate into core-core contact to form a close-packed hexagonal order. If stiffer microgels were only in contact with soft ones, they remained swollen **(ii)**. Only soft microgels in contact with stiffer ones collapsed into core-core contact to form stable flower-like arrangements above a surface pressure of 25 mN m^{-1} **(iii)**. Above 28 mN m^{-1}, all microgels collapsed into core-core contact to form a close-packed hexagonal assembly **(iv)**. For a mixture of soft PNIPAM microgels with stiffer CS microgels, a comparable behavior was observed.

Another approach consists of preparing complex arrangements *via* subsequent deposition of colloids. Fernandez-Rodriguez *et al.* utilized differently sized microgels which were transferred onto the same substrate *via* Langmuir-Blodgett deposition.[48] In brief, the authors applied PNIPAM microgels with D_h of 940 nm at the water/n-hexane interface. During the increase in surface pressure from 1 to 10 mN m^{-1}, the hexagonally ordered monolayer was transferred from the interface to the substrate. Due to the continuous compression of the interfacial area, the monolayer on the substrate exhibited a steadily decreasing interparticle distance. A second monolayer consisting of PNIPAM microgels with a hydrodynamic diameter of 426 nm in bulk was continuously added onto the first one while the surface pressure of the interface increased from 1 to 22 mN m^{-1}. Using this approach, a binary monolayer with two gradients of microgels, ranging from low to high coverage was successfully prepared. The smaller microgels assembled into the interstitial spaces between the larger microgels and the number of small microgels could be tuned by adjusting the surface pressure. At low coverage, five to six small microgels assembled in the interstices, whereas at high coverage, this number decreased to two or three, as shown in **Figure 2.16 c (i) and (ii)**, respectively.

The approach of multiple deposition could also be applied to only one type of microgel to prepare homogeneous yet complex structures. Honold *et al.* created honeycomb arrays by sequential double deposition of assembled microgels from the air/water interface to a glass substrate.[53] The authors first transferred a hexagonally ordered monolayer of Au-PNIPAM microgels from the interface onto a glass substrate and then deposited a second monolayer of microgels on top. Microgels of the second deposition assembled in the voids in between three neighboring microgels of the first

layer leading to a 2D-honeycomb arrangement. As microgels feature a deformable character and shrink in size upon drying, the final structure is a 2D arrangement in contrast to an AB-type multilayer that would typically form from similar assemblies of hard spheres. Furthermore, the authors used the approach to fabricate binary plasmonic lattices by first depositing Au-PNIPAM microgels followed up by a second deposition of Ag-PNIPAM microgels.[53] Later, Volk *et al.* revealed that the drying speed of the second deposited monolayer plays a crucial role for the resulting lattices.[67, 68] If the second monolayer is dried fast, Moiré structures will form, whereas slow drying at ambient condition results in honeycomb lattices (see **Figure 2.17 a**). These findings were supported by Brownian dynamics simulations showing that the mobility of the particles from the second monolayer is the key for the formation of the structure.[67]

By combining double deposition and control of surface pressure, Grillo *et al.* were able to prepare even more complex tessellations of PNIPAM microgels, such as herringbone superlattices.[66] Using a Langmuir-Blodgett trough (LBT), the authors transferred a hexagonally ordered monolayer of PNIPAM microgels during compression from a water/n-hexane interface onto a substrate, as shown in **Figure 2.17 b**. The substrate was rotated by 90 ° and a second monolayer was transferred from the interface on top of the previous monolayer. The rotation led to two orthogonal gradients of packing fraction with the first monolayer acting as template for the second monolayer. The first microgels were rendered immobile and the microgels from the second deposition could assemble in the interstices. Through this approach the following tessellations could be prepared: rectangular and honeycomb lattices, interlocking-S structures and hexagonal and herringbone superlattices. These thermodynamical stable tessellations form due to short-range repulsive interactions as confirmed by molecular dynamics simulations.

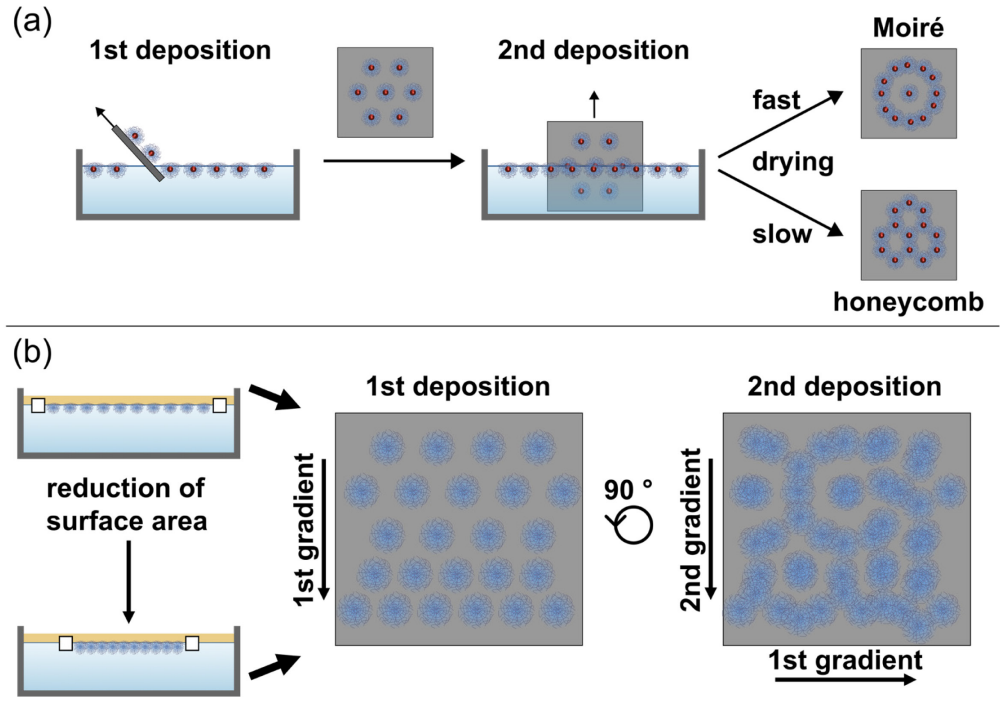

Figure 2.17. Schematic depiction of double deposition methods to prepare complex arrangements. (a) From left to right: First transfer of CS microgels from air/water interface to glass substrate to prepare a hexagonally ordered monolayer (1st deposition). Second monolayer is transferred from the air/water interface to the same glass substrate (2nd deposition). Depending on drying speed, Moiré (top right) or honeycomb (bottom right) lattices are formed. (b) From left to right: Assembly of PNIPAM microgels at the water/n-hexane (yellow) interface in a Langmuir trough with opened barriers (top left) and closed barriers (bottom left). The white squares represent the movable barriers. The substrate in the middle shows the transferred monolayer exhibiting a gradient in interparticle distance due to reduction of surface area (1st deposition). The substrate is turned by 90 ° and a second monolayer of PNIPAM microgels is transferred from the water/n-hexane interface onto the same substrate. The second monolayer also exhibits a gradient in interparticle distance due to reduction of surface area (2nd deposition). The second structure here shown on the glass substrate is only a scheme and not a real experimentally obtained structure.

2.5. Langmuir trough

In this section, the assembly of CS microgels at the air/water interface, as well as the influence of compression on the microstructure are discussed based on measurements conducted using different Langmuir trough (LT) setups. Furthermore, the process to combine *ex situ* and *in situ* analysis of the microstructure will be presented as well.

A common approach to control the packing fraction of microgels at the air/water interface is done by using a Langmuir trough setup equipped with movable barriers and a film pressure balance to measure the surface pressure/tension during the experiment. The well-known Langmuir-Blodgett deposition allows for withdrawing of a substrate from the aqueous phase while the surface area is continuously reduced, as schematically shown in **Figure 2.18 a**. The CS microgels are assembled between the two movable barriers and can be continuously transferred from the interface to the substrate. As the barriers close and thereby reduce the interfacial area, the microgels can adapt to the compression by reducing their interfacial dimensions and by interpenetrating, changing from shell-shell contact, over shell-to-core, to core-core contact. The deposited microstructure on the substrate can be linked to a certain surface pressure measured during the compression. A typical plot of a compression measurement with the surface pressure plotted against relative area is exemplarily depicted in **Figure 2.18 b**. Such a plot is commonly called a compression isotherm. A digital photograph of a glass substrate coated with a monolayer of Au-PNIPAM microgels from such a Langmuir-Blodgett deposition is shown in **Figure 2.18 c**. The intensity in color increases from the top (start of compression) to the bottom (end of compression) of the substrate. This color change is attributed to a decrease in interparticle distance and thus an increase in number of CS microgels per area. The microstructure of the monolayer can be analyzed *ex situ* by AFM measurements (see **Figure 2.18 d**).

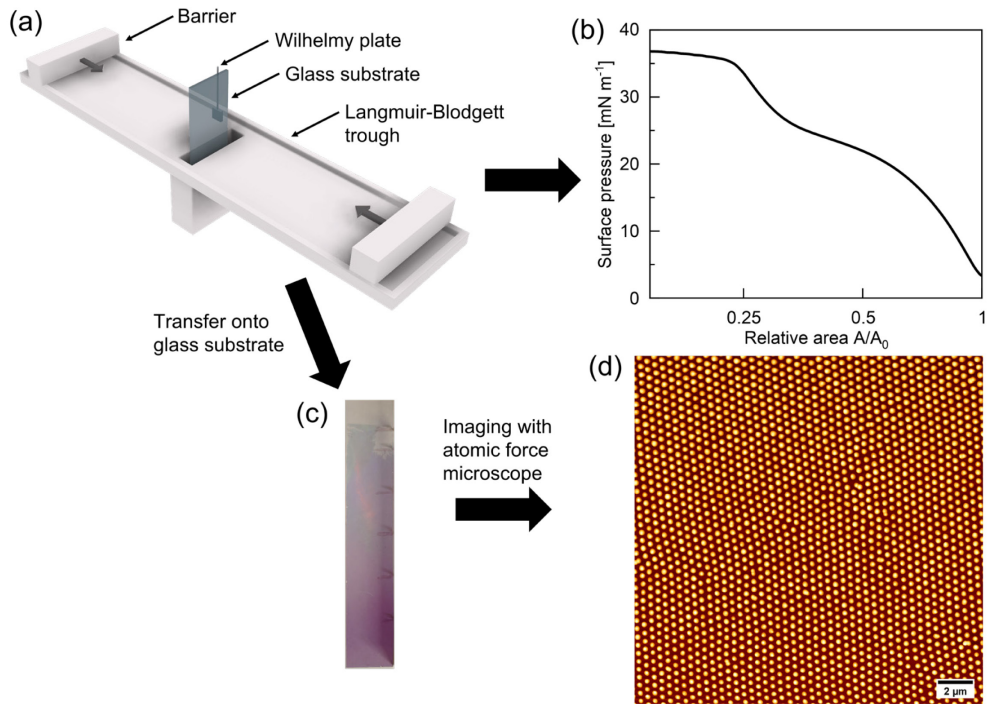

Figure 2.18. (a) Schematical setup of a Langmuir-Blodgett deposition experiment. The grey arrows show the direction of the movement from the barriers. (b) Compression isotherm where surface pressure in mN m^{-1} is plotted against the relative area A/A_0. (c) A photograph of the glass slide with the transferred monolayer. (d) The AFM image shows the hexagonally ordered monolayer. The AFM image is adapted with permission from reference Feller *et al*.[177] Copyright 2024 Springer Nature.

Compression isotherms play a crucial role in one part of this thesis. For this reason, it is important to understand and interpret different regions. Rey *et al*. identified regions in a compression isotherm by analyzing the structure of monolayers *ex situ* by AFM images and linking the images to the isotherm.[44] The authors employed PNIPAM-based microgels with a hydrodynamic diameter of 426 ± 20 nm. The first region, called gas phase, is situated at low surface pressures where microgels are statistically distributed at the interface with interparticle distances larger than their interfacial dimensions. In the second phase, the microgels come into shell-shell contact. This phase can be identified at a relative area of one in the compression isotherm of **Figure 2.18 b**. A steep increase in surface pressure can be identified if the monolayer is compressed. Here, the shells of the microgels are compressed resulting in a continuous decrease of interparticle distances. The course of the surface

pressure, such as the steepness of the curve, can be tuned in this region by changing softness and thickness of the microgel shell.[180] Upon further compression, microgels undergo a transition from shell-shell to core-core contact. According to Rey *et al.*, there is a coexistence between two phases which can be identified as a plateau in the isotherm. This transition is known in literature as isostructural solid-solid phase transition.[44] The phase transition occurs between two solid hexagonal crystalline phases, whereby one corresponds to the compressed shell-shell contact and the other to the core-core contact. This phase transition can be observed on a substrate by *ex situ* AFM images. During further compression, more microgels undergo the phase transition until all microgels are in core-core contact and form a close-packed hexagonal monolayer. If the surface area is further reduced, the microgels can undergo slight compression until the monolayer starts to fail and multilayers form or microgels desorb from the interface into the subphase. All their findings based on *ex situ* analysis, but they could not visualize the interfacial monolayer to validate their findings.

For this reason, one aim of this work was to compare *ex situ* measurements to *in situ* analysis. Similar comparison was already done by Kuk *et al.*[72] The authors recently investigated monolayers of large CS microgels (D_h = 858 ± 41 nm) with silica cores and different crosslinker densities prepared *via* the Langmuir-Blodgett deposition *ex situ*. Additionally, they analyzed the monolayers of the same CS microgels *in situ* at the air/water interface with a setup combining a Langmuir trough with small-angle light scattering (SALS). With this setup, the authors were able to monitor the monolayer directly during the compression. By comparing the *ex situ* and *in situ* results, the authors found the isostructural phase transition only on the glass substrate with the dried transferred monolayer. No evidence for the occurrence of the phase transition at the air/water interface could be found, while the continuous decrease in interparticle distance could be confirmed. The authors concluded that the phase transition is an artifact of the transfer and/or drying process. Based on these findings, Kuk *et al.* further investigated the drying of soft colloidal films.[181] They analyzed the drying process with video microscopy and thin film interference and compared the drying of monolayers on hydrophilic and hydrophobic substrates. The interfacial microstructure was better maintained on hydrophobic, than hydrophilic substrates. Microgels adhere stronger to a substrate with a higher hydrophobicity and thereby their mobility is weakened during the drying. Furthermore, softer microgels can better

maintain the microstructure as they deform and flatten more at the interface. Thus, the water surface is less curved and capillary forces between softer microgels are decreased compared to harder microgels. Hence, the microstructure of the transferred monolayer depends not only on the wettability of the substrate, but also on the softness of the microgels.

All these previous findings emphasize the need for *in situ* measurements in order to fully understand and characterize the microstructure of monolayers at interfaces. Even if *in situ* measurements remain challenging due to the movement of the interface and the small size of microgels, first works showed progress in this field, as well as one *in situ* method is introduced in this thesis.

The 3D shape of microgels at the water/oil interface was visualized *via in situ* AFM measurements by Vialetto *et al*.[75] They reconstructed the interfacial structure of single PNIPAM microgels (D_h = 1150 ± 27 nm) by combining different AFM images taken from both sides, the water and the oil phase. They found the classical ´fried-egg´ structure of microgels with most of the volume of the microgel located in the aqueous phase. By changing the oil phase to an oil in which PNIPAM is highly soluble, the conformation of the microgel changed to an isotropical shape with high swelling in both phases. They also revealed that by increasing the temperature, the volume located in the water phase deswelled and contact between neighboring microgels was suppressed in the water phase. The authors claimed that these findings would help to describe and understand interactions in monolayers, which is also an aim in this thesis. Further works showed by neutron reflectivity of the air/water interface that the crosslinker density in PNIPAM-based microgels had a high impact on the interfacial deformation of the microgels.[182] The higher the crosslinker density in the microgels, the less the microgels were deformed at the interface and more volume of the microgels was located in the air. The part in the air was present as collapsed microgel. By increasing the temperature, the microgel part located in the water collapsed, whereby the part in the air was not affected.[183]

These works investigated mostly the structure of one single microgel at the interface, whereby one aim of this thesis was to further elucidate the interfacial structure of ordered monolayers *via in situ* techniques. For this reason, one part of this thesis consisted of building a setup to investigate Au-PNIPAM microgels assembled at the air/water interface. For this reason, a Langmuir trough was combined with an

extinction spectrometer to exploit the optical properties of the AuNP cores *in situ* at the interface. The setup, as well as the process of data analyzation will be described in the following.

The self-built setup is schematically shown in **Figure 2.19**. It consists of a Langmuir trough with a microscope window which is combined with an extinction spectrometer where optical fibers are connected to the light source and the detector. The Langmuir trough is equipped with two movable barriers and a film pressure balance to measure the surface pressure. Au-PNIPAM microgels are deposited at the air/water interface between the two barriers. During the compression of the interface, extinction spectra can be recorded at every second. These spectra can then be linked to the surface pressure. By comparing spectra at different stages of the compression, information about the microstructure at the interface can be derived.

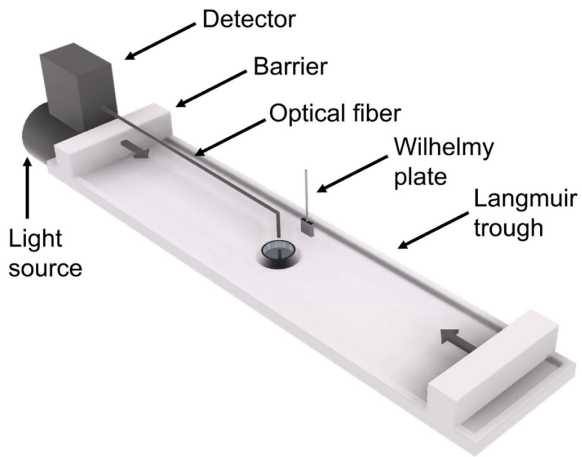

Figure 2.19. Schematical set up of an extinction spectrometer combined with a Langmuir trough. The grey arrows show the direction of the movement from the barriers.

If a Langmuir-Blodgett deposition using a hydrophobic substrate is conducted in the same range of surface pressures with the same microgels, the microstructure analyzed *ex situ* by AFM images can be linked to the *in situ* extinction spectra by comparing the surface pressures. For Au-PNIPAM microgels, it is important to use hydrophobic substrates to maintain the microstructure as effectively as possible. The *ex situ* AFM image corresponding to the largest interfacial surface area with a surface

pressure just above 1 mN m^{-1} is used as reference point to calculate the number of microgels and the $d_{c\text{-}c}$ at the air/water interface. It is assumed that the microstructure on the substrate is not influenced by drying artefacts and that the microgels would be in shell-shell contact at the interface. The total number of microgels (N_{total}) at the air/water interface is then calculated by **equation 2.27**.

$$N_{\text{total}} = \frac{N_{\text{AFM}}}{A_{\text{AFM}}} \cdot A_{\text{trough}} \tag{2.27}$$

with N_{AFM} corresponding to the number of microgels in the AFM image, A_{AFM} to the area depicted in the AFM image and A_{trough} to the available area in the trough between the two barriers. The available area $A_{available}$ at the interface for one microgel is then calculated by **equation 2.28**.

$$A_{\text{available}} = \frac{A_{\text{trough}}}{N_{\text{total}}} \tag{2.28}$$

From the available area of one microgel, it is possible to conclude the distance between two microgels. Here the area fraction in a 2D hexagonal arrangement needs to be considered. For a 2D close-packed hexagonal system (see **Figure 2.20**), the lattice constant *a* corresponds to two times the radius of the circle R_{circle} representing the area occupied by the microgels.

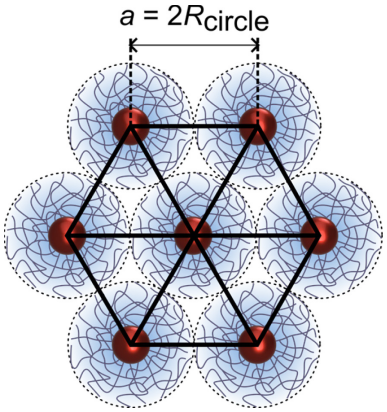

Figure 2.20. Schematical illustration of a 2D close-packed hexagonal arrangement of CS microgels with the lattice constant *a* and the radius of the circle R_{circle}.

The area of the hexagon A_{hex} can be expressed as the area of six equilateral triangles A_{tri} as follows:

$$A_{\mathrm{hex}} = 6A_{\mathrm{tri}} \tag{2.29}$$

$$A_{\mathrm{hex}} = 6\frac{\sqrt{3}}{4}a^2 \tag{2.30}$$

$$A_{\mathrm{hex}} = 6\sqrt{3}R_{\mathrm{circle}}^2 \tag{2.31}$$

The area fraction of the microgels can then be extracted by dividing the circular area occupied by one microgel with A_{hex}:

$$Area\ fraction = \frac{3\pi R_{\mathrm{circle}}^2}{6\sqrt{3}R_{\mathrm{circle}}^2} \approx 0.91 \tag{2.32}$$

Thus, the area fraction of 0.91 here represents the upper limit for hard sphere-like systems. In contrast, microgels can be compressed above this value due to their soft character. However, as the $d_{c\text{-}c}$ is calculated for non-compressed shell-shell contacts, this area fraction will be used as shown in **equation 2.33**.

$$d_{\mathrm{c-c}} = \sqrt{\frac{A_{\mathrm{available}} \cdot 0.91 \cdot 4}{\pi}} \tag{2.33}$$

Under the assumption that the total number of microgels is constant during the compression, the $d_{c\text{-}c}$ at the interface can be calculated for each point during the compression. Thus, the recorded extinction spectra can also be linked to the $d_{c\text{-}c}$ of the microgels at the air/water interface.

2.6. Extinction spectroscopy

Extinction spectroscopy is a common technique to measure the interactions phenomena absorption, refraction and scattering between a sample and incident light. The measurements can provide information about the analyzed system such as their chemical and electronic structure derived from potential electronic states.[184, 185] **Figure 2.21** schematically depicts an array spectrophotometer. In brief, the polychromatic light is focused on a cuvette containing the sample. The sample exemplary absorbs light with wavelengths below 500 nm and only wavelengths above 500 nm passes the cuvette. The light is separated into the individual wavelengths by a dispersing element and then detected as a function of wavelengths.

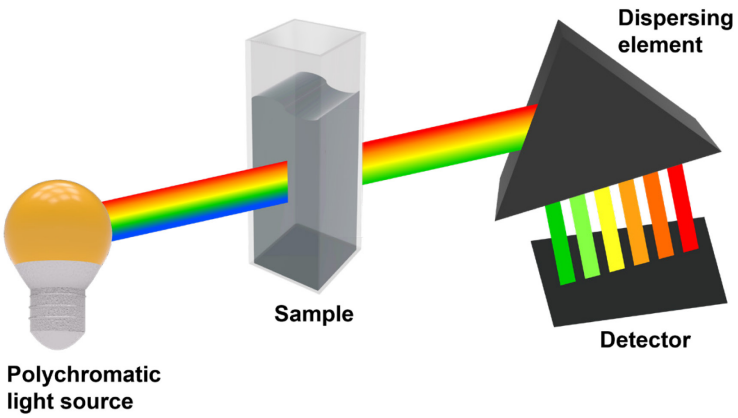

Figure 2.21. Schematic depiction of an extinction measurement with an array spectrophotometer containing a polychromatic light source, a sample, a dispersing element and a detector. Light with wavelengths below 500 nm is absorbed by the sample.

The relation between the intensity of the light illuminating the sample I_0 and the intensity of the transmitted light I is given by the Beer-Lambert law, see **equation 2.34**.

$$E_\lambda = log_{10}\left(\frac{I_0}{I}\right) = \varepsilon_\lambda \cdot c_0 \cdot d_{\text{path}} \tag{2.34}$$

Here, E_λ represents the extinction of material at a specific wavelength of light. The loss in intensity is related to the concentration c_0 of the particles in the sample, the optical path length d_{path} through the sample and the molar attenuation coefficient ε_λ of the particles at a certain wavelength.

When **equation 2.15** is compared with **equation 2.35**, the extinction cross section can be either expressed as sum of absorption and scattering cross section or as follows with N_A representing the Avogadro constant:

$$C_{\text{ext}} = \frac{2.303}{N_A} \varepsilon_\lambda \tag{2.35}$$

With this equation, it is possible to predict the attenuation of light for a specific sample.

2.7. Small-Angle Scattering

Scattering techniques present a powerful method to analyze microgels in respect to their size, shape and internal structure. In the following chapter, the principles of small-angle scattering (SAS) are introduced and extended for visible light, X-ray and neutron scattering experiments.

If an electromagnetic wave illuminates a scattering object, the oscillating electric field induces motion in the electric charges of the scattering object. These charges emit electromagnetic radiation in all directions referred to as scattered radiation. If the energy of the incident and scattered radiation remain unchanged during the process, this phenomenon is identified as elastic scattering.[112] The direction of the scattered radiation is quantified by the scattering vector $\vec{q}$. Thus, $\vec{q}$ gives the difference of the wave vectors of the incident radiation $\vec{k}_{\text{in}}$ and of the scattered radiation $\vec{k}_{\text{out}}$ as follows in **equation 2.36**.

$$\vec{q} = \vec{k}_{\text{in}} - \vec{k}_{\text{out}} \tag{2.36}$$

The geometric definition of $\vec{q}$ is schematically illustrated in **Figure 2.22**. Here, the incident radiation ($\vec{k}_{\mathrm{in}}$) is scattered at the scattering center by the scattering angle θ as scattered radiation ($\vec{k}_{\mathrm{out}}$).[186]

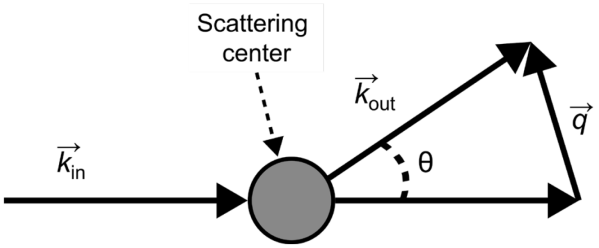

Figure 2.22. Construction of the scattering vector $\vec{q}$ derived by the scattering angle θ, the wave vector of the incident ($\vec{k}_{\mathrm{in}}$) and scattered radiation ($\vec{k}_{\mathrm{out}}$).

The magnitude of the scattering vector quantifies the length scale in a scattering experiment and is given by **equation 2.37**.

$$|\vec{q}| = q = \frac{4\pi}{\lambda}\sin\left(\frac{\theta}{2}\right) \tag{2.37}$$

λ denotes the wavelength of the incident radiation in the medium.[187]

The quantification of *q* gives the possibility to compare different SAS experiments with different radiation sources. A typical SAS setup is shown in **Figure 2.23**. Typically, a polychromatic beam passes through a monochromator, where one wavelength is selected to generate a monochromatic beam. The divergence and shape of the beam is subsequently controlled in the collimator and by the aperture, respectively. The beam is then focused on the sample volume. The scattering by the sample is measured by a 2D detector allowing for simultaneous recording of various scattering angles. This yields a pattern specific for the scattering of the sample. From this 2D pattern, the 1D scattering intensity curve as a function of *q* can be calculated *via* azimuthal integration.

The source of the polychromatic beam differs depending on the type of SAS experiment that is conducted. For SALS experiments, the beam consists of visible and near-infrared light delivered by laser diodes. These lasers are suitable for

laboratory applications, as they generate coherent and monochromatic beams exhibiting a high photon flux. Common X-ray sources, such as X-ray tubes are applied for small-angle X-ray scattering (SAXS) measurements on a laboratory scale. If ultra-high flux X-rays and short acquisition times are required, modern synchrotrons deliver a beam with excellent coherence, polarized light and high brilliance.[188] Performing a SANS measurement is only possible at large scale facilities, as they produce sufficient neutron flux by nuclear reactors and spallation sources. Typically, the distance between the sample and the detector can be adjusted which allows to resolve different scattering angles θ and thus different q. The accessible range defines the resolvable size-range in the analyzed sample. In combination with the short wavelength of X-rays and neutrons (λ < 4 nm), SAXS and SANS measurements can resolve structures between a few nm up to several µm. In contrast, the wavelengths (λ = 350 – 750 nm) in a SALS setup allows to resolve structures between 0.8 to 80 µm. The dimensions that can be resolved are comparable to optical microscopy.

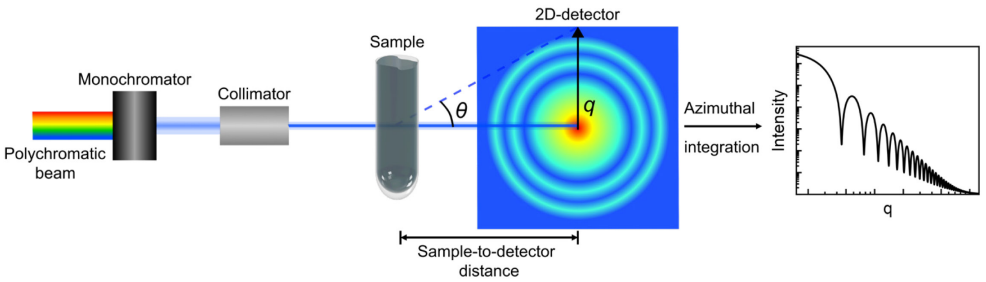

Figure 2.23. Schematic depiction of a SAS setup. The polychromatic beam is filtered by a monochromator into a monochromatic beam that is collimated by the collimator and focused on the sample volume. The sample-to-detector distance can be adjusted. θ gives the scattering angle and q the magnitude of the scattering vector. The scattering curve is obtained by azimuthal integration of the intensities on the detector.

The intensity of the scattering process exhibits an angular dependency, as indicated by the different colors in the 2D pattern on the detector **in Figure 2.23**. The angular dependency is observed, if the scattering objects overcome a certain size limit relative to the wavelength of the incident radiation. In this case, the object is not seen as a single scattering center, but a coalition of multiple centers, whose scattering can interfere. Such scattering objects are defined as Mie-scatterer for visible light experiments, when their dimensions are much larger than the wavelength of the

incident radiation, for instance $D_{\text{scat obj}} > \lambda/20$. If they do not fulfill the condition, i.e., $D_{\text{scat obj}} < \lambda/20$, they are defined as Rayleigh-scatterer and can be described as a single scattering center.[189]

The total intensity of the scattering process as a function of q is based on various parameters as given by **equation 2.38**.

$$I(q) = NV_{\text{scat obj}}^2 \Delta SLD^2 P(q) S(q) + I_{\text{B}} \tag{2.38}$$

N corresponds to the number of scattering objects with volume $V_{\text{scat obj}}$ in the scattering volume. The difference in scattering length densities (ΔSLD) between the scattering object and the environment gives the contrast for SAXS and SANS experiments. For SALS experiments, the contrast is given by the difference of the refractive indices. *P(q)* and *S(q)* refer to the form factor and structure factor, respectively. I_{B} corresponds to the scattering intensity of the background. All parameters, except the latter, will be discussed in the following.

The structure factor *S(q)* applies only to densely packed samples, where the distance between scattering objects is in the same magnitude as distances inside the individual scattering objects. Thus, *S(q)* defines the position of the scattering objects in the sample relative to each other. For dilute samples, as used in this work, *S(q)* can be approximated to the value of 1.

The form factor *P(q)* represents the oscillations of the scattering intensity due to scattering interference of multiple scattering centers in one single object. *P(q)* characterizes the shape of the scattering object. For a homogeneous sphere with a radius R, the form factor is given by the RDG approximation according to **equation 2.39**.[189, 190] **Figure 2.24** presents *P(q)* for a sample of monodisperse, homogeneous spheres (dark blue).

$$P(q) = \left[3\frac{\sin(qR) - qR\cos(qR)}{(qR)^3}\right]^2 \tag{2.39}$$

If the spheres exhibit size-dispersity, the form factors of all individual spheres are summed up to average the form factor of the sample.[191] The influence of size-dispersity is depicted by simulated scattering profiles with increasing

polydispersity (dark blue to brown) in **Figure 2.24**. The size distribution is considered by a Gaussian size distribution function with $\langle R \rangle$ representing the average radius of the spheres in the distribution function and σ_{SD} the respective standard deviation, see **equation 2.40**.

$$D(R, \langle R \rangle, \sigma_{SD}) = \frac{1}{\sqrt{2\pi\sigma_{SD}^2}} exp\left(-\frac{(R - \langle R \rangle)^2}{2\sigma_{SD}^2}\right) \tag{2.40}$$

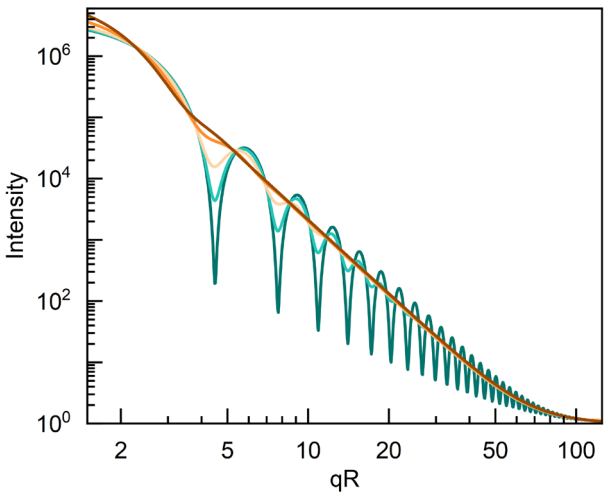

Figure 2.24. Influence of polydispersity on the form factor P(q) of homogeneous spheres. The polydispersity is set to 0.01, 0.05, 0.10, 0.20 and 0.30 from dark blue to brown.

For the lowest polydispersity of 0.01, the profile exhibits well-pronounced oscillations. The minima of the oscillations become less distinct, and their amplitude decreases, as the polydispersity increases. Above a polydispersity of 0.20 (orange), the scattering profile does not display any oscillations and the slope of the intensity follows q^{-4}, characterizing the surface of the spheres as flat. An increase in intensity can be observed at low *qR* for spheres with high polydispersity because the scattering intensity is dependent on the square of the volume *V* as shown in **equation 2.38**. Larger spheres contribute more to the scattering intensity than the smaller ones according to the relation depicted in **equation 2.41**.

$$I(q) \propto R^6 \tag{2.41}$$

As provided by **equation 2.38**, the scattering intensity is dependent on the number concentration of the scattering objects *N*. Especially for SAXS and SANS measurements, *N* can be directly extracted from the scattering profile, if the data is recorded in absolute units. For this, the measurement device needs to be calibrated by using a reference material, such as a sample of glassy carbon with a known thickness.[192] Consequently, *N* can be extracted directly for well-defined scattering objects with known density and composition according to **equation 2.42**.

$$N = \frac{I_0 N_A {\rho_{\text{scat obj}}}^2}{M_{\text{scat obj}} m_{\text{scat obj}} \Delta SLD^2} \tag{2.42}$$

With $\rho_{\text{scat obj}}$ referring to the density of the scattering object, $M_{\text{scat obj}}$ corresponding to its molecular weight and $m_{\text{scat obj}}$ to its average mass. The scattering intensity I_0 at infinitely small *q* can be extracted by the Guinier analysis.[188] The Guinier approximation assumes that the internal structure of the scattering object does not significantly influence the scattering at low *q* and the intensity depends only on its overall size and shape. Therefore, the Guinier approximation is valid in the plateau-like section of scattering profiles at low *qR* (*qR* << 1) and is given by **equation 2.43**.[189]

$$I(q) = I_0 \exp\left(-\frac{q^2 {R_g}^2}{3}\right) \tag{2.43}$$

R_g corresponds to the radius of gyration, representing the center of mass from the scattering centers in the scattering object. R_g does not directly correspond to the dimension or shape of the scattering object, but shape-dependent relations can be calculated with the radius of the object.[189] For a homogeneous sphere with a radius R_{sphere}, the relation is given in **equation 2.44**.[188]

$$R_g = \sqrt{\frac{3}{5}} R_{\text{sphere}} \tag{2.44}$$

The parameter *ΔSLD* in **equation 2.38** is the contrast between the scattering objects and their environment. The contrast situation strongly depends on the type of radiation, i.e., photons or neutrons, used during the scattering experiment. In a SAXS

experiment, the scattering length density (SLD) is proportional to the electron density of the material. More specifically, the SLD is determined by the number of electrons per unit of volume, as X-rays interact with the electron cloud of the material. Thus, scattering objects with higher electron densities contribute more to the overall scattering. For a SANS experiment, the neutrons interact with the nuclei of the material and the strength of this interaction defines the SLD. As a result, the SLD does not correspond to the elements position in the periodic table[188] and the SLD differs for isotopes of the same element. For instance ^{2}H, also known as D, has a higher SLD than ^{1}H. Consequently, a common approach in SANS experiments is to disperse hydrogenated samples in deuterated solvents to achieve an advantageous contrast situation. Furthermore, an advantage of neutron scattering is that the SLD of a material can be matched to the SLD of a H_2O/D_2O mixture.[193, 194] Thus, the ΔSLD becomes zero and the material does not contribute to the scattering intensity. This effect is applied to analyze samples consisting of different materials to vanish the scattering signal of one material. Adequate transmittance of the analyzed samples must be guaranteed for all different contrast situations to record a reliable scattering profile.

In this work, Au-PNIPAM microgels are investigated with SAXS and SANS. The scattering contrast situations in H_2O for Au-PNIPAM microgel swollen with 70 % mass content of water are depicted in **Figure 2.25**. The relative relation between the SLDs of water and microgel is illustrated by the contrast of the colors. As the volume also affects the total scattering intensity (see **equation 2.38**), the illustration only serves to visualize the differences in SLD between the dispersing medium and the AuNP core and the dispersing medium and the PNIPAM shell.

The SLD of the AuNP core is high for both types of radiation compared to the SLD of H_2O. On the contrary, the SLD of PNIPAM microgels is decreased due to its high internal solvent content, but ΔSLD(70%Water-PNIPAM) is sufficient to perform scattering experiments. For Au-PNIPAM microgels, the SLDs of both AuNP core and PNIPAM shell contribute to the total scattering intensity, even though at different length scales, and the overall contrast of the microgels is enhanced due to the core.

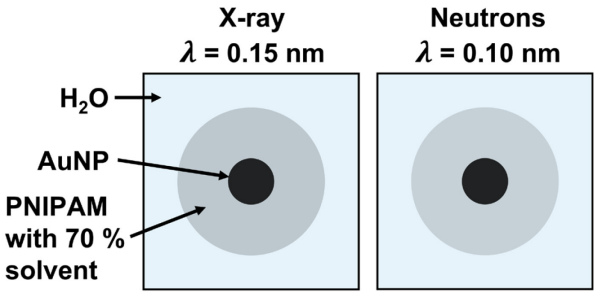

Figure 2.25. Contrast situation for Au-PNIPAM microgel swollen with 70 % mass content of water in respect to H_2O for X-rays (λ = 0.15 nm) and neutrons (λ = 0.10 nm).

The contrast of the PNIPAM shell in SANS experiments can be enhanced or changed by dispersing them in different H_2O/D_2O mixtures, as illustrated in **Figure 2.26**.

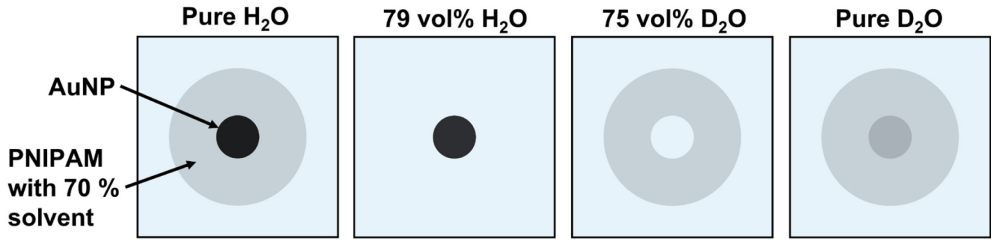

Figure 2.26. Scattering contrast situation for Au-PNIPAM microgel swollen with 70 % mass content of water in different H_2O/D_2O mixtures for SANS measurements. From left to right the composition of the mixtures: 100 vol% H_2O, 79 vol% H_2O, 75 vol% D_2O and 100 vol% D_2O.

In pure H_2O, the SLD of the AuNP core is high compared to the PNIPAM shell. By substituting 21 vol% H_2O with D_2O, the SLD of the PNIPAM shell is matched to the one of the mixture and the total scattering can only be attributed to the scattering of the core. If the mixture consists of 25 vol% H_2O and 75 vol% D_2O, the SLD of the core is matched to the dispersing medium and the scattering intensity is only ascribed to the scattering of the PNIPAM shell. As the core does not contribute to the scattering and the scattering profile is equivalent to that of a hollow sphere microgel. For 100 vol% of D_2O, the contrast of the core in reference to the dispersing medium is weakened and the one of the shell is strengthened. Thus, the core and the shell contribute equally to the scattering intensity in terms of contrast.

To describe the scattering behavior of Au-PNIPAM microgels, multi component models are required. The combination of the hard core with the soft shell containing an inner highly crosslinked part and dangling ends in the outer periphery makes it difficult to find an accurate model. However, the exponential shell form factor model, which is a common model to describe the scattering of microgels, is applied in this thesis. The scattering intensity of the exponential shell form factor model I_{ExpShell} is given by **equation 2.45**.[56, 92]

$$I_{\mathrm{ExpShell}} = \int_0^\infty 4\pi r^2 \frac{\sin(qr)}{qr} SLD_{\mathrm{ExpShell}}(r, R_{\mathrm{core}}, t_{\mathrm{shell}}, \alpha, \phi_{\mathrm{in}}, \phi_{\mathrm{out}}) dr \tag{2.45}$$

With *r* corresponding to the distance in the microgel. SLD_{ExpShell} corresponds to the averaged scattering length density of the complete microgel including core and shell. SLD_{ExpShell} is dependent on the SLD of the core SLD_{core}, the shell SLD_{Exp} and the solvent SLD_{solvent} as given by **equation 2.46**.

$$SLD_{\mathrm{ExpShell}}(r, R_{\mathrm{core}}, t_{\mathrm{shell}}, \alpha, \phi_{\mathrm{in}}, \phi_{\mathrm{out}}) = \begin{cases} SLD_{\mathrm{core}} & r \leq R_{\mathrm{core}} \\ SLD_{\mathrm{Exp}}\left(\dfrac{r - R_{\mathrm{core}}}{t_{\mathrm{shell}}}\right) & R_{\mathrm{core}} < r < R_{\mathrm{core}} + t_{\mathrm{shell}} \\ SLD_{\mathrm{solvent}} & r > R_{\mathrm{core}} + t_{\mathrm{shell}} \end{cases} \tag{2.46}$$

Here, R_{core} represents the radius of the core with a constant SLD. For the Au-PNIPAM microgels, it corresponds to the radius of the AuNP core. t_{shell} corresponds to the thickness of the shell and α to the parameter for the exponential diffuse profile of the shell. ϕ_{in} refers to the amount of solvent at R_{core} and ϕ_{out} to the amount of solvent at $R_{\mathrm{core}} + t_{\mathrm{shell}}$.

In dependence of the sign of α, the decay of the SLD in the shell changes, as shown by **equation 2.47**.

$$SLD_{\mathrm{Exp}}(x) = \begin{cases} SLD_{\mathrm{shell,in}} + \left[SLD_{\mathrm{shell,out}} - SLD_{\mathrm{shell,in}}\right] x \exp\left([1 - x]\alpha\right) & \alpha < 0 \\ \left[SLD_{\mathrm{shell,in}} - SLD_{\mathrm{shell,out}}\right][1 - x] \exp(-x\alpha) + SLD_{\mathrm{shell,out}} & \alpha \geq 0 \end{cases} \tag{2.47}$$

x refers to the quotient of $\frac{r - R_{\mathrm{core}}}{t_{\mathrm{shell}}}$. $SLD_{\mathrm{shell,in}}$ and $SLD_{\mathrm{shell,out}}$ are given by **equations 2.48 and 2.49**, respectively.

$$SLD_{\text{shell,in}} = [\phi_{\text{in}} SLD_{\text{solvent}} + (1 - \phi_{\text{in}}) SLD_{\text{shell}}] \quad (2.48)$$

$$SLD_{\text{shell,out}} = [\phi_{\text{out}} SLD_{\text{solvent}} + (1 - \phi_{\text{out}}) SLD_{\text{shell}}] \quad (2.49)$$

With SLD_{shell} corresponding to the scattering length density of the pure shell material.

A simulated radial *SLD* profile for a CS microgel calculated from the exponential shell form factor model is shown in blue in **Figure 2.27**. Starting from the center of the core and moving outwards, the profile starts with the constant SLD of the core over its radius until the SLD changes to the one of the swollen shell. If the polymer decays linear inside the shell, α = 0 (orange). Alternatively, to a linear decay, the polymer density can decay exponentially. The exponential decay can be either concave or convex in dependence of the amount of solvent that penetrates the shell. If the solvent penetrates further in the shell, α > 0 (red) and if the solvent penetrates the shell less, α < 0 (green). The latter is the case for the Au-PNIPAM microgels investigated in this thesis. The SLD matches the SLD of the solvent at the radius of R_{core} + t_{shell}, which corresponds to the overall radius of the microgel.

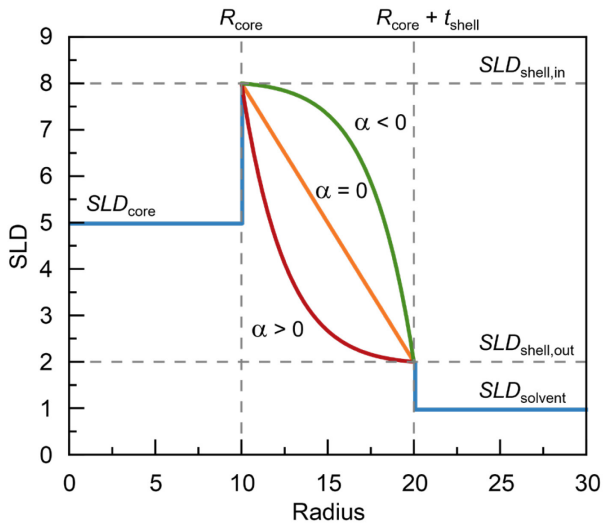

Figure 2.27. Radial SLD profiles calculated from the exponential shell form factor model with radius of core R_{core} and thickness of shell t_{shell}. The *SLD* profiles changes in the shell regime by varying α which describes the penetration of solvent into the shell. For α = 0, the profile changes linear (orange). For α < 0 (green) and α > 0 (red), the solvent enters the shell less or further, respectively.

The form factor model of the exponential shell (dark blue) is compared to the one of a hard sphere (brown) in **Figure 2.28 a** and the corresponding radial SLD profiles are depicted in **Figure 2.28 b**. Both form factor models display distinct oscillations, however the first form factor minimum is shifted to higher *qR* for the exponential shell model. This shift is caused by differences in the distribution of polymer density. Comparison of the radial SLD profiles reveals that the polymer density of the hard sphere (brown) is homogenously distributed. In contrast, the profile of the exponential shell model (dark blue) indicates a homogeneous inner part and a shell where the polymer density decays exponentially. The exponential model simulates that the internal structure of a microgel consists of a core with a high polymer density and an outer periphery with low polymer density leading to a fuzziness of the microgel on the outside.

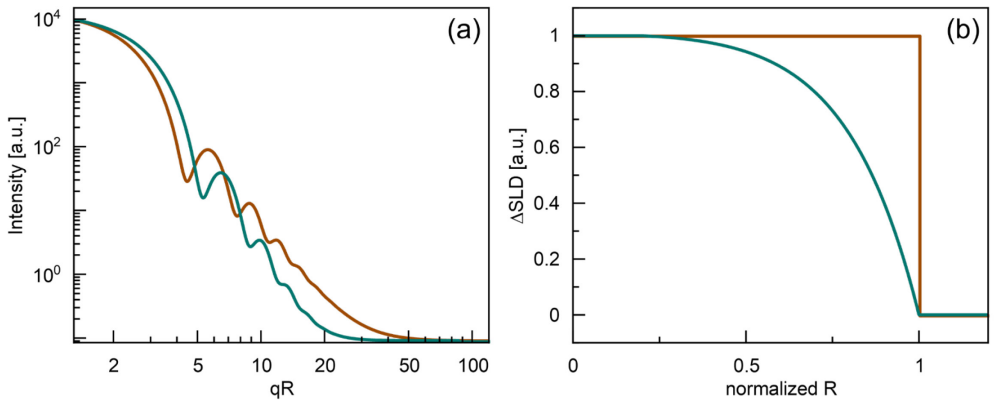

Figure 2.28. Simulated form factors (a) and respective radial SLD profiles (b) corresponding to a hard sphere (brown) and a fuzzy sphere modelled by the exponential shell model (dark blue). For both scattering profiles, the polydispersity was set to 5 % and the same radius of the sphere was considered for the calculations.

A further length scale in microgels contributes to the scattering intensity at larger *q*. This contribution is known as Ornstein-Zernike contribution and caused by the movement of polymer chains in the network.[195, 196] The movement leads to local concentration fluctuations which can be detected in scattering experiments. This dynamic contribution I_{OZ} is considered by a Lorenzian function given in **equation 2.50**.[197]

$$I_{\mathrm{OZ}} = \frac{I_{\mathrm{fluct}}(0)}{1 + \xi^2 q^2} \tag{2.50}$$

With $I_{\mathrm{fluct}}(0)$ corresponding to the Lorenzian intensity and ξ to the correlation length, which is dependent on cross linker content and swelling state.[197] The Ornstein-Zernike contribution is a dynamic contribution, detectable, when microgels are swollen with solvent and polymer chains in the network show movement. If a thermoresponsive microgel is investigated, the Ornstein-Zernike contribution is not detectable, above the VPTT, due to the suppression of the internal movement of the chains after collapse.

3. Synopsis

Over the past years, CS microgels have gained increased attention in research due to their complex phase behavior at the interface and their potential applications in the fields of drug delivery and sensors. [105, 198, 199] Their complex interactions at the interface are highly influenced by not only the composition of the microgels themselves,[35, 43, 69, 200] but also by external aspects such as temperature and compression beyond an equilibrium state.[71, 154, 183] Despite the intensive research, the interfacial behavior of microgels is not yet fully understood. It is known that microgels can spontaneously assemble at interfaces, however achieving precise control over their organization and arrangement remains challenging. This lack of control limits their full utilization in advanced applications, highlighting the need for further research. Facing these challenges, this thesis aims to deepen the understanding of CS microgels and their interfacial behavior. The following work focusses on resolving the internal structure and the interfacial behavior of AuNP core-PNIPAM shell microgels. The chapters address various aspects, ranging from the detailed structural analysis of the individual colloidal building blocks (**Chapter 4**) over the formation of complex lattices (**Chapter 5**) to the investigation of plasmonic monolayers in situ at the air/water interface (**Chapter 6**).

CS microgels with enhanced LSPR behavior are commonly used to prepare periodic assemblies. Thereby, long-ranging coupling between the individual cores is enabled.[59, 123, 201] The study presented in **Chapter 4** systematically investigates such CS microgels by using various techniques. While previous works have analyzed the impact of the core overgrowth on the optical characteristics, the effect on the shell morphology has often been overlooked. Therefore, this work focused on both the AuNP cores and the polymer shell before and after the overgrowth of the core. To investigate the influence of the growth of the core on different shell compositions, Au-PNIPAM microgels with a high and a low crosslinker content were synthesized. The initial microgels contained small cores, which were then overgrown *in situ* by a factor of approximately 6.5 in radius, as schematically depicted in **Figure 3.1 top**. The visualization of the CS microgels by transmission electron microscopy (TEM) showed a denser region of the shell around the core for microgels with higher crosslinker content. This region became even more pronounced after the overgrowth. This phenomenon could be attributed to the compression of the polymer network induced

by the growth of the core. Due to the higher contrast of Au compared to the polymer shell in SAXS measurements, the core size, as well as the number concentration of the microgels before and after the overgrowth were determined by SAXS profiles. As previously shown in literature,[202] the number concentration of microgels was determined based on the assumption that the total number of cores corresponds to the total number of microgels. To gain insights into the internal structure of the shell, temperature-dependent SANS measurements were conducted. The scattering profile was primarily governed by the form factor of the PNIPAM shell. For all four samples, the Ornstein-Zernike regime at high q could be described at low temperatures by **equation 2.50**. An increase in correlation length for the microgels with overgrown cores suggested a change in internal morphology. At high temperatures (T >> VPTT), all CS microgels showed a homogenous distribution of the polymer density inside the shell which could be described by a homogeneous sphere form factor. At low temperatures (T < VPTT), CS microgels with small cores were described by the exponential shell form factor model, enabling the extraction of radial profiles of the polymer density. These profiles indicated an exponential decay in polymer density from the inside to the outside with a more homogenous and denser inner region and a fuzzy corona. These observations aligned with previous findings in literature.[21] However, existing models were inadequate to describe the form factor oscillations and mid q range of CS microgels with the overgrown cores. For this reason, reverse Monte-Carlo (RMC) simulations were performed to compute radial profiles of the CS microgels. The simulated profiles for CS microgels with overgrown cores revealed a compressed polymer region around the core, an effect that was more pronounced in microgels with higher crosslinker content. These findings were consistent with the TEM images, further confirming that core overgrowth did not alter the overall behavior of the microgels but influenced the internal polymer distribution within the shell.

The equilibrium structure of self-assembled microgels and CS microgels at fluid interfaces is the hexagonal close-packing arrangement. A key question in **Chapter 5** was, whether other two-dimensional structures can be realized by controlled deformation of the microgel monolayer induced by transfer conditions to solid substrates. This was motivated by a previous work from Hummel *et al.*,[77] where rigid colloids were used to prepare all five Bravais lattices *via* interface-assisted assembly. Their method was adapted to the soft Au-PNIPAM microgels. The CS microgels were transferred to the air/water interface, where they self-assembled into a hexagonally

ordered monolayer. Here, the PNIPAM shell enabled the adsorption to the fluid interface. Furthermore, the shell acted as spacer between the AuNP cores and thereby directed the periodicity of the final lattices. The monolayer was subsequently transferred onto a substrate, as shown by **Figure 3.1 left box**. The different lattices were received by changing the contact angle of the substrate and the transfer speed and direction of the substrate. The hexagonal arrangement was prepared as reported in literature by first placing a hydrophilic substrate in the aqueous phase below the interface and then retracting it through the monolayer.[57] For square, rectangular and centered rectangular lattices, a hydrophobic substrate was used. For oblique lattices, a strongly hydrophobic substrate with a contact angle larger than 90 ° was used. For these four lattices, the monolayer was transferred to the substrate by immersing through the monolayer in the aqueous phase. The differences in preparation were in transfer speed and angle of substrate in respect to the interface. As a result, the hexagonally ordered monolayer at the interface was differently stretched and deformed to obtain the other lattices. To circumvent strong capillary forces acting upon the deposited microgels during the retraction, the monolayers were thermally annealed to the substrate prior to retraction. This step was found to be crucial to maintain the different lattices. Subsequent rapid drying of the monolayers resulted in one of the five Bravais lattices of non-close-packed dried CS microgels. The optical response of the different lattices was investigated by extinction spectroscopy and compared to simulated extinction spectra. Additionally, the optical response of an oblique ordered monolayer was further investigated in different RI environments. For that, the PNIPAM shell was removed by plasma treatment to obtain non-close-packed lattices of bare AuNPs assembled on a solid substrate with air as superstrate. The removal of the shell was verified by scanning electron microscopy (SEM) before and after plasma treatment. The lattice exhibited an LSPR peak at lower wavelengths compared to the lattice of non-close-packed CS microgels. Furthermore, the lattice of non-close-packed bare AuNPs was coated with a polymer, that showed a similar RI than the substrate. The polymer coating acted as a superstrate to obtain a homogeneous RI environment around the bare AuNPs. By this, SLR was enabled and a sharp narrow peak at higher wavelengths compared to the LSPR peak was detected in the extinction spectrum. The versatility of the preparation method was emphasized as oblique lattices were prepared with CS microgels exhibiting a larger shell size. Thus, the lattice showed the same order, but larger interparticle distances.

The microstructure of such lattices is typically visualized *ex situ* by microscopy techniques, as the visualization *in situ* at interface still remains a challenge. Recently, some works presented the progress in the visualization of the 3D shape of single microgels at interfaces by *in situ* AFM and neutron reflectometry.[75, 183] In this thesis, a novel method is presented in **Chapter 6** to measure *in situ* extinction spectra of assembled Au-PNIPAM microgels at the air/water interface in a Langmuir trough under compression, see **Figure 3.1 right box top**. The setup allowed to record extinction spectra of the interface during the compression, which proceeded over approximately 30 minutes. The optical response of the monolayer could be monitored with high temporal resolution, as spectra were recorded in intervals of one second. A full set of extinction spectra from one compression is depicted in **Figure 3.1 right box bottom**. The recorded *in situ* extinction spectra could be linked to the surface pressure, which was simultaneously tracked during the compression. For Au-PNIPAM microgels with small cores, the LSPR was too weak to resolve the signal from the background noise. Therefore, it was necessary to use CS microgels with overgrown cores that exhibited a stronger LSPR. However, the spectra of the microgels with small cores verified that the PNIPAM shell did not affect the optical response and the signal was only related to the interplay between the AuNP cores. The large cores enhanced the LSPR and provided enough signal at the interface to record the optical response of the monolayer. A sharp extinction peak was observed at low surface pressures which indicated diffractive-plasmonic coupling in the interfacial monolayer. This finding was verified by COMSOL simulations where this experimental observation could be reproduced. From literature, it is known that a homogenous RI environment is needed for the electromagnetic coupling between the LSPR mode and the in-plane diffraction mode.[110, 123] Thus, our results were surprising, as the AuNP cores were encapsulated in a solvated polymer shell with a RI higher than 1.33. They were located in the aqueous phase with a RI of 1.33 near or at the air/water interface with air (RI = 1) above them. So, this presents a rather complex RI environment situation. For our experiment, light incidents at a normal angle to the interface, but the LSPR modes were excited to result in an in-plane SLR, as shown by the simulated E-field maps. This led to the conclusion that as SLR is enabled in the interfacial monolayer, the RI environment around the AuNP cores in the plane was sufficiently homogeneous to support plasmonic-diffractive coupling. Additionally, a Langmuir-Blodgett deposition was performed with Au-PNIPAM microgels over the same range of surface pressure. The *ex situ* analysis of the

monolayer structure by AFM, especially at the lowest surface pressure, was employed as reference to calculate the nearest neighbor center-to-center distance $d_{c\text{-}c}$ at the interface. It was assumed that at this surface pressure, the structure at the interface was maintained during the transfer due to large distances and low capillary forces between microgels. The $d_{c\text{-}c}$ of the microgels at the interface was calculated for every surface pressure in the compression isotherm and then linked to the peak position of the corresponding extinction spectrum. *In situ* extinction spectra were compared to *ex situ* extinction spectra of the coated glass substrate. In contrast to *ex situ*, a continuous shift of the *in situ* peak position in dependence of the compression was observed. This indicated a continuous decrease of the interparticle spacing at the interface which stands in contrast to the assumption that clustering occurs at the interface. These results underlined that the Langmuir-Blodgett deposition can alter the interfacial microstructure during the transfer and the transferred monolayer not necessarily reflect the microstructure from the interface. This emphasizes the need for *in situ* measurements to elucidate the interfacial structure of assembled microgels over a broad range of surface pressures.

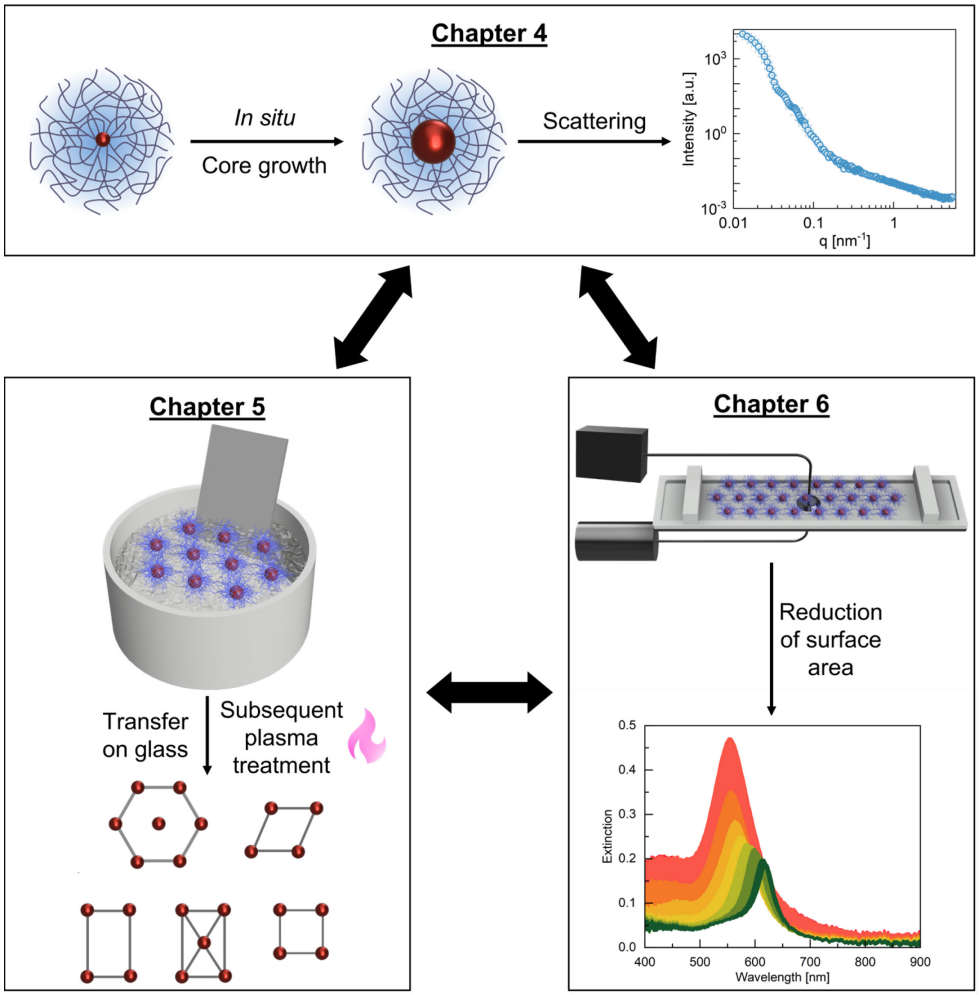

Figure 3.1. Top from left to right: Au-PNIPAM CS microgel with small AuNP core which is then overgrown *in situ* in the PNIPAM shell to obtain CS microgel with large AuNP cores. SANS profile of the CS microgel with the overgrown core at 20 °C. Bottom left from top to bottom: Schematic illustration of the CS microgels assembled at the air/water interface with transfer to a glass substrate. Scheme of the five possible Bravais lattices of non-close-packed AuNPs on substrates after plasma treatment. Bottom right from top to bottom: Schematic depiction of a hexagonally ordered monolayer formed by CS microgels at the air/water interface in a Langmuir trough at the lowest compression. The black cylinder and the grey box represent the light source and the detector, respectively with the glass fibers. During reduction of surface area, extinction spectra are taken at one second intervals from the monolayer at the air/water interface. The compression increases from dark green to dark red.

3.1. Contribution to Joint Publications

Chapter 4: *In situ* overgrowth of gold core-shell microgels: Resolving changes in the polymer shell

Déborah Feller, Julian Oberdisse, Sylvain Prévost and Matthias Karg

Manuscript in preparation for submission

M.K. designed the study, supervised the project and secured project funding. I synthesized all the different core-shell microgels and characterized them by temperature-dependent dynamic light scattering, temperature-dependent extinction spectroscopy. M.H. helped with the recording of small-angle X-ray scattering curves and I analyzed the profiles. Additional synchrotron SAXS data were recorded and reduced by A.S., J.E.H. and J.C. and I analyzed the reduced data. SANS data were recorded by me and M.K. with the help of S.P. as responsible beamline scientist. M.K. supported me during the analysis and interpretation of the SANS data. J.O. and I did some pre-work for the reverse Monte-Carlo simulations. The fine-tuning and the final simulations were done by J.O. I designed and prepared all the figures and wrote the first version of the manuscript. M.K. performed editing and all authors contributed with helpful discussions and proofread the manuscript.

Chapter 5: Non-close-packed plasmonic Bravais lattices through a fluid interface-assisted colloidal assembly and transfer process

Déborah Feller, Marius Otten, Michael S. Dimitriyev, and Matthias Karg

Published in *Colloid and Polymer Science*, **2024**, 302, n/a
DOI: 10.1007/s00396-024-05285-4

M.K. and I designed the study. M.K. supervised the project and secured project funding. I synthesized the core-shell microgels and conducted the characterization of the microgels including dynamic light scattering and transmission electron microscopy images. I prepared all monolayer samples and characterized them by atomic force microscopy. Further processing of the images was conducted by me. The post modifications of the structure were conducted by me. I performed all the finite

difference time domain simulations of the different structures. M.O. conducted scanning and transmission electron microscopy measurements which I then analyzed. M.S.D. computed the Voronoi and Delaunay tessellations and helped with interpretation of the structural analysis. I designed and prepared all the figures and wrote the first version of the manuscript. M.K. performed editing and all authors contributed with helpful discussions and proofread the manuscript.

Chapter 6: Following plasmon resonance coupling in soft, confined colloidal films during continuous compression

Déborah Feller, Jiakai Wang, Julian Kippenberger, Christian Washeim, Jan Meissner, Jan Meisner, Paul Mulvaney and Matthias Karg

Manuscript in preparation for submission

M.K. and I designed the study. M.K. supervised the project and secured project funding. I synthesized the core-shell microgels and performed the characterization including dynamic light scattering and transmission electron microscopy images. J.K. designed and 3D-printed the first version of the fiber holder while taking my ideas into account. C.W. then optimized the holder and conducted preliminary experiments with the self-built setup. I prepared the monolayer via Langmuir-Blodgett deposition and characterized the monolayer by atomic force microscopy and extinction spectroscopy. Further processing of the images was performed by me. I conducted and analyzed the *in situ* experiment and combined the results to the *ex situ* measurements. J.W. and P.M. performed COMSOL simulations to support our experimental findings and helped with the interpretation of the results. J.M. and J.M. provided the PeakAnalyzer script to extract different parameters, such as peak position from the extinction spectra. I designed and prepared all the figures and wrote the first version of the manuscript. M.K. performed editing and all authors contributed with helpful discussions and proofread the manuscript.

4. *In situ* overgrowth of gold core-shell microgels: Resolving changes in the polymer shell

Manuscript in preparation for submission

Déborah Feller[a], Julian Oberdisse[b], Sylvain Prévost[c] and Matthias Karg[a,d]

[a]Institut für Physikalische Chemie I: Kolloide und Nanooptik, Heinrich-Heine-Universität Düsseldorf, Düsseldorf, Germany

[b] Equipe Matière Molle – Soft Matter Group, Laboratoire Charles Coulomb, Université Montpellier, Montpellier, France

[c] Large Scale Structures, Institut Laue-Langevin, Grenoble, France

[d] Physikalische Chemie funktionaler Polymere, Martin-Luther-Universität Halle-Wittenberg, Halle (Saale), Deutschland

4.1. Abstract

Core-shell (CS) microgels stand out due to their combined properties of core and shell. Mostly, the shell is based on crosslinked, thermoresponsive poly(*N*-isopropylacrylamide) (PNIPAM) giving a soft character to these microgels. The core, often gold nanoparticles exhibiting a localized surface plasmon resonance (LSPR), introduce this optical property to the microgel. Such gold-PNIPAM (Au-PNIPAM) microgels were intensively studied in respect to the property of the Au cores. As these cores can be overgrown *in situ* in the shell, the changes in the LSPR dependent on the size are analyzed. However, the influence on the shell is often neglected. Here, we propose to investigate the polymer shell with different crosslinker content before and after modification of the Au cores. The size of the cores, as well as the volume fraction of the microgels in dispersion is determined by small-angle X-ray scattering (SAXS), due to the high scattering contrast of gold cores. We applied a combination of different temperature-dependent measurements to analyze, if the overgrowth leads to inhomogeneities in the shell. We employed small-angle neutron scattering (SANS) to better visualize the scattering and thereby study the internal structure of the shell. Radial profiles of the polymer density are extracted from the scattering curves only for CS microgels with small cores. For this reason, reverse Monte-Carlo (RMC) simulations are performed. Thereby, the experimental radial profiles are validated and insights into the polymer distribution in the shell of microgels with overgrown cores are given, as appropriate fitting models are missing. Thus, our study gives the opportunity to mathematically find an appropriate form factor model for such CS microgels.

4.2. Introduction

Core-shell (CS) microgels present a unique subgroup of colloidal particles that include properties of both, core and shell. This combination offers a vast structural and functional variety for various applications, such as photonic crystals or as nanoreactor for chemical reactions.[203-205] The shell is typically formed by a three-dimensional network of crosslinked polymer. Here softness of the shell can be tuned by the choice

of monomer. For instance, polystyrene (PS) or polymethylmethacrylate (PMMA) microgels are frequently used to mimic the behavior of hard spheres. In contrast, poly(*N*-isopropylacrylamide) (PNIPAM) microgels are commonly used as a model for soft spheres. The advantage of PNIPAM microgels is that the softness can not only be tuned by crosslinker content,[13, 22, 25] but also in response to external stimuli, particularly temperature. PNIPAM microgels undergo a volume phase transition (VPT) at a temperature of about 32 °C,[19, 20] which is related to the lower critical solution temperature (LCST) of the PNIPAM homopolymer. For PNIPAM microgels, this temperature is called volume phase transition temperature (VPTT). Below the VPTT, PNIPAM microgels are highly swollen with water and feature a soft character.[21, 22] By increasing the temperature, water is expelled from the microgels, leading to a transition towards a more rigid sphere. However, even at temperatures above the VPTT, they still contain a large amount of solvent.[21] Such soft and responsive microgels are often employed to study packing fractions in two- or three-dimensional crystallization processes.[30, 154, 206] Similar to hard spheres, they can self-assemble into highly ordered structures. They spontaneously adsorb to the air/water or oil/water interface and form a 2D hexagonally ordered monolayer. Hildebrandt *et al*. demonstrated that they can form three-dimensional colloidal crystals with large domains.[31] In contrast to hard spheres, the volume fraction of PNIPAM microgels can be altered by temperature due to their responsive behavior. However, the exact determination of the volume fraction still remains a challenge, as microgels can interpenetrate, deswell and undergo faceting at high volume fractions changing their form factor. To solve this problem, different works show the incorporation of silica cores into PNIPAM microgels.[202] Here, silica cores exhibit a form factor not influenced by the dense packing. Thus, the volume fraction of the CS microgels can be determined at every concentration due to the silica cores by retaining the properties of the PNIPAM microgels. Besides silica cores, metal cores, such as gold nanoparticles, introduced in a PNIPAM shell gaining more interest over the last years.[45, 67] Such gold-PNIPAM (Au-PNIPAM) microgels are interesting for application in photonics and sensors due to the optical properties of the gold core.[58, 105] The PNIPAM shell acts as an interparticle spacer and supports formation of crystal lattices, while the Au cores feature a localized surface lattice resonance (LSPR). In contrast to silica cores, Au cores can be tuned in terms of size *in situ* in the shell. Thus, postmodification of Au cores by overgrowth is possible without destruction of the PNIPAM shell. Larger Au cores enhance the optical properties of the CS microgels

and enable plasmonic-diffractive coupling leading to a surface lattice resonance (SLR), if the spacing is adjusted to the order of the visible wavelength. Hence, increased research was dedicated to understand the influence of the postmodification onto the properties of the Au cores.[51] However, the effect of the core growth on the morphology of the PNIPAM shell remains nearly unexplored. As the interplay between core and shell is mandatory to optimize the CS microgels in applications, this knowledge is fundamental.

In this context, we aim to get a deeper understanding of the structure of the PNIPAM shell before and after the core overgrowth. We investigate the influence of the core growth for two different nominal crosslinker contents (16.7 and 8 mol%). We exploit the electron density difference of Au and PNIPAM to determine core size and volume fraction of the CS microgels via small-angle X-ray scattering (SAXS). We combine temperature-dependent measurements to obtain an overview on the overall behavior of the CS microgels. To get insights into the internal structure of the PNIPAM shell, we employed small-angle neutron scattering (SANS). As the PNIPAM shell dominates the form factor in the scattering profile, we could extract radial profiles of the difference in scattering length density (ΔSLD) over a broad temperature range for the CS microgels with the small cores. However, as we are lacking of an appropriate form factor model for CS microgels with overgrown cores, we performed reverse Monte-Carlo (RMC) simulations. The simulated radial profiles provide access to discuss changes in the internal structure of the PNIPAM shell after the core overgrowth.

4.3. Experimental section

4.3.1. Materials

Gold(III) chloride trihydrate ($HAuCl_4 \cdot 3H_2O$; Sigma-Aldrich, ≥ 99.999%), sodium citrate dihydrate (Sigma-Aldrich, ≥ 99%), sodium dodecyl sulfate (SDS; Sigma-Aldrich, p.a.), butenylamine hydrochloride (BA; Sigma-Aldrich, 97%), *N*,*N*′-methylenebisacrylamide (BIS; Sigma-Aldrich, ≥ 99%), potassium peroxodisulfate (PPS; Sigma-Aldrich, ≥ 99%), cetyltrimethylammonium chloride

(CTAC; Sigma-Aldrich, 25 wt% in water), ascorbic acid (Roth, p.a.), 1H,1H,2H,2H-Perfluorooctyltriethoxysilane (FOCTS; J&K Scientific, 97%), ethanol (Honeywell, p. a.), ammonia (PanReac Applichem, 30% in water), hydrogen peroxide (Fisher Scientific, > 30% in water), cyclohexane (Fisher Scientific, ≥ 99.8%), and Hellmanex III (Hellma GmbH) were used as received. Heavy water (D_2O, Sigma Aldrich, 99.99 %) was filtered with a 5 µm syringe filter (PTFE, Carl Roth) prior to use. *N*-isopropylacrylamide (NIPAM; TCI, > 98.0%) was recrystallized from cyclohexane. Milli-Q water (Millipore, resistivity > 18 MΩcm) was used for all synthesis and Langmuir trough experiments.

4.3.2. Synthesis

Synthesis of core-shell microgels with different crosslinker densities

Spherical gold nanoparticles (AuNPs) were synthesized via the typical Turkevich method, as previously reported.[207] We performed the synthesis twice, resulting in AuNPs with a radii of 6.6 ± 0.6 nm and 7.3 ± 0.7 nm, respectively. Due to the similarity, we do not differentiate between the two syntheses in the following and label the AuNPs with Au_7, where the index represents the radius according to SAXS measurements.

The AuNPs were then encapsulated as cores into a polymer shell of NIPAM and BIS as crosslinker via a seeded precipitation polymerization, as already reported elsewhere.[76] We synthesized two different batches of CS microgels, one with 16.7 mol% and one with 8 mol% nominal crosslinker content. To differentiate between the two batches, the CS microgels are labelled as Au_7-$PNIPAM_{high}$ and Au_7-$PNIPAM_{low}$, whereby the index behind PNIPAM represents whether the nominal crosslinker content in the shell is high (16.7 mol%) or low (8 mol%).

Additionally, the Au cores were then further overgrown *in situ* in the polymer shell, resulting in Au cores with a radius of 46.3 ± 0.5 nm and 46.2 ± 0.5 nm, respectively according to SAXS measurements. The CS microgels are labelled as follows, Au_{46}-$PNIPAM_{high}$ and Au_{46}-$PNIPAM_{low}$, where the index following Au represents the radius of the final, overgrown cores. For Au_{46}-$PNIPAM_{high}$, the overgrowth protocol

was already reported by Ponomareva *et al*.[55] The overgrowth protocol for Au_{46}-$PNIPAM_{low}$ was adapted from the protocol of Honold *et al*.[51] In brief, 32 mL of an aqueous CTAC solution (10 mM) was stirred at 45 °C in an Erlenmeyer flask. 329.2 µL of an aqueous solution of Au_7-$PNIPAM_{low}$ (2 wt%) was mixed with 800 µL of an aqueous CTAC solution (0.1 M) and 800 µL of this mixture were added to the Erlenmeyer flask. Then, 1.552 mL of an aqueous solution containing ascorbic acid (49 mM) were added in one shot. 116 mL of an aqueous solution containing CTAC (6.2 mM) and HAuCl4 (0.5 mM) were slowly added to the Erlenmeyer flask while the dispersion was heavily stirred at 45 °C. Afterwards, the dispersion was left to stir at 45 °C for further 30 min. The CS microgels were then dialyzed against water for 2 weeks with daily water exchange. After the dialysis, the microgels were centrifuged three times for 30 min at 5400 rcf and redispersed in water, ready for further use.

4.3.3. Methods

Transmission electron microscopy (TEM)

TEM imaging was performed with a JEOL JEM-2100Plus TEM in bright-field mode operated with an acceleration voltage of 80 kV. The samples were prepared on carbon-coated copper grids (200 mesh, Electron Microscopy Science) by drop-casting 7 µL of a dilute aqueous microgel dispersion for 1 minute. After blotting, the grids were placed on a drop of 2 % uranyl acetate solution and immediately blotted. The grids were subsequently placed on a further drop of 2 % uranyl acetate solution for 45 seconds. After blotting, the grids were left to dry at room temperature for at least 30 minutes. Images were analyzed by using the software ImageJ.[208]

Dynamic light scattering (DLS)

DLS measurements were performed with the Zetasizer Nano S (Malvern Panalyctical). The laser used had a wavelength of 633 nm and the scattered light was detected at a scattering angle of 173 °. For the temperature-dependent DLS measurements, a dilute aqueous CS microgel dispersion was measured three times for 60 s in a semi-macro cuvette (polymethacrylate, VWR) in a temperature range of

15 – 50 °C in 1 °C steps. Before the measurement, the samples were left to equilibrate for 300 s. The hydrodynamic radius, R_h, (z-average) was determined by cumulant analysis via the instrument software.

Extinction spectroscopy

Extinction spectra were recorded using a Specord S 600 UV–Vis spectrophotometer (Analytik Jena AG) over a wavelength range of 250 – 1019 nm. The spectra of dilute samples were measured in transmission geometry using PMMA cuvettes with 1 cm pathlength. For the temperature-dependent measurements, the samples were measured in the temperature range from 15 – 51 °C in 2 °C steps. The equilibration time between two temperatures was set to be 600 s. Water in PMMA cuvettes was always measured as background.

Small-angle X-ray scattering (SAXS)

In-house SAXS measurements were conducted on a Xeuss 2.0 (XENOCS) equipped with a Pilatus3R 300K detector. The detector had a sensitive area of 83.8 x 106.5 mm^2 with a total pixel size of 172 x 172 μm^2. The X-ray beam had an energy of 8.048 keV and a wavelength of 0.154 nm (Cu-K_α). The sample-to-detector distance was set to 2.5 m, resulting in an effective q-range of 0.03 nm^{-1} to 2.5 nm^{-1}. Acquisition times were 3600 s and 2700 s, respectively. Dilute samples were measured in 1 mm round quartz glass capillaries (WJM Glas). Milli-Q water was used as background and data were corrected accordingly. All data here are reported in arbitrary units, as the form factor extraction does not need absolute scaling.

To extract the number concentration from the samples measured in the SANS experiment, the samples dispersed in D_2O were measured in 1 mm round quartz glass capillaries (WJM Glas) for 2700 s at a detector distance of 2.5 m. The scattering profiles were background corrected by the scattering of D_2O, normalized to absolute intensities by considering the thickness of the capillary and the scattering of the reference glassy carbon. Then the data was radially averaged with the software Foxtrot provided by Xenocs. The procedure to extract the number concentration from SAXS profiles in absolute units was reported elsewhere.[21, 202]

Synchrotron SAXS measurements were done on the CoSAXS beamline at the MAX IV synchrotron in Sweden, Lund. The scattering profiles were recorded with an Eiger2 4M detector with a sensitive area of 155.1 x 162.2 mm^2 and a total pixel size of 75 x 75 μm^2. The X-ray beam had an energy of 12.4 keV and the sample-to-detector distance was set to 6.85 m, resulting in a *q*-range of 0.01 nm^{-1} to 0.75 nm^{-1}. Samples were measured in 1 mm round capillaries (WJM Glas) at 20 °C. The data was radially averaged and background corrected for D_2O.

All SAXS data were analyzed with the software SasView, an open-source scattering analysis software,[209] to extract form factors from the scattering profiles.

Small-angle neutron scattering (SANS)

SANS experiments were conducted on the D33 instrument at the Institut Laue-Langevin (ILL) in France, Grenoble.(DOI: 10.5291/ILL-DATA.9-11-2100) The instrument was equipped with two different detectors, where the front detector was set to a fix distance of 1.187 m. The front detector was composed of a 4-panel monoblock with a size of 160 x 640 mm^2 for each panel and 32 x 128 $pixels^2$, resulting in a pixel size of 5 x 5 mm^2. The rear detector was a single panel monoblock with a size of 640 x 640 mm^2 and 128 x 128 $pixels^2$, resulting in a pixel size of 5 x 5 mm^2. To cover the broad q-range (from 0.013 nm^{-1} to 5.471 nm^{-1}), we measured with three configurations by varying the neutron wavelength (13 Å and 4.62 Å), the source-to-sample distance for the collimation (12.8 m, 10.3 m and 2.8 m) and the sample-to-detector distance for the rear detector (13.287 m, 1.987 m and 10.287 m). Samples were measured in cylindrical quartz glass cuvettes (Hellma, Germany) with a pathway of 1 mm. The cuvettes were installed in a thermalized copper sample-changer to perform the measurements at different temperatures between 12 °C to 51 °C. Acquisition times were 300 s and 600 s, respectively. The data was processed with the program GRASP. Here, the data were corrected for D_2O and the empty cell scattering and reduced by the sample transmission, sample thickness and the detector noise measured via a $^{10}B_4C$ absorber. The instrumental resolution with respect to q is based on the pixel size, the neutron beam width and the spread of the neutron wavelength ($\Delta\lambda/\lambda$ = 10 % (FWHM)). The data were merged and analyzed using the SASfit software by Kohlbrecher.[92]

Reverse Monte Carlo (RMC) simulation

Smooth average radial distribution functions of monomers in Au-microgel particles which are compatible with the observed SANS and SAXS scattering have been determined using a reverse Monte-Carlo simulation.[91, 210-212] As corroborated by TEM and SAXS, the model supposes particles to be of spherical symmetry, and to obey a fixed size Gaussian distribution function of width 15%. The particle number density has been estimated from SAXS of the gold cores: N/V is typically 10^{12} cm^{-3}. From the small-angle neutron low-q intensities, the number of monomers per particle of average size could then be estimated (typical values for small Au: $1.26 \cdot 10^7$, big Au: $1.3 \cdot 10^7$). Similarly, the number of gold atoms in a core of average size could be determined from SAXS (small Au: $7.7 \cdot 10^4$, big Au: $2.42 \cdot 10^7$). The simulation proceeds by distributing the available gold atoms and monomers in concentric spherical shells, under the constraint not to fill shell volumes to more than 100%. The volume of each gold atom (or monomer) was set to $16.95 \cdot 10^{-3}$ nm^3 and 0.177 nm^3, respectively. The simulation was performed in two steps. First the SAXS intensities were analyzed in order to check that the spatial distribution of gold atoms corresponds indeed to dense cores. As a result, gold densities of 100% in the particle centers were found, and for convenience they have been fixed throughout the rest of the simulation as three gold shells of total radius 6.8 nm and 46.0 nm, for small and big Au-cores, respectively. In the second step concerning the monomers, the latter have been moved in the shells starting outside the gold core, fixing their first thickness to 6.5 nm for small Au (resp. 4.0 nm for big Au), with an exponentially increasing thickness by multiplying it by 1.1 for each successive shell. This keeps the total number of variables low – a density for each shell –, and allows reaching rather large total sizes, of up to ca. 250 nm. The profiles are then plotted at the mid-point of each shell. The initial configuration is usually a constant polymer density in the 20 - 50% range. The basic step of a reverse Monte-Carlo simulation is to move monomers from one (randomly determined) shell to another one. Such a move is accepted if it improves the fit in terms of χ^2, the sum of the squares of the deviations between measured and calculated intensity. The calculated intensity contains also a generalized coil polymer form factor, which however is relevant only at high q and low temperature.[213] In the framework of the standard Metropolis algorithm, the moves are also accepted if they increase $\chi 2$ only slightly, where “slightly” is defined with respect to a “temperature” which is a fraction of χ^2. The maximum initial number of moving monomers was set to about 0.1% of the

total number of monomers in the simulation, and then decreased progressively in a simulated annealing process. Each move consisted in moving a random fraction of the current maximum number of monomers. The minimum (final) number of monomers was set to a few hundred. Simultaneously, the "temperature" was also decreased. As a result of decreasing both the monomer moves and the allowable fluctuations of χ^2, the simulation is progressively frozen. Such an algorithm would lead to a possibly very good fit, with however large fluctuations in the resulting monomer profiles. In order to avoid this, the functions are regularized by simultaneously minimizing the degree of fluctuation in the profile. The latter has been expressed by the average of the squared differences between two successive shell volume fractions, with the exception of the first unavoidable increase in polymer density on the surface of the gold core. The result of the simulation is a monomer volume fraction profile defined over the set of shells. Depending on the initial conditions, different curves may be obtained. All these curves are compatible with the scattering, and their spread gives an idea of the interval of trust of the simulation results. The simulated curves are shown in the **Supporting Information** in **Figure S4.4**.

4.4. Results and Discussion

4.4.1. Au-PNIPAM core-shell microgels

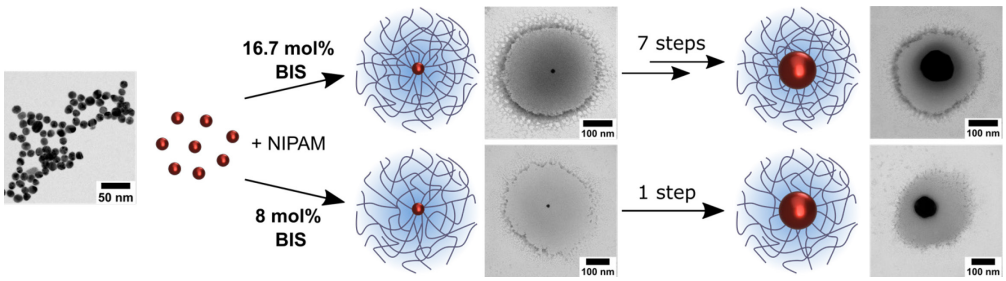

Figure 4.1. Schematical synthesis route of Au-PNIPAM microgels with TEM images of the individual CS microgels at the different steps. The top and bottom rows show the synthesis route for Au-PNIPAM$_{high}$ and Au-PNIPAM$_{low}$, respectively. The number of steps correspond to the number of overgrowth steps for the AuNP core.

We synthesized CS microgels via seeded precipitation polymerization with monodisperse, spherical AuNPs as seeds. The CS microgels containing one single gold core differ in nominal content of crosslinker. The AuNP cores were then further overgrown *in situ* in the polymer shell in seven steps for the highly crosslinked shell and in one step for the low crosslinked shell. **Figure 4.1** shows the schematical synthesis route with TEM images of the different CS microgels. The left TEM image shows the polycrystalline AuNPs prior to the encapsulation. The high electron density of the AuNPs leads to a good contrast. **Figure 4.1** top row and bottom row show the synthesis route for CS microgels with 16.7 mol% (Au-PNIPAM$_{high}$) and 8 mol% (Au-PNIPAM$_{low}$) nominal content of crosslinker, respectively. The TEM images in the middle show the successfully encapsulated AuNPs in the crosslinked PNIPAM shell. Note that the microgels are stained with uranyl acetate solution to enhance the visualization of the polymer shell. The dark spots in the middle are the AuNP cores. The grey corona around the cores represents the PNIPAM shell. When comparing the two batches, the shell of Au-PNIPAM$_{high}$ shows a higher contrast and a more defined border. This can be explained by a denser shell due to a higher crosslinker content. For Au$_7$-PNIPAM$_{high}$, we can detect a region in the middle of the microgel which has a slightly higher contrast than the border. As the crosslinker BIS is faster consumed than NIPAM during the polymerization, the microgel exhibits a core-shell like structure where the inner part is higher crosslinked than the outer part.[21, 89] For lower crosslinker content, this phenomenon is not as pronounced and therefore this structure cannot be clearly identified for Au$_7$-PNIPAM$_{low}$. The TEM images on the left show the stained CS microgels after the overgrowth of the core. The large, overgrown AuNP cores can be clearly identified in the PNIPAM shell. A darker region can be detected around the AuNP core for Au$_{46}$-PNIPAM$_{high}$. During the increase in size of the core, the polymer in the periphery of the core can be compressed to make space for the larger core. This compressed region could then be detected with a higher contrast in the TEM image. However, we will further discuss this later. Such a denser region cannot be detected for Au$_{46}$-PNIPAM$_{low}$. Here the contrast of the shell looks more homogenous with a looser outer region due to dangling ends.

4.4.2. Characterization of CS microgels before and after the overgrowth

We performed SAXS measurements to define the core size before and after the overgrowth for each batch. Note when we compare microgels before and after the overgrowth in the following, the data belonging to the cores before the growth are green and the ones to the cores after the growth are red. The SAXS scattering profiles at 20 °C can be extracted from **Figure 4.2 a and b**. All scattering profiles show clear form factor oscillations. The first form factor minimum shifts from high q to lower q with an increase in size. The oscillations at low q (< 0.08 nm^{-1}) for Au_7-$PNIPAM_{high}$ (a, green) and Au_7-$PNIPAM_{low}$ (b, green) are attributed to the scattering of the shell. As we want to extract the size of the AuNP cores, we can neglect these oscillations. For Au_{46}-$PNIPAM_{high}$ (a, red) and Au_{46}-$PNIPAM_{low}$ (b, red), the scattering of the shell is not detected as here the scattering of the large core dominates the scattering profile. All scattering profiles can be described by a polydisperse homogeneous sphere form factor model and thereby the radius, R_{SAXS}, of the cores can be extracted. For details on the form factor model, see **Supporting Information**. The exact sizes are listed in **Table 4.1**. SAXS profiles of the intermediate steps from the overgrowth synthesis of Au-$PNIPAM_{high}$, as well as the extracted radii, R_{SAXS}, can be found in the **Supporting Information** in **Figure S4.1** and **Table S4.1**.

Table 4.1. Radius (R_{SAXS}) of AuNP cores in CS microgels extracted from SAXS profiles and wavelength of the LSPR peak maximum (λ_{max}).

	R_{SAXS} [nm]	λ_{max} [nm]
Au_7-$PNIPAM_{high}$	6.6 ± 0.6	~ 515
Au_{46}-$PNIPAM_{high}$	46.3 ± 0.5	579
Au_7-$PNIPAM_{low}$	7.3 ± 0.7	~ 515
Au_{46}-$PNIPAM_{low}$	46.2 ± 0.5	575

Furthermore, we analyzed the optical behavior of the CS microgels before and after the overgrowth. The corresponding extinction spectra are shown in **Figure 4.2 c and d**. For Au_7-$PNIPAM_{high}$ (c, green) and Au_7-$PNIPAM_{low}$ (d, green), a

small shoulder around 515 nm can be detected, but no real LSPR peak. Here, the adsorption of the AuNP cores gets outweighed by the Rayleigh-Debye-Gans scattering of the shell.[49, 56] The adsorption shoulder for Au_7-$PNIPAM_{low}$ (d, green) can be slightly better identified, as the shell is less dense due to the lower amount of crosslinker. Thus, the scattering of the shell is less dominant. The spectra for the overgrown CS microgels clearly exhibit an LSPR peak, as the optical properties of the cores dominate the scattering of the shell. The peak positions (λ_{max}) are listed in **Table 4.1**. The slight shift of 4 nm in the peak can be attributed to small differences in the refractive index (RI) of the shell between high and low crosslinker content. Additionally, we want to look at the temperature-dependent optical behavior of the CS microgels after the overgrowth. Temperature-dependent extinction spectra are displayed in **Figure 4.2 e and f**. The temperature increases from blue to red. For both microgels, the LSPR peak maximum shifts to higher wavelengths and the scattering contribution of the PNIPAM shell at 300 nm rises with increasing temperature. During the augmentation of the temperature, the PNIPAM shell starts to collapse due to its thermoresponsive behavior.[21] The shell starts to expel water and therefore the refractive index in the shell increases leading to an increase in scattering at 300 nm.[214] As the LSPR peak is sensitive to any RI changes, the peak also shifts with increasing temperature.[109] The temperature-dependent extinction spectra of the CS microgels before the overgrowth are depicted in the **Supporting Information** in **Figure S4.2 a and b**.

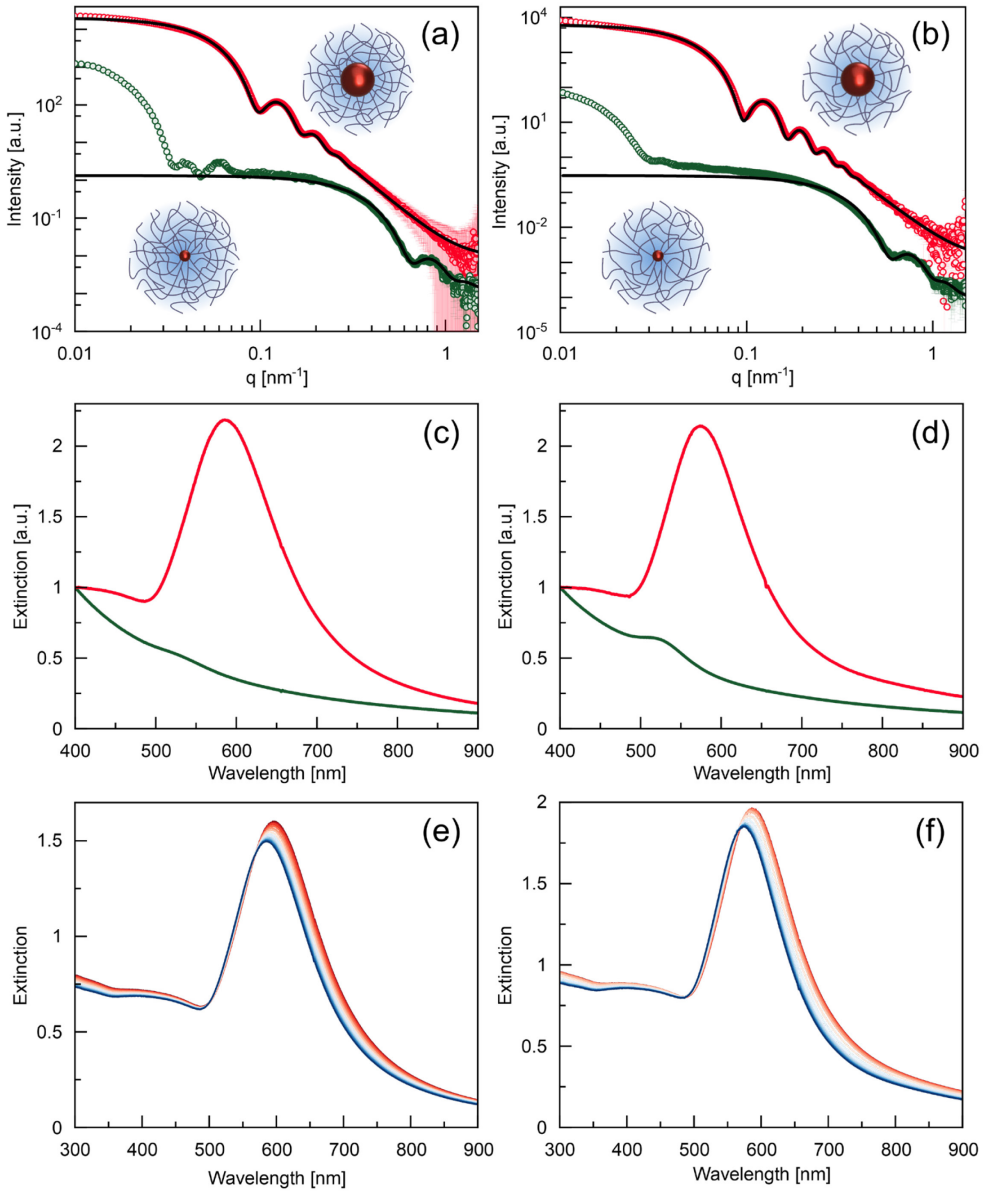

Figure 4.2. Scattering and optical properties of CS microgels before (green) and after (red) the overgrowth of the core. SAXS profiles of Au-PNIPAM$_{high}$ (a) and Au-PNIPAM$_{low}$ (b). The black solid lines correspond to the form factor model of a polydisperse hard sphere. Extinction spectra of Au-PNIPAM$_{high}$ (c) and Au-PNIPAM$_{low}$ (d) normalized to the extinction at 400 nm. Temperature-dependent extinction spectra of Au$_{46}$-PNIPAM$_{high}$ (e) and Au$_{46}$-PNIPAM$_{low}$ (f). The temperature increases from 15 °C to 51 °C (from blue to red) in 1 °C steps.

4.4.3. Thermoresponsive behavior of CS microgels

We want to compare the temperature-dependent swelling behavior of the different CS microgels to look if the size of the core influences this. **Figure 4.3 a and b** show the swelling curves of the four CS microgels, where the hydrodynamic radius R_h is plotted against the temperature. All microgels show the typical thermoresponsive behavior for PNIPAM microgels. R_h decreases with increasing temperature, starting at a nearly plateau at low temperature until R_h drops drastically to reach a new plateau at high temperature. This trend follows a sigmoidal-like function. Thus, the polymer shell remains its thermoresponsive properties even if the core is overgrown. When Au_7-$PNIPAM_{high}$ and Au_{46}-$PNIPAM_{high}$ are compared, they show similar hydrodynamic radii and a similar decrease. There are only some small deviations at higher temperatures. For Au_7-$PNIPAM_{low}$ and Au_{46}-$PNIPAM_{low}$, they also show the highest deviation at high temperatures, but their hydrodynamic radii and the trend with increasing temperatures are similar. To better compare the CS microgels, R_h at 20 °C and 50 °C, as well as the deswelling ratio α at 50 °C are listed in **Table 4.2**. As the core does not response to the temperature, its volume V_{core} needs to be subtracted from the overall volume of the microgel V_h. Thereby, we will get the swellable volume of the PNIPAM shell. Thus, α can be calculated by **equation 4.1**:[94]

$$\alpha = \frac{V_h(50\,°C) - V_{core}}{V_h(20°C) - V_{core}} \tag{4.1}$$

Furthermore, we fit the swelling curves with a sigmoidal function to extract the volume phase transition temperature VPTT of each CS microgel. These temperatures are also listed in **Table 4.2**.

Table 4.2. R_h at 20 °C and 50 °C, VPTT and deswelling ratios α obtained from the swelling curves for the four microgel systems.

	R_h at 20 °C [nm]	R_h at 50 °C [nm]	VPTT [°C]	α
Au_7-PNIPAM$_{high}$	173.2 ± 1.1	119.4 ± 0.1	34.5	0.33
Au_{46}-PNIPAM$_{high}$	172.4 ± 1.0	115.9 ± 0.5	34.4	0.29
Au_7-PNIPAM$_{low}$	181.7 ± 1.6	106.6 ± 0.2	34.2	0.20
Au_{46}-PNIPAM$_{low}$	185.7 ± 1.3	101.5 ± 0.3	33.3	0.15

As the hydrodynamic radii at 20 °C only slightly differ (< 10 %) between the different microgel systems, we can compare the microgels. As the differences of R_h between microgels with the same amount of crosslinker before the overgrowth and its counterpart after the overgrowth are ≤ 5 %, we can claim that they exhibit the same dimensions in dilute aqueous dispersion. Thus, the core growth does not affect the overall dimension of the polymer shell. For the VPTT, there is no real difference between the four systems, so the core does not influence the thermoresponsive behavior nor shifts the VPTT. However, the VPTTs are comparable to the ones known from literature for such Au-PNIPAM core-shell microgels.[21] The lowest deswelling ratio shows the largest change in volume. Thus, the CS microgels with less crosslinker can better deswell and expel more water with increasing temperature, as expected and known from literature.[21, 24]

In the next step, we want to compare the swelling behavior of each microgel system with its temperature-dependent optical properties. The procedure was already reported elsewhere[21, 214] and here we directly plot the normalized extinction against the normalized hydrodynamic radius, see **Figure 4.3 c and d**. The trend for all four microgel systems is similar and follows the black line which shows a slope of minus one. This means that the extinction negatively correlates to R_h and an increase in extinction means directly a decrease in R_h. Ponomareva *et al*. already reported this behavior for CS microgels with small gold cores, thus our CS microgels with the small cores are comparable to the ones in the literature.[21] For Au_{46}-PNIPAM$_{high}$ (c, red) and Au_{46}-PNIPAM$_{low}$ (d, red), we also identify the negative correlation between the extinction and R_h. Thus, the shell exhibits a similar thermoresponsive behavior after the core overgrowth. When we look at the overall behavior of the different CS microgels, there is no real difference between the microgels before and after the

overgrowth. Therefore, we performed SANS measurements to get insights into the internal structure of the polymer shell.

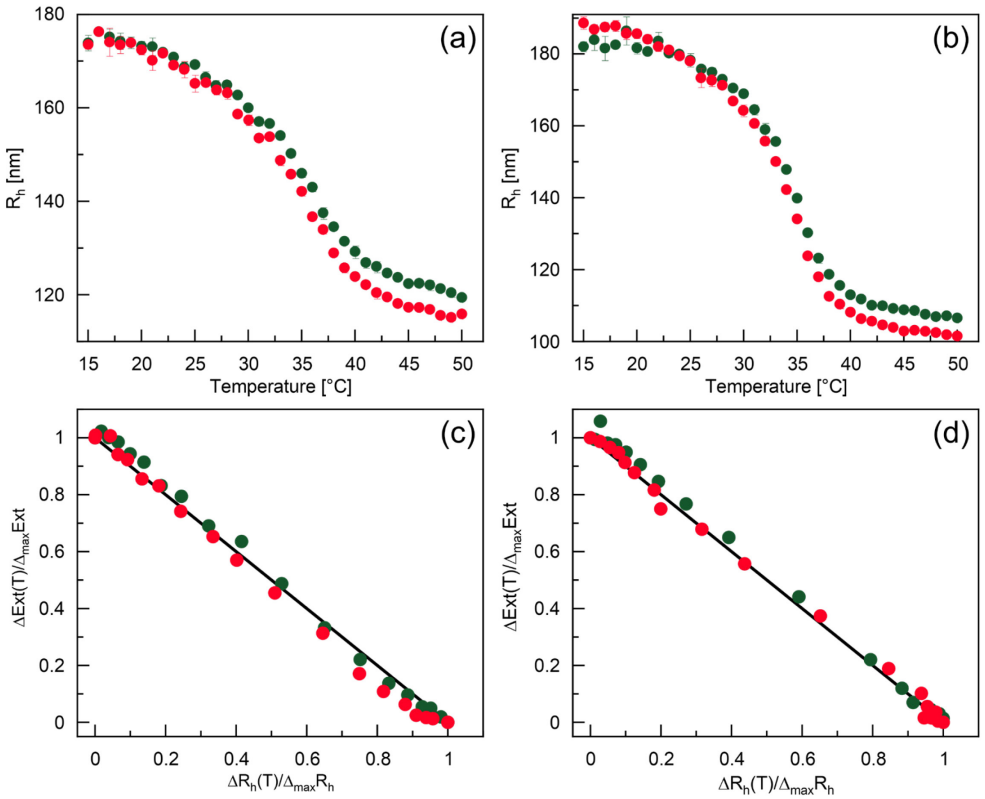

Figure 4.3. Temperature-dependent behavior of CS microgels. Hydrodynamic radius R_h against the temperature for Au-PNIPAM$_{high}$ (a) and Au-PNIPAM$_{low}$ (b). Normalized extinction plotted against the normalized hydrodynamic radius for Au-PNIPAM$_{high}$ (c) and Au-PNIPAM$_{low}$ (d). The black solid lines exhibit a slope of – 1. Green and red closed symbols represent the data of the CS microgels before and after the overgrowth of the core, respectively.

4.4.4. Temperature-dependent scattering behavior of the polymer shell

In the following, we will present the temperature-dependent SANS measurements of the CS microgels with the small cores. We will define the different contributions in the

scattering profile (**Figure 4.4**) and then we will describe the scattering profiles at different temperatures and thereby extract the radial profiles of the difference in scattering length density (*ΔSLD*) (**Figure 4.5**).

The scattering profiles (blue open symbols) of Au_7-$PNIPAM_{high}$ and Au_7-$PNIPAM_{low}$ at 20 °C are depicted in **Figure 4.4 a and b**, respectively. The profiles can be described by a combination of three different scattering contributions. The high *q* regime can be described by the incoherent background, the mid *q* range by the Ornstein-Zernicke (OZ) contribution (grey line) and the mid- to low-*q* range by the exponential shell model (black line). OZ contribution considers the dynamical fluctuations of the network and the exponential shell model considers the form factor of the microgel. The model combines a core with a radius R_{core} and homogenous scattering length density (SLD) and a shell with a thickness t_{shell} and a SLD which decreases exponentially to the outside of the microgel. The core in the model equals here to the gold core and the solvent amount in the shell is also considered in the model. The total radius R_{SANS} of the microgels equals $R_{SANS} = R_{core} + t_{shell}$. More details about the model and its parameters are discussed in the **Supporting Information**.

In **Figure 4.4**, the OZ fit (grey line) can be perfectly matched to the scattering curve in the mid *q* range. Au_7-$PNIPAM_{low}$ exhibits with ξ = 1.81 nm a higher value as Au7-PNIPAMhigh with ξ = 1.60 nm. This was expected as a lower crosslinker density allows more dynamical fluctuations of the network. The form factor oscillations in both experimental scattering profiles can be characterized by the exponential shell model (black line) very well. The artefacts in the fit at around 0.1 nm^{-1} can be neglected as they are due to the merging of the experimental curves in that regime and the thereby resulting differences in *q*-resolution. Previously, Ponomareva *et al*. also investigated SANS curves of Au-PNIPAM CS microgels.[21] In contrast to our procedure, the authors fitted their data with the fuzzy sphere model. This model considers an inner regime with a constant density followed by a decay of the density following a gaussian function to account for the fuzziness at the outer part of the particle. For our curves, the exponential shell model better describes the form factor oscillations, see comparison in **Figure S4.3** in the **Supporting Information**. Thus, the decrease of the polymer density in our microgel shell follows an exponential function instead of a gaussian function. Hildebrandt *et al*. also concluded by comparing different fitting models for SAXS profiles of CS microgels that an exponential decay describes the

shell more realistically.[31] The parameters extracted from the fit are listed in **Table S4.2 to S4.5** and discussed in the following.

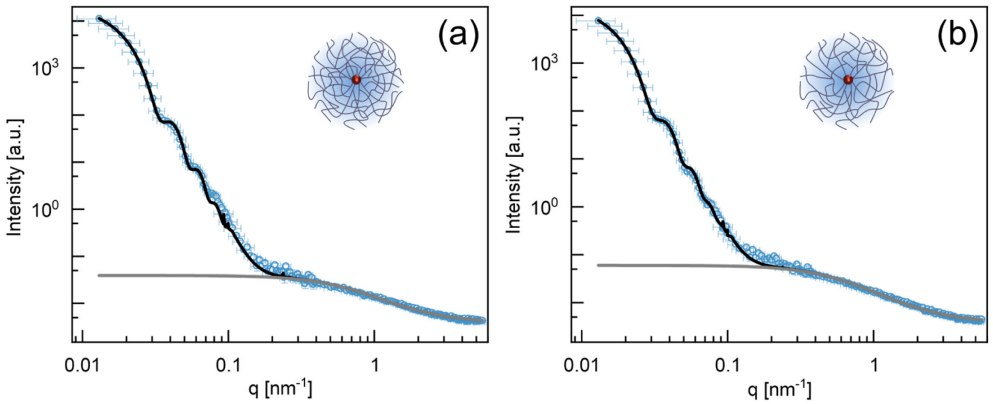

Figure 4.4. SANS profiles (blue open dots) of Au_7-$PNIPAM_{high}$ (a) and Au_7-$PNIPAM_{low}$ (b) at 20 °C. The grey line represents the Ornstein-Zernike contribution with the background. The black line corresponds to the form factor of the exponential shell model with the Ornstein-Zernike contribution and the background.

Figure 4.5 a and b show the temperature-dependent SANS measurements of Au_7-$PNIPAM_{high}$ and Au_7-$PNIPAM_{low}$ in the temperature range of 12 to 51 °C (from dark blue to dark red). All scattering profiles, except the ones at 51 °C are analyzed by the combination of incoherent background, OZ contribution and the exponential shell model. The profiles at 51 °C are only described by the incoherent background and the exponential shell model. At this temperature, dynamical fluctuations of the network are suppressed due to the collapse of the thermoresponsive polymeric shell. For both CS microgel systems, the fits nicely describe the experimental curves and the first form factor minimum shifts to higher *q* with increasing temperature. Thus, the microgel dimensions decrease with increasing temperature due to the collapse of the shell. The parameters extracted from the fit are listed in **Table S4.2 to S4.5**. The parameters for the lowest (12 °C) and highest (51 °C) temperature are listed in **Table 4.3**.

For Au_7-$PNIPAM_{high}$, the shell thickness decreases from t_{shell} = 169.17 ± 5.00 nm to t_{shell} = 102.54 ± 7.50 nm, resulting in a decrease of R_{SANS} = 66.63 nm. For

Au_7-$PNIPAM_{low}$, the shell thickness decreases from t_{shell} = 184.13 ± 7.00 nm to t_{shell} = 92.25 ± 7.00 nm, resulting in a decrease of R_{SANS} = 91.88 nm. Thus, the collapse of the shell for the CS microgels with the lower crosslinker content is larger than the collapse for the CS microgels with the higher crosslinker content. This confirms the temperature-dependent DLS measurements, where Au_7-$PNIPAM_{low}$ also exhibits a lower deswelling ratio, so a higher deswelling capacity. From the fits, we can extract the radial profiles of the difference in scattering length density (*ΔSLD*) between the CS microgels and water as dispersion medium, shown in **Figure 4.5 c and d**.

All profiles start at the same value of *ΔSLD*, which corresponds to the difference between the SLD of the gold core and the SLD of water. For the lower temperatures, the value then drops as the shell is highly swollen with water. The density of polymer in the shell then decays exponentially until R_{SANS} is reached. The microgels exhibit a microgel structure with a more homogenous-like inner part and a fuzzy corona highly swollen with water. With increasing temperature, the exponential decay becomes more pronounced, and the polymer density decays faster. The increase in exponential decay is also translated by the decrease in the value of α in **Table S4.2 to S4.5**. As the microgel shell starts to collapse, see decreasing R_{SANS}, and to expel water, the value for *ΔSLD* increases. Hence, the polymer volume fraction in the shell starts to increase. At 51 °C, the profiles do not really show an exponential decay, but *ΔSLD* shows a constant value until it drops to zero. The microgels exhibit a box-like profile, which is typical for homogenous spheres.[215-217] Thus, the microgels undergo a transition from a microgel with a fuzzy corona to a homogenous sphere-like microgel.

When comparing the microgels with different crosslinker content, a difference in the amount of water in the polymer shell can be observed. *ΔSLD* at 12 °C is higher for Au_7-$PNIPAM_{high}$ than for Au_7-$PNIPAM_{low}$. Thus, the shell of Au_7-$PNIPAM_{low}$ is more swollen with water. In numbers this means that Au_7-$PNIPAM_{low}$ contains 89 % of water by volume in the inner part of the microgel, whereby Au_7-$PNIPAM_{high}$ only contains 80 % of water. The higher crosslinked microgels are more rigid and can therefore swell less with water. At 51 °C, the amount of water in the inner region is reduced to 51 % and 52 % for Au_7-$PNIPAM_{low}$ and Au_7-$PNIPAM_{high}$, respectively. Consequently, the microgels show a crosslinker-dependent uptake of solvent at low temperature, but at high temperatures there is no real difference. These findings are in accordance with the literature.[21, 31]

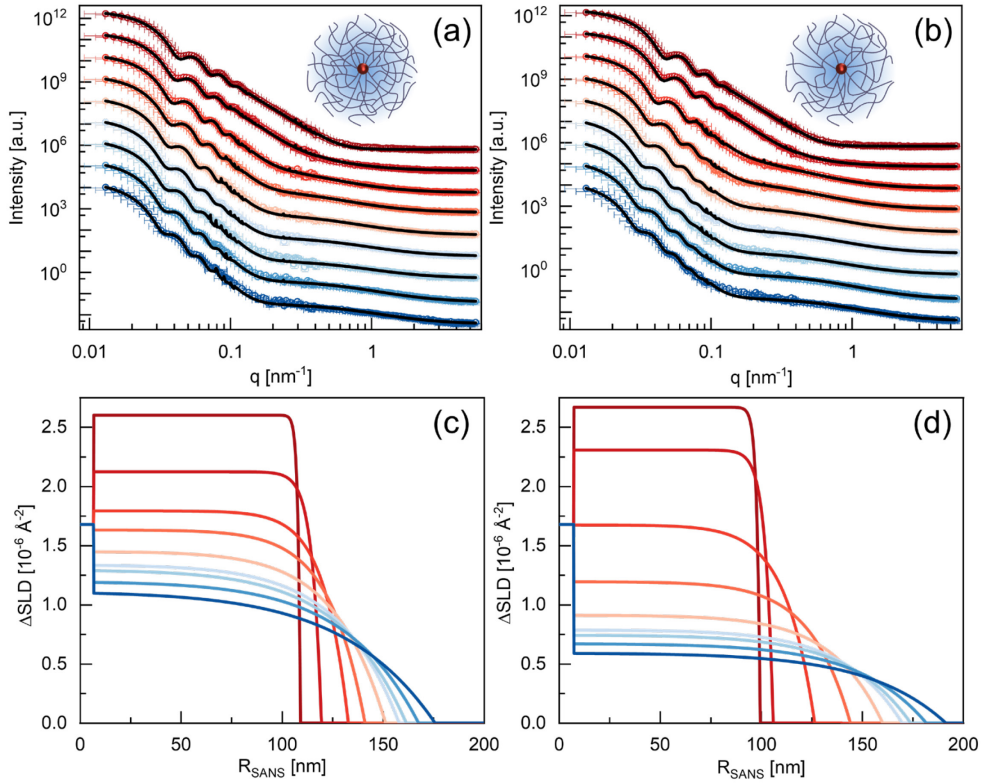

Figure 4.5. Temperature-dependent SANS profiles of CS microgels with small cores. SANS profiles (open dots) of Au_7-$PNIPAM_{high}$ (a) and Au_7-$PNIPAM_{low}$ (b). The black solid line represents the form factor of the exponential shell model. Radial profiles of the difference in scattering length density (*ΔSLD*) between CS microgel and water as dispersion medium for Au_7-$PNIPAM_{high}$ (c) and Au_7-$PNIPAM_{low}$ (d). The radial profiles are extracted from the form factor model. Temperature increases from dark blue (12 °C) to dark red (51 °C).

Table 4.3. Parameters obtained from fitting of the SANS curves at 12 °C and 51 °C for Au_7-$PNIPAM_{high}$ and Au_7-$PNIPAM_{low}$.

	Au_7-$PNIPAM_{high}$		**Au_7-$PNIPAM_{low}$**	
	12 °C	**51 °C**	**12 °C**	**51 °C**
t_{shell} [nm]	169.17	102.54	184.13	92.25
R_{SANS} [nm]	175.78	109.14	191.43	99.55
ϕ_{in}	0.80	0.52	0.89	0.51
α	-2.86	-84.03	-3.88	-56.96

Temperature-dependent SANS data of Au_{46}-$PNIPAM_{high}$ and Au_{46}-$PNIPAM_{low}$ are shown in **Figure 4.6 a and b**, respectively. The scattering curves can neither be fitted by the exponential shell model nor by the conventional models, such as the fuzzy sphere or core-shell microgel. The models fail to describe the oscillations and mid q range accurately. Thus, the internal structure of the microgels with the overgrown, large cores differs from the microgels with the small cores. For this reason, we only discuss the curves qualitatively in this part. The form factor oscillations for both microgel systems are smeared at low temperatures and become more pronounced with increasing temperature. An OZ contribution can be seen for both microgel systems in the high to low q range, except for the curve at 51 °C. Furthermore, the first form factor minimum shifts to higher q with increasing temperatures. This indicates a collapse of the shell and a decrease of the overall dimension of the microgel. For Au_{46}-$PNIPAM_{low}$, a bump in the intensity at low temperatures can be observed at around 0.1 nm^{-1}, which is not present in the scattering curve of Au_{46}-$PNIPAM_{high}$.

We fitted the OZ regime (black solid line) in the scattering curve at 20 °C (light blue open symbols) for both microgels, as shown in **Figure 4.6 c and d**. The extracted correlation lengths show a value of ξ = 1.89 nm and ξ = 2.44 nm for Au_{46}-$PNIPAM_{high}$ and Au_{46}-$PNIPAM_{low}$, respectively. This is an increase of 15 % and 26 % compared to their counterparts with the small cores. Thus, we can conclude that the internal structure of the microgel shell changes during the overgrowth of the core. However, it does not affect the overall dimension of the microgel, and the change needs to be homogeneous, according to the previous results of the temperature-dependent DLS and extinction spectroscopy measurements. For the scattering curves at 51 °C (dark red opened symbols), we applied a polydisperse hard sphere form factor model (black solid line). The fit describes the form factor oscillations of the curves very well. The fit gives a radius of R_{SANS} = 112.21 ± 8.50 nm and R_{SANS} = 102.54 ± 6.00 nm for Au_{46}-$PNIPAM_{high}$ and Au_{46}-$PNIPAM_{low}$, respectively. Hence, microgels with the overgrown cores also show a homogenous polymer density in the shell at the highest temperature.

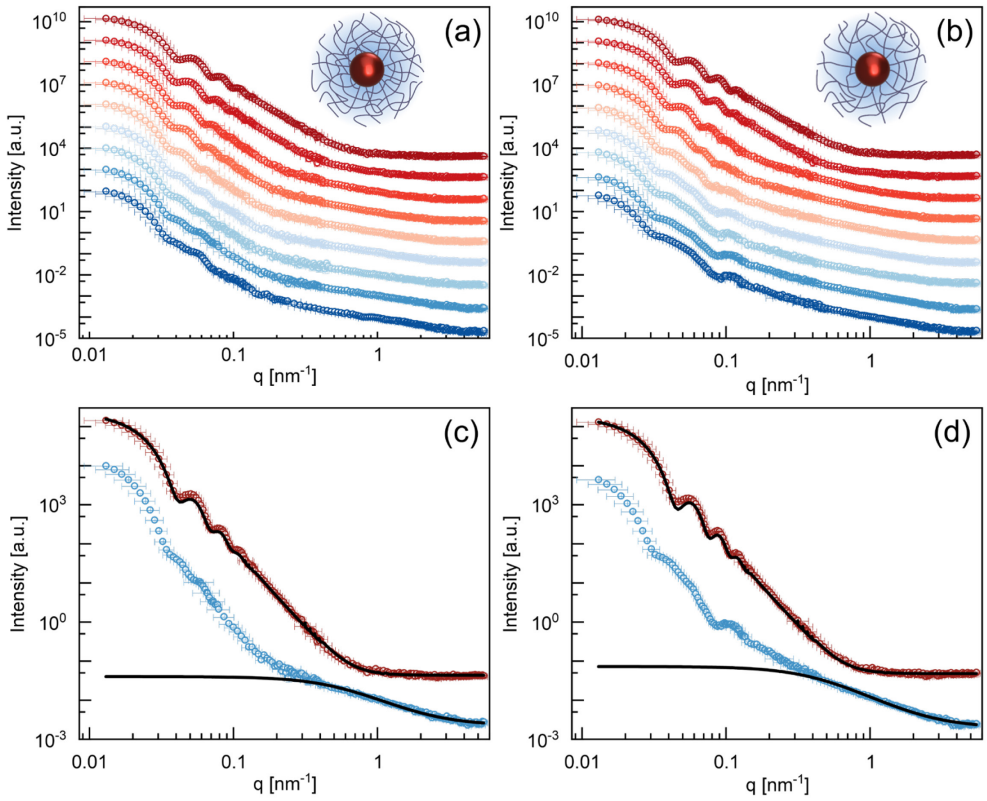

Figure 4.6. Temperature-dependent SANS profiles of CS microgels with large cores. SANS profiles (open dots) of Au_{46}-$PNIPAM_{high}$ (a) and Au_{46}-$PNIPAM_{low}$ (b). Temperature increases from dark blue (12 °C) to dark red (51 °C). SANS profiles at 20 °C (blue) and at 51 °C (dark red) for Au_{46}-$PNIPAM_{high}$ (c) and Au_{46}-$PNIPAM_{low}$ (d). The black solid lines represent the Ornstein-Zernike contribution for 20 °C and the form factor model of a polydisperse hard sphere for 51 °C.

4.4.5. Radial profiles of the CS microgels via Reverse Monte-Carlo (RMC) simulations

We tried to find an accurate method to describe the SANS curves and to extract the polymer volume fraction in the shell in function of the temperatures. We tried to deconvolute the profiles via inverse Fourier transformation (IFT) method, but it failed because of the low contrast of the gold core in the SANS experiment. Thus, it is not possible to really extract a reasonable density profile with IFT. For this reason, we

performed RMC simulations, where we used the SANS curves at 20 °C and 51 °C as input for the program. The radial profiles extracted from the SANS curves of the microgels with the small cores, as well as simulated radial profiles for all four microgel batches at 20 °C and 51 °C are depicted in **Figure 4.7**. We introduced the radius of the core obtained from the SAXS data as an input parameter for the calculations, as described in the methods section. The black symbols present the volume fraction of the gold core. Here the volume fraction is equal to one, as the core purely consists of gold atoms. The simulated scattering curves in respect to the experimental curves are shown in **Figure S4.4 in the Supporting Information**. The experimental radial profiles for the microgels with small cores, shown in **Figure 4.7 a and b**, were already discussed in the previous part. In brief, with increasing temperature both microgels exhibit a transition from a microgel with a more homogenous-like inner part and a fuzzy corona to a microgel with a constant polymer volume fraction similar to a homogeneous sphere. The calculated radial profiles of the CS microgels with small cores are presented in **Figure 4.7 c and d**, whereby the profiles of the microgels with the overgrown cores are depicted in **Figure 4.7 e and f**. Here we plotted the calculated volume fraction against the radius extracted from the RMC, R_{RMC}. For 51 °C (red closed symbols), a rather constant polymer volume fraction of around 0.5 in the shell is found for Au_7-$PNIPAM_{high}$ and Au_7-$PNIPAM_{low}$. Furthermore, the dimensions of the CS microgels are similar for the experiment and the simulations. The rise in volume fraction at around R_{RMC} = 100 nm is attributed to calculation artefacts and is not a realistic rise in polymer volume fraction. Both microgels with overgrown cores show a higher polymer volume fraction for a similar overall microgel dimension than their counterpart with the small cores. Due to conservation of mass during the overgrowth process, the same amount of polymer needs to be filled in a smaller volume. As a result, the dimensions of all microgels are similar, but the polymer density for Au_{46}-$PNIPAM_{high}$ and Au_{46}-$PNIPAM_{low}$ is higher. Moreover, we observe a more prominent rise in the polymer density near the core. This can be an indication for the compression of polymer during the overgrowth in the periphery of the core. This would underline our findings in the stained TEM images in **Figure 4.1**, where the higher polymer density near the core was also observed. Nevertheless, Au_{46}-$PNIPAM_{high}$ and Au_{46}-$PNIPAM_{low}$ show also more or less a homogenous polymer volume fraction in the shell. Therefore, it was possible to analyze the SANS curves with the polydisperse hard sphere form factor model. In conclusion, the simulations validate that all

microgels independent of the core size feature a hard sphere-like profile at high temperatures.

The radial profiles at 20 °C (blue closed symbols) show some difference between the four microgel types. Au_7-$PNIPAM_{high}$ and Au_7-$PNIPAM_{low}$ exhibit a volume fraction of around 0.29 and 0.14, respectively. Here, the higher crosslinked microgels show a higher polymer density which is in accordance with the previous findings. The decay of the polymer volume fraction follows an exponential trend. Additionally, the dimensions of both microgels are similar to the dimensions extracted from the scattering curves. Thus, the simulations reflect the experimental data quite realistically. For Au_{46}-$PNIPAM_{high}$ and Au_{46}-$PNIPAM_{low}$, the profiles at 20 °C look different. However, both systems show a higher polymer volume fraction than their counterparts for similar dimensions. Thus, the conservation of mass is also confirmed at lower temperatures. Au_{46}-$PNIPAM_{high}$ presents a sharp increase of the polymer volume fraction near the core at around R_{RMC} = 55 nm, which underlines the hypothesis of polymer compression during the overgrowth process. After the sharp increase, the density decays in an exponential trend. However, the profile is not as smooth as for the microgels with the small cores. This is due to small mismatches between experimental and simulated scattering curves. Note, we want to get an idea of what happens with the internal structure of the shell during the overgrowth. Here the qualitative analyzation of the simulated profiles is sufficient for our scope at this point. For Au_{46}-$PNIPAM_{low}$, we also observe a region with a higher polymer density at around R_{RMC} = 75 nm. Between 50 and 75 nm, the polymer density slowly increases and the increase is less sharp than for Au_{46}-$PNIPAM_{high}$. The lower crosslinker density probably allows more freedom of movement and rearrangement of the polymer chains. Thus, the compressed region is not as distinct and therefore not clearly visible in the stained TEM images. After the polymer density increases, the polymer volume fraction also decays in an exponential trend. In conclusion, the simulated data gives an idea of how the internal structure of the shell looks like before and after the overgrowth of the core. The hypothesis of a compressed polymer region around the core after the overgrowth is supported. This phenomenon is more pronounced for the higher crosslinked microgels as there is more polymer to be displaced and less freedom of movement for the polymer chains.

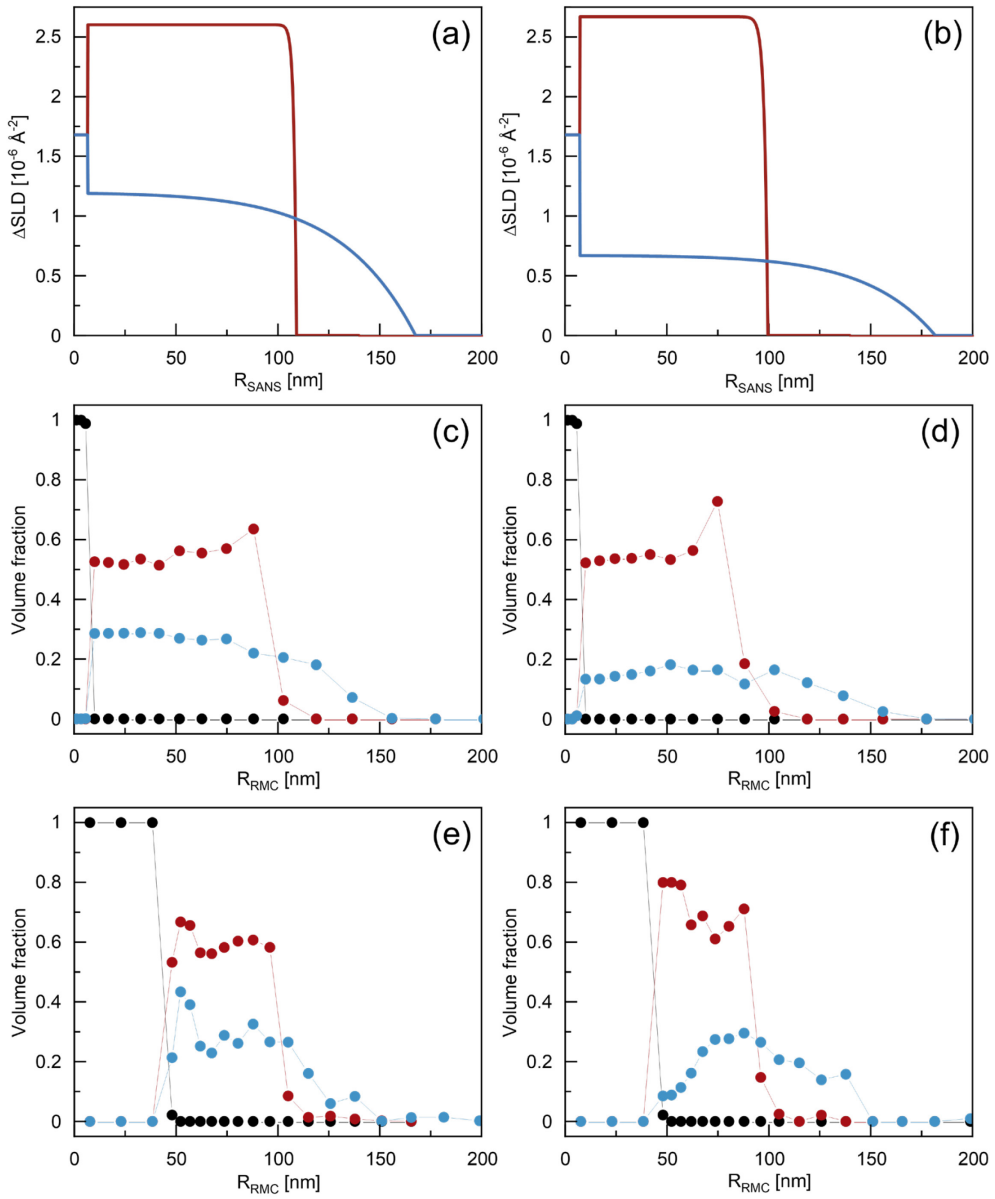

Figure 4.7. Comparison of experimental and simulated radial profiles of the CS microgels at 20 °C (blue) and 51 °C (red). Radial profiles extracted from the form factor model for Au_7-$PNIPAM_{high}$ (a) and Au_7-$PNIPAM_{low}$ (b). Radial profiles simulated via RMC simulations for Au_7-$PNIPAM_{high}$ (c), Au_7-$PNIPAM_{low}$, (d) Au_{46}-$PNIPAM_{high}$ (e) and Au_{46}-$PNIPAM_{low}$ (f). The black closed symbols and lines represent the volume fraction of the gold core. The blue and red closed symbols and lines correspond to the volume fraction of the polymer in the shell at the respective temperature.

4.5. Conclusion

We synthesized CS microgels with 16.7 mol% and 8 mol% nominal crosslinker content containing monodisperse, spherical gold cores. We successfully increased the size of the cores by a factor of 6.6 via an overgrowth process *in situ* in the shell. Thus, we obtained four microgel batches differing in crosslinker content and/or core size. All four batches were intensively characterized with different methods, such as TEM and extinction spectroscopy. TEM images and SAXS curves do not only confirm the successful syntheses, but the radius of the cores can be extracted from the SAXS curves with a high statistic. The extinction spectroscopy elucidates the differences in the optical behavior of the CS microgels. While the scattering of the shell mainly contributes to the extinction of CS microgels with small cores, the extinction of CS microgels with overgrown cores is dominated by the adsorption of the gold cores. Temperature-dependent DLS measurements reveal that the overall dimensions and thermoresponsive behavior of the CS microgels before and after the overgrowth are comparable and not influenced by the core size, but only by the crosslinker content. By combining these measurements with temperature-dependent extinction spectroscopy, as previously reported in the literature,[214] we could observe the same thermoresponsive behavior for CS microgels before and after the overgrowth. Thus, we performed SANS measurements to obtain information about the internal structure of the shell before and after the core overgrowth.

SANS curves of the CS microgels with the small cores can be described by the exponential shell model over a broad temperature range. Additionally, the OZ contribution can be fitted giving a higher correlation length for CS microgels with lower crosslinker density. This means that the dynamical fluctuations of the network are more pronounced and the network is less rigid. The extracted radial profiles show that the CS microgels with lower crosslinker content are more swollen with water compared to the ones with higher crosslinker content at low temperatures. At high temperatures, they show a similar content of water. Nevertheless, both microgel types show a transition from a microgel with a homogenous inner region and a fuzzy corona to a hard sphere-like microgel.

For CS microgels with overgrown, no adequate form factor model could be applied. Only the OZ contribution is fitted at low temperatures giving larger correlation length

compared to their counterparts with the small cores. This indicates a change in the internal structure of the shell. However, the CS microgels also show a homogeneous sphere-like scattering behavior at high temperatures. To extract the polymer volume fraction in the shell, we performed RMC simulations. The dimensions of the CS microgels before and after the overgrowth are similar according to the calculations, but the polymer volume fraction increased for the ones with the overgrown cores due to mass conservation. Furthermore, we observed a domain around the core with a higher polymer density, which can be attributed to a compressed polymer region. The cores compress the polymer in its periphery during the overgrowth, which leads to the higher polymer volume fraction. This effect is more pronounced for the higher crosslinked microgels as there is more polymer around the core. This phenomenon is supported by stained TEM images, where a region with a higher polymer density around the core could also be observed.

However, an adequate form factor model to describe the SANS curves and thereby extract the real radial profile is currently missing. Here, we hope our work is the start to establish a form factor model comprising a dense core and a microgel shell with a compressed inner part and an exponential decaying outer part. Currently, it is only possible to describe particles with the exponential shell model or the core-shell microgel model, which both do not implement this compressed inner part. With a reasonable model, it would be possible to better describe the internal structure of the shell. Thereby, we could understand what happens to the shell during the overgrowth leading to a better understanding and characterization of the CS microgel, especially of the polymer shell.

Declaration of conflicts of interest

There are no conflicts to declare.

Acknowledgments

The authors acknowledge the German Research Foundation (DFG) and the state of NRW for funding the cryo-TEM (INST 208/749–1 FUGG) and Marius Otten and Jonas Schmitz from Heinrich-Heine-University Düsseldorf for his assistance with the

operation and image recording. The authors acknowledge Elena Vanselow for acquiring knowledge about the temperature-dependent DLS and extinction spectroscopy measurements of the samples. The authors thank Andrea Scotti, Judith E. Houston and Jérôme Crassous for performing the SAXS measurements at the MAX IV laboratory in Lund, Sweden. The authors thank Tobias Honold and Nico Carl for the pre-work which was done on similar samples. The authors thank Martin Dulle for the fruitful discussions and for testing IFT on our SANS and SAXS profiles. D.F. acknowledges the Luxembourg National Research Fund (FNR), Project Reference 15688439.

4.6. Supporting Information

Intermediate steps of core overgrowth in Au-PNIPAM$_{high}$

The SAXS profiles are dominated by the scattering of the AuNP cores and can be described by a polydisperse homogeneous sphere form factor. The form factor only considers the scattering of the core and the scattering of the shell is neglected. The homogeneous sphere form factor model *P(q)* is given by **equation S4.1** for a sphere with a radius *R*.

$$P(q) = \left[3\frac{\sin(qR) - qRcos(qR)}{(qR)^3}\right]^2 \tag{S4.1}$$

The polydispersity of the cores is taken into account by a Gaussian size distribution function with σ_{SD} representing the standard deviation, as shown by **equation S4.2**.

$$D(R, \langle R\rangle, \sigma_{\mathrm{SD}}) = \frac{1}{\sqrt{2\pi\sigma_{\mathrm{SD}}^2}} exp\left(-\frac{(R - \langle R\rangle)^2}{2\sigma_{\mathrm{SD}}^2}\right) \tag{S4.2}$$

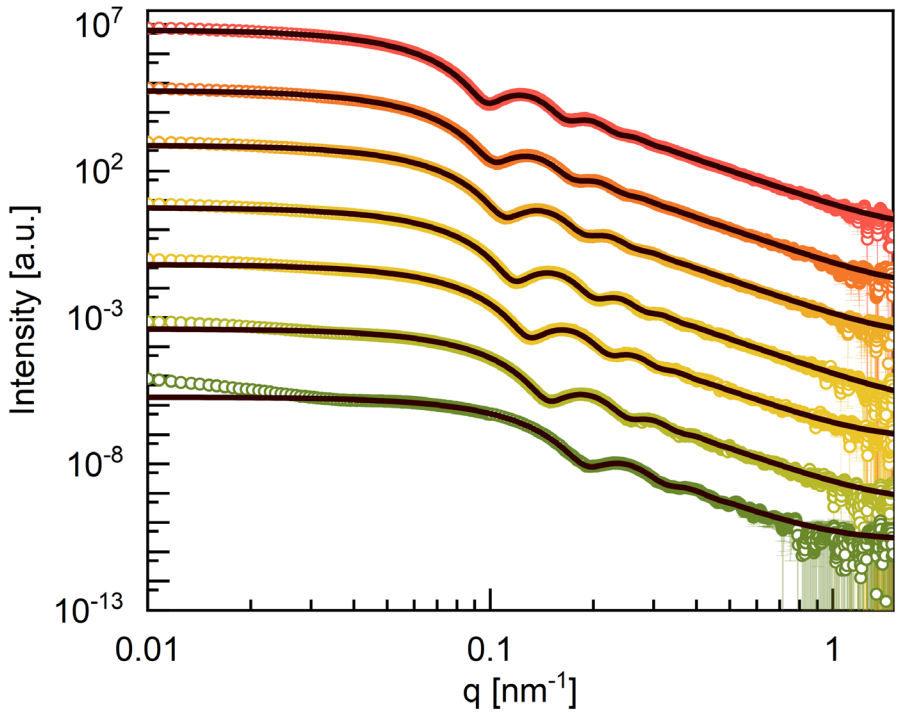

Figure S4.1. SAXS profiles of the intermediate steps from the overgrowth synthesis of Au-PNIPAM$_{high}$ with increasing core size from green to red. The black solid lines correspond to the form factor model of a polydisperse hard sphere.

The form factor oscillations for all samples can be nicely described by the polydisperse hard sphere form factor model in **Figure S4.1**. Thus, the radius of the AuNP cores can be extracted and are listed in **Table S4.1**.

Table S4.1. Radius (R_{SAXS}) of AuNP cores in CS microgels extracted from SAXS profiles.

	R_{SAXS} [nm]
Au$_{23}$-PNIPAM$_{high}$	22.6 ± 2.8
Au$_{29}$-PNIPAM$_{high}$	29.2 ± 3.1
Au$_{33}$-PNIPAM$_{high}$	33.3 ± 3.4
Au$_{37}$-PNIPAM$_{high}$	36.6 ± 3.6
Au$_{39}$-PNIPAM$_{low}$	39.3 ± 4.3
Au$_{42}$-PNIPAM$_{low}$	41.6 ± 4.8
Au$_{44}$-PNIPAM$_{low}$	43.6 ± 4.8

Temperature-dependent extinction spectra

The temperature-dependent extinction spectra for both CS microgels with small cores show an increase in extinction with increasing temperatures, as depicted in **Figure S4.3** (dark blue to dark red). This increase is more pronounced at lower wavelengths (< 500 nm). The LSPR peak of the AuNP cores can be detected as small shoulder around 520 nm. The Rayleigh-Debye-Gans scattering of the PNIPAM shell dominates the extinction spectra for all the temperatures and overweighs the absorption of the AuNP cores.[49, 56]

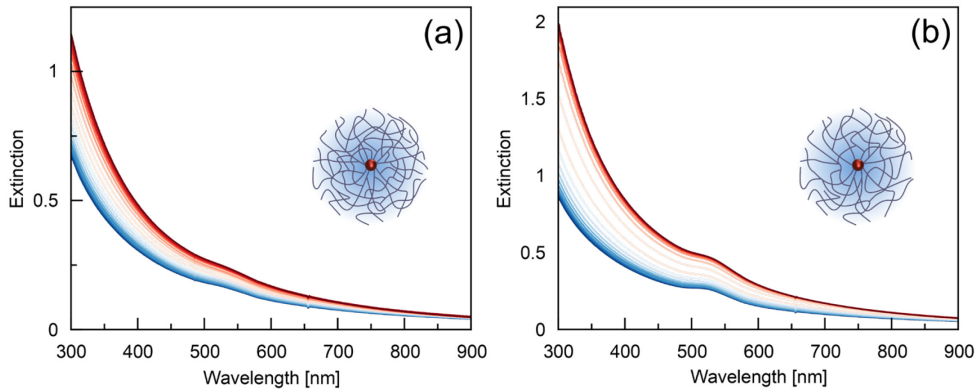

Figure S4.2. Temperature-dependent extinction spectra of Au_7-$PNIPAM_{high}$ (a) and Au_7-$PNIPAM_{low}$ (b). The temperature increases from 15 °C to 51 °C (from blue to red) in 1 °C steps.

Exponential shell form factor model

We performed temperature-dependent SANS measurements for all four CS microgels and the scattering profiles were analyzed with the SASfit software.[92] The instrumental resolution was considered during the analyzation process.

The intensity $I(q)$ of the scattering profiles of Au_7-$PNIPAM_{high}$ and Au_7-$PNIPAM_{low}$ is composed of three different intensity terms as shown by **equation S4.3**.

$$I(q) = I_{\mathrm{ExpShell}} + I_{\mathrm{OZ}} + I_{\mathrm{B}} \qquad \text{(S4.3)}$$

Here I_{ExpShell} corresponds to the scattering intensity from the exponential shell form factor model which describes the static scattering contribution. I_{OZ} represents the dynamical fluctuation in the Ornstein-Zernike regime at mid to high *q*.[195, 196] I_{B} corresponds to the scattering of the background which is a *q*-independent offset.

The exponential shell form factor model is typically used for swollen microgels with a gradient of the polymer density in the shell. The form factor is given by **equation S4.4**.[56, 92]

$$I_{\mathrm{ExpShell}} = \int_0^\infty 4\pi r^2 \frac{\sin(qr)}{qr} SLD_{\mathrm{ExpShell}}(r, R_{\mathrm{core}}, t_{\mathrm{shell}}, \alpha, \phi_{\mathrm{in}}, \phi_{\mathrm{out}}) dr \qquad \text{(S4.4)}$$

r gives the distance in the CS microgel and the total scattering length density of the microgel SLD_{ExpShell} is composed of three different SLDs ranging at different length scales in the microgel as given by **equation S4.5**.

$$SLD_{\mathrm{ExpShell}}(r, R_{\mathrm{core}}, t_{\mathrm{shell}}, \alpha, \phi_{\mathrm{in}}, \phi_{\mathrm{out}}) = \begin{cases} SLD_{\mathrm{core}} & r \leq R_{\mathrm{core}} \\ SLD_{\mathrm{Exp}}\left(\frac{r - R_{\mathrm{core}}}{t_{\mathrm{shell}}}\right) & R_{\mathrm{core}} < r < R_{\mathrm{core}} + t_{\mathrm{shell}} \\ SLD_{\mathrm{solvent}} & r > R_{\mathrm{core}} + t_{\mathrm{shell}} \end{cases} \qquad \text{(S4.5)}$$

R_{core} corresponds to the radius of the core, t_{shell} to the thickness of the shell and α to the parameter for the exponential diffuse profile of the shell. ϕ_{in} and ϕ_{out} refer to the amount of solvent at R_{core} and at R_{core} + t_{shell}, respectively. The scattering length density of the core, the shell and the solvent are given by SLD_{core}, SLD_{Exp} and SLD_{solvent}, respectively. SLD_{Exp} decays exponentially to the outside of the microgel and is given by **equation S4.6**.

$$SLD_{\mathrm{Exp}}(x) = SLD_{\mathrm{shell,in}} + \left[SLD_{\mathrm{shell,out}} - SLD_{\mathrm{shell,in}}\right] x \exp\left([1 - x]\alpha\right) \qquad \text{(S4.6)}$$

Here x refers to $\frac{r - R_{\mathrm{core}}}{t_{\mathrm{shell}}}$ and $SLD_{\mathrm{shell,in}}$ and $SLD_{\mathrm{shell,out}}$ are given by **equations S4.7** and **S4.8**, respectively.

$$SLD_{\mathrm{shell,in}} = [\phi_{\mathrm{in}} SLD_{\mathrm{solvent}} + (1 - \phi_{\mathrm{in}}) SLD_{\mathrm{shell}}] \qquad \text{(S4.7)}$$

$$SLD_{\mathrm{shell,out}} = [\phi_{\mathrm{out}} SLD_{\mathrm{solvent}} + (1 - \phi_{\mathrm{out}}) SLD_{\mathrm{shell}}] \qquad \text{(S4.8)}$$

SLD_{shell} corresponds to the scattering length density of the pure shell material.

The exponential shell form factor model is used to describe the form factor oscillations at low *q* in the scattering profiles. The Ornstein-Zernike contribution I_{OZ} is taken into account by a Lorenzian function as given by **equation S4.9**.[197]

$$I_{\mathrm{OZ}} = \frac{I_{\mathrm{fluct}}(0)}{1 + \xi^2 q^2} \tag{S4.9}$$

Here, $I_{\mathrm{fluct}}(0)$ represents the Lorenzian intensity and ξ the correlation length.

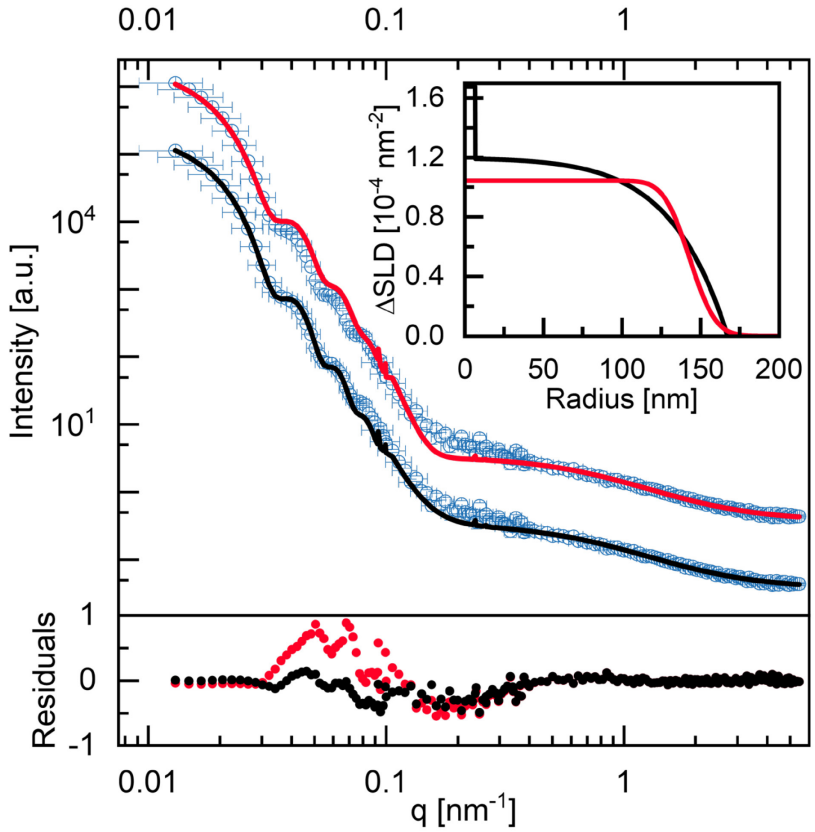

Figure S4.3. Comparison of different form factor models. (a) SANS profile recorded from Au_7-$PNIPAM_{high}$ at 20 °C. The solid lines correspond to fits using fuzzy sphere model with a gaussian decay in the SLD of the shell (red) and exponential shell model with an exponential decay in the SLD of the shell (black). The inset shows the radial profiles of the differences in SLD based on the form factor fits with the same color code. The bottom graph shows the residuals between the experimental curve and the fitted curve with the same color code.

Table S4.2. Overview of parameters for the analysis of the SANS data of Au_7-$PNIPAM_{high}$ for temperatures of 12 °C, 20 °C, 25 °C, 27 °C and 30 °C.

	Au_7-$PNIPAM_{high}$				
	12 °C	**20 °C**	**25 °C**	**27 °C**	**30 °C**
N [10^{12} cm^{-3}]	1.39	1.39	1.39	1.39	1.39
I_B [cm^{-1}]	0.0037	0.0035	0.0054	0.0058	0.0059
R_{core} [nm]	6.61	6.61	6.61	6.61	6.61
t_{shell} [nm]	169.17	161.00	154.90	151.36	144.65
σ_{SD} [nm]	8.46	7.24	10.84	10.59	7.96
R_{SANS} [nm]	175.78	167.61	161.51	157.97	151.26
ϕ_{in}	0.80	0.78	0.76	0.76	0.73
ϕ_{out}	1	1	1	1	1
α	- 2.86	- 3.49	- 3.71	- 4.09	- 4.82
SLD_{core} [10^{-4} nm^{-2}]	4.66	4.66	4.66	4.66	4.66
SLD_{shell} [10^{-4} nm^{-2}]	0.869	0.869	0.869	0.869	0.869
$SLD_{solvent}$ [10^{-4} nm^{-2}]	6.34	6.34	6.34	6.34	6.34
$I_{fluct}(0)$ [cm^{-1}]	0.028	0.035	0.030	0.039	0.048
ξ [nm]	1.51	1.60	1.61	1.74	2.12

Table S4.3. Overview of parameters for the analysis of the SANS data of Au_7-$PNIPAM_{high}$ for temperatures of 34 °C, 36 °C, 40 °C and 51 °C.

	Au_7-$PNIPAM_{high}$			
	34 °C	**36 °C**	**40 °C**	**51 °C**
N [10^{12} cm^{-3}]	1.39	1.39	1.39	1.39
I_B [cm^{-1}]	0.0068	0.0058	0.0064	0.0064
R_{core} [nm]	6.61	6.61	6.61	6.61
t_{shell} [nm]	134.48	126.23	112.913	102.54
σ_{SD} [nm]	8.07	6.94	9.03	7.69
R_{SANS} [nm]	141.09	132.84	119.52	109.15
ϕ_{in}	0.70	0.67	0.61	0.52
ϕ_{out}	1	1	1	1
α	- 6.56	- 9.52	- 24.03	- 84.03
SLD_{core} [10^{-4} nm^{-2}]	4.66	4.66	4.66	4.66
SLD_{shell} [10^{-4} nm^{-2}]	0.869	0.869	0.869	0.869
$SLD_{solvent}$ [10^{-4} nm^{-2}]	6.34	6.34	6.34	6.34
$I_{fluct}(0)$ [cm^{-1}]	0.069	0.085	0.104	/
ξ [nm]	2.71	3.60	5.17	/

Table S4.4. Overview of parameters for the analysis of the SANS data of Au_7-$PNIPAM_{low}$ for temperatures of 12 °C, 20 °C, 25 °C, 27 °C and 30 °C.

	Au_7-$PNIPAM_{low}$				
	12 °C	**20 °C**	**25 °C**	**27 °C**	**30 °C**
N [10^{12} cm^{-3}]	1.91	1.91	1.91	1.91	1.91
I_B [cm^{-1}]	0.0037	0.0039	0.0059	0.0059	0.0059
R_{core} [nm]	7.30	7.30	7.30	7.30	7.30
t_{shell} [nm]	184.13	174.42	166.69	162.48	152.82
σ_{SD} [nm]	12.89	13.95	16.67	11.37	10.70
R_{SANS} [nm]	191.43	181.717	173.99	169.78	160.12
ϕ_{in}	0.89	0.88	0.86	0.86	0.83
ϕ_{out}	1	1	1	1	1
α	- 3.88	- 4.27	- 4.49	- 4.71	- 5.17
SLD_{core} [10^{-4} nm^{-2}]	4.66	4.66	4.66	4.66	4.66
SLD_{shell} [10^{-4} nm^{-2}]	0.869	0.869	0.869	0.869	0.869
$SLD_{solvent}$ [10^{-4} nm^{-2}]	6.34	6.34	6.34	6.34	6.34
$I_{fluct}(0)$ [cm^{-1}]	0.042	0.056	0.060	0.071	0.084
ξ [nm]	1.62	1.81	2.14	2.27	2.56

Table S4.5. Overview of parameters for the analysis of the SANS data of Au_7-$PNIPAM_{low}$ for temperatures of 34 °C, 36 °C, 40 °C and 51 °C.

	Au_7-$PNIPAM_{low}$			
	34 °C	**36 °C**	**40 °C**	**51 °C**
N [10^{12} cm^{-3}]	1.91	1.91	1.91	1.91
I_B [cm^{-1}]	0.0070	0.0067	0.0073	0.0068
R_{core} [nm]	7.30	7.30	7.30	7.30
t_{shell} [nm]	136.58	119.22	98.67	92.25
σ_{SD} [nm]	9.56	8.34	6.91	6.46
R_{SANS} [nm]	143.83	126.52	105.97	99.55
ϕ_{in}	0.78	0.69	0.58	0.51
ϕ_{out}	1	1	1	1
α	- 5.94	- 7.23	- 24.49	- 56.96
SLD_{core} [10^{-4} nm^{-2}]	4.66	4.66	4.66	4.66
SLD_{shell} [10^{-4} nm^{-2}]	0.869	0.869	0.869	0.869
$SLD_{solvent}$ [10^{-4} nm^{-2}]	6.34	6.34	6.34	6.34
$I_{fluct}(0)$ [cm^{-1}]	0.147	0.257	0.169	/
ξ [nm]	3.57	5.55	7.56	/

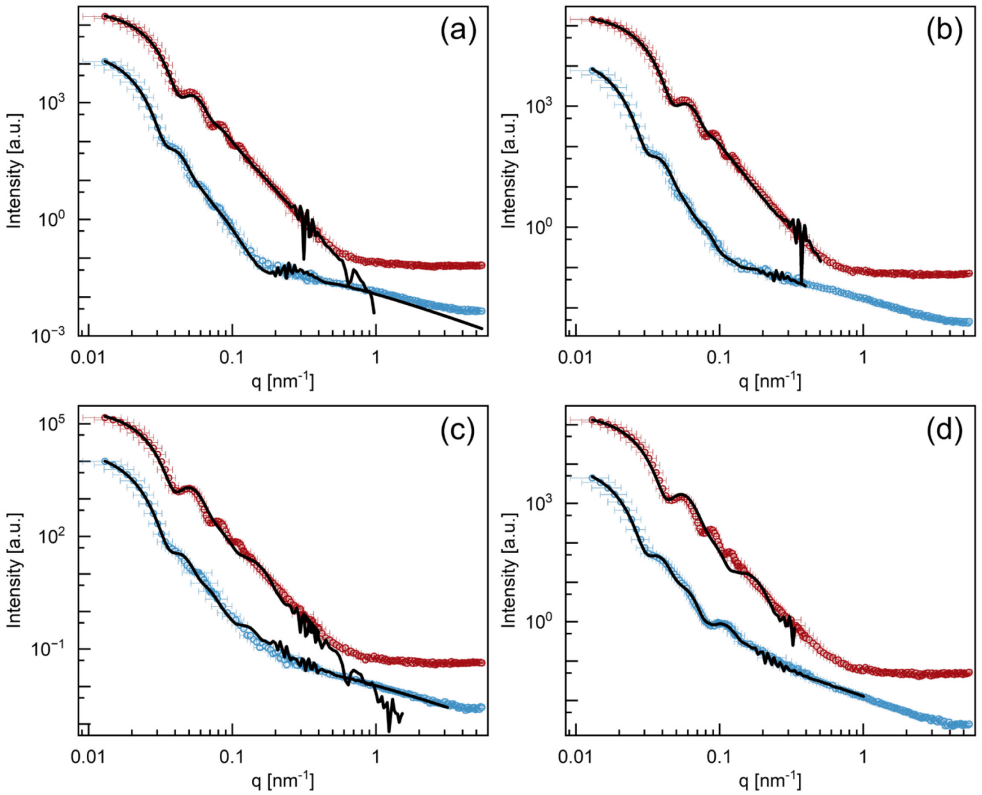

Figure S4.4. SANS profiles at 20 °C (blue) and at 51 °C (dark red) for Au_7-$PNIPAM_{high}$ (a), Au_7-$PNIPAM_{low}$ (b), Au_{46}-$PNIPAM_{high}$ (c) and Au_{46}-$PNIPAM_{low}$ (d). The black solid lines represent the profile simulated by RMC simulations.

5. Non-close-packed plasmonic Bravais lattices through a fluid interface-assisted colloidal assembly and transfer process

Published in *Colloid and Polymer Science*, **2024**, 302, n/a

DOI: 10.1007/s00396-024-05285-4

Déborah Feller,[a] Marius Otten,[a] Michael S. Dimitriyev,[b] and Matthias Karg[a]*

[a]Institut für Physikalische Chemie I: Kolloide und Nanooptik, Heinrich-Heine-Universität Düsseldorf, Universitätsstr. 1, 40225 Düsseldorf, Germany

[b]Department of Materials Science and Engineering, Texas A&M University, College Station, TX 77807, USA

Keyword: core-shell microgels, 2-dimensional Bravais lattices, fluid interface-assisted self-assembly, localized surface plasmon resonance, plasmon resonance coupling

5.1. Abstract

The assembly of colloids at fluid interfaces followed by their transfer to solid substrates represents a robust bottom-up strategy for creating colloidal monolayers over large, macroscopic areas. In this study, we showcase how subtle adjustments in the transfer process, such as varying the contact angle of the substrate and controlling deposition speed and direction, enable the realization of all five two-dimensional Bravais lattices. Leveraging plasmonic core-shell microgels as the building blocks, we successfully engineered non-close-packed plasmonic lattices exhibiting hexagonal, square, rectangular, centered rectangular, and oblique symmetries. Beyond characterizing the monolayer structures and their long-range order, we employed extinction spectroscopy alongside finite difference time domain simulations to comprehensively investigate and interpret the plasmonic response of these monolayers. Additionally, we probed the influence of the refractive index environment on the plasmonic properties by two methods: first, by plasma treatment to remove the microgel shells, and second, by overcoating the resulting gold nanoparticle lattices with a homogeneous refractive index polymer film.

5.2. Introduction

Fluid interface-assisted assembly of colloidal particles is a powerful method for the preparation of periodic colloidal assemblies.[144, 218-220] Colloids tend to adsorb to fluid interfaces where they are energetically trapped and can self-assemble into ordered arrangements. These arrangements can be transferred from the fluid interface to solid substrates for applications in optics,[221, 222] photonics[223] and lithography.[143, 224] Conventionally, incompressible particles such as silica or polystyrene particles are used for these processes.[174, 225-227] By varying different parameters such as the amount of particles applied to the interface or by reducing the interfacial area in a Langmuir trough setup, one can obtain either non-close-packed or close-packed ordered monolayers.[175, 218] The typical equilibrium structure of such monolayers is the hexagonal lattice where each colloid is surrounded by six neighbors at equal

distances. When the particles are densely packed and the monolayer is further compressed, the rigidity of the particles will induce collapse of the monolayer.

Recently, Hummel et al. have shown that any of the possible two-dimensional (2D) Bravais lattices can be prepared using fluid interface-assisted colloidal assembly of rigid and non-deformable colloids.[77] Starting from the hexagonally ordered equilibrium structure at the liquid interface, the final monolayer structure could simply be controlled by the contact angle of the solid substrate applied to transfer the monolayer from the liquid to the solid interface. The observed structures resulted, basically, as a consequence of uniaxial deformation of the close-packed monolayer during transfer to the solid substrates.

In contrast to assemblies of rigid colloids at fluid interfaces, soft and deformable particle-like objects such as poly(*N*-isopropylacrylamide) (PNIPAM) microgels[5] allow for compression over a wide range of packing fractions.[47, 149, 228, 229] Such microgels can laterally stretch out or be compressed at the interface to interfacial dimensions much larger or much smaller than their dimensions in bulk, respectively.[41] The same behavior is observed for core-shell (CS) microgels with rigid, non-deformable cores and soft microgel shells that ultimately allow for the preparation of functional periodic nanoparticle arrays.[51, 54, 55, 57] While the microgel shell facilitates the assembly at fluid interfaces, it also acts as a spacer that can control the periodicity of assembled nanoparticle arrays.[230]

In this work, we build upon our previous study of the preparation of all possible two-dimensional (2D) Bravais lattices from rigid colloids[77] and demonstrate applicability for soft and deformable, colloid-like objects. Our approach involves the utilization of deformable CS microgels containing AuNP cores, which undergo self-assembly at air/water interfaces. The resulting monolayer, comprised of microgels arranged in a hexagonal lattice, is then transferred onto glass substrates modified with various surface properties.

By carefully controlling the substrate's contact angle and the direction and speed of deposition, we achieve precise control over the structure of the resulting substrate-supported colloidal monolayer. Rapid drying of the thin film leads to the formation of all possible 2D Bravais lattices, characterized by large domain sizes and a non-close-packed arrangement of dried CS microgels. Subsequent plasma

treatment allows for the transformation of these lattices into non-close-packed arrangements of bare AuNPs, demonstrating the versatility of our method.

Furthermore, we demonstrate additional structural control by varying the shell sizes of the CS microgels, which enables us to adjust the lattice period. Finally, we investigate the plasmonic response of the different lattices using UV-Vis spectroscopy. This work highlights the adaptability of our transfer protocol, originally developed for uniaxially deforming hexagonally ordered monolayers of rigid colloids at fluid interfaces, to not only soft colloid-like objects but also multifunctional hybrid systems containing plasmonic NP cores.

5.3. Experimental Section

5.3.1. Materials

Gold(III) chloride trihydrate ($HAuCl4 \cdot 3H_2O$; Sigma-Aldrich, ≥99.999%), sodium citrate dihydrate (Sigma-Aldrich, ≥99%), sodium dodecyl sulfate (SDS; Sigma-Aldrich, p.a.), butenylamine hydrochloride (BA; Sigma-Aldrich, 97%), *N*,*N*′-methylenebisacrylamide (BIS; Sigma-Aldrich, ≥99%), potassium peroxodisulfate (PPS; Sigma-Aldrich, ≥99%), cetyltrimethylammonium chloride (CTAC; Sigma-Aldrich, 25 wt % in water), ascorbic acid (Roth, p.a.), 3-(Trimethoxysilyl)propylmethacrylate (MPS; Aldrich, 98 %), 1H,1H,2H,2H-Perfluorooctyltriethoxysilane (FOCTS; J&K Scientific, 97 %), ethanol (Honeywell, p. a.), 1,4-dioxane (p.a., Fisher Chemicals), ammonia (PanReac Applichem, 30 % in water), hydrogen peroxide (Fisher Scientific, > 30 % in water), cyclohexane (Fisher Scientific, ≥ 99.8 %) and Hellmanex III (Hellma GmbH) were used as received.

N-isopropylacrylamide (NIPAM; TCI, >98.0%) was recrystallized from cyclohexane.

Milli-Q water (Millipore, resistivity > 18 MΩcm) was used for all synthesis and self-assembly procedures.

5.3.2. Synthesis

Synthesis of gold seeds

Gold nanoparticles (AuNP seeds) were synthesized via the well-known Turkevich method.[207] In brief, 500 mL of aqueous $HAuCl_4 \cdot 3H_2O$ (0.5 mM) were brought to heavy boiling under stirring. 25 mL of a hot aqueous solution of sodium citrate dihydrate (1 wt%) were quickly added. The color of the reaction medium changed from light yellow to grey, black and then to deep red. Heating was continued for further 20 min while stirring. Afterwards, the dispersion was allowed to cool down to room temperature.

Following the protocol of Rauh et al.,[76] 3 mL of an aqueous SDS solution (1 mM) was added while stirring the dispersion at room temperature to increase the colloidal stability. After 20 min, 1.63 mL of an ethanolic BA solution (1.4 mM) was added to functionalize the surface of the AuNP seeds. The dispersion was left to stir for another 20 min and then concentrated by centrifugation at 1000 rcf for 16 h to yield a total of 30 mL AuNP seed dispersion.

Synthesis of CS microgels

Au-PNIPAM CS microgels were synthesized by seeded precipitation polymerization.[76] For this, the BA-functionalized AuNPs were used as seeds. In brief, NIPAM (0.588 g, 5.20 mmol) and BIS (0.134 g, 0.87 mmol) as chemical crosslinker were dissolved in 100 mL of Milli-Q water and then degassed with argon at 70 °C. After 1 h, 5 mL of the dispersion of the functionalized AuNP seeds ($c(Au^0)$ = 4.55 mM) were added. Degassing was continued for 30 min. The polymerization was initiated by adding 2.2 mg of PPS dissolved in 1 mL of water. When the reaction mixture became turbid, the reaction was continued for 4 h. After cooling down to room temperature, the CS microgels were purified by three consecutive centrifugation steps, each at 9400 rcf for 1 h. After the first two steps/the last step, the residue was redispersed in 30 mL/15 mL of water, respectively. The Au-PNIPAM microgels were then freeze-dried for three days. The description of the synthesis details of larger Au-PNIPAM microgels can be found in the SI.

In situ overgrowth of the gold cores

The overgrowth protocol used to increase the size of the spherical gold cores was adapted from Ponomareva et al.[55] Briefly, an aqueous solution of Au-PNIPAM microgels (4.68 wt%) was mixed with an aqueous CTAC solution (10 mM) in a 1:1 volume ratio. 800 µL of this dispersion were added to 32 mL of an aqueous CTAC solution (2.4 mM) while stirring in an Erlenmeyer flask. One overgrowth step consisted of the addition of 624 µL of an aqueous ascorbic acid solution (49 mM) in one shot followed by the dropwise addition of 48 mL of an aqueous solution containing CTAC (6.2 mM) and $HAuCl_4 \cdot 3H_2O$ (0.5 mM). The overgrowth process was allowed to proceed for 30 min while slow stirring. The overgrowing procedure required seven steps to reach core sizes of about 100 nm in diameter. This was followed by UV-Vis spectroscopy after each step in order to reach a LSPR maximum at about 580 nm. After the seventh growth steps, the reaction medium was stirred overnight. The final CS microgels were then dialyzed against water for four days with water exchange twice a day. After the dialysis, the microgels were centrifuged three times for 30 min at 5400 rcf. After each step, the final residue was dispersed in 600 µL of ethanol.

Hydrophobization of glass substrates

Glass substrates (2.4 x 2.4 cm^2) were cleaned by sonification in an aqueous solution of Hellmanex (2 vol%), followed by water and then ethanol for 15 min each. Afterwards, the substrates were dried with a stream of compressed N_2 resulting in hydrophilic substrates with a contact angle of 15 °. A clean substrate was then placed on a spin-coater and 40 µL of a PS solution (1 wt% in 1,4-dioxane, 120,000 g/mol) were placed in the middle of the substrate. Spin-coating was performed at 2000 rpm for 20 s resulting in a hydrophobic substrate with a contact angle of 96 °.

Prior to functionalization of glass substrates with FOCTS and MPS, glass substrates (2.4 x 2.4 cm^2) were cleaned by the RCA-1 method.[231] Five parts of water were mixed with one part of ammonia (30 %) and heated to 80 °C while stirring. When the temperature of the solution was constant, one part of H_2O_2 (30 %) was added. Glass substrates were immersed into the solution for 15 min, when the temperature was between 75 °C and 85 °C. Afterwards, the glass substrates were rinsed thoroughly with water and left in water for 5 min before drying in a stream of compressed N_2.

The functionalization of the glass substrates was done using chemical vapor deposition. Therefore, the substrates were placed in a desiccator with 120 µL of the functionalizing agent (FOCTS or MPS) and the pressure was reduced to 150 mbar. The functionalization was allowed to proceed overnight. The glass substrates were then removed and baked at 60 °C in an oven for 2 h. After the baking process, the substrates were sonicated for 10 min in ethanol and then dried with N_2. This procedure resulted in hydrophobic substrates with a contact angle of 114 ° for FOCTS and 87 ° for MPS, respectively.

Contact angles were measured with the drop shape analyzer Krüss DSA 25 by applying a droplet of 10 µL of Milli-Q water on the functionalized substrates.

Monolayer preparation and transfer

The preparation process to obtain the different Bravais lattices is schematically shown in **Scheme 5.1**. The process is inspired by the one reported by Hummel et al. for rigid spheres[77] and uses the assembly of freely floating monolayers in a crystallizing dish instead of using a Langmuir trough. In other words, for the current preparation we cannot control the degree of compression, i.e. the total accessible interfacial area, and thereby we cannot control the packing fraction. For the freely floating monolayers we expect surface pressures to be low and interparticle distances to be large as we will later confirm in the **Results & Discussion** section. While our aim here was to follow the process from literature and provide an easy, low-tech preparation scheme, for a future work it might be interesting to perform such experiments at different states of monolayer compression.

A crystallizing dish was filled with Milli-Q water and 7 µL of the Au-PNIPAM microgels dispersed in ethanol were carefully injected directly to the air/water-interface, where the microgels self-assembled into a freely floating monolayer (d). Depending on the targeted Bravais lattice (b), different transfer geometries (c) and contact angles of the substrates (a) were used. The hexagonally ordered structure was prepared by using a hydrophilic substrate ($\theta < 90$ °) according to the protocol of Volk et al.[57] Here the substrate was immersed in the bulk water phase vertically and then placed below the monolayer-covered air/water interface. By retracting the substrate through the monolayer at a shallow angle, the monolayer was transferred from the interface to the

substrate. The sample was dried with a heat gun by blowing warm air from below the glass substrate (uncovered side). The other four lattices were prepared by adapting the protocol of Hummel et al.[77] Hydrophobic substrates with a contact angle of 96 ° for square, 87 ° for rectangular and centered rectangular and 114 ° for oblique structures were used. In order to transfer the monolayer from the interface to the glass substrates, the substrates were immersed through the monolayer into the bulk phase. For the square lattice, the substrate was immersed vertically at a rather slow speed of 15 mm/s using a dip-coater. For the rectangular structure, the glass was immersed vertically and significantly faster by hand. It is important to note that the square lattices were only obtained at the slow transfer speed with best results using a dip-coater, while the manual transfer for the rectangular structure had to be performed significantly faster and was found more robust against variation in the transfer speed. The centered rectangular structure, as well as the oblique structure were received by immersing the respective substrate through the monolayer at a shallow angle. For all cases, where the substrate was pushed through the monolayer for the transfer, the substrates were placed at the bottom of the crystallizing dish with the monolayer facing up. The substrates were then thermally annealed for 10 min by placing the crystallizing dish on a hotplate at 130 °C in order to increase the adhesion of the monolayer to the substrate. Then the glass substrates were removed and dried with a heat gun from underneath.

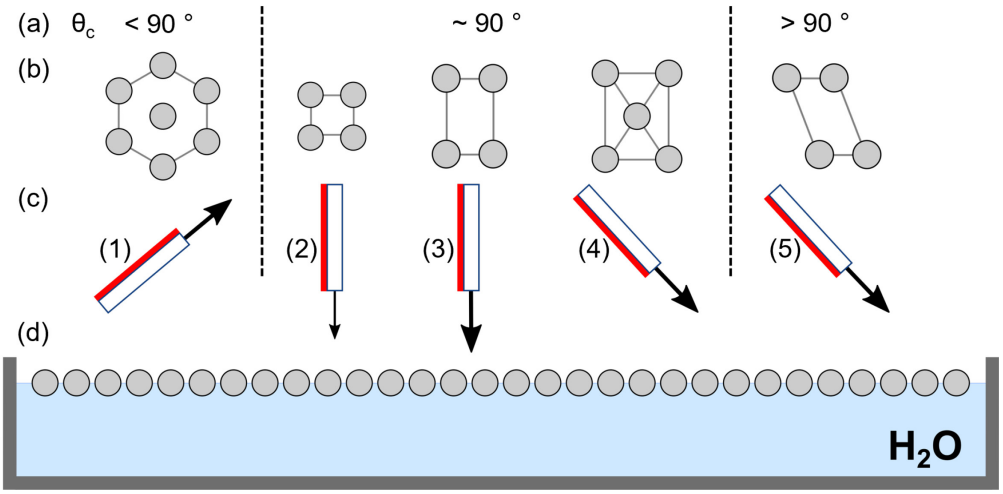

Scheme 5.1. Schematical depiction of the preparation method for the five different Bravais lattices. The Au-PNIPAM microgels are represented by the grey circles (over simplified). (a) The contact angle θ_c of the substrates can be divided into three ranges. (b) Structural illustration of the five different Bravais lattices. (c) Illustration of the retraction/immersion procedure to immobilize the assembled particles on the red colored side of the substrates. (1) Retraction of monolayer at a shallow angle. (2), (3) Vertical immersion of the substrate through the monolayer. (4), (5) Immersion at a shallow angle through the monolayer. The thickness of the arrow illustrates the retraction/immersion speed. Contact angles of the substrate used in experiment are (1) 15 °, (2) 96 °, (3) 87 °, (4) 87 ° and (5) 114 ° respectively. (d) Crystallizing dish with particles assembled into a monolayer at the air/water interface.

Plasma treatment of the substrate-supported monolayers

In order to remove the microgel shell of the Au-PNIPAM monolayers on the glass substrates, plasma treatment was performed for 45 min at 300 W in an oxygen atmosphere using a PlasmaFlecto 10 (plasma technology GmbH). Afterwards, the glass substrates were washed with Milli-Q water to remove any polymeric residues and dried in a stream of compressed N_2.

Superstrate coating of the AuNP monolayers

In order to embed the substrate-supported AuNP monolayers (after plasma treatment) in a homogenous refractive index environment, linear PNIPAM homopolymer (85,000 g/mol, synthesized via the protocol by Ebeling et al.[232]) was spincoated on top of the monolayer. To accomplish this, 60 µL of linear PNIPAM solution (5 wt% in 1,4-dioxane) was placed in the middle of the glass substrate. Spin-coating was then

performed at 2000 rpm for 60 s resulting in a homogeneous polymer film with a thickness of 1.5 µm as determined by atomic force microscopy (AFM).

5.3.3. Methods

Transmission Electron Microscopy (TEM)

TEM was used to examine the morphology of the CS microgels and to verify the success of the polymer encapsulation of the AuNP cores. Imaging was performed with a JEOL JEM-2100Plus TEM in bright-field mode operated with an acceleration voltage of 80 kV. The samples were prepared on carbon-coated copper grids (200 mesh, Electron Microscopy Science) by drop-casting 7 µL of a dilute aqueous Au-PNIPAM microgel dispersion. The grids were dried at room temperature for one hour. Core sizes were measured using the software ImageJ.[208]

Atomic Force Microscopy (AFM)

AFM height images were recorded in intermittent contact mode against air with a Nanowizard 4 (JPK Instruments). The images were recorded with an OTESPA-R3 AFM probe (Bruker). The tip geometry was a visible apex with a nominal tip radius of 7 nm. According to the manufacturer, the cantilever possesses a resonance frequency of 300 kHz and a spring constant of 26 N/m. Exact values were not measured. The recorded images of 20 x 20 μm^2 had a resolution of 1024 x 1024 $pixel^2$. The software ImageJ was used to analyze the images and to create the FFT, as well as the autocorrelation images.[208]

UV-Vis Spectroscopy

Extinction spectra were recorded using a Specord S 600 UV-Vis spectrophotometer (Analytik Jena AG) in the wavelength range of 250 – 1019 nm. The spectra of dilute samples were measured in transmission geometry using 1 cm PMMA cuvettes. Coated glass substrates were held upright in the light path with the particle monolayer facing towards the detector. Cuvettes with water or clean glass substrates were used

as reference, respectively. The PNIPAM coated monolayers were also background corrected with a clean glass substrate, as there was no detectable difference between clean glass and PNIPAM coated glass (see **Figure S5.14**).

Scanning Electron Microscopy (SEM)

SEM images were recorded with a ZEISS SUPRA 55V equipped with a field emission gun (FEG). The instrument was operated at acceleration voltages of 10 and 20 kV. The images were recorded with either a secondary electron (SE2) or an angle selective backscattered (AsB) detector. The AsB detector enhanced the material contrast making it possible to visualize the cores in the PNIPAM shell. Prior to the measurements, the samples were sputtered with a layer of gold to enhance the conductivity.

Finite Difference Time Domain (FDTD) Simulations

Extinction spectra of the five Bravais lattices were calculated with the finite difference time domain (FDTD) method. The calculation software is commercially available from Lumerical Solutions, Inc. (FDTD Solutions, Version 8.18.1332). We simulated the spectra for finite size lattices in a box with perfectly matched layer (PML) boundary conditions in all three spatial directions. A total-field scattered-field source with incident wavelengths of 290 – 910 nm was used. Two boxes of power monitors, one in the total field region and one in the scattered field region were used to calculate the absorption and the scattering. The lattices were constructed with a domain size of three for all five structures. The size of the dried CS microgels was estimated from the AFM height image by taking the full width half maximum of a cross-section from a dried CS microgel as the diameter. Core sizes were determined from TEM images. The interparticle distances in the different Bravais lattices for the comparison between experiment and simulation were taken from the experimental AFM height images. For the calculated extinction spectra of the Bravais lattices with the same period, we choose to use a period of 350 nm, which was close to the experimental period of the square lattice. As the refractive index (RI) of gold is wavelength dependent, values from literature were taken.[233] The PNIPAM shell of the microgels was simulated with a RI of 1.49,[234] which is slightly smaller than 1.50 known from Brasse et al.[235] to

account for the residual water content in the shell. The air background and the glass substrate were simulated with a RI of 1 and 1.52, respectively. Uniform meshes of 2.5 nm (centered rectangular), 3.5 nm (square), 4 nm (hexagonal and rectangular) and 7.5 nm (oblique) were used in the area of the lattice in addition to a nonuniform mesh. The auto shut-off of the calculation was set to 10^{-5}, which was already reached before a simulation time of 1000 fs.

Voronoi and Delaunay tessellations

Local order analyses of the core positions, including the generation of Voronoi and Delaunay tessellations, were performed using codes developed in Wolfram Mathematica v13.2. To exclude boundary artifacts in the tessellations, cells closest to the boundary (within 10% of the full width of the region of interest) were excluded from the analyses.

5.4. Results & Discussion

5.4.1. Characterization of the colloidal building blocks

Similar to our previous work,[55] CS microgels with single, nanocrystalline gold cores and soft, deformable PNIPAM shells were chosen as the colloidal building blocks. These hybrid microgels were synthesized via seeded precipitation polymerization followed by the controlled *in situ* overgrowth of the gold cores. The overgrowth of the cores can easily be tracked by UV-Vis extinction spectroscopy due to the dependencies of the LSPR position and resonance strength on the core size. **Figure 5.1a** shows the normalized extinction spectra of the initial CS microgels (dark green) and of the batches after each of the seven growing steps (from green to red). The dark green curve shows the Rayleigh-Debye-Gans scattering of the PNIPAM shell which dominates the absorption of the Au core, so the LSPR peak is not visible in the spectrum.[49, 56] After the first step, the cores grow in size and the LSPR peak becomes visible. The maximum of the LSPR peak shifts from 542 nm and a full width

half-maximum (FWHM) of 68 nm after the first step to 581 nm and a FWHM of 88 nm after the seventh step with an increase in intensity. The LSPR peak is ascribed to a dipolar mode, which is the only mode to be expected for the size range of the cores.[55]

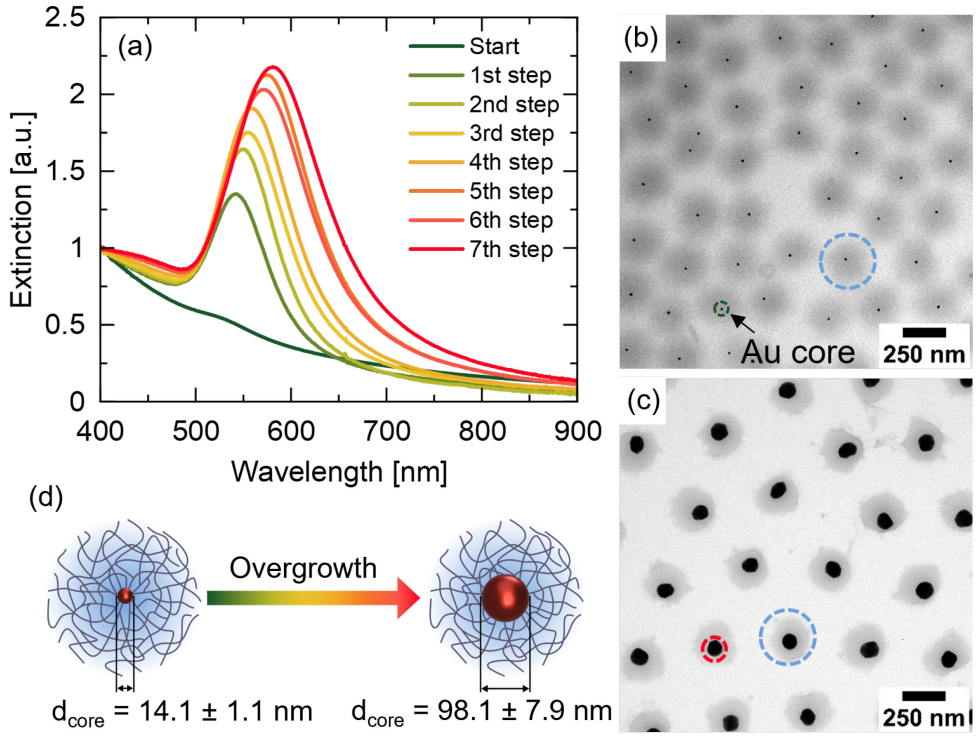

Figure 5.1. Overgrowth of Au cores in the PNIPAM shell via seven step synthesis. (a) Extinction spectra normalized to the extinction at 400 nm. The spectra show the evaluation of the LSPR peak over the seven overgrow steps from dark green to red. (b) TEM image of the Au-PNIPAM microgels prior to the core overgrowth. The Au core is highlighted by the dark green dashed circle and the PNIPAM shell by the blue dashed circle. (c) TEM image of the Au-PNIPAM microgels after the seventh overgrow step. The overgrown Au core is highlighted by the red dashed circle and the PNIPAM shell by the blue dashed circle. (d) Schematical representation of Au-PNIPAM microgels before and after the overgrow synthesis with the corresponding core diameters. The color coding of the arrow corresponds to the color of the overgrowing steps in (a).

TEM images recorded from samples before (**Figure 5.1b**) and after (**Figure 5.1c**) the overgrowth confirm the successful encapsulation, as well as the increase in size of the cores in the polymer shell. The cores are nicely located in the center of the shell, which is expected for CS microgels with 16.5 mol% nominal BIS content, i.e. high

crosslinker density.[140] The microgels have core diameters, d_{core} of 14.1 ± 1.1 nm and 98.1 ± 7.9 nm in **Figure 5.1b and 5.1c**, respectively. The size distribution of the overgrown cores can be found in the **Supporting Information Figure S5.1**. The hydrodynamic radius, R_h, of the final microgels after the seventh step of core growth was determined as 172.9 ± 3.4 nm using DLS at 20 °C.

5.4.2. Fluid interface-assisted assembly and characteristics of the hexagonal equilibrium structure

The CS microgels were self-assembled at the air/water interface to form a freely floating monolayer of hexagonally ordered microgels as the equilibrium structure. By using the common retraction method with a hydrophilic glass substrate,[57] the microgels are hexagonally ordered on the substrate as shown in **Figure 5.2a**. In contrast to previously reported by Kuk et al.,[72] we do not see any drying artefacts in our monolayer. Here, the drying effects are suppressed by the fast drying of the substrate with a heat gun. Thus, the microgels do not have sufficient time to rearrange and the structure on the substrate is expected to resemble closely the one at the air/water interface.[67] The AFM height image shows a highly ordered monolayer with only a few local defects in the structure. In addition, predominately one domain can be identified which confirms the long-ranging order of the monolayer over a distance of several micrometers. To further analyze the structure and degree of order, the AFM height profile from **Figure 5.2a** was first transformed into a point map shown in **Figure 5.2b.** This point map shows only the center of mass of each CS microgel, which was then used to compute the fast Fourier transform (FFT) shown as inset. The FFT shows sharp Bragg peaks of several orders revealing the six-fold symmetry of the monolayer and the long-range order. In **Figure 5.2c**, the point map is used for mapping onto real space, bulk dimension of the CS microgels. The NP cores are represented by black circles and the microgel shells as light corona with a radius of 173 nm which corresponds to the hydrodynamic radius from bulk measurements (DLS). With these dimensions the lattice appears non-close-packed with almost all microgels being not in contact, except for two pairs of microgels, as shown by the red lines. These pairs are the result of the deformability of the microgel shells which can compensate for

lattice defects. Furthermore, in the initial monolayer at the air/water interface the shells stretch laterally into a 'fried-egg' like shape occupying a larger area at the interface.[46] Thus, the diameter of the microgels at the interface is expected to be larger than the diameter in bulk which explains the high degree of order. Upon drying, the shell shrinks and particles seem to not be in contact anymore, as also suggested by the AFM height image in **Figure 5.2a**. These findings are also confirmed by the Voronoi tessellation in **Figure 5.2d**, generated from the point map. The majority of the microgels show a sixfold coordination (orange hexagons) with neighboring microgels, which is also expected for a hexagonal array. Some defects in the monolayer can be detected by the 5-coordinated (yellow pentagons) and by the 7-coordinated (green heptagons) microgels, often appearing as bound disclination pairs, indicative of a lattice dislocation. Nucleation sites for pairs of bound dislocations can be found at the groupings of four disclinations, consisting of a pair of 5-coordinated and a pair of 7-coordinated. While the presence of unbound dislocations indicates the potential development of a hexatic phase, the effect on the overall order of the monolayer seems to be minimal. This robustness can be rationalized by the softness of the microgels, as the shell is able to compensate some disorder in the arrangement.

The freely floating monolayer with hexagonally arranged microgels with laterally stretched shells in shell-shell contact is the starting point for the preparation of the four remaining 2D Bravais lattices that will be addressed in the following.

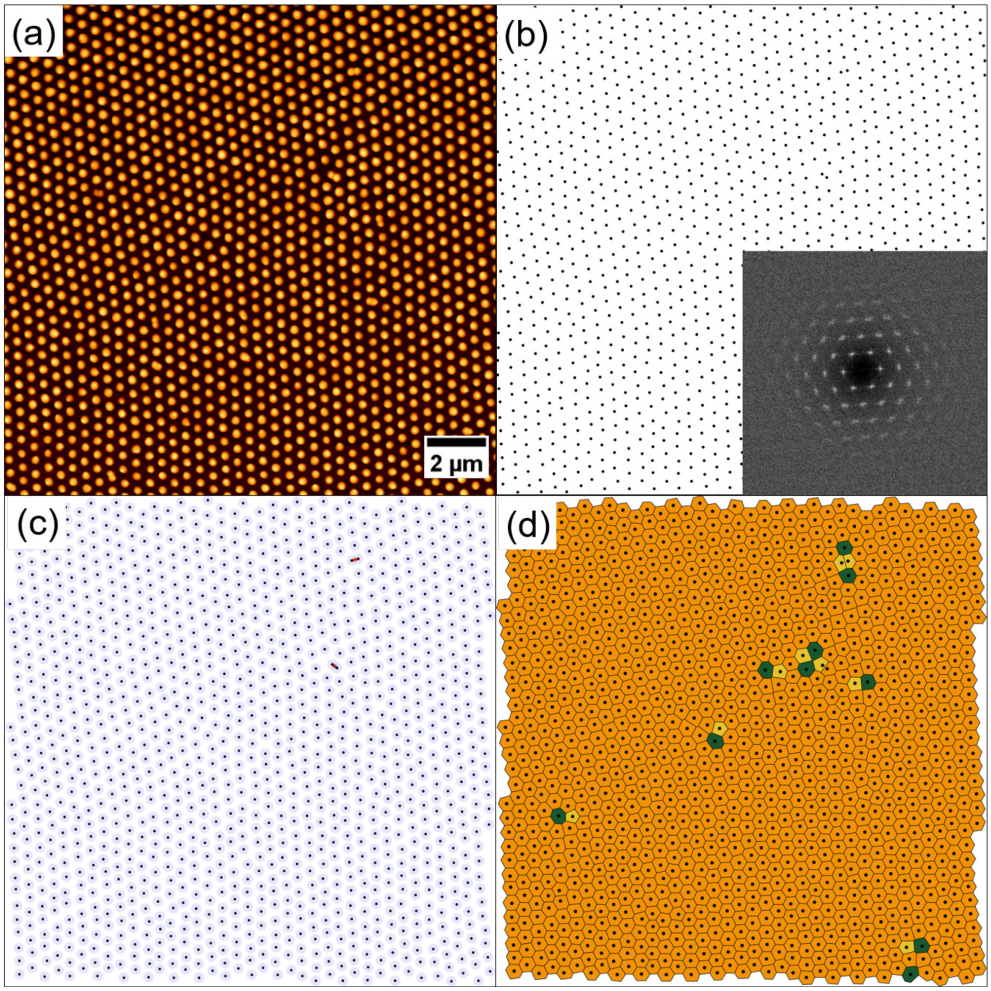

Figure 5.2. Hexagonally ordered monolayer of Au-PNIPAM CS microgels. (a) AFM height image of the monolayer. (b) Point map of the center of mass of the CS microgels extracted from the AFM height images. The inset shows the FFT of the point map. (c) Scheme of the microgels ordered on the substrate. The black points represent the cores and the shell is shown in light blue. The shells have a radius which corresponds to the hydrodynamic radius of nearly 173 nm. The red lines show particles which are in contact, with overlapping shells. (d) Voronoi tessellation generated from the point map. 6-coordinated particles are shown as orange hexagons. 5- and 7- coordinated disclination defect pairs are shown as yellow pentagons and green heptagons, respectively. Scalebar in (a) is representative for all four images.

5.4.3. Bravais lattices of soft CS microgels

We prepare Bravais lattices from soft microgels via a fluid interface-assisted process. The resulting lattice strongly depends on the immersion angle and speed, as well as on the contact angle of the glass substrate, as shown in **Scheme 5.1**. We want to note that in the previous work of Hummel et al. using hard spheres, the monolayer deformation was dominantly controlled via the substrate wettability affecting the ratio of flow velocity to substrate immersion velocity.[77] In case of our microgels, we could not obtain similar results as for the rigid spheres by simply varying the substrate wettability. While we believe that the general mechanism of lattice deformation is similar and driven by the flow velocity towards the contact line, we will see that the mechanism is more complex for soft and deformable microgels where interparticle and particle-to-substrate interactions differ significantly compared to rigid spheres.[72] We immersed hydrophobic substrates through the monolayer at the interface to prepare the other four Bravais lattices, namely square, rectangular, centered rectangular and oblique.[77] In **Figure 5.3**, the top row shows the AFM images of the resulting five Bravais lattices. The microgels are highly ordered in predominately one domain nearly without any visible defects. The type of the lattice is represented by a hexagon **(a)**, a square **(b)**, a rectangular **(c)**, a centered rectangular **(d)** and an oblique tetragon **(e)**, all marked in red. Larger AFM images with the corresponding FFTs and autocorrelation images of all five Bravais lattices can be found in **Figure S5.2** to **Figure S5.6**.

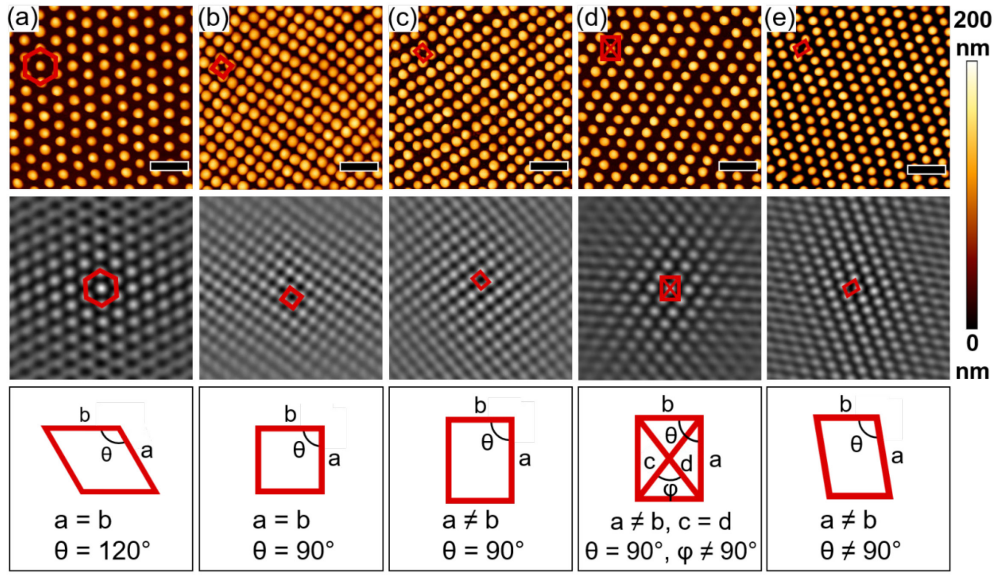

Figure 5.3. Bravais lattices prepared on glass substrates with CS microgels via self-assembly at the air/water interface. The top and middle row show AFM height images and their autocorrelation images, respectively. The scale bar corresponds to 1 µm. The Bravais lattice is marked in red. The bottom row shows the different unit cells of the Bravais lattices with the corresponding lengths of the cell edges *a*, *b*, *c* and *d* and the angles θ and φ. The five Bravais lattices: hexagonal (a), square (b), rectangular (c), centered rectangular (d) and oblique (e).

The middle row in **Figure 5.3** shows 2D autocorrelation functions computed from the AFM images shown in the top row. The autocorrelation functions not only nicely reveal the different lattice symmetries, they also confirm the long-range order due to the large number of correlation peaks. Blurring at the edges of the autocorrelation images is due to the finite dimension of the AFM images. The length of the edges, as well as the angle of the unit cell from the Bravais lattices (shown in **Figure 5.3** bottom row) were determined by measuring four unit cells in the autocorrelation function. The results are listed in **Table 5.1**.

Table 5.1. Values of the edge lengths *a* and *b* respectively and of the angle θ for the five Bravais lattices. Values were determined by measuring four unit cells in the autocorrelation function of the corresponding Bravais lattice.

Parameter	Hexagonal	Square	Rectangular	Centered Rectangular	Oblique
***a* [nm]**	471 ± 15	353 ± 5	375 ± 1	647 ± 2	381 ± 2
***b* [nm]**	471 ± 15	330 ± 1	324 ± 1	501 ± 3	314 ± 1
θ [°]	119 ± 2	89 ± 3	89 ± 3	91 ± 5	103 ± 1

For the square structure, the lengths of the edges *a* and *b* match closely with only 7 % deviation from the mean. We want to note that the real deviation is potentially smaller because of the limited resolution of the images where one pixel corresponds to approximately 20 nm. When comparing the lengths, *a* and *b* of all structures, the hexagonally structure shows larger spacings than the square, rectangular and oblique ones, which can be attributed to the different preparation method. The edge length *a* for the centered rectangular arrangement of 647 ± 2 nm is nearly the double of the edge lengths for the square arrangement. This can be explained by the period of the structure. For the square lattice, the period equals the edge length, but for the centered rectangular lattice, the period equals the half of the edge length *a*. Thus, we can conclude that the spacing of all prepared Bravais lattices range in the same magnitude. Voronoi and Delaunay tessellations of the square, rectangular, centered rectangular and oblique lattices are provided in **Figure S5.7** and **S5.8** of the **Supporting Information**.

5.4.4. Surface coverage at different substrate positions

We performed several AFM measurements on a cm^2-large substrate coated with an oblique structured monolayer to confirm the homogeneity of the colloidal monolayer. In **Figure 5.4**, six AFM height images and a schematical depiction of a substrate marked with the analyzed positions are shown. The images reveal multi-domain

structures with several defects (mostly voids and local clusters. Nevertheless, the oblique symmetry of the monolayers can be identified in all images independent from the position on the glass substrate.

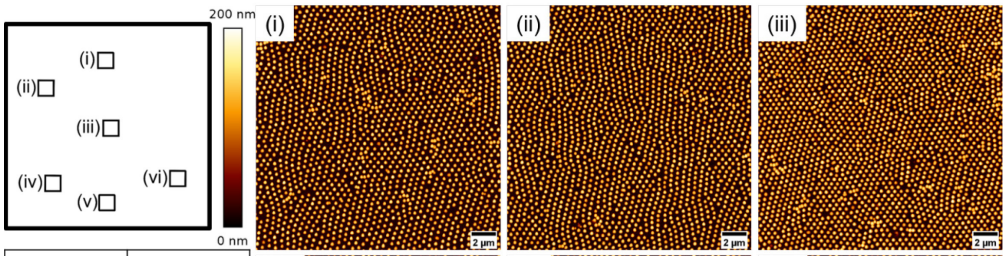

position	N/µm²
i	4.6
ii	4.9
iii	5.4
iv	5.5
v	5.4
vi	5.3

Figure 5.4. AFM height images of an oblique structured monolayer from different locations on a cm^2-scale glass substrate ((i) – (vi)). Top left shows a schematical depiction of the substrate where the analyzed positions are marked by small squares. Bottom left represents a table with the number of particles (*N*) per area in µm^2 for the six positions. Particle numbers were determined from the AFM height images considering areas of 400 µm^2 each.

We determined the particle number (*N*) per area (in µm^2) as a measure for the surface coverage and homogeneity. For this, CS microgels were counted in each AFM image of 400 µm^2 size each. The values for each position are summarized in the table shown in the bottom left of **Figure 5.4**. On average, 5.2 ± 0.3 particles per µm^2 cover the substrate. The deviation of less than 10 % indicates a uniform coating and thus similar interparticle distances. Furthermore, extinction spectra at the respective positions were recorded (see **Figure S5.9**). The average plasmon peak position is 584 ± 1 nm and spectra show very little variation supporting the homogeneity of the monolayer. We now want to look deeper into the plasmonic response of the different monolayers.

5.4.5. Plasmonic properties of the Bravais lattices

The optical properties of the Bravais lattices were investigated by UV-Vis extinction spectroscopy in normal transmission geometry. All five structures show single resonance peaks in the visible wavelength range that are related to the extinction of a dipolar LSPR of the gold NP cores (see **Figure 5.5a**). The peak positions and widths vary slightly within the different samples (see also **Table 5.2**). With peak positions ranging between λ_{LSPR} = 570 nm (rectangular) and λ_{LSPR} = 599 nm (hexagonal) the resonances are close to the value of λ_{LSPR} = 581 nm measured in dilute dispersion. At a closer look we find that the hexagonal lattice shows a redshifted resonance peak with respect to the spectrum from dispersion. This shift to higher wavelength can be attributed to a slightly higher RI environment of the gold NP cores on the glass substrate and with the collapsed PNIPAM shell (dried) in between and on top of the NPs.[55] Interestingly, the other lattices show significantly blueshifted peaks with smaller peak width compared to the hexagonal lattice. We attribute these changes to long-range radiative interactions within the periodic lattices.[55, 236-238] In contrast, without such far-field interactions, given the RI conditions are the same for all lattices, one would expect perfectly overlapping normalized spectra. This is clearly not the case.

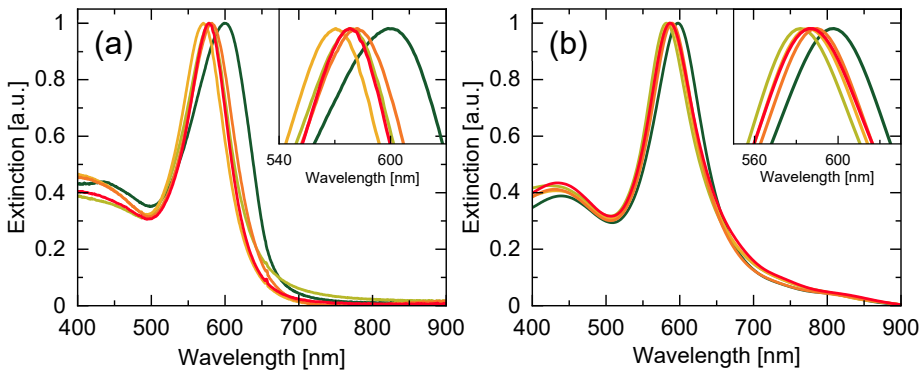

Figure 5.5. Extinction spectra of the different Bravais lattices on glass substrates. Experimental (a) and simulated (b) extinction spectra of the hexagonal (dark green), square (light green), rectangular (yellow), centered rectangular (orange) and oblique lattice (red). Values of $d_{c\text{-}c}$ used in the simulation were adapted from experiment. All spectra are normalized to the extinction at the respective peak maximum. The insets show a magnification of the different peak maxima.

To support our experimental findings, we performed FDTD calculations of all five Bravais lattices. We first start with results from simulations that use the same period of 350 nm independent of the lattice geometry. The simulated extinction spectra are provided in **Figure S5.10**. In contrast to our experimental findings, the LSPR positions are significantly redshifted and show only slight variations between the different lattices (see also **Table S5.2** in the **Supporting Information**). The simulated LSPR peaks lie in the range of 609 to 618 nm. In accordance to the literature, peak positions show only a slight deviation.[239]

Next, we simulated extinction spectra using the experimentally determined spacings (**Figure 5.5b)**. This time the simulated resonance positions are much closer to the experimental ones. Experimental and simulated spectra generally agree well albeit slightly larger deviations in resonance position for the non-hexagonal lattices. Differences in peak position and width (see also **Table 5.2**) can be attributed to defects and limited domain sizes in the experimental samples in contrast to the defect-free, simulated lattices. We want to note that the standard extinction spectroscopy in our experiments probes large, macroscopic areas thus averaging over many domains. The direct comparison of experimental and simulated spectra of our lattices shows that the interparticle distance is the dominant parameter influencing the plasmon resonance position rather than the lattice symmetry.

Table 5.2. Wavelength of the LSPR peak maximum (λ_{LSPR}) for the five Bravais lattices in the experiment and the corresponding simulation. Full width half maximum (FWHM) of the LSPR peak for the five Bravais lattices in the experiment and the corresponding simulation.

	Hexagonal		**Square**		**Rectangular**		**Centered Rectangular**		**Oblique**	
	Exp	**Sim**	**Exp**	**Sim**	**Exp**	**Sim**	**Exp**	**Sim**	**Exp**	**Sim**
λ_{LSPR} [nm]	599	597	578	583	570	586	581	589	578	587
FWHM [nm]	88	66	59	58	62	58	66	57	56	61

5.4.6. Influence of lattice spacing on plasmonic response

In order to further investigate the influence of the interparticle distance on the optical response, we prepared oblique lattices using differently sized CS microgels. While these CS microgels feature similar AuNP core sizes of 98.1 ± 7.9 nm and 94.9 ± 9.8 nm, respectively, their total hydrodynamic radii are 172.9 ± 3.4 nm for the smaller and 230.2 ± 7.3 nm for the larger microgels, respectively. Due to the similar core dimensions, the LSPR positions measured from dilute aqueous dispersion were found to be 584 nm and 588 nm for the smaller and larger microgels, respectively. TEM images, as well as extinction spectra of both batches of CS microgels can be found in the Supporting Information in **Figure S5.11**. **Figure 5.6a and 5.6b** show AFM height images recorded from oblique monolayers prepared from both microgel batches. Both images reveal the oblique structure with the multi-domain character and some defects. The larger microgel size and thus the lower surface coverage for the monolayer prepared from the large CS microgels can be clearly seen in **Figure 5.6b** as compared to 5.**6a**. The edge lengths *a* and *b*, as well as the angle θ were measured from autocorrelation images and the corresponding values are listed in the table in the bottom right of **Figure 5.6**. As expected, the edge lengths increase with the total size of the microgels.

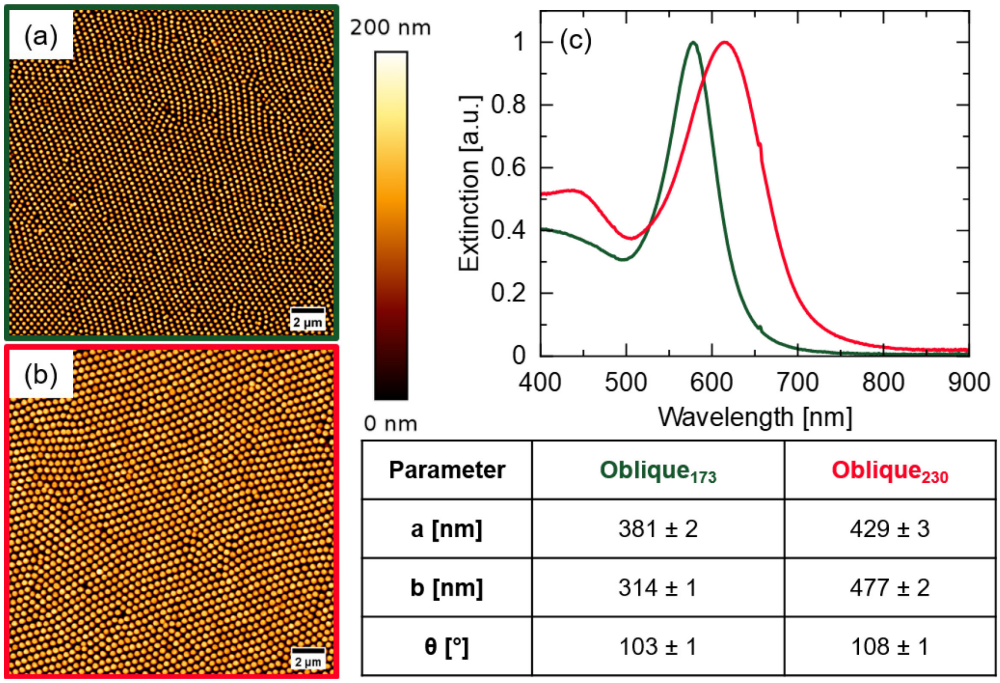

Parameter	Oblique$_{173}$	Oblique$_{230}$
a [nm]	381 ± 2	429 ± 3
b [nm]	314 ± 1	477 ± 2
θ [°]	103 ± 1	108 ± 1

Figure 5.6. Variation of an oblique structured monolayer by using particles with different R_h. AFM height images of an oblique structured monolayer prepared with particles with R_h = 172.9 ± 3.4 nm (a) and R_h = 230.2 ± 7.3 nm (b), respectively. (c) Extinction spectra of the two monolayers. Extinction spectra normalized to the extinction at the respective peak maximum. Bottom right shows a table with values of the edge lengths *a* and *b* respectively and of the angle θ for the two monolayers. Values were determined by measuring four unit cells in the autocorrelation function of the corresponding monolayer. The subscripted numbers indicate the hydrodynamic radius R_h of the CS microgels.

The extinction spectra of both monolayers are depicted in **Figure 5.6c**. Both spectra show single plasmon resonance peaks in the orange to red part of the visible spectrum, i.e. close to 600 nm wavelength. The direct comparison of the spectra reveals a significantly redshifted resonance with higher FWHM for the lattice prepared from the larger CS microgels (red spectrum), i.e. the lattice with larger interparticle spacings. For that sample long-range electromagnetic coupling – if present – is expected to be significantly lower than for the sample with the smaller lattice spacing. Thus, the latter experiments do not only underline the relevance of the interparticle distance on the optical response of the monolayers but also support the versatility of our assembly protocol that can be applied successfully to differently sized microgels. Generally, due to the rather large dimensions of the microgel shells as compared to the much smaller inorganic cores, we believe that the colloidal assembly is determined

by shell-shell interactions with little to zero influence of the cores. Thus, our protocol will not be limited to Au-PNIPAM CS microgels, meaning that also non-close-packed 2D Bravais lattices of other nanoparticles will be accessible.

5.4.7. Influence of the superstrate on plasmonic response

In order to study the influence of the RI environment and the homogeneity of the superstrate, we performed different post modifications to an oblique lattice and followed the changes in the optical response. In all cases glass is the underlying substrate and measurements were performed in standard transmission geometry. **Figure 5.7a** compares normalized extinction spectra where the spectrum in yellow corresponds to the as prepared lattice of the CS microgels. For that sample the AuNP cores are embedded in anisotropic shells of dried PNIPAM with some residual water[234] and the superstrate is air. This inhomogeneous RI environment results in a resonance peak at λ_{LSPR} = 578 nm with a peak width of 56 nm (FWHM). **Figure 5.7b** shows the corresponding SEM image of the sample. By plasma treatment the PNIPAM can be removed as shown by the SEM image in **Figure 5.7c** and schematically illustrated in **Figure 5.7d**. Additional SEM images before and after plasma treatment can be found in the **Supporting Information** (**Figure S5.12** and **S5.13**). In **Figure 5.7a** the spectrum in green shows the optical response of the plasma treated sample with a significantly blueshifted resonance at 524 nm with a peak width of 60 nm (FWHM). The blueshift can be explained by a decrease of the effective RI due to the removal of the PNIPAM shell and air as the superstrate. Upon coating this AuNP lattice with a homogeneous film using spin-coating with a solution of linear PNIPAM homopolymer[55] we observe a strongly redshifted resonance at 617 nm with a rather narrow peak width of 40 nm (FWHM) shown by the spectrum in red in **Figure 5.7a**.

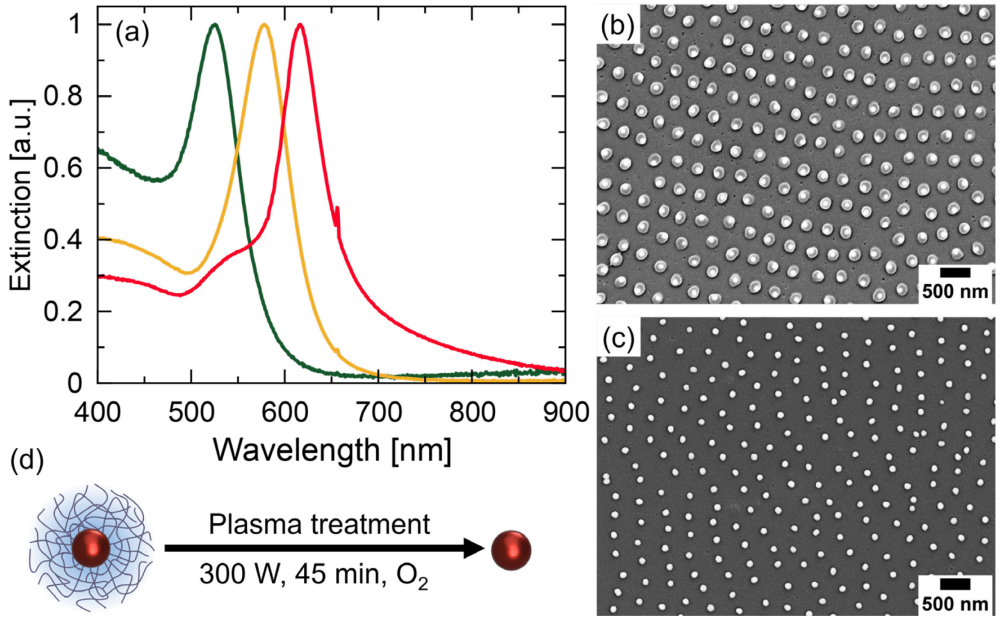

Figure 5.7. Post treatment of an oblique lattice. (a) Normalized extinction spectra of the as prepared lattice of Au-PNIPAM CS microgels (orange), of the resulting AuNP lattice after plasma treatment (green) and of the plasma-treated lattice after coating with a homogenous PNIPAM film as superstrate (red). SEM images of the as prepared lattice of CS microgels (b) and of the resulting AuNP lattice after plasma treatment (c). SEM images were recorded with an angle-selective backscattered electron detector (b) and a secondary electron detector (c). (d) Schematical depiction of the plasma treatment step to remove the PNIPAM shell.

Despite the narrow FWHM this spectrum is also characterized by a small shoulder at lower wavelength at approximately 540 nm that was not observed in the other two spectra. This shoulder is ascribed to a purely plasmonic contribution while the strong resonance at 617 nm is the result of plasmonic-diffractive coupling, i.e. a surface lattice resonance (SLR). This SLR is caused by the collective excitation of individual plasmons driven by an in-plane diffractive mode that is only enabled in a homogeneous RI environment.[55, 110] Due to the limited domain size and defects in the experimental lattice, the Q-factor ($Q = \lambda/\Delta\lambda$) is limited and with a value of 15 rather small compared to lattices prepared by e-beam lithography, for example.[130, 201]

5.5. Conclusion

Through the utilization of a fluid interface-assisted assembly and transfer methodology employing plasmonic core-shell microgels and substrates with varying wettability, we successfully prepared all five 2-dimensional Bravais lattices. Beginning with hexagonal arrangements of microgels at air/water interfaces, we achieved diverse lattice structures by strategically deforming the monolayer during transfer onto solid substrates. Notably, this deformation process was meticulously controlled solely by the substrate's wettability, specifically its contact angle for water and the angle and speed of deposition onto the target substrate.

The resulting lattices exhibited a non-close-packed arrangement of plasmonic gold nanoparticles over extensive areas, showcasing pronounced long-range order with minimal local defects, as confirmed by advanced image analysis techniques. Plasmonic properties were comprehensively analyzed using extinction spectroscopy, revealing spectra that aligned well with theoretically simulated ones. Depending on the lattice spacings, resonance shifts were predominantly attributed to alterations in the refractive index environment or a combination of refractive index and long-range resonance coupling effects.

Upon removal of the microgel shell via plasma treatment, a significant blueshift of the plasmon resonance was observed. Conversely, coating the non-close-packed array of gold nanoparticles with a thin but uniform polymer film resulted in a narrow and considerably redshifted resonance, identified as a surface lattice resonance arising from plasmonic-diffractive coupling in periodic plasmonic arrays with wavelength-scale interparticle distances.

This study builds upon our prior research focused on assembly of rigid colloids, demonstrating the versatility of fluid interface-assisted assembly and transfer for soft colloid-like objects, specifically microgels. Furthermore, the utilization of core-shell microgels with plasmonic cores facilitated the formation of arrays comprising non-close-packed plasmonic nanoparticles. In light of recent endeavors to achieve complex tessellations from the (self-)assembly of soft colloids,[62] our work not only expands the repertoire of reported structures but also underscores the potential for

fabricating intricate, functional nanoparticle assemblies using core-shell building blocks.

Author Information

Corresponding Author

*Matthias Karg

E-mail: karg@hhu.de

Acknowledgments

The authors would like to acknowledge the Center for Advanced Imaging (CAi) at Heinrich-Heine University Düsseldorf for providing access to the SEM microscope ZEISS Supra 55VP and especially Steffen Köhler for performing the imaging. We would like to thank Jonathan Garthe for the assistance with the dip-coater and Philipp Hammers for providing the larger CS microgels.

Declarations

Ethical Approval Not applicable.

Funding The authors acknowledge the German Research Foundation (DFG) and the state of NRW for funding the cryo-TEM (INST 208/749-1 FUGG). M.K. acknowledges the DFG for funding under grant KA3880/6-1. D.F. acknowledges the Luxembourg National Research Fund (FNR), Project Reference 15688439. M.S.D. was supported by the U.S. Department of Energy (DOE), under award DE-SC0022229. This research was supported in part by grant NSF PHY-1748958 to the Kavli Institute for Theoretical Physics (KITP).

Availability of data and materials Data are available from the authors upon reasonable request. The Mathematica code used for image analysis (generation of Voronoi and Delaunay tessellations) is available from Zenodo and GitHub (DOI: 10.5281/zenodo.11974759).

5.6. Supporting Information

Determination of core size

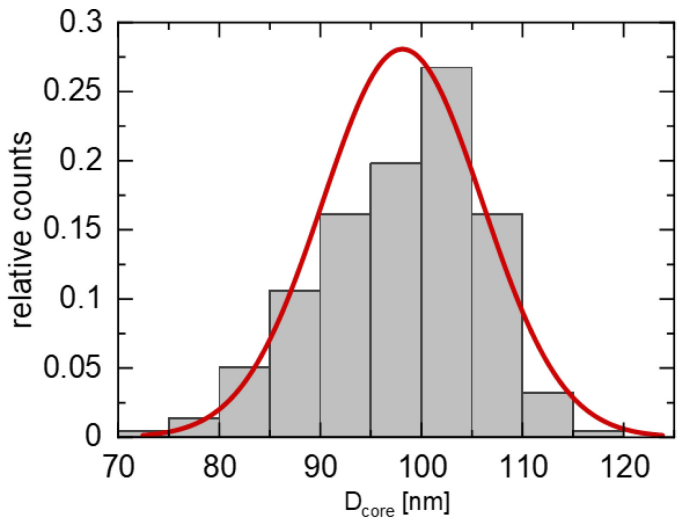

Figure S5.1. Size distribution of Au cores from the overgrown Au-PNIPAM microgels, as determined by TEM. The data was fitted with a Gaussian distribution function to determine the average diameter and standard variation (red line)

The size distribution of the overgrown Au cores is shown in **Figure S5.1**. The size was measured from several individual TEM images using the software ImageJ.[208] The size distribution was fitted with a Gaussian distribution function (red line) to determine the average core diameter of 98.1 ± 7.9 nm.

AFM height images of the five Bravais lattices

Figures S5.2 – S5.6 show low magnification AFM height (20 x 20 μm^2) recorded from the five different Bravais lattices with resolutions of 1024 x 1024 $pixel^2$. The height scale is the same for all five images and corresponds to the one shown in the main manuscript in **Figure 5.3**.

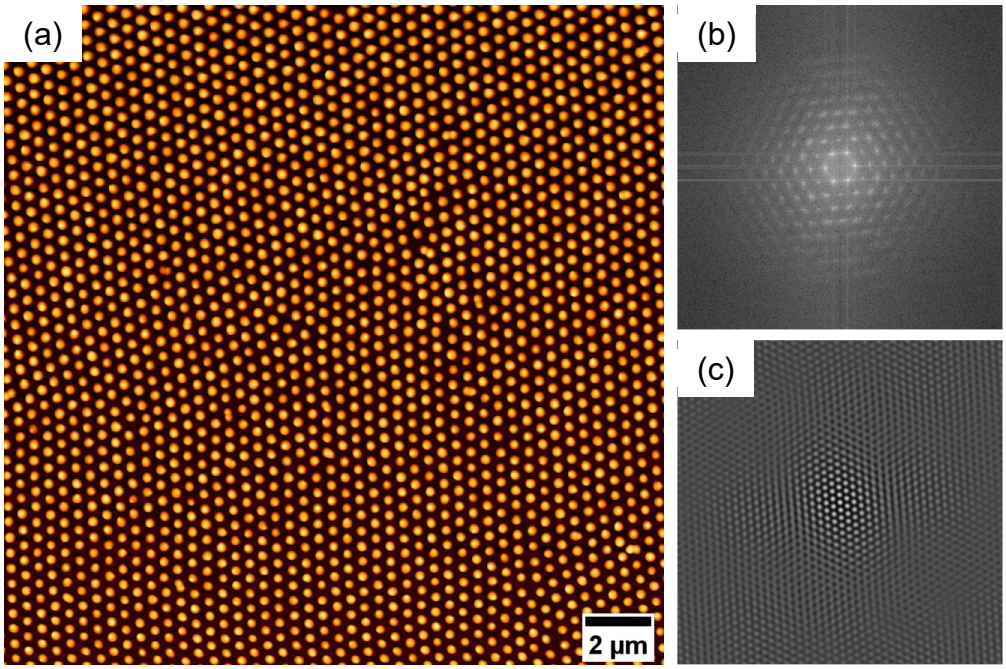

Figure S5.2. AFM height image (a), the corresponding FFT (b) and autocorrelation image (c) of a hexagonally ordered monolayer

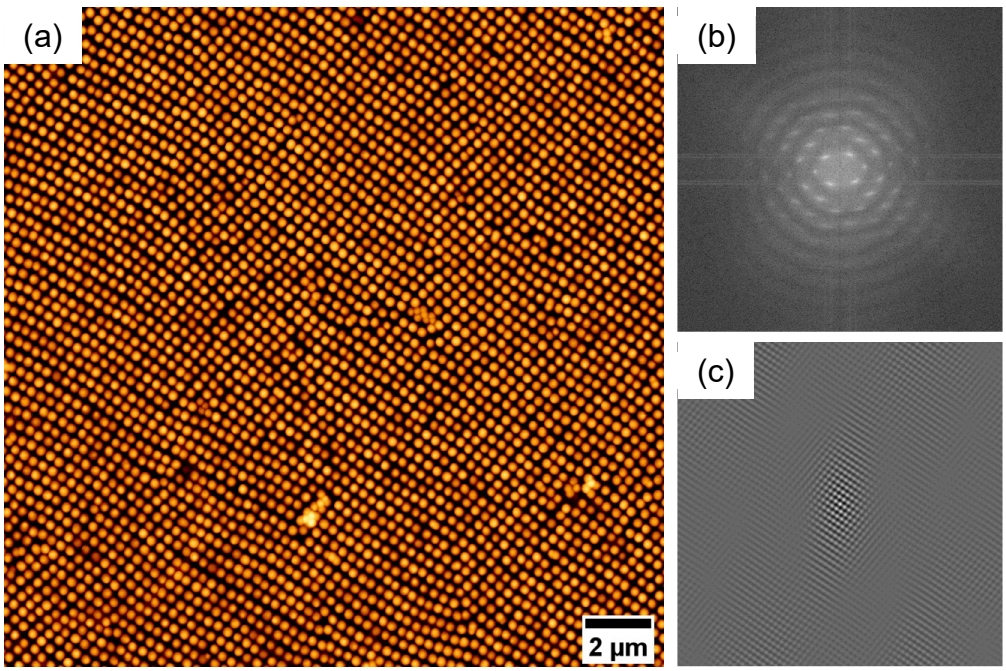

Figure S5.3. AFM height image (a), the corresponding FFT (b) and autocorrelation image (c) of a square ordered monolayer

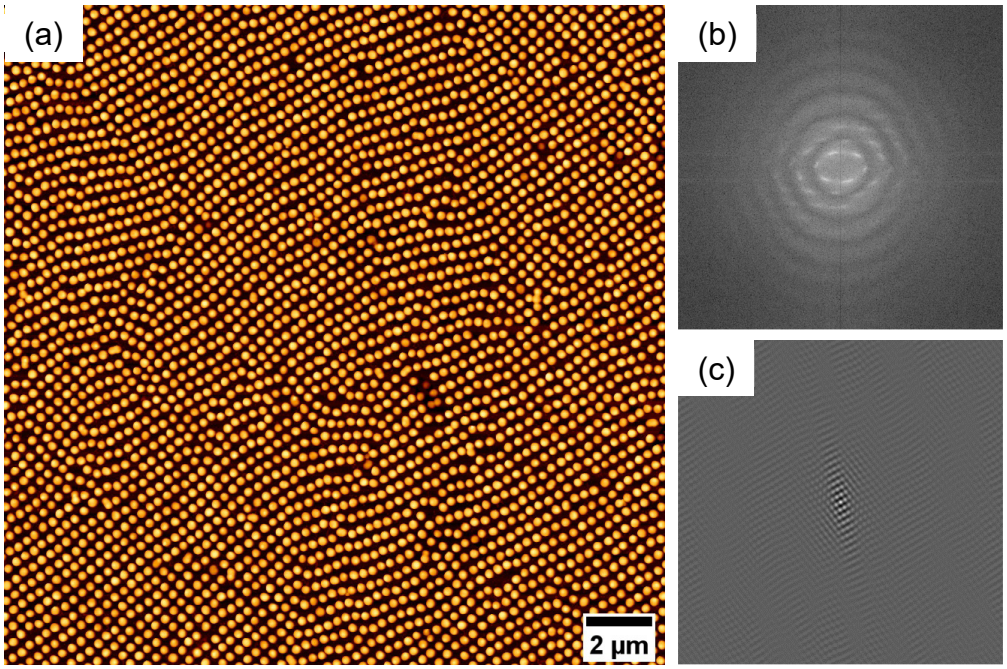

Figure S5.4. AFM height image (a), the corresponding FFT (b) and autocorrelation image (c) of a rectangular ordered monolayer

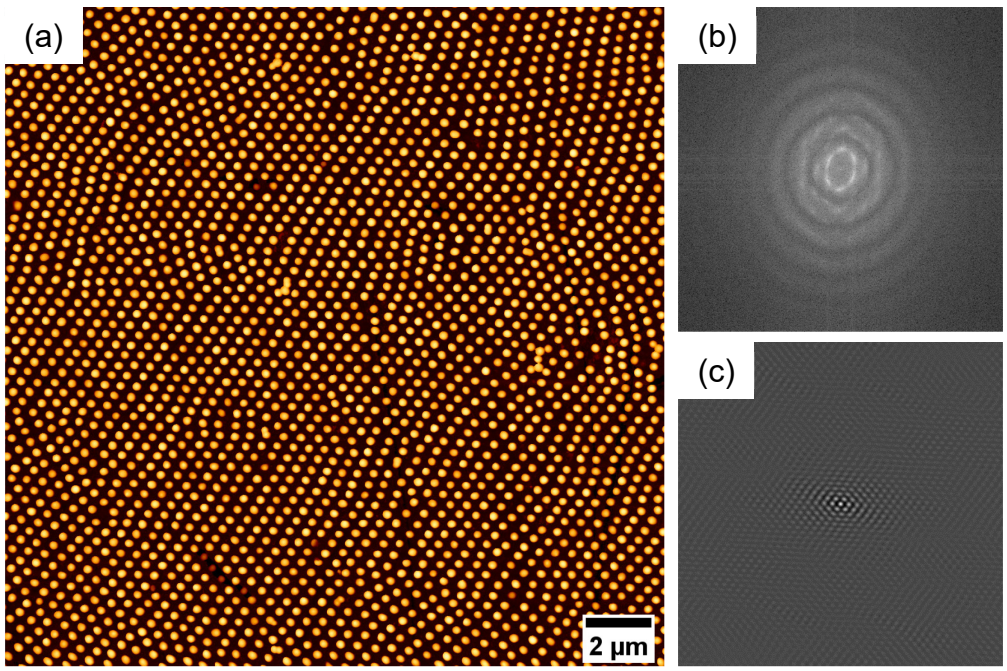

Figure S5.5. AFM height image (a), the corresponding FFT (b) and autocorrelation image (c) of a centered rectangular ordered monolayer

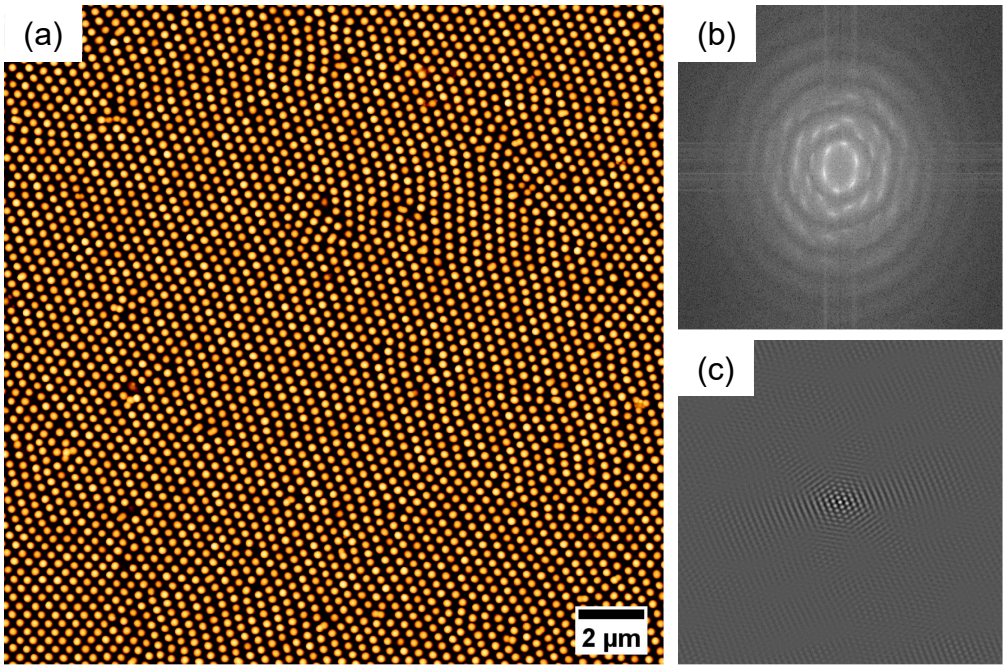

Figure S5.6. AFM height image (a), the corresponding FFT (b) and autocorrelation image (c) of an oblique ordered monolayer

All five Bravais lattices show a high degree of order, as only few defects and few different domains are observed. This is also confirmed by the FFTs and the autocorrelation images. Multiple orders can be detected in the FFTs. As expected, the FFT becomes anisotropic and stretched into one dimension for structures other than the hexagonal one. The lattice geometries can clearly be identified from the autocorrelation images.

Voronoi and Delaunay tessellations

The structure of the non-hexagonal Bravais lattices was further investigated by computing Voronoi and Delaunay tessellations using point maps created from AFM height images. Under the protocol in which the floated monolayer is transferred to the substrate, it is reasonable to expect that the non-hexagonal Bravais lattices were created by a uniaxial deformation of the hexagonal lattice, which is a close-packed configuration. Therefore, it is expected that these lattices should have interparticle spacing that differs from the hexagonal lattice. **Figure S5.7** reveals that there are

variations in particle spacing, often involving clusters of particles forming relatively dense regions, with others forming relatively dilute regions. Given that particle softness and density fluctuations are related in systems under thermodynamic equilibrium via the bulk modulus, it is reasonable to expect that the observed density fluctuations from shear alignment may be similarly related. Furthermore, the fact that each lattice maintains long-range order despite these fluctuations suggests that disruptions to the lattice are highly localized, and that lattice spacing and orientation resumes after a "healing length" of a few particles. This is supported by an analysis of particle-particle contact, as revealed by the Delaunay tessellation in **Figure S5.8**, for which only "compressive" neighbor bonds with edge length $r_{\mathrm{edge}} \leq 2R_{\mathrm{h}}$ are drawn. The textures provided by these contact chains reveal (i) some degree of compression transverse to the apparent uniaxial stretching direction, (ii) some localized variations order (i.e. lattice defects), yet (iii) seemingly persistent long-range order without indication of grain boundaries. Such enhanced order may be attributed to the mechanism of shear-aligning used to select for each Bravais lattice: rather than requiring each crystal to undergo nucleation and growth, which leads to polycrystals, consistent mechanical shear across the sample introduces a long-range correlations *a priori*. However, while there are strong long-range correlations on position, there is, nevertheless, some degree of local variation of particle contacts to the extent that contact chains have short lengths. While these short, non-percolating contact chains indicate a lack of overall mechanical rigidity in the monolayers, this also means that the response to variations in particle density or defects is similarly localized, decreasing potential disruptions to the overall order.

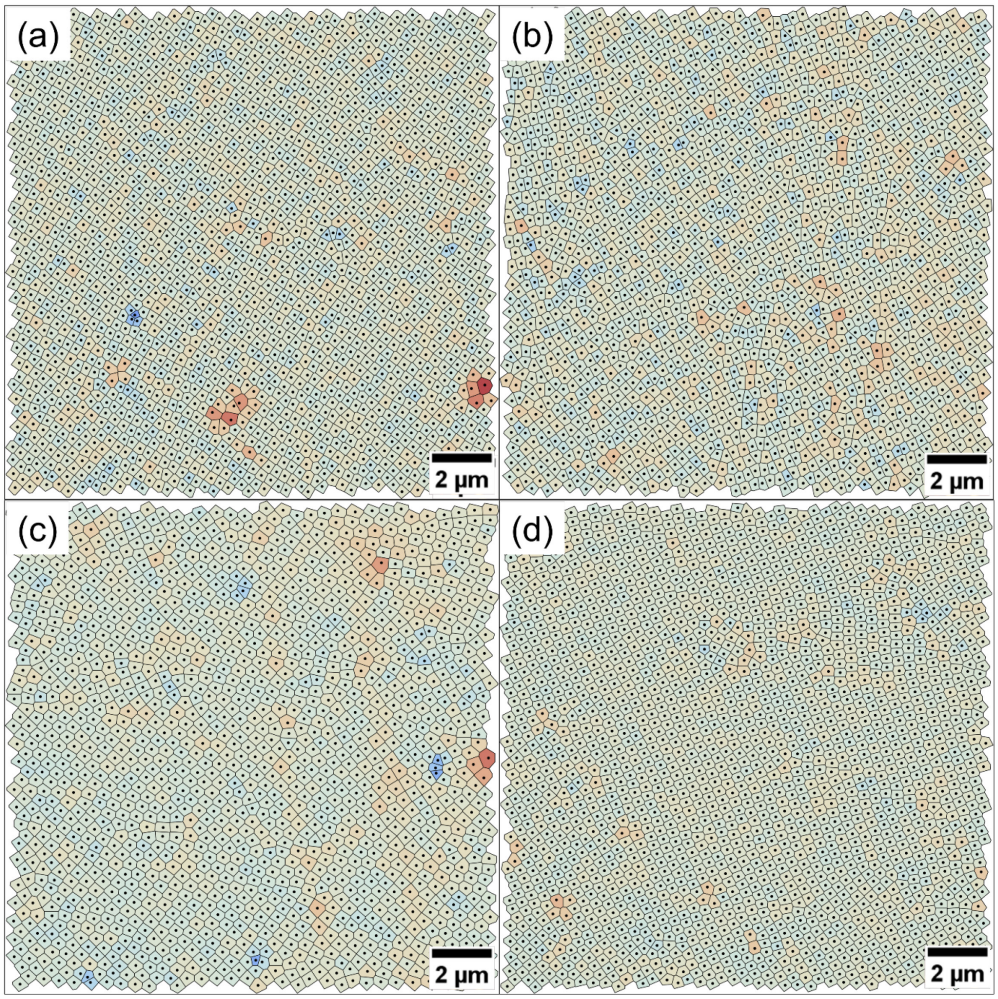

Figure S5.7. Voronoi tessellations of a region of CS microgels ordered into a square (a), rectangular (b), centered rectangular (c) and oblique (d) lattice, respectively. The tessellations were generated from the point maps of the respective AFM images. The color of each cell represents the deviation of the cell area from the mean area per particle (cell with larger area are red; cells with smaller area are blue)

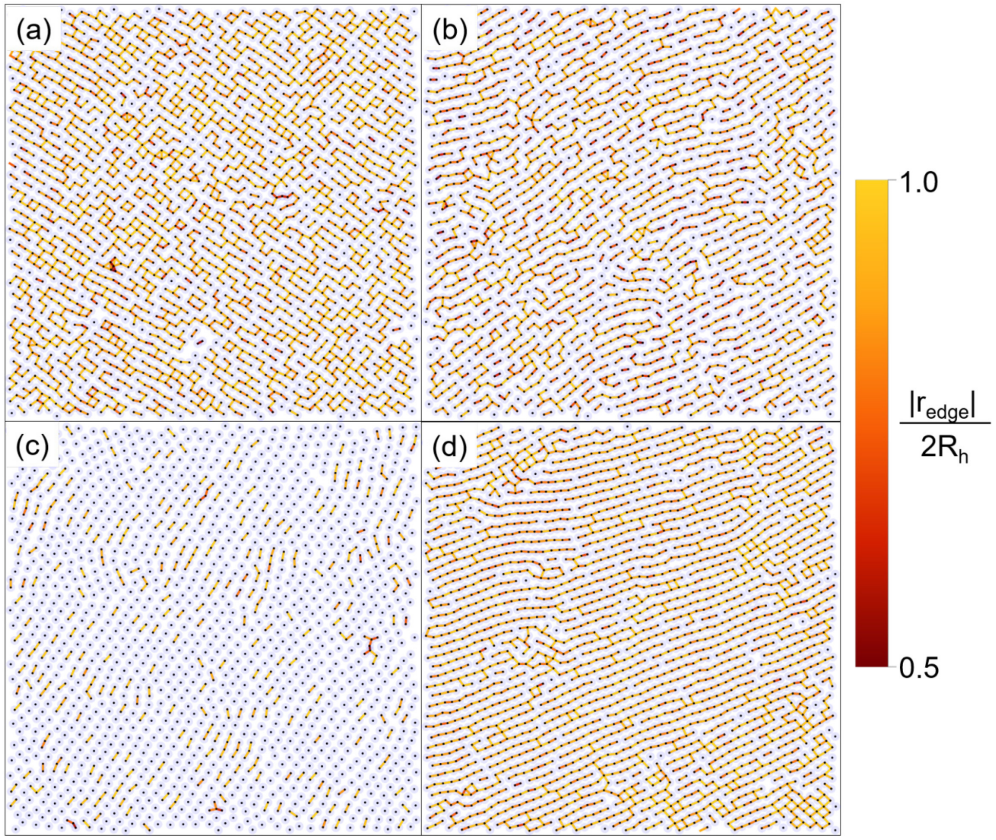

Figure S5.8. Depiction of contacts for square (a), rectangular (b), centered rectangular (c) and oblique (d) lattices. Here, neighboring microgels are assumed to be in contact when the distance between adjacent particles, given as the length of an edge $|r_{edge}|$ separating neighbors on a Delaunay graph, is less than $2R_h$. As indicated by the color bar, darker lines correspond to microgels that are closer together

Homogeneity of oblique structured Bravais lattice on a cm^2-large area

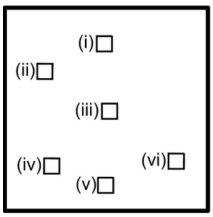

position	λ_{LSPR}
i	586 nm
ii	584 nm
iii	583 nm
iv	583 nm
v	582 nm
vi	583 nm

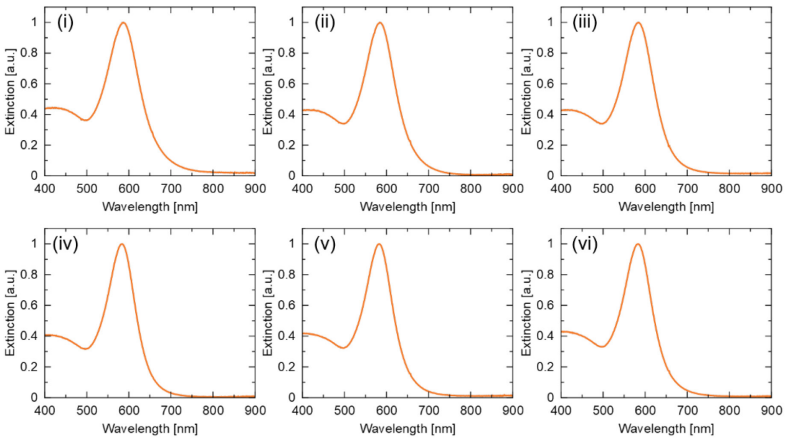

Figure S5.9. Normalized extinction spectra of an oblique structured monolayer measured at different locations on a glass substrate ((i) – (vi)). Top left shows a schematic depiction of the substrate where the analyzed positions are marked by small squares. Bottom left represents a table with wavelengths of the LSPR maximum (λ_{LSPR})

Extinction spectra from six different positions on a glass substrate coated with an oblique structured monolayer are shown in **Figure S5.9**. The peaks look similar with only small variation in the position of the maximum (**Figure S5.9 bottom left**). The values of the extinction at the LSPR maximum (λ_{LSPR}) and at a wavelength of 400 nm are listed in **Table S5.1**. On average, extinctions of 0.239 ± 0.022 and of 0.097 ± 0.009 are measured at λ_{LSPR} and at 400 nm, respectively. The similar peak positions and the similar values of the extinction confirm that the substrate is homogenously coated with particles having a similar interparticle distance. Different interparticle distances would show a large shift of the peak position and variations in the extinction.

Table S5.1. Wavelengths of the LSPR maximum (λ_{LSPR}) and the values of the extinction at the LSPR maximum (λ_{LSPR}) and at a wavelength of 400 nm for the different locations on the glass substrate

	λ_{LSPR} [nm]	**Extinction at λ_{LSPR}**	**Extinction at 400 nm**
i	586	0.227	0.102
ii	584	0.208	0.084
iii	583	0.225	0.090
iv	583	0.257	0.097
v	582	0.258	0.101
vi	583	0.258	0.107

Calculated extinction spectra of Bravais lattices with a period of 350 nm

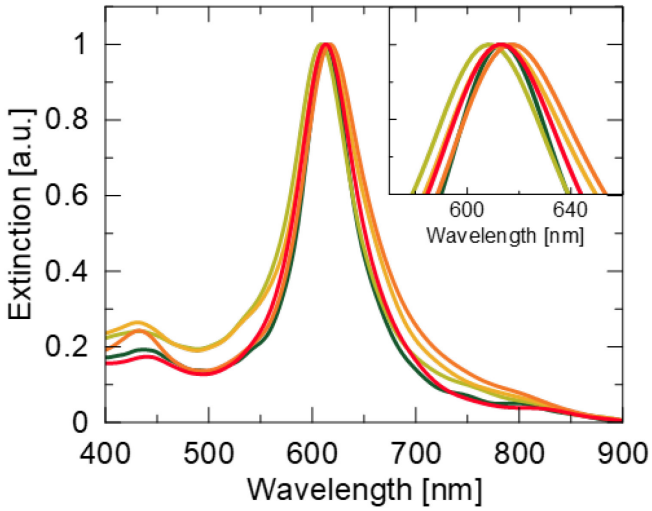

Figure S5.10. Calculated extinction spectra of five Bravais lattices with the same period of 350 nm. The five Bravais lattices: hexagonal (dark green), square (light green), rectangular (yellow), centered rectangular (orange) and oblique (red). All spectra are normalized to the extinction at the respective peak maximum. The inset shows a magnification of the plasmon peak maximum of the five spectra

To compare the optical response of the Bravais lattices, we choose to calculate extinction spectra of the lattices with the same period of 350 nm. Spectra normalized to the extinction at the respective peak maximum are shown in **Figure S5.10**. The inset shows a magnification of the peak maxima. Peak positions and FWHM are listed in **Table S5.2**. The positions are rather independent of the lattice geometry, as the maximum shifts only a few nanometers.

Table S5.2. Wavelengths of the LSPR maximum (λ_{LSPR}) and the corresponding full width half maximum (FWHM) for the five Bravais lattices simulated with periods of 350 nm

	Hexagonal	Square	Rectangular	Centered Rectangular	Oblique
λ_{LSPR} [nm]	614	609	614	618	614
FWHM	43	51	56	60	56

Synthesis of CS microgels with a hydrodynamic Radius R_h of 230 nm

Large CS microgels with 15 mol% crosslinker were synthesized via a seeded precipitation polymerization. In order to get large microgels (R_h > 200 nm), we performed the synthesis over three days and increased the temperature from 50 °C to 60 °C within intervals of 24 hours. The PNIPAM shell is crosslinked by the crosslinker *N*,*N*′-methylenebisacrylamide (BIS). In brief, NIPAM (0.700 g, 6.19 mmol) and BIS (0.143 g, 0.93 mmol) were dissolved in 150 mL of Milli-Q water and then degassed with argon at 50 °C. After 1 h, 1.62 mL of the functionalized AuNP seeds ($c(Au^0)$ = 8.63 mM) were added and degassing was continued for 30 min. The reaction was initiated by adding 2 mg of PPS dissolved in 1 mL of water. The reaction mixture was stirred at 50 °C for 24 hours, then the temperature was increased to 55 °C for the next 22 hours. As last step, the temperature was increased to 60 °C for further 4 hours. After cooling down to room temperature, the core-shell microgels were purified by three consecutive centrifugation steps, each at 9400 rcf for 1 h. After the last step, the residue was redispersed in 15 mL of Milli-Q water. The Au-PNIPAM microgels were then freeze-dried for three days.

Overgrowth of the cores of Au-PNIPAM$_{230}$

The overgrowth protocol of the Au cores was adapted from the protocol of Honold et al.[51] In summary, 286 µL of an aqueous solution of CS particles (2 wt%) was mixed with 200 µL of an aqueous CTAC solution (0.2 M). 200 µL of this dispersion were added while stirring to 8 mL of an aqueous CTAC solution (2.4 mM) in an Erlenmeyer

flask. Then 388 µL freshly prepared ascorbic acid solution (49 mM) were added in one shot. Next, a feed solution was prepared by mixing 184 µL of an aqueous CTAC solution (0.756 M), 112 µL of an aqueous $HAuCl_4$ solution (0.130 M) and 29 mL Milli-Q water. The feed solution was added dropwise to the dispersion in the Erlenmeyer flask under heavy stirring. The reaction was allowed to proceed for 20 minutes. The microgels were then centrifuged three times at 5400 rcf for 30 min. The residue was dispersed in 150 µL Ethanol.

Au-PNIPAM microgels with different hydrodynamic radii R_h

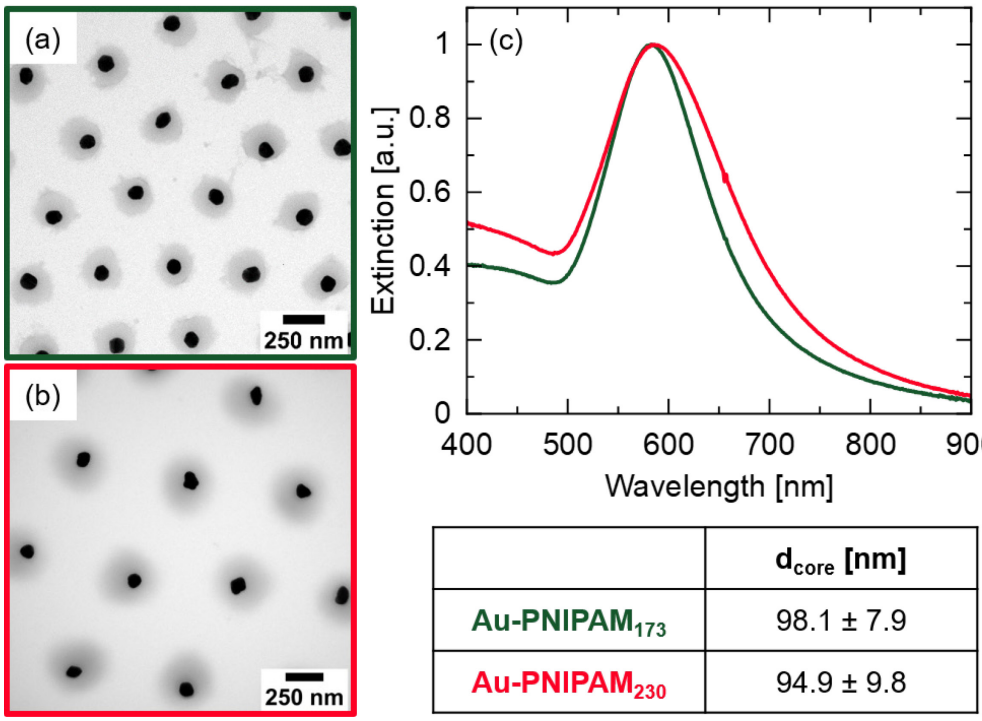

	d_{core} [nm]
Au-PNIPAM$_{173}$	98.1 ± 7.9
Au-PNIPAM$_{230}$	94.9 ± 9.8

Figure S5.11. Comparison of differently sized Au-PNIPAM CS microgels. TEM images of Au-PNIPAM microgels with a hydrodynamic radius R_h of 172.9 ± 3.4 nm (a) and of 230.2 ± 7.3 nm (b), respectively. (c) Normalized extinction spectra of CS microgels measured from dilute aqueous dispersion (bulk). Bottom right shows a table with the diameter of the cores d_{core} for the respective microgels. The numbers in subscript indicate the hydrodynamic radius R_h of the CS microgels

Two batches of overgrown CS microgels with different R_h are shown in the TEM images in **Figure S5.11a and S5.11b**. The microgels displayed in (a) and (b) exhibit a R_h of 172.9 ± 3.4 nm and 230.2 ± 7.3 nm, respectively. The core sizes are listed in the table in **Figure S5.11 bottom right**. The subscripted numbers indicate the R_h of the microgels. The cores can be clearly seen in both TEM images as black dots in the grey PNIPAM shell. The differences in contrast for the core and the shell can be attributed to the different electron densities. The cores of Au-PNIPAM$_{170}$ appear more spherical than the ones of Au-PNIPAM$_{240}$. However, the sizes of 98.1 ± 7.9 nm and 94.9 ± 9.8 nm, respectively, indicate that the cores of both batches are similar. This is also confirmed by the UV-Vis spectra shown in **Figure S5.11c**. For Au-PNIPAM$_{170}$ and Au-PNIPAM$_{240}$, the peak maximum is located at 584 nm with a FWHM of 102 nm and at 588 nm with a FWHM of 157 nm, respectively. The peak of Au-PNIPAM$_{240}$ shows a larger FHWM, which can be attributed to a slightly larger polydispersity of the cores.

SEM images of oblique structured monolayer

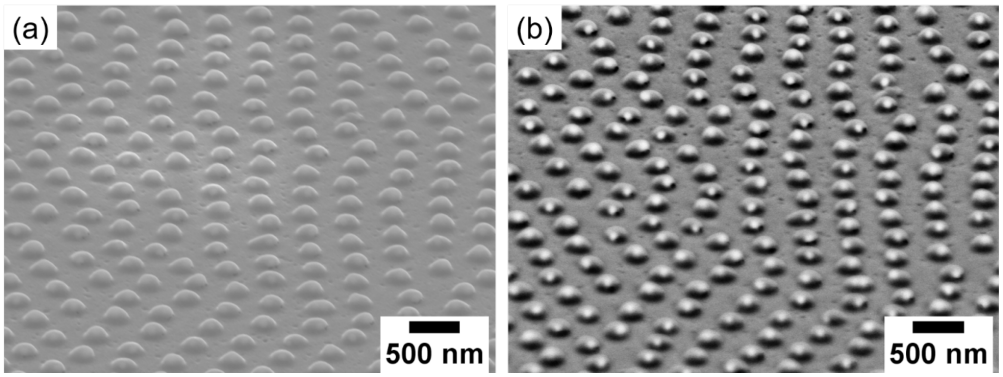

Figure S5.12. SEM images of CS microgels ordered into an oblique structure recorded with secondary electron detector (a) and backscattering detector (b). The sample was tilted at an angle of 60.3 °

SEM images of the oblique monolayer from CS microgels were recorded with a secondary electron detector (**Figure S5.12a**) and an angle-selective backscattering detector (**Figure S5.12b**). The backscattering detector was used to enhance the

material contrast and to visualize the AuNP cores in the PNIPAM shell. As the sample holder was tilted at an angle of 60.3 °, the 'fried-egg' like structure of the microgels on the glass substrate can be clearly identified in both images.

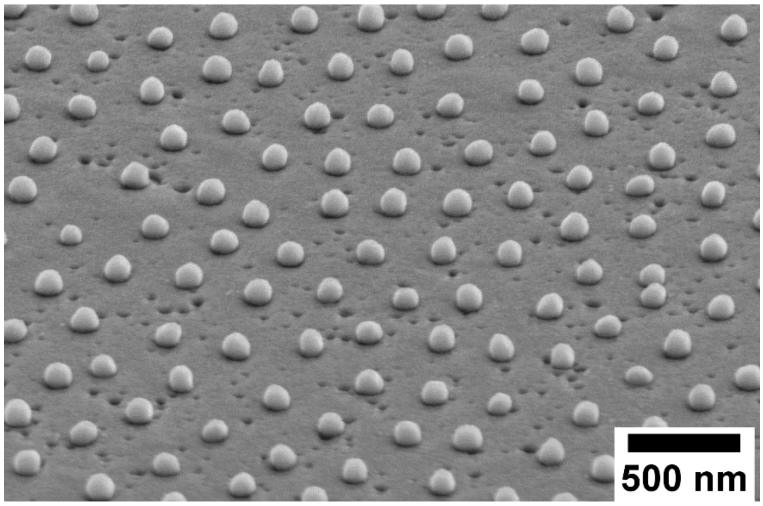

Figure S5.13. SEM image of the oblique lattice of the CS microgels upon removal of the PNIPAM shell by plasma treatment. A secondary electron detector was used and the samples was tilted at an angle of 65.4 °

To confirm the success of the plasma treatment, SEM images of the sample after the treatment tilted at an angle of 65.4 ° are recorded. In **Figure S5.13**, the bare Au cores are clearly visible without any polymer shell.

Extinction of glass substrate with a coating of linear PNIPAM homopolymer

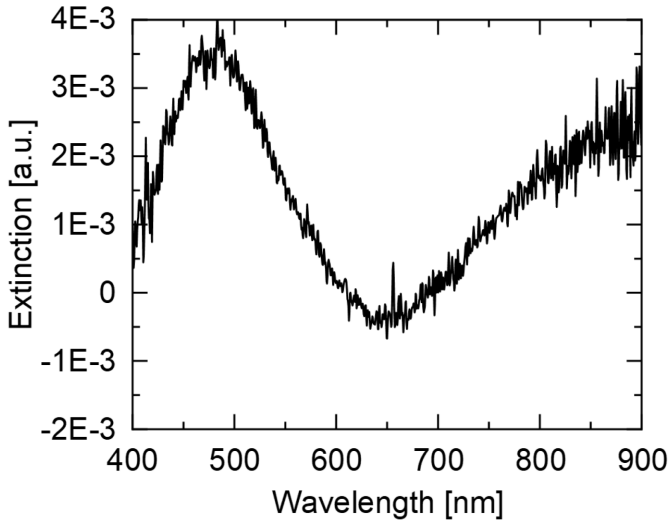

Figure S5.14. Extinction spectra of a glass substrate coated with linear PNIPAM. A clean glass substrate was used as reference

We measured the extinction of a linear PNIPAM coated glass substrate with a clean glass substrate as reference. The extinction spectrum is shown in **Figure S5.14**. The extinction of the PNIPAM varies in a small range of – 0.0005 to 0.004. Thus, the extinction of linear PNIPAM does not affect the extinction spectrum of the monolayers and a clean glass substrate can be used as reference for all UV-Vis extinction measurements.

6. Following plasmon resonance coupling in soft, confined colloidal films during continuous compression

Manuscript in preparation for submission

Déborah Feller,[a] Jiakai Wang,[b] Julian Kippenberger,[a] Christian Washeim,[a] Jan Meissner,[c] Jan Meisner,[c] Paul Mulvaney[b] and Matthias Karg[a,d,*]

[a]Institut für Physikalische Chemie I: Kolloide und Nanooptik, Heinrich-Heine-Universität Düsseldorf, Universitätsstr. 1, 40225 Düsseldorf, Germany

[b]ARC Centre of Excellence in Exciton Science, School of Chemistry, The University of Melbourne, Parkville VIC 3010, Australia

[c]Institut für Physikalische Chemie, Heinrich-Heine-Universität Düsseldorf, Universitätsstr. 1, 40225 Düsseldorf, Germany

[d]Physical Chemistry of Functional Polymers, Institute of Chemistry, Martin Luther University Halle-Wittenberg, 06120 Halle (Saale), Germany

6.1. Abstract

Plasmon resonance coupling is a strongly distance-dependent phenomenon that also critically depends on the spatial arrangement of its plasmonic constituents, e.g., plasmonic nanoparticles in periodic or random assemblies. Here, we study electromagnetic coupling in ordered monolayers of gold nanoparticles within a range of interparticle distances of twice up to almost six times the particle diameter. We do this by continuously monitoring the optical response of a soft colloidal film that is confined at the air/water interface and compressed through the barriers of a Langmuir trough. The colloidal building blocks contain monodisperse, spherical gold nanoparticles that are homogeneously encapsulated in soft, deformable microgel shells. The soft shell enables continuous tuning of the interparticle distance simply defined by the accessible interfacial area in the trough. We directly compare the optical response measured *in situ* at the fluid interface to the response of monolayers that were transferred to glass substrates followed by subsequent drying. Supported by COMSOL simulations we revealed plasmonic-diffractive coupling for large spacings at the fluid interface that weakens as the monolayer is compressed leading to a reduction in the interparticle distance.

6.2. Introduction

Nanocrystals (NCs) can be synthesized with excellent control over size, shape and their distribution – parameters that define the properties of these nanoscale building blocks, e.g., optical, electrical and magnetic.[240-244] When NCs are assembled into ordered 2- or 3-dimensional superstructures new nanomaterials with unique properties can be tailored.[80, 245-247] Crucial for structural control are the surface properties that ultimately define the colloidal interactions.

A common example are steric stabilizers such as macromolecular ligands[248-253] or polymeric networks that encapsulate the NCs.[49, 52, 230, 254] Depending on the molecular weight of such surface decorations different regimes of interparticle spacing can be entered: Macromolecular ligands typically cover interparticle distances in the range of a few to a few tenth of nanometers while cross-linked polymer shells as for example

hydrogel shells, cover spacings from tenths to many hundreds of nanometers depending on the shell thickness.[255]

Such polymeric decorations not only render NCs colloidally stable but also with long-range soft interactions.[27, 29, 256] In contrast to rigid bodies with a steep interaction potential, soft colloidal building blocks can be assembled into periodic superstructures with a range of periodicities that are governed by the packing fraction.[31, 46, 64, 140] For example, when confined at a fluid interface, i.e., air/water or oil/water interfaces, reduction of the available interfacial area leads to a compression of the thin colloidal film with a continuous decrease in interparticle spacing.[72, 73, 257] When using core-shell (CS) building blocks with NC cores and rather thick, hydrogel shells, i.e., CS microgels, lattices with the same lattice structure but varying lattice constant can be achieved by using one type of building blocks.[44, 45, 51, 54, 55, 258] This is particularly interesting for studying distance-dependent collective effects. One important example for this, is the electromagnetic coupling between plasmonic NCs. At small interparticle distances localized surface plasmon resonances (LSPR) couple via the electric near field.[59, 247, 259, 260] Approaching wavelength-scale interparticle distances that are much larger than the individual NC diameter, coupling vanishes unless the NCs are arranged in periodic lattices. In the latter case diffractive modes can couple with the plasmonic modes leading to surface lattice resonances (SLRs).[55, 110, 123, 201] Understanding, tuning and optimizing such coupling effects has been an intense field of research in the last decade. However, most of the studies so far rely on investigation of superstructures on solid supports and the 1-to-1 preparation and investigation of samples. A few studies exist were flexible substrates were used to post-modify the lattice spacing and/or lattice geometry via substrate deformation.[261-263] Approaches that maintain the lattice structure while allowing for dynamic control over lattice period with incremental stepsize are non-existing so far.

In this work, we present a method to analyze the optical response of assembled Au-PNIPAM microgels at the air/water interface *in situ* in a Langmuir trough upon uniaxial compression. We are able to monitor in real-time the optical behavior and to record spectra at one-second intervals throughout the entire compression isotherm, resulting in more than 1800 spectra for one compression cycle of the colloidal film. Our *in situ* spectroscopic measurements allow us to relate resonance position, strength and width to changes in interparticle distance from almost six down to two times the interparticle distance. By this method, the optical response of the colloidal

film is recorded for steps of interparticle distances smaller than 0.2 nm. We observed a continuous blueshift and broadening of the resonance peak with decreasing interparticle distance as controlled by the available interfacial area in the Langmuir trough. Our findings are directly compared to spectral results from colloidal films transferred to solid (glass) substrates followed by drying that induced changes in microstructure due to capillary interactions. COMSOL simulations were performed to underline that we deal with plasmonic-diffractive coupling at large interparticle spacings that transition to a purely plasmonic mode as the interparticle distances are reduced. With our findings we do not only deepen the understanding of the distance-dependence of long-range electromagnetic coupling but also support the most recent understanding of the phase behavior of soft colloidal monolayers confined at fluid interfaces.

6.3. Experimental section

6.3.1. Materials

Gold(III) chloride trihydrate ($HAuCl_4 \cdot 3H_2O$; Sigma-Aldrich, ≥ 99.999%), sodium citrate dihydrate (Sigma-Aldrich, ≥ 99%), sodium dodecyl sulfate (SDS; Sigma-Aldrich, p.a.), butenylamine hydrochloride (BA; Sigma-Aldrich, 97%), *N*,*N*′-methylenebisacrylamide (BIS; Sigma-Aldrich, ≥ 99%), potassium peroxodisulfate (PPS; Sigma-Aldrich, ≥ 99%), cetyltrimethylammonium chloride (CTAC; Sigma-Aldrich, 25 wt% in water), ascorbic acid (Roth, p.a.), 1H,1H,2H,2H-Perfluorooctyltriethoxysilane (FOCTS; J&K Scientific, 97%), ethanol (Honeywell, p. a.), ammonia (PanReac Applichem, 30% in water), hydrogen peroxide (Fisher Scientific, > 30% in water), cyclohexane (Fisher Scientific, ≥ 99.8%), and Hellmanex III (Hellma GmbH) were used as received.

N-isopropylacrylamide (NIPAM; TCI, > 98.0%) was recrystallized from cyclohexane.

Milli-Q water (Millipore, resistivity > 18 MΩcm) was used for all synthesis and Langmuir trough experiments.

6.3.2. Synthesis

Synthesis of core-shell microgels

Monodisperse, nanocrystalline gold nanoparticles (AuNPs) of near spherical shape were synthesized using the established Turkevich method.[207] By this, we obtained AuNPs with a diameter of 14.1 ± 1.1 nm determined by TEM analysis of at least 150 particles. These NPs were then used as seeds in a seeded precipitation polymerization to synthesize Au-PNIPAM core-shell (CS) microgels following the protocol reported by Rauh *et al*.[76] In short, the surface of the AuNP seeds was functionalized with BA prior to the encapsulation. NIPAM as monomer and BIS as chemical crosslinker (16.7 mol % (nominal) with respect to the amount of NIPAM) were used to grow the microgel shell. PPS was used as radical initiator. Upon successful encapsulation and purification, the CS microgels were used to overgrow the AuNP cores to enhance the plasmonic properties. The overgrowth of the cores was done following a protocol reported previously by us (Ponomareva *et al*.[55]). After multiple steps of overgrowth, the AuNP cores reached a size of 96.3 ± 8.2 nm in diameter. The details of the synthesis can be found in the **Supporting Information**.

The final structure of the microgels with the hydrodynamic diameter D_h is schematically shown in **Figure 6.1 a**. A TEM image of the final CS microgels is shown in **Figure 6.1 d**.

Preparation of glass substrates for monolayer transfer

Standard microscopy glass slides were cleaned by the RCA-1 method.[264] This involved mixing five parts of water with one part of ammonia solution (30 %) and heating the mixture to 80 °C under stirring. Once this temperature was reached, one part of H_2O_2 solution (30 %) was added. The glass slides were then immersed in the solution for 15 minutes and the solution temperature was maintained between 75 and 85 °C. Afterwards, the glass slides were removed and thoroughly rinsed with water. Before drying with a stream of compressed N_2, the cleaned substrates were left in water for an additional 5 minutes.

The hydrophobization of the glass slides was carried out using chemical vapor deposition. The slides were placed in a desiccator with 120 µL FOCTS and the pressure was reduced to 150 mbar. The functionalization was allowed to proceed overnight. Following this, the glass slides were removed and treated at 60 °C in an oven for 2 h. Afterwards, the slides were sonicated for 10 min in ethanol and then dried with N_2.

The slides were cut in half along the length and horizontal lines were scratched on the back of the slide for further use. From the bottom of the slide, five lines with a distance of 1 cm and a last line with a distance of 0.5 cm were marked.

6.3.3. Methods

Atomic force microscopy (AFM)

AFM height images were recorded in intermittent contact mode in air using a Nanowizard 4 (JPK Instruments). Imaging was performed with OTESPA-R3 AFM probes (Bruker), that feature a visible apex tip geometry with a nominal tip radius of 7 nm. The cantilevers had a resonance frequency of 300 kHz and a spring constant of 26 N/m according to the manufacturer. Exact values were not measured. The images were tilt-corrected and flattened with the JPK Data Processing software and further analyzed with the software ImageJ.[208]

Transmission electron microscopy (TEM)

TEM imaging was performed with a JEOL JEM-2100Plus TEM in bright-field mode operated with an acceleration voltage of 80 kV. The samples were prepared on carbon-coated copper grids (200 mesh, Electron Microscopy Science) by drop-casting 7 µL of a dilute aqueous microgel dispersion. The grids were dried at room temperature. Core sizes were measured using the software ImageJ.[208]

Dynamic light scattering (DLS)

DLS measurements were performed with the Zetasizer Nano S (Malvern Panalyctical). The used laser had a wavelength of 633 nm and the scattered light was detected at a scattering angle of 173 °. A dilute aqueous CS microgel dispersion was measured three times for 60 s in a semi-macro cuvette (polymethacrylate, VWR). The hydrodynamic diameter, D_h, (z-average) was determined by cumulant analysis via the instrument software.

Extinction spectroscopy

Extinction spectra were recorded using a Specord S 600 UV–Vis spectrophotometer (Analytik Jena AG) over a wavelength range of 250 – 1019 nm. The spectra of dilute samples were measured in transmission geometry using PMMA cuvettes with 1 cm pathlength. Water was measured as background. Substrate supported monolayer samples (on glass) were placed vertically in the light path with the monolayer facing towards the detector. We recorded spectra at each marked line. Clean glass slides were measured as background.

Computational simulation

A finite element analysis (FEA) method was used to simulate the near-field electric field distribution and optical extinction of the hexagonally close-packed (HCP) gold nanoparticles (AuNPs) with COMSOL Multiphysics Wave Optics Module. The simulation solves Maxwell's equations in the frequency domain to model the interaction of electromagnetic waves (EM waves) with the AuNP monolayer, governed by the **equation 6.1**.

$$\nabla \times \frac{1}{\mu_r}(\nabla \times E) - k_0^2\left(\epsilon_r - \frac{j\sigma}{\omega\epsilon_0}\right)E = 0 \qquad (6.1)$$

where E is the electric field, $\nabla \times E$ is the curl of the electric field, μ_r is the relative permeability, k_0 is the free-space wavenumber, ϵ_r is the relative permittivity, σ is the conductivity of the material, ω is the angular frequency of the wave and ϵ_0 is the

vacuum permittivity. Electromagnetic differential equations are solved to model wave propagation and interactions within the system.

The model consists of two parts: the physical domain and the perfectly matched layers (PMLs). The physical domain consists of two layers: an air layer and an environment layer containing the HCP AuNPs. The HCP unit cell comprises of a whole AuNP with a radius of 46 nm placed in the center and four quarter-spheres at the corners. The environment layer has the same thickness as the diameter of the AuNPs, and the air layer is directly above the environment layer. Periodic boundary conditions are applied along both the x- and y-axes to simulate an infinite monolayer array. Perfectly matched layers (PMLs) are set to surround the entire physical domain to absorb any outgoing waves and prevent internal reflections which may interfere with the simulations. A periodic port was set at the boundary between the environment layer and the bottom PML for excitation of the incident wave. A second periodic port was set at the boundary between the air layer and the top PML for the measurement of transmittance. The incident wave was set to be normal to the AuNP monolayer, x-polarized, with an electric field amplitude of 1 V m^{-1} and an input power of 1W. The refractive index of air was set to be 1.0, and the optical constants of gold (*n* and *k*) were sourced from Babar and Weaver.[265] Different illustrations of the simulation environments are depicted in the **Supporting Information (Figure S6.2 – S6.4)**.

Compression experiments

For compression experiments, we used polytetrafluorethylene (PTFE) barriers and a film balance to measure the surface pressure (π). Prior to the experiment, the trough and the barriers were rigorously cleaned with water, followed by ethanol and water. Before installing the Wilhelmy plate to the film balance, it was heated in a flame until red-hot to remove any residues. The clean trough was filled with water while the barriers were closed until the water reached the edges of the trough. Then the barriers were opened and the Wilhelmy plate was immersed in the water at the middle of the trough, but in the last third of the width of the trough. The microgels were applied only if π was below 0.1 mN m^{-1}. For our experiment, we applied 70 µL of the diluted stock solution at the air/water interface using a micropipette. The side view of the microgels at the interface with their interfacial diameter D_i is schematically shown in **Figure 6.1 b**. The microgels are expected to show a ´fried-egg´ like shape at the

interface with D_i larger than D_h.[46, 155] As schematically shown in the top view of the interface in **Figure 6.1 c**, the microgels arrange into a hexagonally ordered assembly with spacings here denoted as nearest neighbor center-to-center distance $d_{c\text{-}c}$.[46, 177, 266] In **Figure 6.1 e and f**, photographs of the interface with open barriers are depicted. The light pinkish color is attributed to the plasmonic behavior of the AuNP cores that are part of the immersed colloidal film. In addition, the slightly visible structural coloration indicates the periodic arrangement of the CS microgels in the thin colloidal film. After 15 min of equilibration time, we started to close the barriers with a speed of 10 mm min^{-1}. A photograph with fully closed barriers is depicted in **Figure 6.1 g**. Here the intense pink color indicates that the distance between the AuNPs is reduced compared to the start. Thus, compressed microgels are assembled at the interface.

Continuous monolayer transfer for *ex situ* analysis

To analyze the microstructure of the CS microgels assemblies, we performed Langmuir-Blodgett (LB) deposition onto a glass substrate that was continuously retracted through the air/water interface during reduction of the surface area.[46, 69, 72, 266] We used the LB trough (Microtrough G2, Kibron Inc.) and a dip-coater to retract the glass slide. The glass slide was mounted to the dip coater at the center of the trough. The glass slide was placed perpendicular to the air/water interface and parallel to the barriers and then immersed for 55 mm below the interface, so that the meniscus of the water level touches the upper mark. The glass slide was retracted as soon as the compression started. The retraction speed of the dip coater (1.719 mm min^{-1}) was adjusted to the closing speed of the barriers. Thus, it is possible to map spatial positions on the substrate after the experiment to the surface pressure at the interface during the experiment. After complete drying of the glass slide, AFM height images were recorded at the marked positions. The nearest neighbor center-to-center distance ($d_{c\text{-}c}$) was determined by the radial distribution function (RDF).

In situ spectroscopic investigation during uniaxial monolayer compression

For the *in situ* experiment, we used a microscopy trough (Microtrough G2, Kibron Inc.) that was combined with a fiber optics-based VIS-NIR spectrometer (Ocean Optics). To position the optical fibers below and above the microscopy window of the trough, we used a self-designed, 3D-printed holder. The STL file of the holder is available from the **Supporting Information**. The fiber from the light source was placed below the microscopy window (not in contact) of the trough, while the fiber leading to the detector was placed 2.6 cm above it. The total distance between the two fibers is 4.4 cm. The setup is schematically shown in **Figure 6.1 h**. The large black arrows indicate the direction of the compression, so of the movement of the barriers. Photographs of the complete setup (without sample) are shown in **Figure 6.1 i, j and k**. For better visualization, the cover box was removed in **Figure 6.1 j and k**. A tungsten halogen lamp (HL-2000-LL, Ocean Optics) was used as light source covering a wavelength range of 360 to 2000 nm. The stability, as well as the drift of the lamp is 0.5 % and < 0.3 % per hour, respectively. The lamp exhibits a bulb color temperature of 2800 K. The used optical fiber (P400-1-VIS-NIR, Ocean Optics) showed the best efficiency from 400 to 2100 nm and has a fiber core diameter of 400 ± 8 µm. As detector, we used a Sony CCD array detector (FLAME-S-VIS-NIR-ES, Ocean Optics) with 2048 pixels and a minimal integration time of 1 ms. The operating wavelength range is from 350 to 1000 nm with an optical resolution of 1.33 nm. The connected optical fiber (P600-1-VIS-NIR, Ocean Optics) exhibits the best efficiency from 400 to 2100 nm and has a fiber core diameter of 600 ± 10 µm. We used Ocean View (Ocean Optics) as software to visualize and record the spectra.

The light source was left to equilibrate for 15 minutes before we adjusted the integration time to around 85 % of the measure capacity of the detector. The exact integration times for all experiments are listed in **Table S6.1** in the **Supporting Information**. Each spectrum is an average of five scans with boxcar widths of three. Reference spectra of the clean and empty air/water interface with and without illumination of the light source were recorded, respectively. For these two measurements, the ceiling light of the laboratory was switched off to eliminate any perturbation from other light sources. Extinction spectra were already recorded during the equilibration time with a time resolution of 1 s. During the following compression

of the colloidal film, we recorded extinction spectra in intervals of 1 s while the surface pressure was continuously measured, leading to a total of 1856 spectra per compression. The spectra were analyzed by a self-written python script called PeakAnalyzer.

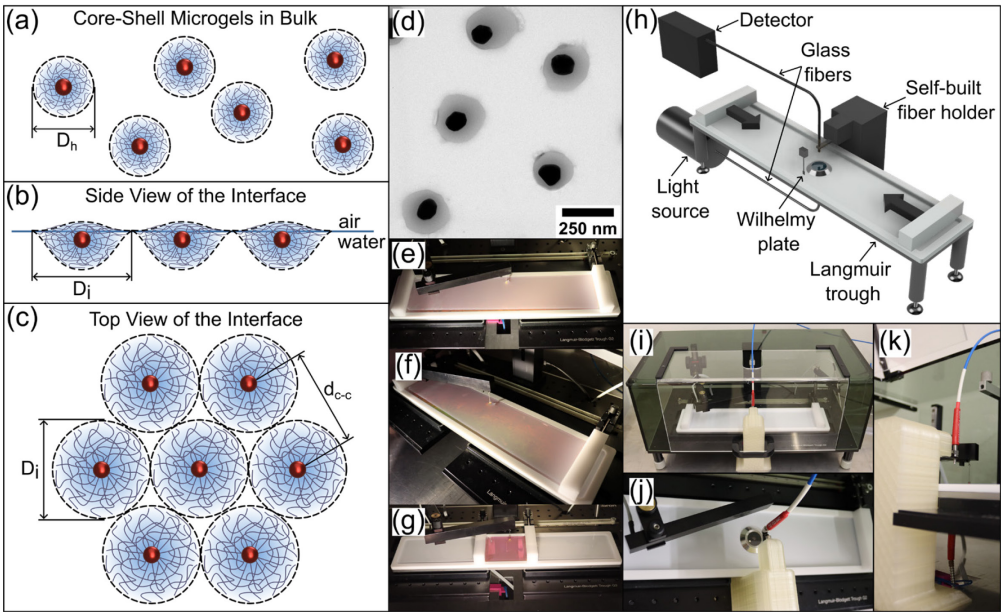

Figure 6.1. (a) Illustration of the structure of the CS microgels in bulk with the hydrodynamic diameter D_h indicated as dashed circles. Side (b) and top (c) view of the microgels hexagonally assembled at the air/water interface with the diameter at the interface D_i highlighted by the dashed circles. (d) Representative TEM image of the microgels. Photographs of the microgels assembled at the air/water interface at low (e,f) and high (g) compression. (h) Three-dimensional illustration of the set up combining extinction spectroscopy with a Langmuir trough. The large arrows show the direction of the movement of the barriers. (i), (j) and (k) Photographs of the experimental set up with the self-built fiber holder with mounted optical fibers taken from different persepctives.

Spectroscopic investigation of monolayers transferred to a glass substrate

The coated glass substrate was measured with the same fiber optics-based spectrometer as described in the previous section. A clean glass substrate was used to record reference spectra. Then the coated substrate was mounted into a dip-coater

that allowed for continuous translational movement of the substrate between the two fibers with a speed of 1.719 mm min^{-1} starting at the first marked position. Here the coated side faced towards the detection fiber. A spectrum was recorded at every second from the first marked position to the edge of the coated substrate. The first 18 spectra were rejected, as the fiber illuminated the coated and uncoated area of the substrate. Here, the spectra were not fully representative for the monolayer on the substrate. Thereby, we got a total of 1837 spectra covering the optical response of the retracted monolayer. The recorded spectra were analyzed by a self-written python script called PeakAnalyzer.

PeakAnalyzer script

The Python script automates the analysis of spectral data by processing multiple files containing wavelength and intensity information. It fits Lorentzian functions to the data to extract key parameters such as peak position, peak intensity, and full width half-maximum (FWHM). The code generates graphical representations of the fit for each dataset and compiles the results, including averaged peak values and absorbance at 400 nm, into a summary file. Additionally, the script can create a video of the fitting process for visual inspection of the data trends. Data analysis and curve fitting were performed using Python libraries, including numpy, pandas, matplotlib, and scipy.[267-270] The code is available at GitHub: https://github.com/jthemmaster/PeakAnalyzer.

6.4. Results and Discussion

6.4.1. LB deposition

The CS microgels were self-assembled at the air/water interface in a Langmuir trough starting with open barriers, i.e., maximum available trough area. The spontaneously formed monolayer was visible by its light pinkish color as seen in **Figure 6.1 e**. During the following uniaxial compression, the monolayer was continuously transferred to a hydrophobically modified glass slide. Previous works found that microgels exhibit better adhesion towards hydrophobic than hydrophilic substrates, as the polymer

chains of the microgels can replace unfavorable contacts of water molecules to the hydrophobic substrate.[271] On the substrate the microgels stretch into a ´fried-egg´ like conformation to maximize the contact towards the substrate, similar to the situation at the air/water interface, that is schematically shown in **Figure 6.1 b**.[46, 155] The better adhesion to the substrate can help to counteract attractive capillary forces that alters the microgel arrangement during the process of drying of the thin colloidal film.[181] As we will see later in this work, at a certain range of $d_{c\text{-}c}$ capillary interaction nevertheless become relevant to the CS microgels used here. With the known speed of substrate withdrawal and the speed of the barriers of the LB trough, we can link the recorded surface pressure to the vertical position on the substrate. Thereby it becomes possible to link the local microstructure of the monolayer on the substrate to the compression isotherm. A photograph of the glass slide with the continuously transferred monolayer in **Figure 6.2 bottom left** reveals a color change from light pinkish at the top to intense pink at the bottom. This change is attributed to an increase of the number of CS microgels per area. Due to the monolayer compression in the trough, $d_{c\text{-}c}$ decreases from top to bottom, i.e., with increasing surface pressure. Furthermore, opalescence can be identified towards the top of the substrate, i.e., low compressions, which points to the periodic arrangement of the microgels with rather large domain sizes. The horizontal, dashed lines with the corresponding surface pressures indicate the positions on the glass slide where AFM height images were recorded (see **Figure 6.2 i to vi**). The microgels are hexagonally ordered with only some local defects, which do not affect the overall arrangement at low compressions (images **i** to **iii**). These exemplary images show single crystalline domains over at least the scanned 100 μm^2 area. This underlines the very low size polydispersity of the CS microgels. Similarly large domains were also previously reported for similar CS microgels.[55, 177] From image **i** to **iii** values of $d_{c\text{-}c}$ decrease from 502 ± 14 nm to 435 ± 2 nm, as determined from the radial distribution functions (RDF) that were calculated from the AFM height images. These distances being significantly larger than D_h = 350.2 ± 3.2 nm measured from dilute dispersion in the swollen state (20 °C), is related to the lateral deformation (stretching) to a diameter D_i at the interface as shown in **Figure 6.1 a, b, c**. The ratio D_i/D_h depends on the shell-to-core size ratio, the shell softness as well as the overall dimensions.[38, 41, 46] We want to note that AFM images depict the monolayer in the dried state with significantly reduced microgel dimensions leading to the non-close-packed appearance. Upon further compression, we observe further reduction in $d_{c\text{-}c}$ and the appearance of small clusters of microgels

with significantly smaller spacings at 19.5 mN m^{-1}. The fraction of clusters of microgels in close proximity increases upon further compression. This clustering is attributed to drying artefacts, that will be further discussed in the next chapters. Despite these local changes the overall microstructure still resembles hexagonal packing as confirmed by the fast Fourier transforms (FFTs) provided in the **Supporting Information**. At 30.5 mN m^{-1}, we reach $d_{c\text{-}c}$ = 259 ± 3 nm, which is now significantly smaller than D_h indicating that the microgel shells are in a compressed state. At higher surface pressures collapse of the monolayer was observed. **Table 6.1** summarizes the determined values of $d_{c\text{-}c}$ from AFM and the corresponding surface pressures that were measured at the air/water interface during compression.

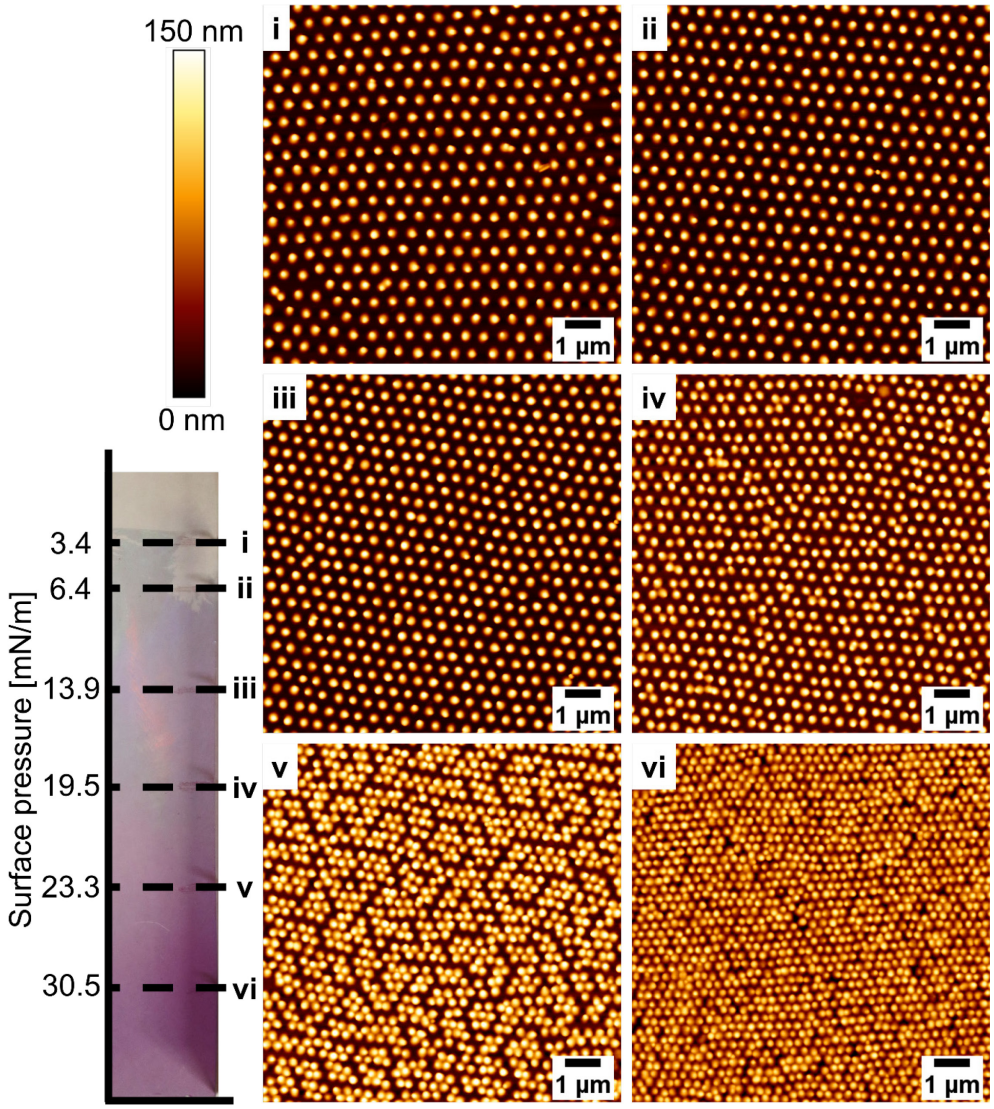

Figure 6.2. *Ex situ* analysis of the microgel monolayer after Langmuir-Blodgett deposition and subsequent drying. Bottom, left: Photograph of the glass substrate carrying the CS microgel monolayer. Horizontal, dashed lines mark surface pressure values and the corresponding positions where AFM analysis was performed. AFM height images of the monolayer corresponding to different surface pressures (i – vi). The z-scale bar (height) is shown on the top right and is the same for all presented AFM images.

Table 6.1. Measured surface pressures and corresponding values of $d_{c\text{-}c}$ determined from the position of the first peak in RDFs computed from AFM height images.

π [mN m^{-1}]	$d_{c\text{-}c}$ [nm]
3.4	502 ± 14
6.4	476 ± 7
13.9	435 ± 2
19.5	388 ± 1
23.3	286 ± 1
30.5	259 ± 3

6.4.2. Optical response of the assembled microgels: Comparison *in situ* vs. *ex situ*

During the compression of the monolayer, we observe a color change from light pinkish with structural colors (**Figure 6.1 e and f**) to intense pink (**Figure 6.1 g**). This color change is analyzed without any influence of the drying process at the interface. Therefore, we combined a Langmuir trough with an optical fiber-based extinction spectrometer. With this setup, it is possible to measure the surface pressure and extinction spectra simultaneously during the continuous compression of the monolayer at the air/water interface. We perform such a measurement with assembled Au-PNIPAM microgels with d_{core} = 14 nm as a reference, see **Figure S6.6** for the extinction spectra. During the compression, no optical response is measured. Thus, the absorbance of the small cores is too low to measure a plasmonic contribution and the shell does not contribute to the extinction, even at high surface pressures. Therefore, only Au-PNIPAM microgels with large cores are analyzed in the following. For these CS microgels, the measured extinction is solely attributed to the optical response of the AuNP cores. The extinction spectra of the interface can be

compared to the extinction spectra of the coated glass slide after the LB deposition. The isotherm of the CS microgels is depicted in **Figure 6.3 a**. The colored dots mark the surface pressures at which *ex situ* extinction spectra are recorded and compared to the corresponding *in situ* spectra. These surface pressures correspond to the ones where AFM height images were taken. The color code used indicates the increase in surface pressure from dark green to dark red.

The *in situ* spectra shown in **Figure 6.3 b** exhibit only one distinct resonance peak. With increasing surface pressure, the peak becomes more intense due to the increase in number of particles per area, N_p, as the interparticle spacing is reduced upon compression. At a closer look, we observe that the peak width (FWHM) increases and the peak position (λ_{max}) shifts to smaller wavelengths with increasing surface pressure. For the lowest surface pressure of 3.4 mN m^{-1}, the peak is at λ_{max} = 618.6 nm with a FWHM of 33 nm. Here the peak is strongly redshifted and narrower than compared to the spectrum of the CS microgels in aqueous dispersion which features a peak with λ_{max} = 581 nm and a FWHM of 92 nm (**Figure S6.1**). The narrow redshifted peak of the interfacial monolayer is a result of plasmonic-diffractive coupling. Here, the overlap of the LSPR of the single AuNPs and the in-plane diffraction mode is strong enough to result in a peak with a reduced linewidth, corresponding to the surface lattice resonance (SLR). Previous works showed that a homogeneous refractive index (RI) environment is necessary to enable the plasmonic-diffractive coupling.[55, 110, 123, 201] Thus, the SLR peak in our measurement is unexpected because of the rather complex RI environment of the AuNP cores. The cores are encapsulated into a PNIPAM (n = 1.52) shell which is solvated with water, resulting in an expected, effective RI of 1.333. Furthermore, the microgels are assembled at the interface between air (n = 1.00) and water (n = 1.33). However, we can conclude that the RI around the AuNP cores is homogeneous enough to enable the coupling. With increasing surface pressure and decreasing interparticle spacing, the peak becomes broader which is an indication that the coupling strength reduces. At the highest surface pressure of 30.5 mN m^{-1}, the peak position is at λ_{max} = 554.8 nm, which is at significantly smaller wavelengths compared to the peak measured from dilute dispersion. This blueshift is ascribed to long-range radiative interactions between the dipoles of the AuNPs.[55] Thus, we have a change from diffractive-plasmonic coupling to long-radiative interactions in our monolayer upon compression. This change happens around a surface pressure of 19.5 mN m^{-1}, as the peak is here

at λ_{max} = 575.5 nm, so already slightly blueshifted compared to the spectrum of the dispersion. The complete shift of the peak during the compression is 63.8 nm in total and thus much larger than it would be expected to be caused by simply changes of the RI environment as the monolayer is compressed and the polymer density in the interstitial space is increased.

The *ex situ* spectra that were recorded from the substrate supported monolayer are shown in **Figure 6.3 c**. Similarly to the air/water interface, we observe a peak that becomes more intense and shifts to smaller wavelengths with increasing surface pressure, thus with decreasing interparticle distance. The increase in intensity can also be attributed to the increase in particle density. This is also confirmed by the photograph of the glass slide and the AFM height images in **Figure 6.2**, showing more microgels per area with increasing surface pressure. Opposite to the *in situ* spectra, the peak becomes narrower with increasing surface pressure. At the lowest surface pressure, the peak with λ_{max} = 604.5 nm and FWHM = 112 nm is redshifted and broader than the peak from dilute dispersion. As reported by Ponomareva *et al*.,[55] the redshift is caused by the change in effective RI. On the glass slide, the effective RI is increased due to the combination of the glass (n = 1.52) with the air (n = 1.00) as superstrate. Furthermore, the PNIPAM shell that surrounds the AuNP cores increases also the effective RI. For the highest surface pressure, the blueshift and narrowing of the peak is attributed to long-range radiative interactions between the dipoles of the AuNPs.

The peak positions of the spectra for *in situ* (closed symbols) and *ex situ* (opened symbols) analysis are plotted against the surface pressure in **Figure 6.3 d**. For the spectrum of the monolayer at the interface, the peak positions exhibit an approximately continuous shift to lower wavelength as surface pressure increases. Thus, we can conclude that the polymer shell of the microgel is continuously compressed leading to a continuous decrease of the interparticle spacing. For the spectrum of the coated glass substrate, the peak position shifts in sigmoidal like trend. This behavior can be attributed to the clustering of the microgels, which is detected in the AFM images in **Figure 6.2**. Due to the clustering, not all AuNP are equidistant influencing the optical response of the monolayer.

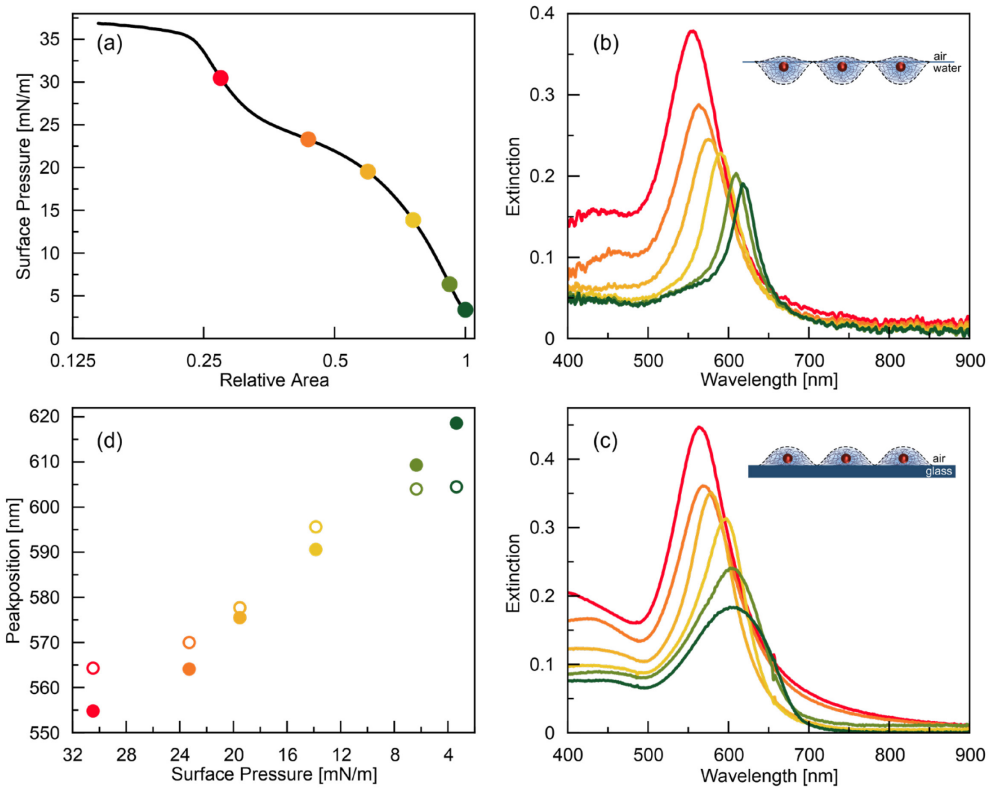

Figure 6.3. Optical response of assembled microgels with increasing surface pressures. (a) Isotherm of the CS microgels. (b) *In situ* extinction spectra of the assembled microgels at the air/water interface taken at the marked surface pressures. (c) *Ex situ* extinction spectra of the assembled microgels transferred from the interface to a glass substrate. (d) Peak position against the surface pressure. Closed symbols represent the peak position of the spectrum at the interface and the opened symbols the peak position of the spectrum from the glass substrate. The surface pressure increases from dark green to dark red.

6.4.3. Combining *ex situ* and *in situ* measurements

To determine the spacing of the microgels at the interface during the compression, AFM images taken from the coated glass slide at 3.4 mN m^{-1} are used as a reference point. At this surface pressure, the microgels are highly ordered with no evidence of clustering as shown in **Figure 6.2 i**. We assume that the arrangement on the glass slide accurately represents the structure at the interface and that the microgels remain

unaffected by the drying process. Thus, the $d_{c\text{-}c}$ in the AFM image corresponds to the $d_{c\text{-}c}$ at the interface.

To estimate the total number of microgels (N_{total}) at the interface, the microgels in three different AFM images are counted resulting in the number of microgels per area (*N/area*). By multiplying *N/area* by the total area of the trough (A_{trough}) at 3.4 mN m^{-1}, N_{total} for this experiment can be derived. The area of the trough is subsequently divided by N_{total} to get an idea of the available area ($A_{available}$) for one single microgel. As the microgels are hexagonally packed, this area needs to be multiplied by the packing factor of 0.91 resulting in the area of a circle occupied by one microgel. The $d_{c\text{-}c}$ corresponds then to the diameter of this circle and can be calculated as follows in **equation 6.2**:

$$d_{\mathrm{c-c}} = \sqrt{\frac{A_{\mathrm{available}} \cdot 0.91 \cdot 4}{\pi}} \tag{6.2}$$

As N_{total} is known, it is possible to calculate $d_{c\text{-}c}$ of the microgels for the whole compression. The calculated $d_{c\text{-}c}$ are plotted against the area of the trough as shown in **Figure 6.4 a**. As expected, $d_{c\text{-}c}$ decreases with reduction of available area in the trough, due to the compressibility of the soft microgels. The peak positions of both *in situ* (closed black symbols) and *ex situ* (opened brown symbols) spectra are plotted as function of the calculated $d_{c\text{-}c}$, as shown in **Figure 6.4 b**. In both experiments, the peak position shifts toward lower wavelength as the $d_{c\text{-}c}$ decreases until reaching a plateau at around 300 nm and 275 nm for the *ex situ* and *in situ* experiment, respectively. At the start of the compression, the wavelength of the peak position for the *ex situ* spectra is lower than that for the *in situ* spectra. For $d_{c\text{-}c}$ values smaller than 480 nm, the wavelengths of both experiments converge and overlap until 435 nm. The grey shaded section between 435 nm to 388 nm, shown as magnification in **Figure 6.4 c**, marks the region where clustering of microgels is observed in the AFM images. In this region, the wavelength of the peak position for the *ex situ* spectra remains lower than that for the in situ spectra. For the *in situ* spectra, the wavelength decreases approximately linearly, whereas in the *ex situ* experiment the slope of the decrease changes in this region, as shown by the green lines in **Figure 6.4 c**. This change in the slope could result from the isostructural phase transition, so from the clustering of the microgels on the glass slide. The phase transition is then not

observed at the interface, as the peak shifts continuously to lower wavelengths. At a $d_{c\text{-}c}$ of 350 nm, both curves intersect and the peak position of the *ex situ* spectra is located at higher wavelengths than of the *in situ* spectra. The red dashed line at 263 nm in **Figure 6.4 b and d** indicates the $d_{c\text{-}c}$ where the monolayer collapse. In **Figure 6.4 d**, the peak intensity (left axis, black) and the full-with half maximum (FWHM, right axis, grey) are plotted against the calculated $d_{c\text{-}c}$. The peak intensity increases, as more microgels are pushed into the detection area during the compression. The FWHM increases with decreasing $d_{c\text{-}c}$ as the optical response of the monolayer at the interface changes over the compression. First, the peak is a result of diffractive-plasmonic coupling and therefore has a FWHM of less than 25 nm. With increasing compression, the peak is due to long-range radiative interactions which exhibits a larger FWHM. The aforementioned collapse can be seen as a sharp increase of the peak intensity and FWHM starting at a $d_{c\text{-}c}$ of 263 nm. Here the peak intensity increases with decreasing $d_{c\text{-}c}$, as more microgels will be detected. Some microgels will be pushed into the bulk phase leading also to an increase of the peak intensity.

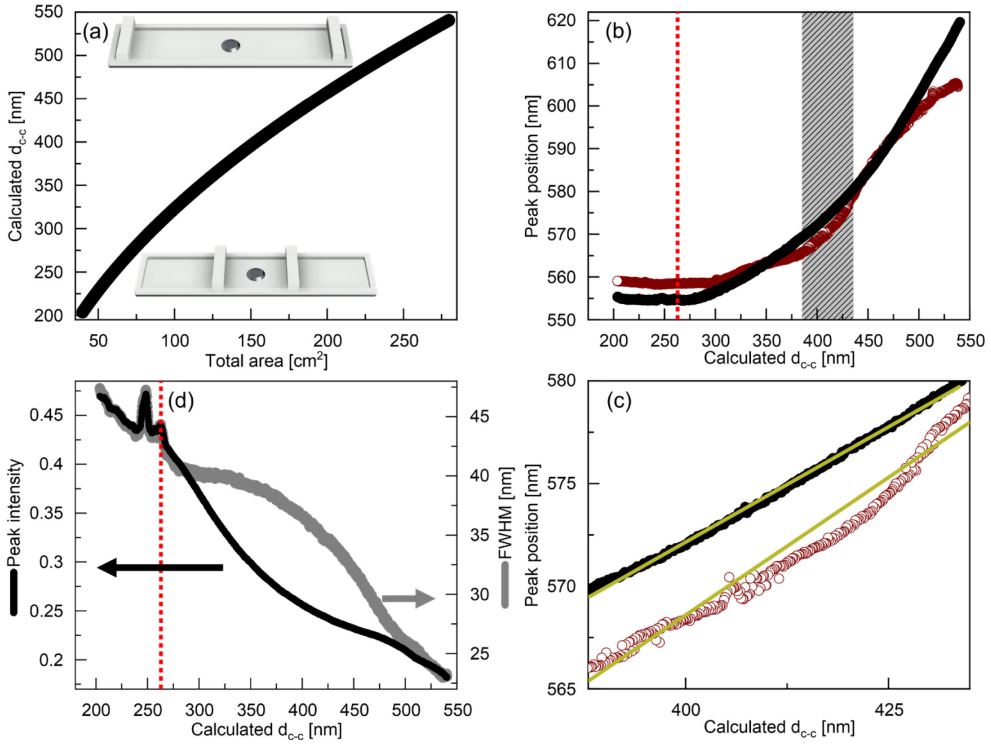

Figure 6.4. Combination of *ex situ* and *in situ* measurements. (a) Calculated d_{c-c} of the microgels at the interface against the total area available at the interface. AFM images of the monolayer at fully opened barriers were taken as a reference point to calculate d_{c-c} for the whole compression. The error bars are in the order of magnitude of the characters. The schemes show the Langmuir trough with fully opened and closed barriers. (b) Peak position of the extinction spectra taken from the monolayer at the interface (black circles) and at the glass substrate after the transfer (open brown circles) against the calculated d_{c-c}. The grey shaded section marks the clustering of the monolayer on the glass substrate. The red dashed lines indicate the collapse of the monolayer at the interface. (c) Peak position against the calculated d_{c-c} of the grey shaded section in (b). The green lines show a linear fit for both curves. (d) Peak intensity (black) and FWHM (grey) of the extinction spectra taken from the interface against the calculated d_{c-c}. The red dashed lines indicate the collapse of the monolayer at the interface.

6.4.4. Comparison of experiments with COMSOL calculations

The optical response of the AuNP monolayer at the air/water interface was investigated via a FEA calculation using COMSOL Multiphysics. **Figure 6.5 a** shows

the simulated extinction spectra of the interfacial monolayers with $d_{c\text{-}c}$ ranging from 592 nm to 142 nm, with 50 nm steps. With decreasing $d_{c\text{-}c}$ we observe a continuous blue shift of the resonance peak. This agrees well with the experimental results discussed in the previous sections. For larger $d_{c\text{-}c}$ values, the extinction peaks are intense and narrow. As $d_{c\text{-}c}$ decreases, there is continuous broadening, while the intensity of the peaks undergoes more complex changes. Initially above a $d_{c\text{-}c}$ value around 392 nm, the intensity gradually decreases. However, once a turning point is passed, the peak intensity begins to increase again. The intensity of the final extinction peak at the smallest value of $d_{c\text{-}c}$ = 142 nm was found to be higher than the initial one. A possible explanation is that the periodic arrangement of AuNPs forms a two-dimensional diffraction grating. The optical response of the monolayer is subject to the coupling of the diffractive modes and the plasmonic modes. For a 2D periodic grating with interplanar spacing *d*, the RA condition for a given diffraction order *m* can be expressed as

$$\lambda_m = \frac{d(\sin\theta \pm m)}{n_{eff}} \tag{6.3}$$

Where λ_m is the wavelength at which RA occurs for diffraction order *m*, θ is the incident angle of light and n_{eff} is the effective RI of the surrounding medium. Since we illuminate the periodic monolayer perpendicular to the interface, both in experiment and simulation, θ is 90 ° and thus sin θ = 1. When RAs spectrally overlap with the LSPR mode of the individual AuNPs, plasmonic-diffractive coupling can occur. In our case the diffraction leads to in-plane. This leads to the initial high intensities of the extinction peaks. When $d_{c\text{-}c}$ decreases but above turning point, the RA conditions are no longer met, yet the AuNPs are still relatively far apart. The local enhancement of the electromagnetic field is suppressed, while coupling remains weak, resulting in decreased extinction intensities. As $d_{c\text{-}c}$ becomes even smaller with compression, beyond the turning point, the AuNPs are closer to each other. Strong interparticle coupling enhances collective plasmonic modes, resulting in higher extinction intensities. This was previously reported by Ponomareva *et al*. for a homogeneous RI environment of 1.49 around the AuNPs.[55] In this work, the RI is slightly lower. The optical response of the monolayer exhibits a more photonic character while the plasmonic nature is reduced, and we expect the extinction intensity for the largest values of $d_{c\text{-}c}$ to be smaller than that for the lower values of $d_{c\text{-}c}$. The broadening of the

extinction peaks potentially arises from the presence of a range of near-field couplings when AuNPs are brought closer to each other. In addition, when AuNPs are brought together, coupling between non-neighboring AuNPs is possible. Multipolar or higher order resonances are also possible. This could possibly explain the origin of the broadening of the peak.

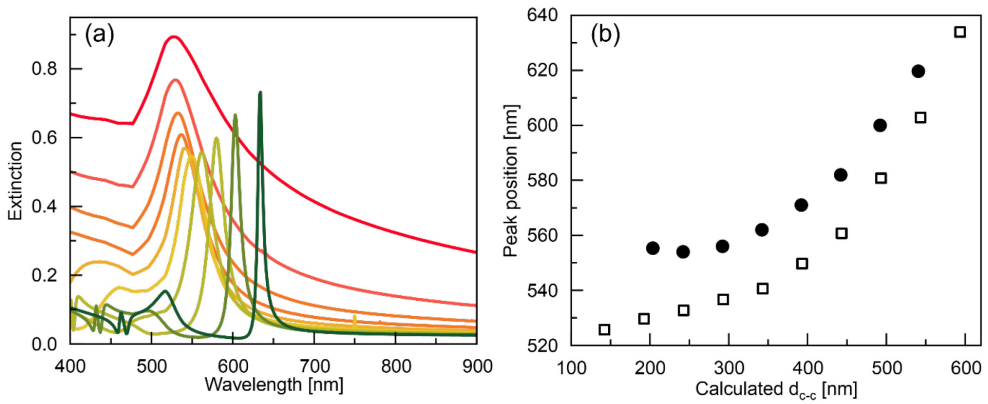

Figure 6.5. Comparison of the experiment with simulations. (a) Simulated extinction spectra of assembled AuNPs at the air/water interface with $d_{c\text{-}c}$ from 142 nm to 592 nm in 50 nm steps. The $d_{c\text{-}c}$ increases from dark red to dark green. (b) Resonance peak position plotted against $d_{c\text{-}c}$ from the experiment (filled circles) and simulation (open squares).

Figure 6.5 b shows a comparison of the peak positions between simulations and experiments. They show a very similar trend, while there are slight differences in terms of the exact peak positions. The experimental peak positions always occur at higher wavelengths compared with those from the simulations. The differences may arise from assumptions made in the simulations. A model of perfect monolayer consisting of only AuNPs in a homogeneous medium with a fixed RI is used for simulations. However, in actual experiments, the presence of microgel shells outside the AuNPs potentially alters the local RI slightly. This inhomogeneity in RI is a possible reason for the systematic differences between simulation and experimental results.

We then studied the optical response of the monolayer at different stages of compression. We decided on three different $d_{c\text{-}c}$ values, 538 nm, 467 nm and 292 nm, which represented the start, the middle and the end of compression process

respectively. The near-field electromagnetic intensity maps were simulated and constructed for the three cases, as shown in **Figure 6.6**. The intensities were calculated at the incident wavelength corresponding to their respective extinction peaks from the experiment. In all three maps, the excitation of the dipolar resonance can be clearly identified around the AuNPs. At the highest value of $d_{c\text{-}c}$, the high field intensity between the particles can be ascribed to the in-plane diffractive band. This confirms that the narrow peak is due to the coupling of the diffractive and plasmonic mode resulting in a surface lattice resonance (SLR). As compression increases, the intensity of the diffractive mode decreases which leads to an uncoupling of the two modes. At larger $d_{c\text{-}c}$ values, RA conditions for certain diffractive orders are met, making them couple strongly with LSPRs. At smaller $d_{c\text{-}c}$ values, RA conditions are gone, diminishing the e-field enhancement. In addition, a broader resonance peak also corresponds to a less intense field surrounding single nanoparticles. This agrees well with the extinction spectra discussed in the previous sections.

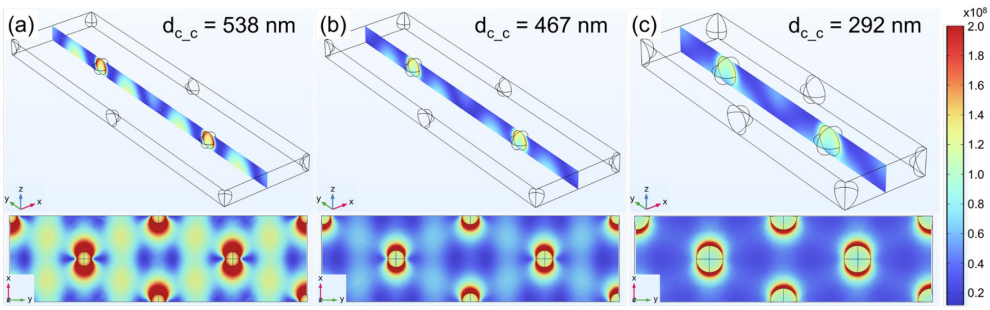

Figure 6.6. Calculated electromagnetic intensity maps for the hexagonally ordered monolayer at the beginning (a), at the middle (b) and at the end (c) of the compression, respectively. The top and bottom row show two different angles of view. The color scale corresponds to all maps.

6.5. Conclusion

In this work, we analyzed the optical response of plasmonic core-shell microgels at the air/water interface *in situ* under continuous compression in a Langmuir trough. The experimental setup allowed for measurements of the monolayer extinction in transmission geometry with temporal resolution of seconds – very fast as compared

to the duration of the total compression experiment. Thereby we could follow changes in the optical response related to sub-nm changes in interparticle spacing. We calculated the interparticle distance of the microgels at the interface by analyzing their microstructure *ex situ* at the maximum available area, i.e., low states of compression where monolayer transfer to solid substrates was not affected by capillary interactions leading to microgel clustering. This allowed us to correlate the $d_{c\text{-}c}$ of the microgels with the peak positions in the *in situ* extinction spectra. Comparison between *ex situ* and *in situ* extinction spectra revealed different trends in peak position. In contrast to *ex situ* experiments, the peak position of the *in situ* spectra continuously shifts to lower wavelength, indicating a steady decrease in $d_{c\text{-}c}$. These findings suggest that the clustering observed in the AFM images occurs only during the drying of the colloidal monolayer, rather than at the air/water interface.

Furthermore, we observed a sharp narrow peak at the highest $d_{c\text{-}c}$ which broadened upon compression. We confirmed by COMSOL calculations that an intense diffractive in-plane mode was present at the highest $d_{c\text{-}c}$ and diminished as $d_{c\text{-}c}$ decreased. Thus plasmonic-diffractive coupling was enabled resulting in a SLR peak. This means that the microgel shell swollen in water provided a sufficiently homogenous refractive index around the AuNPs to facilitate the coupling.

This study demonstrates a relatively easy, fast and non-destructive approach to analyze plasmonic colloidal monolayers at the air/water interface upon reduction of the interparticle distance. Small changes in the optical response can be directly monitored and linked to the surface pressure providing a direct link to the interparticle distance. The setup not only facilitates on-demand tailoring of the microstructure of the monolayer, but also enables further studies of the microgel shell and its behavior at different surface pressure. The high sensitivity of the peak position offers immediate feedback on any change between the microgels. This enables studies to get a better understanding of core-shell microgels too small for light microscopy analysis.

Supporting Information

Supporting Information is available from the Wiley Online Library or from the author.

Acknowledgments

The authors acknowledge the German Research Foundation (DFG) and the state of NRW for funding the cryo-TEM (INST 208/749–1 FUGG) and Marius Otten from Heinrich Heine University Düsseldorf for his assistance with the operation and image recording. M.K. acknowledges the German Research Foundation (DFG) for funding under grant KA3880/6-1. D.F. acknowledges the Luxembourg National Research Fund (FNR), Project Reference 15688439. Open access funding enabled and organized by Projekt DEAL.

Conflict of interest

The authors declare no conflict of interest.

Data Availability Statement

The data that support the findings of this study are openly available in Zenodo.

Keywords

Localized surface plasmon resonance, electromagnetic coupling, plasmonic-diffractive coupling, core-shell microgels, fluid interface, self-assembly, *in situ* spectroscopy

6.6. Supporting Information

Synthesis of gold seeds

The gold nanoparticles (AuNPs) were synthesized via the Turkevich method.[207] Specifically, 500 mL of an aqueous solution of $HAuCl_4 \cdot 3H_2O$ (0.5 mM) was brought to a vigorous boil while stirring. Subsequently, 25 mL of a hot aqueous solution of sodium citrate dihydrate (1 wt%) was added rapidly in one shot. Heating was continued for

further 20 minutes under continuous stirring. The resulting dispersion was then allowed to cool to room temperature.

Synthesis of core-shell microgels

The colloidal stability was enhanced by adding 3 mL of an aqueous SDS solution (1 mM) to the dispersion while stirring, in accordance with the protocol of Rauh *et al*.[76] To functionalize the surface of the AuNP seeds, 1.63 mL of an ethanolic BA solution (1.4 mM) was added after 20 min. The mixture was stirred for an additional 20 minutes and subsequently concentrated via centrifugation at 1000 rcf for 16 hours, resulting in a final volume of 30 mL of AuNP seed dispersion.

Au-PNIPAM core-shell (CS) microgels were then synthesized via seeded precipitation polymerization following the protocol of Rauh *et al*.[76] Here the BA-functionalized AuNPs served as seeds for this process. Initially, *N*-isopropylacrylamide (NIPAM, 0.588 g, 5.20 mmol) and *N*,*N*'-methylenebisacrylamide (BIS, 0.134 g, 0.87 mmol) as chemical crosslinker were dissolved in 100 mL of Milli-Q water. The solution was degassed with argon gas at 70 °C for 1 hour. Subsequently, 5 mL of the BA-functionalized AuNP seed dispersion ($c(Au^0)$ = 4.55 mM) was added while degassing was continued for an additional 30 minutes. Polymerization was initiated by adding 2.2 mg of potassium persulfate (PPS) dissolved in 1 mL of water. As the reaction mixture turned turbid, the polymerization was allowed to proceed for 4 hours.

Upon completion of the reaction, the mixture was cooled to room temperature. The CS microgels were purified through three sequential centrifugation steps, each performed at 9400 rcf for 1 hour. After the first two centrifugation steps, the residue was redispersed in 30 mL of water, and after the final step, it was redispersed in 15 mL of water. The resulting Au-PNIPAM microgels were then freeze-dried for 3 days.

Overgrowth of the core in the microgel shell

The AuNP cores were overgrown with gold following the protocol reported by Ponomareva *et al*.[55] An aqueous solution of Au-PNIPAM microgels (4.68 wt%) was added to an aqueous cetyltrimethylammonium chloride (CTAC) solution (10 mM) in a 1:1 volume ratio. 800 µL of this mixture were then added to 32 mL of an aqueous CTAC solution (2.4 mM) while stirring in an Erlenmeyer flask.

Each overgrowth step involved the rapid addition of 624 µL of an aqueous ascorbic acid solution (49 mM), followed by the dropwise addition of 48 mL of an aqueous solution containing CTAC (6.2 mM) and $HAuCl_4$ (0.5 mM) while heavy stirring. The overgrowth reaction was allowed to proceed for 30 minutes with gentle stirring. This procedure was repeated for seven cycles to achieve core sizes 96.3 ± 8.2 nm in diameter. An extinction spectrum was recorded after each cycle to follow the localized surface plasmon resonance (LSPR) maximum, aiming for a target wavelength of approximately 580 nm. After the seventh overgrowth cycle, the reaction mixture was stirred overnight.

The final CS microgels were purified by dialysis against water for four days, with daily exchange of water. After dialysis, the microgels were centrifugated three times at 5400 rcf for 30 minutes each. After each centrifugation step, the residue was resuspended in 600 µL of ethanol. This dispersion was used as stock solution for further use. For the Langmuir trough experiments, the stock solution was diluted by a factor of three with ethanol.

Optical property of CS microgels in aqueous dispersion

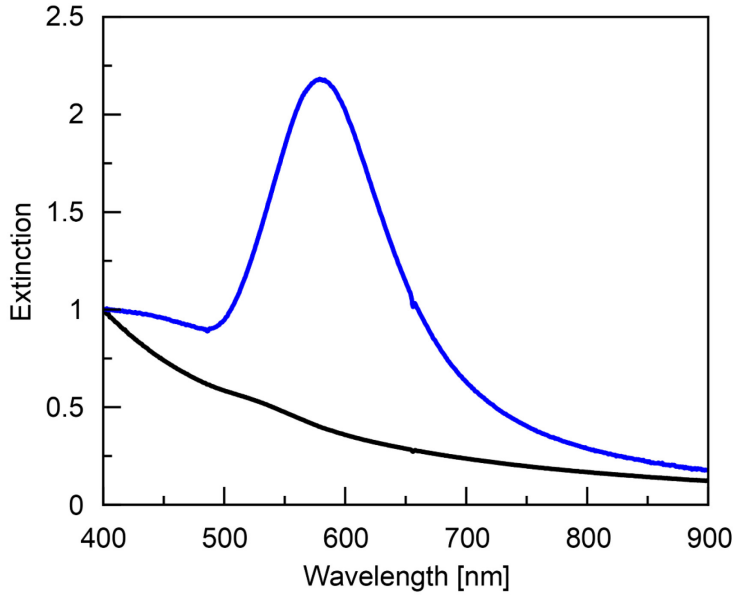

Figure S6.1. Optical property of CS microgels. Extinction spectra of CS microgels with D_{core} = 14.1 nm (black) and D_{core} = 96.3 ± 8.2 nm (blue). Extinction spectra are normalized to the extinction at 400 nm.

The spectrum of the CS microgels with the small core is dominated by the Rayleigh-Debye-Gans scattering of the PNIPAM shell and the LSPR peak of the Au core can be detected as shoulder around 520 nm in **Figure S6.1**.[49, 56] For the microgels with the large cores, the LSPR peak can be clearly detected at 581 nm. Here, the extinction of the Au cores dominates the spectrum and overweighs the scattering of the shell.

Simulation environments for COMSOL calculations

In the following, we show the simulation for the AuNP monolayer used in the COMSOL calculations.

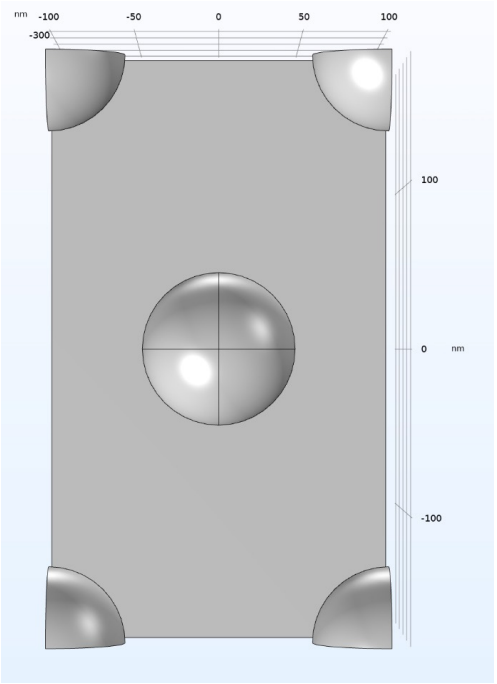

Figure S6.2. The HCP unit cell of the AuNP monolayer.

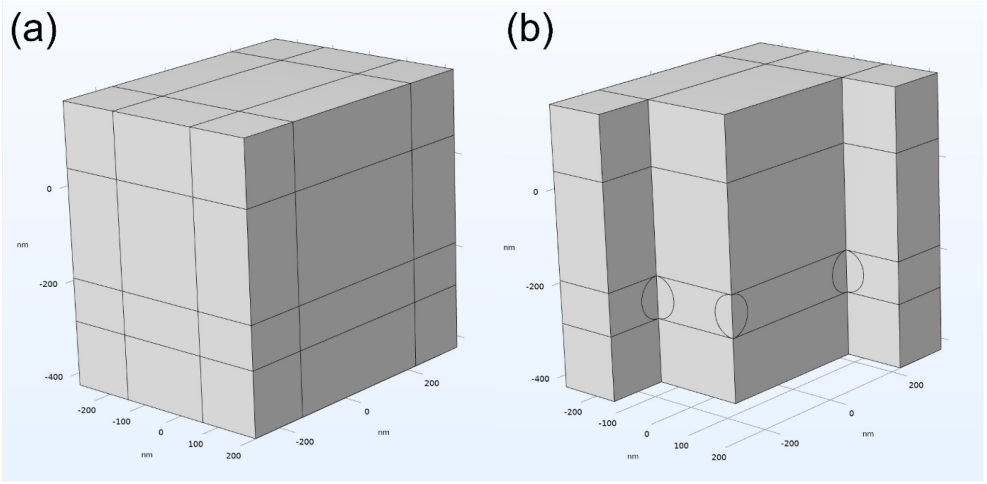

Figure S6.3. (a) Illustration of the simulation model and (b) scheme of both the physical domain and the PMLs.

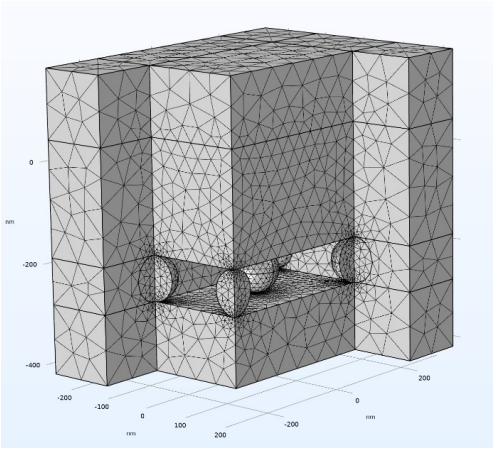

Figure S6.4. Meshing of the model.

In situ experiments

The different integration times are listed in **Table S6.1**.

Table S6.1. Integration time in ms for the different *in situ* experiments

Sample	Integration time [ms]
CS microgels with large cores	1.17
CS microgels with small cores	5.20
Coated glass substrate	7.29

FFT of AFM images

Figure S6.5 presents the FFTs which were generated from the point maps of the AFM images. For all six FFTs, six Bragg peaks in the first order can be identified. Thus, the monolayer shows a hexagonal order at every surface pressure. The number of orders decreases with increasing surface pressure, so it means that the long-range order also decreases.

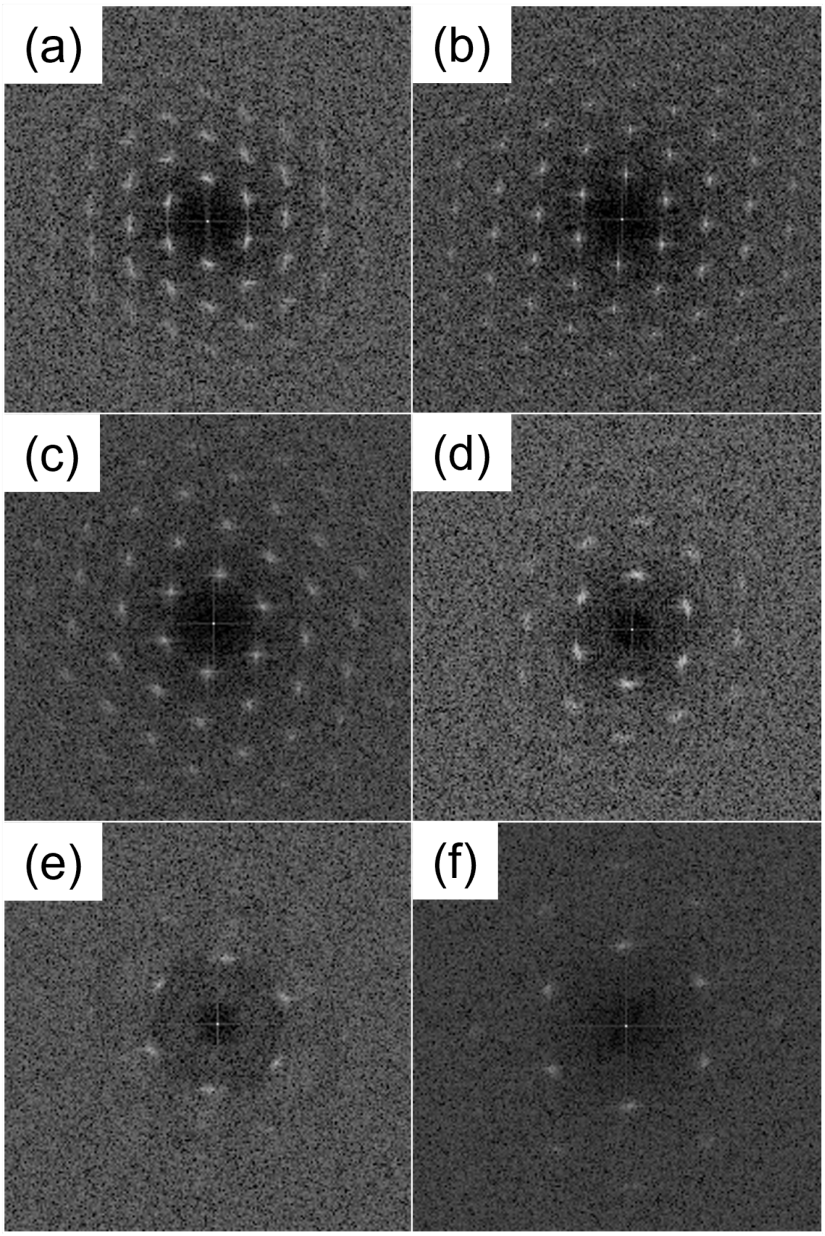

Figure S6.5. FFTs generated from the point maps of the AFM images.

In situ extinction spectra of CS microgels with small cores

Figure S6.6 a and b show the isotherm and the extinction spectra recorded at low (dark green), mid (yellow) and high surface pressure (dark green), respectively. The three spectra superimpose and no peak or extinction can be detected. Thus, the PNIPAM shell does not contribute to the extinction over the whole surface pressure range even at high compression.

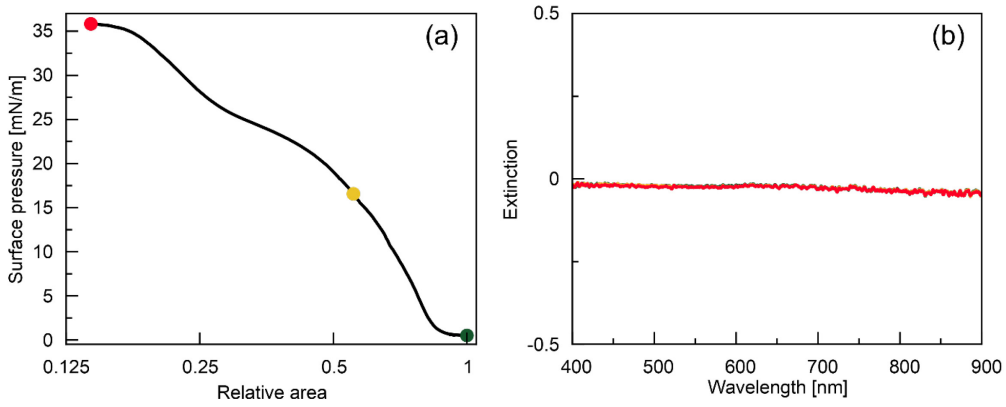

Figure S6.6. (a) Isotherm of the CS microgels with D_{core} = 14.1 nm. (b) *In situ* extinction spectra of the assembled microgels at the air/water interface recorded at the beginning (dark green), in the middle (yellow) and at the end (dark red) of the compression experiment.

7. Conclusion and Perspectives

In this thesis, Au-PNIPAM microgels were employed as colloidal building blocks to investigate microgels and their assembly at fluid interfaces. First, different Au-PNIPAM microgels were intensively characterized with focus on the internal morphology of the polymer shell. A deeper understanding of the shell structure could be a first step to better describe interactions of microgels at interfaces. Then, these microgels were utilized to prepare Bravais lattices of non-close-packed AuNP by a fluid interface-assisted assembly. Starting from a hexagonally ordered monolayer at the interface, different lattices were obtained by varying the transfer process, as well as the wettability of the substrates used. The last part of this thesis focused on the *in situ* investigation of assembled Au-PNIPAM microgels at the air/water interface. The effect of compression on the optical response of such monolayers was studied for a broad range of surface pressures.

In this first part of the thesis, Au-PNIPAM microgels with varying crosslinker content (16.7 mol% and 8 mol%) and core sizes were systematically studied by various techniques to get insights into the structure and properties of both the core and the shell. Information about the internal morphology of the shell is crucial to better understand the assembly of these microgels at fluid interfaces, where the characteristics of the shell govern the interfacial interactions. For that, Au-PNIPAM microgels were synthesized and the cores were overgrown *in situ* in the shell by a factor of approximately 6.5 in radius. Due to the high electron density of the gold cores, SAXS enabled the analysis of the form factor of the cores within the microgel shells. Temperature-dependent DLS confirmed the thermoresponsive behavior for all CS microgels independent of core size and revealed that the growth of the core did not significantly alter the overall hydrodynamic dimensions of the microgels. Extinction spectra confirmed that for microgels with small cores, the scattering of the shell dominated the optical response, while for microgels with overgrown cores, the LSPR of the cores became the dominant contribution. This change is attributed to the scaling of scattering (~ R^6) and absorption (~ R^3) of the core with the size of the core, while the scattering of the shell remained constant due to an unchanged hydrodynamic size. To get insights in the internal morphology of the shell in dependence of the temperature, temperature-dependent SANS measurements were performed. Here, the scattering was dominated by the shell, which allowed to extract density profiles of

the shell with adequate form factor models. The fuzzy sphere form factor model, known from literature,[89] failed to properly describe the form factor oscillations, as well as the mid *q* regime of the microgels with the small cores. In contrast, the exponential shell form factor model provided consistent description of the scattering curves over a broad range of temperatures. The model described the CS microgels with a homogeneously dense inner region of the shell, which then decays exponentially to the outside at low temperatures. At temperatures below the VPTT, the scattering profiles of the microgels with the overgrown cores showed significant deviations in the form factor oscillations, which could not be described by common form factor models. Moreover, increased correlation lengths for the microgels with overgrown cores were observed, indicating that the growth of the core altered both the internal structure of the shell and the dynamical fluctuations of the network. However, at temperatures above the VPTT, all microgel systems displayed a homogeneous polymer density in the shell. This suggested that the influence of the increased core size diminished in the collapsed state.

To extract information of the shell from the scattering curves of the microgels with overgrown cores, RMC simulations were used to compute density profiles. For microgels with small cores and all microgels in the collapsed state, simulation results were consistent with the model-derived profiles. In the microgels with overgrown cores, simulations revealed a denser polymer region around the core. This was attributed to the compression of polymer during the growth of the core – a feature also observed in TEM images. This local densification was more pronounced in microgels with higher crosslinker content. In contrast, lower crosslinker content allowed for greater movement and rearrangement of polymer chains during the increase in core size.

For further work, it would be of great interest to establish a form factor model from the simulated radial profiles. This form factor model could then be applied to describe the scattering profile of similar CS microgels. Additionally, simulations of the dynamics of the core growth could further elucidate the experimental process and the effect of core overgrowth on the microgel shell. For the microgel systems used in this work, experimental diameters of the core could not be increased beyond 100 nm *via* in situ overgrowth without compromising the integrity of the shell or the spherical shape of the cores. For this reason, simulating the maximum achievable core size within the shell would be of interest to explore potential size limitations and to assess whether

the densification of the polymer near the core becomes more pronounced with increasing core size. In further works, the influence of this dense polymer region on the interactions of microgels in bulk or at interfaces could be investigated. Another open question is whether the core is symmetrically centered inside of the microgel shell independent on the crosslinker content. This could be resolved by TEM and cryo-TEM images of the CS microgels. If not centered, its impact on the structural and optical behavior of such plasmonic CS microgels, particularly at fluid interfaces, needs to be further investigated.

The second part of this thesis focused on the fabrication of non-hexagonal 2D lattices of CS microgels by a controlled interface-assisted assembly method. The aim was to prepare all five Bravais lattices of non-close-packed AuNP, with an easy and fast bottom-up strategy applicable to other soft colloids. Au-PNIPAM microgels with overgrown cores were used for their enhanced LSPR behavior and assembled at the air/water interface into hexagonally ordered monolayers. Non-hexagonal lattices were achieved by deforming/stretching the monolayer during transfer onto substrates, with the final structure controlled by substrate wettability (contact angle) and transfer conditions. Hydrophilic substrates (contact angle < 90 °) yielded hexagonal lattices, while hydrophobic ones (> 90 °) produced oblique structures. Square, rectangular, and centered rectangular lattices were obtained using substrates with ~ 90 ° contact angle. To preserve the non-hexagonal monolayer structure during deposition, substrates were immersed through the interface and thermally annealed in the bulk phase before retraction to minimize capillary forces-induced rearrangement. This step was found to be crucial to realize lattices showing long-range order with only a few defects.

Extinction spectroscopy revealed distinct LSPR peaks for all five lattices of non-close-packed AuNPs. The experimental spectra were in good agreement with simulations aside from minor shifts due to differences in the refractive index (RI) environment and/or long-range resonance coupling effects. Further, CS microgels with larger shell thickness were used to prepare oblique lattices and to study the influence of lattice periodicity on the optical response. Increased shell size resulted in larger interparticle spacings and a shift of the peak to higher wavelengths in the extinction spectrum. The shift was attributed to weaker long-range electromagnetic coupling. The successful and reproducible preparation of lattices with the same order using differently sized microgels demonstrated the high versatility of the preparation

method. As the size of the shell significantly exceeded those of the core, the assembly process is governed by shell-shell interactions. Consequently, the periodicity of non-close-packed Bravais lattices can be tuned over a broad range of interparticle distances by adjusting the size of the shell. Furthermore, the optical response of an oblique lattice was investigated in different RI environments. By removal of the PNIPAM shell *via* plasma treatment, the LSPR peak of the non-close-packed bare AuNPs shifted to lower wavelengths compared to the peak of the same sample prior to the removal of the shell. This shift was solely attributed to the different RI environment of the AuNPs. Subsequent coating of the bare AuNPs with a polymer film as superstrate induced a narrow, redshifted SLR peak. SLR was enabled by plasmonic-diffractive coupling in the homogeneous RI environment around the AuNPs. This highlights the tunability of the optical response through controlled modification of the surrounding dielectric medium of the AuNPs. Given that the assembly process is dominated by shell–shell interactions, this interface-assisted assembly is not limited to plasmonic cores. It can be readily extended to other CS microgels, such as those with, e.g., silica cores, enabling the fabrication of non-close-packed, ordered lattices with tailored structural or photonic properties beyond plasmonic functionalities.

While the microstructure of transferred monolayers is typically characterized *ex situ* via microscopy, *in situ* analysis of monolayers at fluid interfaces remains challenging. For this reason, the last part of this thesis introduced a method to measure *in situ* extinction spectra of monolayers during compression at fluid interfaces and to indirectly correlate changes in the spectra to changes in the interfacial microstructure. Au-PNIPAM microgels were assembled at the air/water interface and extinction spectra were recorded at intervals of one second upon reduction of the surface area with 10 mm min^{-1}. This enabled to resolve shifts of the plasmonic peak in the sub-nm range, which corresponds to sub-nm changes in the interparticle distance at the interface. Furthermore, the extinction spectra, as well as the shifts in peak position and the changes in peak width within the spectra were linked to the surface pressure measured simultaneously. To compare *in situ* and *ex situ* results, a Langmuir-Blodgett deposition was performed over the same range of surface pressures. The microstructure of the transferred monolayer was visualized by AFM and extinction spectra were recorded to assess the optical response of the dried monolayer. Assuming that the microstructure on the substrate at low surface pressures

represented the interfacial structure, AFM images provided a reference value for calculating the $d_{c\text{-}c}$ of the microgels at the interface. It was further possible to calculate the $d_{c\text{-}c}$ across the compression isotherm under the assumption that the total number of microgels at the interface remains unchanged. This allowed for correlation of the peak position with interparticle spacing. The *in situ* spectra revealed a continuous shift of the peak position to lower wavelength during the compression. This indicated a continuous decrease of the interparticle spacing at the interface. In contrast, *ex situ* measurements exhibited a discontinuous spectral shift probably attributed to clustering of the microgels observed in AFM images. In combination with the results of the *in situ* measurements the clustering was identified as a drying artifact rather than an interfacial phenomenon, which was in stark contrast to previous works.[44, 46]

For the lowest compression, i.e., the largest available total interface area, the *in situ* extinction spectrum featured a sharp narrow peak that broadened upon compression. COMSOL simulations confirmed that at the highest interparticle spacing of this experiment, coupling between the LSPR mode of the AuNP cores and the in-plane diffraction mode resulted in a sharp SLR peak. Thus, the RI environment of the AuNP cores was sufficiently homogeneous to enable plasmonic-diffractive coupling. As $d_{c\text{-}c}$ decreased, the coupling diminished due to a reduced overlap of the two modes. To the best of our knowledge, this is the first time that SLR modes were detected for self-assembled plasmonic monolayers at fluid interfaces.

The strong agreement between experiment and simulation suggests the potential for an analytical model to predict LSPR behavior in similar systems. Furthermore, peak position in *in situ* extinction spectra could be used to deduce interparticle spacings at the interface for a given system. This would make it possible to tailor the microstructure of the monolayer on demand. The *in situ* extinction spectrometer presents a fast and non-destructive method to further investigate plasmonic CS microgels at fluid interfaces in the future. Due to the high sensitivity of the LSPR, any change in its wavelength would be direct feedback on any changes in the interactions of the microgels. With this methodology it might also be possible to not only gather information on optical coupling phenomena in dependence of monolayer compression, but also get insights into the phase behavior of microgels with, e.g., different softness. It is known that microgels with higher crosslinker density are stiffer, deform less at the interface and show steeper compression isotherms. Thus,

interfacial behavior in microgels of varying stiffness can be further elucidated by comparing compression isotherms and corresponding interfacial spectral responses.

This work has shown that core-shell microgels with sufficiently large gold nanoparticle cores are a) ideal building blocks to prepare non-hexagonal lattices of non-close-packed gold nanoparticles with pronounced extinction properties and b) allow for *in situ* spectroscopic analysis during monolayer compression at fluid interfaces.

8. References

1. A. Z. Pich and H. J. P. Adler, Composite aqueous microgels: an overview of recent advances in synthesis, characterization and application. *Polym Int* **2007**, 56 (3), 291-307.
2. A. Fernández-Barbero, I. J. Suárez, B. Sierra-Martín, A. Fernández-Nieves, F. J. de las Nieves, M. Marquez, J. Rubio-Retama and E. López-Cabarcos, Gels and microgels for nanotechnological applications. *Adv Colloid Interfac* **2009**, 147-48 88-108.
3. M. Karg and T. Hellweg, New "smart" poly(NIPAM) microgels and nanoparticle microgel hybrids: Properties and advances in characterisation. *Curr Opin Colloid In* **2009**, 14 (6), 438-450.
4. F. Scheffold, Pathways and challenges towards a complete characterization of microgels. *Nat Commun* **2020**, 11 (4315).
5. M. Karg, A. Pich, T. Hellweg, T. Hoare, L. A. Lyon, J. J. Crassous, D. Suzuki, R. A. Gumerov, S. Schneider, I. I. Potemkin and W. Richtering, Nanogels and Microgels: From Model Colloids to Applications, Recent Developments, and Future Trends. *Langmuir* **2019**, 35 (19), 6231-6255.
6. R. Pelton, Temperature-sensitive aqueous microgels. *Adv Colloid Interfac* **2000**, 85 (1), 1-33.
7. B. R. Saunders, N. Laajam, E. Daly, S. Teow, X. H. Hu and R. Stepto, Microgels: From responsive polymer colloids to biomaterials. *Adv Colloid Interfac* **2009**, 147-48 251-262.
8. L. A. Lyon and M. J. Serpe, Hydrogel Micro and Nanoparticles. *Wiley-VCH Verlag GmbH & Co. KGaA* **2012**.
9. J. Brijitta and P. Schurtenberger, Responsive hydrogel colloids: Structure, interactions, phase behavior, and equilibrium and nonequilibrium transitions of microgel dispersions. *Curr Opin Colloid In* **2019**, 40 87-103.
10. A. Fernandez-Nieves, H. M. Wyss, J. Mattsson and D. Weitz, Microgel Suspensions. *Wiley-VCH Verlag GmbH & Co. KGaA* **2011**, 1.
11. F. A. Plamper and W. Richtering, Functional Microgels and Microgel Systems. *Accounts Chem Res* **2017**, 50 (2), 131-140.
12. A. Pich, A. Tessier, V. Boyko, Y. Lu and H. J. P. Adler, Synthesis and characterization of poly(vinylcaprolactam)-based microgels exhibiting temperature and pH-sensitive properties. *Macromolecules* **2006**, 39 (22), 7701-7707.
13. Y. Hertle and T. Hellweg, Thermoresponsive copolymer microgels. *J Mater Chem B* **2013**, 1 (43), 5874-5885.
14. A. V. Petrunin, M. M. Schmidt, R. Schweins, J. E. Houston and A. Scotti, Self-Healing of Charged Microgels in Neutral and Charged Environments. *Langmuir* **2023**, 39 (22), 7530-7538.
15. R. Atkin, M. Bradley and B. Vincent, Core-shell particles having silica cores and pH-responsive poly(vinylpyridine) shells. *Soft Matter* **2005**, 1 (2), 160-165.
16. A. Fernández-Nieves, A. Fernández-Barbero, B. Vincent and F. J. de las Nieves, Charge controlled swelling of microgel particles. *Macromolecules* **2000**, 33 (6), 2114-2118.
17. T. Hoare and R. Pelton, Highly pH and temperature responsive microgels functionalized with vinylacetic acid. *Macromolecules* **2004**, 37 (7), 2544-2550.
18. R. H. Pelton and P. Chibante, Preparation of Aqueous Lattices with N-Isopropylacrylamide. *Colloid Surface* **1986**, 20 (3), 247-256.
19. M. Heskins and J. E. Guillet, Solution Properties of Poly(N-isopropylacrylamide). *Journal of Macromolecular Science: Part A - Chemistry* **1968**, 2 (8), 1441-1455.
20. A. Halperin, M. Kröger and F. M. Winnik, Poly(N-isopropylacrylamide) Phase Diagrams: Fifty Years of Research. *Angew Chem Int Edit* **2015**, 54 (51), 15342-15367.
21. E. Ponomareva, B. Tadgell, M. Hildebrandt, M. Krüsmann, S. Prévost, P. Mulvaney and M. Karg, The fuzzy sphere morphology is responsible for the increase in light scattering during the shrinkage of thermoresponsive microgels. *Soft Matter* **2022**, 18 (4), 807-825.
22. S. Sbeih, P. S. Mohanty, M. R. Morrow and A. Yethiraj, Structural parameters of soft PNIPAM microgel particles as a function of crosslink density. *J Colloid Interf Sci* **2019**, 552 781-793.
23. T. Brändel, M. Dirksen and T. Hellweg, Tuning the Swelling Properties of Smart Multiresponsive Core-Shell Microgels by Copolymerization. *Polymers-Basel* **2019**, 11 (8), 1269.
24. K. Kratz and W. Eimer, Swelling properties of colloidal poly(N-isopropylacrylamide) microgels in solution. *Ber Bunsen Phys Chem* **1998**, 102 (6), 848-854.
25. I. Varga, T. Gilányi, R. Mészáros, G. Filipcsei and M. Zrínyi, Effect of cross-link density on the internal structure of Poly(N-isopropylacrylamide) microgels. *J Phys Chem B* **2001**, 105 (38), 9071-9076.
26. F. Scheffold, P. Díaz-Leyva, M. Reufer, N. Ben Braham, I. Lynch and J. L. Harden, Brushlike Interactions between Thermoresponsive Microgel Particles. *Phys Rev Lett* **2010**, 104 (12), 128304.

27. M. J. Bergman, N. Gnan, M. Obiols-Rabasa, J. M. Meijer, L. Rovigatti, E. Zaccarelli and P. Schurtenberger, A new look at effective interactions between microgel particles. *Nat Commun* **2018**, 9 5039.
28. H. Senff and W. Richtering, Temperature sensitive microgel suspensions: Colloidal phase behavior and rheology of soft spheres. *J Chem Phys* **1999**, 111 (4), 1705-1711.
29. P. S. Mohanty, D. Paloli, J. J. Crassous, E. Zaccarelli and P. Schurtenberger, Effective interactions between soft-repulsive colloids: Experiments, theory, and simulations. *J Chem Phys* **2014**, 140 (9), 094901.
30. D. Lapkin, N. Mukharamova, D. Assalauova, S. Dubinina, J. Stellhorn, F. Westermeier, S. Lazarev, M. Sprung, M. Karg, I. A. Vartanyants and J. M. Meijer, Characterization of crystallization and melting of soft, thermoresponsive microgels by small-angle X-ray scattering. *Soft Matter* **2022**, 18 (8), 1591-1602.
31. M. Hildebrandt, D. P. Thuy, J. Kippenberger, T. L. Wigger, J. E. Houston, A. Scotti and M. Karg, Fluid-solid transitions in photonic crystals of soft, thermoresponsive microgels. *Soft Matter* **2023**, 19 (37), 7122-7135.
32. Y. F. Gao, X. Li and M. J. Serpe, Stimuli-responsive microgel-based etalons for optical sensing. *Rsc Adv* **2015**, 5 (55), 44074-44087.
33. Q. M. Zhang, W. D. Wang, Y. Q. Su, E. J. M. Hensen and M. J. Serpe, Biological Imaging and Sensing with Multiresponsive Microgels. *Chem Mater* **2016**, 28 (1), 259-265.
34. M. Dirksen, C. Dargel, L. Meier, T. Brändel and T. Hellweg, Smart microgels as drug delivery vehicles for the natural drug aescin: uptake, release and interactions. *Colloid Polym Sci* **2020**, 298 (6), 505-518.
35. J. Zhang and R. Pelton, Poly(N-isopropylacrylamide) microgels at the air-water interface. *Langmuir* **1999**, 15 (23), 8032-8036.
36. B. Brugger and W. Richtering, Emulsions stabilized by stimuli-sensitive poly(N-isopropylacrylamide)-co-methacrylic acid polymers: Microgels versus low molecular weight polymers. *Langmuir* **2008**, 24 (15), 7769-7777.
37. T. Ngai, H. Auweter and S. H. Behrens, Environmental responsiveness of microgel particles and particle-stabilized emulsions. *Macromolecules* **2006**, 39 (23), 8171-8177.
38. M. Destribats, V. Lapeyre, M. Wolfs, E. Sellier, F. Leal-Calderon, V. Ravaine and V. Schmitt, Soft microgels as Pickering emulsion stabilisers: role of particle deformability. *Soft Matter* **2011**, 7 (17), 7689-7698.
39. T. Ngai, S. H. Behrens and H. Auweter, Novel emulsions stabilized by pH and temperature sensitive microgels. *Chem Commun* **2005**, DOI: 10.1039/b412330a(3), 331-333.
40. B. Brugger, S. Rütten, K. H. Phan, M. Möller and W. Richtering, The Colloidal Suprastructure of Smart Microgels at Oil-Water Interfaces. *Angew Chem Int Edit* **2009**, 48 (22), 3978-3981.
41. K. Geisel, L. Isa and W. Richtering, Unraveling the 3D Localization and Deformation of Responsive Microgels at Oil/Water Interfaces: A Step Forward in Understanding Soft Emulsion Stabilizers. *Langmuir* **2012**, 28 (45), 15770-15776.
42. L. Isa, F. Lucas, R. Wepf and E. Reimhult, Measuring single-nanoparticle wetting properties by freeze-fracture shadow-casting cryo-scanning electron microscopy. *Nat Commun* **2011**, 2 (438).
43. C. Picard, P. Garrigue, M. C. Tatry, V. Lapeyre, S. Ravaine, V. Schmitt and V. Ravaine, Organization of Microgels at the Air-Water Interface under Compression: Role of Electrostatics and Cross-Linking Density. *Langmuir* **2017**, 33 (32), 7968-7981.
44. M. Rey, M. A. Fernández-Rodríguez, M. Steinacher, L. Scheidegger, K. Geisel, W. Richtering, T. M. Squires and L. Isa, Isostructural solid-solid phase transition in monolayers of soft core-shell particles at fluid interfaces: structure and mechanics. *Soft Matter* **2016**, 12 (15), 3545-3557.
45. N. Vogel, C. Fernández-López, J. Pérez-Juste, L. M. Liz-Marzán, K. Landfester and C. K. Weiss, Ordered Arrays of Gold Nanostructures from Interfacially Assembled Au@PNIPAM Hybrid Nanoparticles. *Langmuir* **2012**, 28 (24), 8985-8993.
46. A. Rauh, M. Rey, L. Barbera, M. Zanini, M. Karg and L. Isa, Compression of Hard Core-Soft Shell Nanoparticles at Liquid-Liquid Interfaces: Influence of the Shell Thickness. *Soft Matter* **2017**, 13 (1), 158-169.
47. L. Scheidegger, M. A. Fernández-Rodríguez, K. Geisel, M. Zanini, R. Elnathan, W. Richtering and L. Isa, Compression and deposition of microgel monolayers from fluid interfaces: particle size effects on interface microstructure and nanolithography. *Phys Chem Chem Phys* **2017**, 19 (13), 8671-8680.
48. M. A. Fernández-Rodríguez, R. Elnathan, R. Ditcovski, F. Grillo, G. M. Conley, F. Timpu, A. Rauh, K. Geisel, T. Ellenbogen, R. Grange, F. Scheffold, M. Karg, W. Richtering, N. H. Voelcker and L. Isa, Tunable 2D binary colloidal alloys for soft nanotemplating. *Nanoscale* **2018**, 10 (47), 22189-22195.
49. M. Karg, S. Jaber, T. Hellweg and P. Mulvaney, Surface Plasmon Spectroscopy of Gold-Poly-*N*-isopropylacrylamide Core-Shell Particles. *Langmuir* **2011**, 27 (2), 820-827.
50. M. Karg, T. Hellweg and P. Mulvaney, Self-Assembly of Tunable Nanocrystal Superlattices Using Poly-(NIPAM) Spacers. *Adv Funct Mater* **2011**, 21 (24), 4668-4676.

51. T. Honold, K. Volk, A. Rauh, J. P. S. Fitzgerald and M. Karg, Tunable Plasmonic Surfaces via Colloid Assembly. *J Mater Chem C* **2015**, 3 (43), 11449-11457.
52. R. Contreras-Cáceres, A. Sánchez-Iglesias, M. Karg, I. Pastoriza-Santos, J. Pérez-Juste, J. Pacifico, T. Hellweg, A. Fernández-Barbero and L. M. Liz-Marzán, Encapsulation and growth of gold nanoparticles in thermoresponsive microgels. *Adv Mater* **2008**, 20 (9), 1666-1670.
53. T. Honold, K. Volk, M. Retsch and M. Karg, Binary plasmonic honeycomb structures: High-resolution EDX mapping and optical properties. *Colloid Surface A* **2016**, 510 198-204.
54. K. Volk, J. P. S. Fitzgerald, M. Retsch and M. Karg, Time-Controlled Colloidal Superstructures: Long-Range Plasmon Resonance Coupling in Particle Monolayers. *Adv Mater* **2015**, 27 (45), 7332-7337.
55. E. Ponomareva, K. Volk, P. Mulvaney and M. Karg, Surface Lattice Resonances in Self-Assembled Gold Nanoparticle Arrays: Impact of Lattice Period, Structural Disorder, and Refractive Index on Resonance Quality. *Langmuir* **2020**, 36 (45), 13601-13612.
56. M. Dulle, S. Jaber, S. Rosenfeldt, A. Radulescu, S. Förster, P. Mulvaney and M. Karg, Plasmonic gold-poly(N-isopropylacrylamide) core-shell colloids with homogeneous density profiles: a small angle scattering study. *Phys Chem Chem Phys* **2015**, 17 (2), 1354-1367.
57. K. Volk, J. P. S. Fitzgerald, P. Ruckdeschel, M. Retsch, T. A. F. König and M. Karg, Reversible Tuning of Visible Wavelength Surface Lattice Resonances in Self-Assembled Hybrid Monolayers. *Adv Opt Mater* **2017**, 5 (9), 1600971.
58. C. R. Singh, T. Honold, T. P. Gujar, M. Retsch, A. Fery, M. Karg and M. Thelakkat, The role of colloidal plasmonic nanostructures in organic solar cells. *Phys Chem Chem Phys* **2016**, 18 (33), 23155-23163.
59. J. P. S. Fitzgerald and M. Karg, Plasmon resonance coupling phenomena in self-assembled colloidal monolayers. *Phys Status Solidi A* **2017**, 214 (8).
60. A. K. Yang, Z. Y. Li, M. P. Knudson, A. J. Hryn, W. J. Wang, K. Aydin and T. W. Odom, Unidirectional Lasing from Template-Stripped Two-Dimensional Plasmonic Crystals. *Acs Nano* **2015**, 9 (12), 11582-11588.
61. M. Mayer, M. J. Schnepf, T. A. F. König and A. Fery, Colloidal Self-Assembly Concepts for Plasmonic Metasurfaces. *Adv Opt Mater* **2019**, 7 (1).
62. D. Feller and M. Karg, Fluid Interface-Assisted Assembly of Soft Microgels: Recent Developments for Structures Beyond Hexagonal Packing. *Soft Matter* **2022**, 18 (34), 6301-6312.
63. M. A. Fernández-Rodríguez, M. N. Antonopoulou and L. Isa, Near-zero surface pressure assembly of rectangular lattices of microgels at fluid interfaces for colloidal lithography. *Soft Matter* **2021**, 17 (2), 335-340.
64. M. Rey, A. D. Law, D. M. A. Buzza and N. Vogel, Anisotropic Self-Assembly from Isotropic Colloidal Building Blocks. *J Am Chem Soc* **2017**, 139 (48), 17464-17473.
65. J. Harrer, S. Ciarella, M. Rey, H. Löwen, L. M. C. Janssen and N. Vogel, Collapse-induced phase transitions in binary interfacial microgel monolayers. *Soft Matter* **2021**, 17 (17), 4504-4516.
66. F. Grillo, M. A. Fernandez-Rodriguez, M. N. Antonopoulou, D. Gerber and L. Isa, Self-templating assembly of soft microparticles into complex tessellations. *Nature* **2020**, 582 (7811), 219-224.
67. K. Volk, F. Deißenbeck, S. Mandal, H. Löwen and M. Karg, Moiré and Honeycomb Lattices Through Self-Assembly of Hard-Core/Soft-Shell Microgels: Experiment and Simulation. *Phys Chem Chem Phys* **2019**, 21 (35), 19153-19162.
68. K. Volk, T. Honold, D. Feller and M. Karg, Surface Lattice Resonances in Self-Templated Plasmonic Honeycomb and Moire Lattices. *Adv Mater Interfaces* **2021**, 8 (13), 2100317.
69. M. Rey, X. A. Hou, J. S. J. Tang and N. Vogel, Interfacial arrangement and phase transitions of PNiPAm microgels with different crosslinking densities. *Soft Matter* **2017**, 13 (46), 8717-8727.
70. K. Geisel, W. Richtering and L. Isa, Highly ordered 2D microgel arrays: compression versus self-assembly. *Soft Matter* **2014**, 10 (40), 7968-7976.
71. S. Bochenek, A. Scotti, W. Ogieglo, M. A. Fernández-Rodríguez, M. F. Schulte, R. A. Gumerov, N. V. Bushuev, I. I. Potemkin, M. Wessling, L. Isa and W. Richtering, Effect of the 3D Swelling of Microgels on Their 2D Phase Behavior at the Liquid-Liquid Interface. *Langmuir* **2019**, 35 (51), 16780-16792.
72. K. Kuk, V. Abgarjan, L. Gregel, Y. Zhou, V. Carrasco Fadanelli, I. Buttinoni and M. Karg, Compression of Colloidal Monolayers at Liquid Interfaces: *In Situ* vs. *Ex Situ* Investigation. *Soft Matter* **2023**, 19 (2), 175-188.
73. A. Rubio-Andrés, D. Bastos-González and M. A. Fernandez-Rodriguez, In-situ characterization of microgel monolayers: Controlling isostructural phase transitions for homogeneous crystal drying patterns. *J Colloid Interf Sci* **2025**, 688 328-340.
74. T. Kawamoto, K. Yanagi, Y. Nishizawa, H. Minato and D. Suzuki, The compression of deformed microgels at an air/water interface. *Chem Commun* **2023**, 59 (89), 13289-13292.
75. J. Vialetto, S. N. Ramakrishna and L. Isa, In situ imaging of the three-dimensional shape of soft responsive particles at fluid interfaces by atomic force microscopy. *Sci Adv* **2022**, 8 (45), 1-10.

76. A. Rauh, T. Honold and M. Karg, Seeded Precipitation Polymerization for the Synthesis of Gold-Hydrogel Core-Shell Particles: The Role of Surface Functionalization and Seed Concentration. *Colloid Polym Sci* **2016**, 294 (1), 37-47.
77. M. E. J. Hummel, C. Stelling, B. A. F. Kopera, F. A. Nutz, M. Karg, M. Retsch and S. Förster, Ordered Particle Arrays via a Langmuir Transfer Process: Access to Any Two-Dimensional Bravais Lattice. *Langmuir* **2019**, 35 (4), 973-979.
78. D. A. Dillard, A. V. Pocius and M. Chaudhury, Adhesion Science and Engineering. *Elsevier Science B.V.* **2002**, 2.
79. M. Stieger, J. S. Pedersen, P. Lindner and W. Richtering, Are thermoresponsive microgels model systems for concentrated colloidal suspensions? A rheology and small-angle neutron scattering study. *Langmuir* **2004**, 20 (17), 7283-7292.
80. C. L. Bassani, G. van Anders, U. Banin, D. Baranov, Q. Chen, M. Dijkstra, M. S. Dimitriyev, E. Efrati, J. Faraudo, O. L. Gang, N. Gaston, R. Golestanian, G. I. Guerrero-Garcia, M. Gruenwald, A. Haji-Akbari, M. Ibañez, M. Karg, T. Kraus, B. Lee, R. C. Van Lehn, R. J. Macfarlane, B. M. Mognetti, A. Nikoubashman, S. Osat, O. V. Prezhdo, G. M. Rotskoff, L. Saiz, A. C. Shi, S. Skrabalak, I. I. Smalyukh, M. Tagliazucchi, D. V. Talapin, A. V. Tkachenko, S. Tretiak, D. Vaknin, A. Widmer-Cooper, G. C. L. Wong, X. C. Ye, S. Zhou, E. Rabani, M. Engel and A. Travesset, Nanocrystal Assemblies: Current Advances and Open Problems. *Acs Nano* **2024**, 18 (23), 14791-14840.
81. K. Kratz, T. Hellweg and W. Eimer, Influence of charge density on the swelling of colloidal poly(N-isopropylacrylamide-co-acrylic acid) microgels. *Colloid Surface A* **2000**, 170 (2-3), 137-149.
82. T. Hoare and R. Pelton, Titrametric characterization of pH-induced phase transitions in functionalized microgels. *Langmuir* **2006**, 22 (17), 7342-7350.
83. M. Shibayama, F. Ikkai, S. Inamoto, S. Nomura and C. C. Han, pH and salt concentration dependence of the microstructure of poly(N-isopropylacrylamide-co-acrylic acid) gels. *J Chem Phys* **1996**, 105 (10), 4358-4366.
84. M. Karg, I. Pastoriza-Santos, B. Rodriguez-González, R. von Klitzing, S. Wellert and T. Hellweg, Temperature, pH, and ionic strength induced changes of the swelling behavior of PNIPAM-poly(allylacetic acid) copolymer microgels. *Langmuir* **2008**, 24 (12), 6300-6306.
85. C. Wu and S. Q. Zhou, Volume phase transition of swollen gels: Discontinuous or continuous? *Macromolecules* **1997**, 30 (3), 574-576.
86. M. Karg, I. Pastoriza-Santos, L. M. Liz-Marzán and T. Hellweg, A versatile approach for the preparation of thermosensitive PNIPAM core-shell microgels with nanoparticle cores. *Chemphyschem* **2006**, 7 (11), 2298-2301.
87. M. Karg, S. Wellert, I. Pastoriza-Santos, A. Lapp, L. M. Liz-Marzán and T. Hellweg, Thermoresponsive core-shell microgels with silica nanoparticle cores: size, structure, and volume phase transition of the polymer shell. *Phys Chem Chem Phys* **2008**, 10 (44), 6708-6716.
88. X. Wu, R. H. Pelton, A. E. Hamielec, D. R. Woods and W. Mcphee, The Kinetics of Poly(N-Isopropylacrylamide) Microgel Latex Formation. *Colloid Polym Sci* **1994**, 272 (4), 467-477.
89. M. Stieger, W. Richtering, J. S. Pedersen and P. Lindner, Small-angle neutron scattering study of structural changes in temperature sensitive microgel colloids. *J Chem Phys* **2004**, 120 (13), 6197-6206.
90. N. Boon and P. Schurtenberger, Swelling of micro-hydrogels with a crosslinker gradient. *Phys Chem Chem Phys* **2017**, 19 (35), 23740-23746.
91. M. Cors, L. Wiehemeier, Y. Hertle, A. Feoktystov, F. Cousin, T. Hellweg and J. Oberdisse, Determination of Internal Density Profiles of Smart Acrylamide-Based Microgels by Small-Angle Neutron Scattering: A Multishell Reverse Monte Carlo Approach. *Langmuir* **2018**, 34 (50), 15403-15415.
92. J. Kohlbrecher and I. Bressler, SASfit: A program for fitting simple structural models to small angle scattering data, Paul Scherrer Institut, Laboratory for Neutron Scattering. *Paul Scherrer Institut* **2008**.
93. K. Kratz, T. Hellweg and W. Eimer, Structural changes in PNIPAM microgel particles as seen by SANS, DLS, and EM techniques. *Polymer* **2001**, 42 (15), 6631-6639.
94. T. Hellweg, K. Kratz, S. Pouget and W. Eimer, Internal dynamics in colloidal PNIPAM microgel particles immobilised in mesoscopic crystals. *Colloid Surface A* **2002**, 202 (2-3), 223-232.
95. N. Dingenouts, C. Norhausen and M. Ballauff, Observation of the volume transition in thermosensitive core-shell latex particles by small-angle X-ray scattering. *Macromolecules* **1998**, 31 (25), 8912-8917.
96. N. Dingenouts, S. Seelenmeyer, I. Deike, S. Rosenfeldt, M. Ballauff, P. Lindner and T. Narayanan, Analysis of thermosensitive core-shell colloids by small-angle neutron scattering including contrast variation. *Phys Chem Chem Phys* **2001**, 3 (7), 1169-1174.
97. M. Siebenbürger, M. Fuchs and M. Ballauff, Core-shell microgels as model colloids for rheological studies (vol 8, pg 4014, 2012). *Soft Matter* **2012**, 8 (48), 12133-12133.
98. T. Hellweg, C. D. Dewhurst, W. Eimer and K. Kratz, PNIPAM-co-polystyrene core-shell microgels: Structure, swelling behavior, and crystallization. *Langmuir* **2004**, 20 (11), 4330-4335.

99. M. Laurenti, P. Guardia, R. Contreras-Cáceres, J. Pérez-Juste, A. Fernandez-Barbero, E. Lopez-Cabarcos and J. Rubio-Retama, Synthesis of Thermosensitive Microgels with a Tunable Magnetic Core. *Langmuir* **2011**, 27 (17), 10484-10491.
100. N. Carl, J. Sindram, M. Gallei, S. U. Egelhaaf and M. Karg, From normal diffusion to superdiffusion: Photothermal heating of plasmonic core-shell microgels. *Phys Rev E* **2019**, 100 (5), 052605.
101. M. Magnozzi, Y. Brasse, T. A. F. König, F. Bisio, E. Bittrich, A. Fery and M. Canepa, Plasmonics of Au/Polymer Core/Shell Nanocomposites for Thermoresponsive Hybrid Metasurfaces. *Acs Appl Nano Mater* **2020**, 3 (2), 1674-1682.
102. M. Karg, Multifunctional inorganic/organic hybrid microgels. *Colloid Polym Sci* **2012**, 290 (8), 673-688.
103. J. Dubbert, K. Nothdurft, M. Karg and W. Richtering, Core-Shell-Shell and Hollow Double-Shell Microgels with Advanced Temperature Responsiveness. *Macromol Rapid Comm* **2015**, 36 (2), 159-164.
104. J. Dubbert, T. Honold, J. S. Pedersen, A. Radulescu, M. Drechsler, M. Karg and W. Richtering, How Hollow Are Thermoresponsive Hollow Nanogels? *Macromolecules* **2014**, 47 (24), 8700-8708.
105. M. Toma, U. Jonas, A. Mateescu, W. Knoll and J. Dostalek, Active Control of SPR by Thermoresponsive Hydrogels for Biosensor Applications. *J Phys Chem C* **2013**, 117 (22), 11705-11712.
106. K. A. Willets and R. P. Van Duyne, Localized surface plasmon resonance spectroscopy and sensing. *Annu Rev Phys Chem* **2007**, 58 267-297.
107. A. Danilov, G. Tselikov, F. Wu, V. G. Kravets, I. Ozerov, F. Bedu, A. N. Grigorenko and A. V. Kabashin, Ultra-narrow surface lattice resonances in plasmonic metamaterial arrays for biosensing applications. *Biosens Bioelectron* **2018**, 104 102-112.
108. P. Drude, Zur Elektronentheorie der Metalle. *Annalen der Physik* **1900**, 306 566-613.
109. S. A. Maier, Plasmonics: Fundamentals and Applications. *Springer New York, NY* 1.
110. V. G. Kravets, A. V. Kabashin, W. L. Barnes and A. N. Grigorenko, Plasmonic Surface Lattice Resonances: A Review of Properties and Applications. *Chem Rev* **2018**, 118 (12), 5912-5951.
111. B. I. Bleaney and B. Bleaney, Electricity and magnetism. *Oxford University Press* **1965**, 2 (3).
112. C. F. Bohren and D. R. Huffman, Absorption and Scattering of Light by Small Particles. *John Wiley & Sons, Inc.* **1983**.
113. C. L. Nehl and J. H. Hafner, Shape-dependent plasmon resonances of gold nanoparticles. *J Mater Chem* **2008**, 18 (21), 2415-2419.
114. J. J. Mock, M. Barbic, D. R. Smith, D. A. Schultz and S. Schultz, Shape effects in plasmon resonance of individual colloidal silver nanoparticles. *J Chem Phys* **2002**, 116 (15), 6755-6759.
115. B. Rodríguez-González, A. Burrows, M. Watanabe, C. J. Kiely and L. M. Liz-Marzán, Multishell bimetallic AuAg nanoparticles: synthesis, structure and optical properties. *J Mater Chem* **2005**, 15 (17), 1755-1759.
116. K. L. Kelly, E. Coronado, L. L. Zhao and G. C. Schatz, The optical properties of metal nanoparticles: The influence of size, shape, and dielectric environment. *J Phys Chem B* **2003**, 107 (3), 668-677.
117. J. Rodríguez-Fernández, J. Pérez-Juste, F. J. G. de Abajo and L. M. Liz-Marzán, Seeded growth of submicron Au colloids with quadrupole plasmon resonance modes. *Langmuir* **2006**, 22 (16), 7007-7010.
118. P. Mulvaney, Surface plasmon spectroscopy of nanosized metal particles. *Langmuir* **1996**, 12 (3), 788-800.
119. M. A. Moram and M. E. Vickers, X-ray diffraction of III-nitrides. *Rep Prog Phys* **2009**, 72 (3).
120. Y. Z. Chu, E. Schonbrun, T. Yang and K. B. Crozier, Experimental observation of narrow surface plasmon resonances in gold nanoparticle arrays. *Appl Phys Lett* **2008**, 93 (18).
121. K. Volk, J. P. S. Fitzgerald and M. Karg, In-Plane Surface Lattice and Higher Order Resonances in Self Assembled Plasmonic Monolayers: From Substrate-Supported to Free-Standing Thin Films. *Acs Appl Mater Inter* **2019**, 11 (17), 16096-16106.
122. S. R. K. Rodriguez, A. Abass, B. Maes, O. T. A. Janssen, G. Vecchi and J. G. Rivas, Coupling Bright and Dark Plasmonic Lattice Resonances. *Phys Rev X* **2011**, 1 (2).
123. B. Auguié and W. L. Barnes, Collective resonances in gold nanoparticle arrays. *Phys Rev Lett* **2008**, 101 (14), 143902.
124. W. J. Wang, M. Ramezani, A. I. Väkeväinen, P. Törmä, J. G. Rivas and T. W. Odom, The rich photonic world of plasmonic nanoparticle arrays. *Mater Today* **2018**, 21 (3), 303-314.
125. W. J. Wang, N. Watkins, A. K. Yang, R. D. Schaller, G. C. Schatz and T. W. Odom, Ultrafast Dynamics of Lattice Plasmon Lasers. *J Phys Chem Lett* **2019**, 10 (12), 3301-3306.
126. C. Sönnichsen, T. Franzl, T. Wilk, G. von Plessen, J. Feldmann, O. Wilson and P. Mulvaney, Drastic reduction of plasmon damping in gold nanorods *Phys Rev Lett* **2002**, 88 (7), 077402.

127. A. I. Väkeväinen, R. J. Moerland, H. T. Rekola, A. P. Eskelinen, J. P. Martikainen, D. H. Kim and P. Törmä, Plasmonic Surface Lattice Resonances at the Strong Coupling Regime. *Nano Lett* **2014**, 14 (4), 1721-1727.
128. J. O. Grepstad, M. M. Greve, B. Holst, I. R. Johansen, O. Solgaard and A. Sudbo, Finite-size limitations on Quality Factor of guided resonance modes in 2D Photonic Crystals. *Opt Express* **2013**, 21 (20), 23640-23654.
129. S. L. Zou, N. Janel and G. C. Schatz, Silver nanoparticle array structures that produce remarkably narrow plasmon lineshapes. *J Chem Phys* **2004**, 120 (23), 10871-10875.
130. S. R. K. Rodriguez, M. C. Schaafsma, A. Berrier and J. G. Rivas, Collective Resonances in Plasmonic Crystals: Size Matters. *Physica B* **2012**, 407 (20), 4081-4085.
131. M. Gouy, Sur la constitution de la charge électrique à la surface d'un électrolyte. *J. Phys. Theor. Appl.* **1910**, 9 (1), 457-468.
132. H.-J. Butt, K. Graf and M. Kappl, Physics and Chemistry of Interfaces. *Wiley-VCH Verlag GmbH & Co. KGaA* **2003**, 2.
133. V. A. Hernáandez, An overview of surface forces and the DLVO theory. *Chemtexts* **2023**, 9 (4).
134. B. Derjaguin and L. Landau, Theory of the Stability of Strongly Charged Lyophobic Sols and of the Adhesion of Strongly Charged-Particles in Solutions of Electrolytes. *Prog Surf Sci* **1993**, 43 (1-4), 30-59.
135. G. Lagaly, O. Schulz and R. Zimehl, in *Dispersionen und Emulsionen: Eine Einführung in die Kolloidik feinverteilter Stoffe einschließlich der Tonminerale*, Steinkopff, Heidelberg, 1997, pp. 15-73.
136. E. Guzmán, I. Abelenda-Núñez, A. Maestro, F. Ortega, A. Santamaria and R. G. Rubio, Particle-laden fluid/fluid interfaces: physico-chemical foundations. *J Phys-Condens Mat* **2021**, 33 (33),
137. E. J. W. Verwey and J. T. G. Overbeek, Theory of the Stability of Lyophobic Colloids. *J Phys Colloid Chem* **1948**.
138. B. W. Ninham, On progress in forces since the DLVO theory. *Adv Colloid Interfac* **1999**, 83 (1-3), 1-17.
139. E. Dickinson and L. Eriksson, Particle Flocculation by Adsorbing Polymers. *Adv Colloid Interfac* **1991**, 34 1-29.
140. A. Rauh, N. Carl, R. Schweins and M. Karg, Role of Absorbing Nanocrystal Cores in Soft Photonic Crystals: A Spectroscopy and SANS Study. *Langmuir* **2018**, 34 (3), 854-867.
141. P. Pieranski, Two-Dimensional Interfacial Colloidal Crystals. *Phys Rev Lett* **1980**, 45 (7), 569-572.
142. R. McGorty, J. Fung, D. Kaz and V. N. Manoharan, Colloidal self-assembly at an interface. *Mater Today* **2010**, 13 (6), 34-42.
143. N. Vogel, C. K. Weiss and K. Landfester, From Soft to Hard: The Generation of Functional and Complex Colloidal Monolayers for Nanolithography. *Soft Matter* **2012**, 8 (15), 4044-4061.
144. N. Vogel, M. Retsch, C. A. Fustin, A. del Campo and U. Jonas, Advances in Colloidal Assembly: The Design of Structure and Hierarchy in Two and Three Dimensions. *Chem Rev* **2015**, 115 (13), 6265-6311.
145. P. A. Kralchevsky and K. Nagayama, Capillary Forces between Colloidal Particles. *Langmuir* **1994**, 10 (1), 23-36.
146. P. A. Kralchevsky and K. Nagayama, Capillary interactions between particles bound to interfaces, liquid films and biomembranes. *Adv Colloid Interfac* **2000**, 85 (2-3), 145-192.
147. K. D. Danov, P. A. Kralchevsky, B. N. Naydenov and G. Brenn, Interactions between particles with an undulated contact line at a fluid interface: Capillary multipoles of arbitrary order. *J Colloid Interf Sci* **2005**, 287 (1), 121-134.
148. H. Minato, M. Murai, T. Watanabe, S. Matsui, M. Takizawa, T. Kureha and D. Suzuki, The deformation of hydrogel microspheres at the air/water interface. *Chem Commun* **2018**, 54 (8), 932-935.
149. M. Rey, M. A. Fernandez-Rodriguez, M. Karg, L. Isa and N. Vogel, Poly-*N*-isopropylacrylamide Nanogels and Microgels at Fluid Interfaces. *Accounts Chem Res* **2020**, 53 (2), 414-424.
150. R. W. Style, L. Isa and E. R. Dufresne, Adsorption of soft particles at fluid interfaces. *Soft Matter* **2015**, 11 (37), 7412-7419.
151. A. Scotti, M. F. Schulte, C. G. Lopez, J. J. Crassous, S. Bochenek and W. Richtering, How Softness Matters in Soft Nanogels and Nanogel Assemblies. *Chem Rev* **2022**, 122 (13), 11675-11700.
152. H. J. Butt, W. J. P. Barnes, A. del Campo, M. Kappl and F. Schönfeld, Capillary forces between soft, elastic spheres. *Soft Matter* **2010**, 6 (23), 5930-5936.
153. H. J. Butt, Capillary forces: Influence of roughness and heterogeneity. *Langmuir* **2008**, 24 (9), 4715-4721.
154. F. Camerin, N. Gnan, J. Ruiz-Franco, A. Ninarello, L. Rovigatti and E. Zaccarelli, Microgels at Interfaces Behave as 2D Elastic Particles Featuring Reentrant Dynamics. *Phys Rev X* **2020**, 10 (3), 031012.

155. S. A. Vasudevan, A. Rauh, M. Kröger, M. Karg and L. Isa, Dynamics and Wetting Behavior of Core-Shell Soft Particles at a Fluid-Fluid Interface. *Langmuir* **2018**, 34 (50), 15370-15382.
156. S. Schmidt, H. Motschmann, T. Hellweg and R. von Klitzing, Thermoresponsive surfaces by spin-coating of PNIPAM-co-PAA microgels: A combined AFM and ellipsometry study. *Polymer* **2008**, 49 (3), 749-756.
157. S. Jaber, M. Karg, A. Morfa and P. Mulvaney, 2D assembly of gold-PNIPAM core-shell nanocrystals. *Phys Chem Chem Phys* **2011**, 13 (13), 5576-5578.
158. A. Burmistrova and R. von Klitzing, Control of number density and swelling/shrinking behavior of P(NIPAM-AAc) particles at solid surfaces. *J Mater Chem* **2010**, 20 (17), 3502-3507.
159. J. Sindram, K. Volk, P. Mulvaney and M. Karg, Silver Nanoparticle Gradient Arrays: Fluorescence Enhancement of Organic Dyes. *Langmuir* **2019**, 35 (26), 8776-8783.
160. A. Mihi, M. Ocaña and H. Míguez, Oriented colloidal-crystal thin films by spin-coating microspheres dispersed in volatile media. *Adv Mater* **2006**, 18 (17), 2244-2249.
161. K. Horigome and D. Suzuki, Drying Mechanism of Poly(N-isopropylacrylamide) Microgel Dispersions. *Langmuir* **2012**, 28 (36), 12962-12970.
162. M. Takizawa, Y. Sazuka, K. Horigome, Y. Sakurai, S. Matsui, H. Minato, T. Kureha and D. Suzuki, Self-Organization of Soft Hydrogel Microspheres during the Evaporation of Aqueous Droplets. *Langmuir* **2018**, 34 (15), 4515-4525.
163. H. Minato, M. Takizawa, S. Hiroshige and D. Suzuki, Effect of Charge Groups Immobilized in Hydrogel Microspheres during the Evaporation of Aqueous Sessile Droplets. *Langmuir* **2019**, 35 (32), 10412-10423.
164. N. D. Denkov, O. D. Velev, P. A. Kralchevsky, I. B. Ivanov, H. Yoshimura and K. Nagayama, Mechanism of Formation of 2-Dimensional Crystals from Latex-Particles on Substrates. *Langmuir* **1992**, 8 (12), 3183-3190.
165. R. Micheletto, H. Fukuda and M. Ohtsu, A Simple Method for the Production of a 2-Dimensional, Ordered Array of Small Latex-Particles. *Langmuir* **1995**, 11 (9), 3333-3336.
166. J. Hur and Y. Y. Won, Fabrication of high-quality non-close-packed 2D colloid crystals by template-guided Langmuir-Blodgett particle deposition. *Soft Matter* **2008**, 4 (6), 1261-1269.
167. E. Armstrong, W. Khunsin, M. Osiak, M. Blömker, C. M. S. Torres and C. O'Dwyer, Ordered 2D Colloidal Photonic Crystals on Gold Substrates by Surfactant-Assisted Fast-Rate Dip Coating. *Small* **2014**, 10 (10), 1895-1901.
168. L. Malaquin, T. Kraus, H. Schmid, E. Delamarche and H. Wolf, Controlled particle placement through convective and capillary assembly. *Langmuir* **2007**, 23 (23), 11513-11521.
169. B. G. Prevo and O. D. Velev, Controlled, rapid deposition of structured coatings from micro- and nanoparticle suspensions. *Langmuir* **2004**, 20 (6), 2099-2107.
170. X. Zhang, J. H. Zhang, D. F. Zhu, X. A. Li, X. M. Zhang, T. Q. Wang and B. Yang, A Universal Approach To Fabricate Ordered Colloidal Crystals Arrays Based on Electrostatic Self-Assembly. *Langmuir* **2010**, 26 (23), 17936-17942.
171. K. M. Chen, X. P. Jiang, L. C. Kimerling and P. T. Hammond, Selective self-organization of colloids on patterned polyelectrolyte templates. *Langmuir* **2000**, 16 (20), 7825-7834.
172. X. H. Meng and D. Qiu, Gas-Flow-Induced Reorientation to Centimeter-Sized Two-Dimensional Colloidal Single Crystal of Polystyrene Particle. *Langmuir* **2014**, 30 (11), 3019-3023.
173. J. T. Zhang, L. L. Wang, D. N. Lamont, S. S. Velankar and S. A. Asher, Fabrication of Large-Area Two-Dimensional Colloidal Crystals. *Angew Chem Int Edit* **2012**, 51 (25), 6117-6120.
174. M. Retsch, Z. C. Zhou, S. Rivera, M. Kappl, X. S. Zhao, U. Jonas and Q. Li, Fabrication of Large-Area, Transferable Colloidal Monolayers Utilizing Self-Assembly at the Air/Water Interface. *Macromol Chem Phys* **2009**, 210 (3-4), 230-241.
175. N. Vogel, S. Goerres, K. Landfester and C. K. Weiss, A Convenient Method to Produce Close- and Non-close-Packed Monolayers using Direct Assembly at the Air-Water Interface and Subsequent Plasma-Induced Size Reduction. *Macromol Chem Phys* **2011**, 212 (16), 1719-1734.
176. E. Sirotkin, J. D. Apweiler and F. Y. Ogrin, Macroscopic Ordering of Polystyrene Carboxylate-Modified Nanospheres Self-Assembled at the Water-Air Interface. *Langmuir* **2010**, 26 (13), 10677-10683.
177. D. Feller, M. Otten, M. S. Dimitriyev and M. Karg, Non-close-packed plasmonic Bravais lattices through a fluid interface-assisted colloidal assembly and transfer process. *Colloid Polym Sci* **2024**, 302.
178. E. A. Jagla, Phase behavior of a system of particles with core collapse. *Phys Rev E* **1998**, 58 (2), 1478-1486.
179. E. A. Jagla, Minimum energy configurations of repelling particles in two dimensions. *J Chem Phys* **1999**, 110 (1), 451-456.
180. F. Pinaud, K. Geisel, P. Massé, B. Catargi, L. Isa, W. Richtering, V. Ravaine and V. Schmitt, Adsorption of microgels at an oil-water interface: correlation between packing and 2D elasticity. *Soft Matter* **2014**, 10 (36), 6963-6974.

181. K. Kuk, J. Ringling, K. Graeff, S. Haensch, V. Carrasco-Fadanelli, A. A. Rudov, I. I. Potemkin, R. von Klitzing, I. Buttinoni and M. Karg, Drying of Soft Colloidal Films. *Adv Sci* **2024**, 11 (47), 2406977.
182. K. Zielinska, H. H. Sun, R. A. Campbell, A. Zarbakhsh and M. Resmini, Smart nanogels at the air/water interface: structural studies by neutron reflectivity. *Nanoscale* **2016**, 8 (9), 4951-4960.
183. S. Bochenek, F. Camerin, E. Zaccarelli, A. Maestro, M. M. Schmidt, W. Richtering and A. Scotti, In-situ study of the impact of temperature and architecture on the interfacial structure of microgels. *Nat Commun* **2022**, 13 (1).
184. M. S. H. Akash and K. Rehman, Ultraviolet-Visible (UV-VIS) Spectroscopy. In: Essentials of Pharmaceutical Analysis. *Springer Nature* **2020**,
185. H.-H. Perkampus, UV-VIS Spectroscopy and Its Applications. *Springer Berlin, Heidelberg* **2012**, 1.
186. W. Schärtl, Light Scattering from Polymer Solutions and Nanoparticle Dispersions. *Springer-Verlag* **2007**.
187. P. Lindner and T. Zemb, Neutrons, X-rays and Light: Scattering Methods Applied to Soft Condensed Matter *North-Holland Delta Series* **2002**.
188. I. W. Hamley, Small-Angle Scattering. *John Wiley & Sons* **2021**.
189. O. Glatter, Scattering Methods and their Application in Colloid and Interface Science. *Elsevier Inc.* **2018**.
190. A. Guinier and G. Fournet, Small-angle scattering of X-rays. *John Wiley & Sons, Inc.* **1955**.
191. H. Schnablegger and Y. Singh, The SAXS Guide. *Anton Paar GmbH* **2023**.
192. A. J. Allen, F. Zhang, R. J. Kline, W. F. Guthrie and J. Ilavsky, NIST Standard Reference Material 3600: Absolute Intensity Calibration Standard for Small-Angle X-ray Scattering. *J Appl Crystallogr* **2017**, 50 462-474.
193. A. Scotti, Characterization of the volume fraction of soft deformable microgels by means of small-angle neutron scattering with contrast variation. *Soft Matter* **2021**, 17 (22), 5548-5559.
194. S. Nöjd, P. Holmqvist, N. Boon, M. Obiols-Rabasa, P. S. Mohanty, R. Schweins and P. Schurtenberger, Deswelling behaviour of ionic microgel particles from low to ultra-high densities. *Soft Matter* **2018**, 14 (20), 4150-4159.
195. M. Shibayama, T. Tanaka and C. C. Han, Small-Angle Neutron-Scattering Study on Poly(N-Isopropyl Acrylamide) Gels near Their Volume-Phase Transition-Temperature. *J Chem Phys* **1992**, 97 (9), 6829-6841.
196. M. Daoud, J. P. Cotton, B. Farnoux, G. Jannink, G. Sarma, H. Benoit, R. Duplessix, C. Picot and P. G. D. Gennes, Solutions of Flexible Polymers - Neutron Experiments and Interpretation. *Macromolecules* **1975**, 8 (6), 804-818.
197. A. M. Hecht, R. Duplessix and E. Geissler, Structural Inhomogeneities in the Range 2.5-2500 Å in Polyacrylamide Gels. *Macromolecules* **1985**, 18 (11), 2167-2173.
198. M. Hamidi, A. Azadi and P. Rafiei, Hydrogel nanoparticles in drug delivery. *Adv Drug Deliver Rev* **2008**, 60 (15), 1638-1649.
199. J. K. Oh, R. Drumright, D. J. Siegwart and K. Matyjaszewski, The development of microgels/nanogels for drug delivery applications. *Prog Polym Sci* **2008**, 33 (4), 448-477.
200. F. Camerin, M. A. Fernández-Rodríguez, L. Rovigatti, M. N. Antonopoulou, N. Gnan, A. Ninarello, L. Isa and E. Zaccarelli, Microgels Adsorbed at Liquid-Liquid Interfaces: A Joint Numerical and Experimental Study. *Acs Nano* **2019**, 13 (4), 4548-4559.
201. V. G. Kravets, F. Schedin and A. N. Grigorenko, Extremely Narrow Plasmon Resonances Based on Diffraction Coupling of Localized Plasmons in Arrays of Metallic Nanoparticles. *Phys Rev Lett* **2008**, 101 (8), 087403.
202. M. Hildebrandt, S. Lazarev, J. Pérez, I. A. Vartanyants, J. M. Meijer and M. Karg, SAXS Investigation of Core-Shell Microgels with High Scattering Contrast Cores: Access to Structure Factor and Volume Fraction. *Macromolecules* **2022**, 55 (7), 2959-2969.
203. L. A. Lyon, J. D. Debord, S. B. Debord, C. D. Jones, J. G. McGrath and M. J. Serpe, Microgel colloidal crystals. *J Phys Chem B* **2004**, 108 (50), 19099-19108.
204. N. Welsch, A. Wittemann and M. Ballauff, Enhanced Activity of Enzymes Immobilized in Thermoresponsive Core-Shell Microgels. *J Phys Chem B* **2009**, 113 (49), 16039-16045.
205. N. Welsch, M. Ballauff and Y. Lu, Microgels as Nanoreactors: Applications in Catalysis. *Adv Polym Sci* **2010**, 234 129-163.
206. S. V. Nikolov, A. Fernandez-Nieves and A. Alexeev, Behavior and mechanics of dense microgel suspensions. *P Natl Acad Sci USA* **2020**, 117 (44), 27096-27103.
207. J. Turkevich, P. C. Stevenson and J. Hillier, A Study of the Nucleation and Growth Processes in the Synthesis of Colloidal Gold. *Discuss Faraday Soc* **1951**, (11), 55-75.
208. C. A. Schneider, W. S. Rasband and K. W. Eliceiri, NIH Image to ImageJ: 25 Years of Image Analysis. *Nat Methods* **2012**, 9 (7), 671-675.
209. M. Doucet, J. H. Cho, G. Alina, Z. Attala, J. Bakker, P. Beaucage, W. Bouwman, R. Bourne, P. Butler, I. Cadwallader-Jones, K. Campbell, T. Cooper-Benun, C. Durniak, L. Forster, P. Gilbert, M. Gonzalez, R. Heenan, A. Jackson, S. King, P. Kienzle, J. Krzywon, B. Maranville, N. Martinez,

R. Murphy, T. Nielsen, L. O'Driscoll, W. Potrzebowski, S. Prescott, R. Ferraz Leal, P. Rozyczko, T. Snow, A. Washington, L. Wilkins and C. Wolf, SasView version 5.0.6. *Zenodo. https://doi.org/10.5281/zenodo.7581379* **2023**.

210. L. Liénafa, J. Oberdisse, S. Mora, S. Monge and J. J. Robin, Rheology and SANS on PET-b-PLAc-b-P(DMAEMAq) Triblock Copolymers: Impact of the PET and Polyelectrolyte Chain Length. *Macromolecules* **2011**, 44 (13), 5326-5335.
211. T. Ribaut, J. Oberdisse, B. Annighofer, B. Fournel, S. Sarrade, H. Haller and P. Lacroix-Desmazes, Solubility and Self-Assembly of Amphiphilic Gradient and Block Copolymers in Supercritical CO_2. *J Phys Chem B* **2011**, 115 (5), 836-843.
212. C. Rufier, A. Collet, M. Viguier, J. Oberdisse and S. Mora, Influence of Surfactants on Hydrophobically End-Capped Poly(ethylene oxide) Self-Assembled Aggregates Studied by SANS. *Macromolecules* **2011**, 44 (18), 7451-7459.
213. B. Hammouda, Small-Angle Scattering From Branched Polymers. *Macromol Theor Simul* **2012**, 21 (6), 372-381.
214. M. Otten, M. Hildebrandt, B. Pfeffing, V. C. Voigt, F. Scheffold, T. Hellweg and M. Karg, Volume Phase Transition of Thermoresponsive Microgels Scrutinized by Dynamic Light Scattering and Turbidity: Correlations Depend on Microgel Homogeneity. *Langmuir* **2024**, 40 (28), 14515-14526.
215. O. Wrede, Y. Reimann, S. Lülsdorf, D. Emmrich, K. Schneider, A. J. Schmid, D. Zauser, Y. Hannappel, A. Beyer, R. Schweins, A. Gölzhäuser, T. Hellweg and T. Sottmann, Volume phase transition kinetics of smart *N*-*n*-propylacrylamide microgels studied by time-resolved pressure jump small angle neutron scattering. *Sci Rep-Uk* **2018**, 8.
216. V. Y. Rudyak, E. Y. Kozhunova and A. V. Chertovich, Towards the realistic computer model of precipitation polymerization microgels. *Sci Rep-Uk* **2019**, 9.
217. A. Scotti, S. Bochenek, M. Brugnoni, M. A. Fernandez-Rodriguez, M. F. Schulte, J. E. Houston, A. P. H. Gelissen, I. I. Potemkin, L. Isa and W. Richtering, Exploring the colloid-to-polymer transition for ultra-low crosslinked microgels from three to two dimensions. *Nat Commun* **2019**, 10.
218. N. Vogel, L. de Viguerie, U. Jonas, C. K. Weiss and K. Landfester, Wafer-Scale Fabrication of Ordered Binary Colloidal Monolayers with Adjustable Stoichiometries. *Adv Funct Mater* **2011**, 21 (16), 3064-3073.
219. E. S. A. Goerlitzer, M. C. Zhan, S. Choi and N. Vogel, How Colloidal Lithography Limits the Optical Quality of Plasmonic Nanohole Arrays. *Langmuir* **2023**, 39 (14), 5222-5229.
220. L. Isa, I. Buttinoni, M. A. Fernandez-Rodriguez and S. A. Vasudevan, Two-Dimensional Assemblies of Soft Repulsive Colloids Confined at Fluid Interfaces. *Epl-Europhys Lett* **2017**, 119 (2), 26001.
221. S. A. Maier, M. L. Brongersma, P. G. Kik, S. Meltzer, A. A. G. Requicha and H. A. Atwater, Plasmonics - A Route to Nanoscale Optical Devices. *Adv Mater* **2001**, 13 (19), 1501-1505.
222. S. G. Romanov, N. Vogel, K. Bley, K. Landfester, C. K. Weiss, S. Orlov, A. V. Korovin, G. P. Chuiko, A. Regensburger, A. S. Romanova, A. Kriesch and U. Peschel, Probing Guided Modes in a Monolayer Colloidal Crystal on a Flat Metal Film. *Phys Rev B* **2012**, 86 (19), 195145.
223. B. Ai, Y. Yu, H. Möhwald, G. Zhang and B. Yang, Plasmonic Films based on Colloidal Lithography. *Adv Colloid Interfac* **2014**, 206 5-16.
224. A. Nemiroski, M. Gonidec, J. M. Fox, P. Jean-Remy, E. Turnage and G. M. Whitesides, Engineering Shadows to Fabricate Optical Metasurfaces. *Acs Nano* **2014**, 8 (11), 11061-11070.
225. S. M. Weekes, F. Y. Ogrin, W. A. Murray and P. S. Keatley, Macroscopic Arrays of Magnetic Nanostructures from Self-Assembled Nanosphere Templates. *Langmuir* **2007**, 23 (3), 1057-1060.
226. M. Szekeres, O. Kamalin, P. G. Grobet, R. A. Schoonheydt, K. Wostyn, K. Clays, A. Persoons and I. Dékány, Two-Dimensional Ordering of Stöber Silica Particles at the Air/Water Interface. *Colloid Surface A* **2003**, 227 (1-3), 77-83.
227. C. van Baalen, J. Vialetto and L. Isa, Tuning Electrostatic Interactions of Colloidal Particles at Oil-Water Interfaces with Organic Salts. *Phys Rev Lett* **2023**, 131 (12), 128202.
228. K. Nakahama and K. Fujimoto, Thermosensitive Two-Dimensional Arrays of Hydrogel Particles. *Langmuir* **2002**, 18 (26), 10095-10099.
229. J. Vialetto, N. Nussbaum, J. Bergfreund, P. Fischer and L. Isa, Influence of the Interfacial Tension on the Microstructural and Mechanical Properties of Microgels at Fluid Interfaces. *J Colloid Interf Sci* **2022**, 608 2584-2592.
230. M. Karg, Functional Materials Design through Hydrogel Encapsulation of Inorganic Nanoparticles: Recent Developments and Challenges. *Macromol Chem Phys* **2016**, 217 (2), 242-255.
231. W. Kern and D. A. Puotinen, Cleaning Solutions Based on Hydrogen Peroxide for Use in Silicon Semiconductor Technology. *Rca Rev* **1970**, 31 (2), 187-206.
232. B. Ebeling and P. Vana, RAFT-Polymers with Single and Multiple Trithiocarbonate Groups as Uniform Gold-Nanoparticle Coatings. *Macromolecules* **2013**, 46 (12), 4862-4871.

233. P. B. Johnson and R. W. Christy, Optical Constants of Noble Metals. *Phys Rev B* **1972**, 6 (12), 4370-4379.
234. M. B. Müller, C. Kuttner, T. A. F. König, V. V. Tsukruk, S. Förster, M. Karg and A. Fery, Plasmonic Library Based on Substrate-Supported Gradiential Plasmonic Arrays. *Acs Nano* **2014**, 8 (9), 9410-9421.
235. Y. Brasse, M. B. Müller, M. Karg, C. Kuttner, T. A. F. König and A. Fery, Magnetic and Electric Resonances in Particle-to-Film-Coupled Functional Nanostructures. *Acs Appl Mater Inter* **2018**, 10 (3), 3133-3141.
236. C. L. Haynes, A. D. McFarland, L. L. Zhao, R. P. Van Duyne, G. C. Schatz, L. Gunnarsson, J. Prikulis, B. Kasemo and M. Käll, Nanoparticle Optics: The Importance of Radiative Dipole Coupling in Two-Dimensional Nanoparticle Arrays. *J Phys Chem B* **2003**, 107 (30), 7337-7342.
237. J. A. Jenkins, Y. D. Zhou, S. Thota, X. D. Tian, X. W. Zhao, S. L. Zau and J. Zhao, Blue-Shifted Narrow Localized Surface Plasmon Resonance from Dipole Coupling in Gold Nanoparticle Random Arrays. *J Phys Chem C* **2014**, 118 (45), 26276-26283.
238. S. K. Ghosh and T. Pal, Interparticle Coupling Effect on the Surface Plasmon Resonance of Gold Nanoparticles: From Theory to Applications. *Chem Rev* **2007**, 107 (11), 4797-4862.
239. A. D. Humphrey and W. L. Barnes, Plasmonic Surface Lattice Resonances on Arrays of Different Lattice Symmetry. *Phys Rev B* **2014**, 90 (7), 075404.
240. Y. N. Xia, Y. J. Xiong, B. Lim and S. E. Skrabalak, Shape-Controlled Synthesis of Metal Nanocrystals: Simple Chemistry Meets Complex Physics? *Angew Chem Int Edit* **2009**, 48 (1), 60-103.
241. L. M. Liz-Marzán, Tailoring surface plasmons through the morphology and assembly of metal nanoparticles. *Langmuir* **2006**, 22 (1), 32-41.
242. K. Van Gordon, R. Girod, F. Bevilacqua, S. Bals and L. M. Liz-Marzan, Structural and Optical Characterization of Reaction Intermediates during Fast Chiral Nanoparticle Growth. *Nano Lett* **2025**, 25 (7), 2887-2893.
243. L. Qiao, Z. Fu, J. Li, J. Ghosen, M. Zeng, J. Stebbins, P. N. Prasad and M. T. Swihart, Standardizing Size- and Shape-Controlled Synthesis of Monodisperse Magnetite (Fe_3O_4) Nanocrystals by Identifying and Exploiting Effects of Organic Impurities. *Acs Nano* **2017**, 11 (6), 6370-6381.
244. K. Boldt, N. Kirkwood, G. A. Beane and P. Mulvaney, Synthesis of Highly Luminescent and Photo-Stable, Graded Shell CdSe/$Cd_xZn_{1-x}S$ Nanoparticles by In Situ Alloying. *Chem Mater* **2013**, 25 (23), 4731-4738.
245. M. Grzelczak, J. Vermant, E. M. Furst and L. M. Liz-Marzán, Directed Self-Assembly of Nanoparticles. *Acs Nano* **2010**, 4 (7), 3591-3605.
246. M. A. Boles, M. Engel and D. V. Talapin, Self-Assembly of Colloidal Nanocrystals: From Intricate Structures to Functional Materials. *Chem Rev* **2016**, 116 (18), 11220-11289.
247. S. J. Tan, M. J. Campolongo, D. Luo and W. L. Cheng, Building plasmonic nanostructures with DNA. *Nat Nanotechnol* **2011**, 6 (5), 268-276.
248. C. A. Mirkin, R. L. Letsinger, R. C. Mucic and J. J. Storhoff, A DNA-based method for rationally assembling nanoparticles into macroscopic materials. *Nature* **1996**, 382 (6592), 607-609.
249. A. P. Alivisatos, K. P. Johnsson, X. G. Peng, T. E. Wilson, C. J. Loweth, M. P. Bruchez and P. G. Schultz, Organization of 'nanocrystal molecules' using DNA. *Nature* **1996**, 382 (6592), 609-611.
250. S. Y. Park, A. K. R. Lytton-Jean, B. Lee, S. Weigand, G. C. Schatz and C. A. Mirkin, DNA-programmable nanoparticle crystallization. *Nature* **2008**, 451 (7178), 553-556.
251. D. Nykypanchuk, M. M. Maye, D. van der Lelie and O. Gang, DNA-guided crystallization of colloidal nanoparticles. *Nature* **2008**, 451 (7178), 549-552.
252. N. K. Beyeh, Nonappa, V. Liljeström, J. Mikkilä, A. Korpi, D. Bochicchio, G. M. Pavan, O. Ikkala, R. H. A. Ras and M. A. Kostiainen, Crystalline Cyclophane-Protein Cage Frameworks. *Acs Nano* **2018**, 12 (8), 8029-8036.
253. M. Girard, J. A. Millan and M. O. de la Cruz, DNA-Driven Assembly: From Polyhedral Nanoparticles to Proteins. *Annu Rev Mater Res* **2017**, 47 33-49.
254. S. L. Wu, M. N. Zhu, Q. Lian, D. D. Lu, B. Spencer, D. J. Adlam, J. A. Hoyland, K. Volk, M. Karg and B. R. Saunders, Plasmonic and colloidal stability behaviours of Au-acrylic core-shell nanoparticles with thin pH-responsive shells. *Nanoscale* **2018**, 10 (39), 18565-18575.
255. M. Karg, T. A. F. König, M. Retsch, C. Stelling, P. M. Reichstein, T. Honold, M. Thelakkat and A. Fery, Colloidal self-assembly concepts for light management in photovoltaics. *Mater Today* **2015**, 18 (4), 185-205.
256. D. Paloli, P. S. Mohanty, J. J. Crassous, E. Zaccarelli and P. Schurtenberger, Fluid-solid transitions in soft-repulsive colloids. *Soft Matter* **2013**, 9 (11), 3000-3004.
257. H. Robertson, J. Zimmer, A. S. Name, C. Lux, S. Stock, R. von Klitzing and O. Soltwedel, In situ vs ex situ: Comparing the structure of PNIPAM microgels at the air/water and air/solid interfaces. *arXiv* **2025**, DOI: arxiv.org/abs/2503.1418

258. Y. C. Zhou, J. J. Crassous and M. Karg, Core-Shell Microgels at Air/Water Interfaces: Role of Interfacial Tension in Monolayer Evolution. *Langmuir* **2025**, 41 (14), 9274-9287.
259. A. M. Funston, C. Novo, T. J. Davis and P. Mulvaney, Plasmon Coupling of Gold Nanorods at Short Distances and in Different Geometries. *Nano Lett* **2009**, 9 (4), 1651-1658.
260. P. K. Jain, W. Y. Huang and M. A. El-Sayed, On the universal scaling behavior of the distance decay of plasmon coupling in metal nanoparticle pairs: A plasmon ruler equation. *Nano Lett* **2007**, 7 (7), 2080-2088.
261. V. Gupta, P. T. Probst, F. R. Gossler, A. M. Steiner, J. Schubert, Y. Brasse, T. A. F. König and A. Fery, Mechanotunable Surface Lattice Resonances in the Visible Optical Range by Soft Lithography Templates and Directed Self-Assembly. *Acs Appl Mater Inter* **2019**, 11 (31), 28189-28196.
262. Y. Brasse, V. Gupta, H. C. T. Schollbach, M. Karg, T. A. F. König and A. Fery, Mechanotunable Plasmonic Properties of Colloidal Assemblies. *Adv Mater Interfaces* **2020**, 7 (5), 1901678.
263. U. Cataldi, R. Caputo, Y. Kurylyak, G. Klein, M. Chekini, C. Umeton and T. Bürgi, Growing gold nanoparticles on a flexible substrate to enable simple mechanical control of their plasmonic coupling. *J Mater Chem C* **2014**, 2 (37), 7927-7933.
264. W. Kern and D. A. Puotinen, Cleaning Solutions Based on Hydrogen Peroxide for Use in Silicon Semiconductor Technology. *Rca Rev* **1970**, 31 (2), 187.
265. S. Babar and J. H. Weaver, Optical constants of Cu, Ag, and Au revisited. *Appl Optics* **2015**, 54 (3), 477-481.
266. J. S. J. Tang, R. S. Bader, E. S. A. Goerlitzer, J. F. Wendisch, G. R. Bourret, M. Rey and N. Vogel, Surface Patterning with SiO_2@PNiPAm Core-Shell Particles. *Acs Omega* **2018**, 3 (9), 12089-12098.
267. C. R. Harris, K. J. Millman, S. J. van der Walt, R. Gommers, P. Virtanen, D. Cournapeau, E. Wieser, J. Taylor, S. Berg, N. J. Smith, R. Kern, M. Picus, S. Hoyer, M. H. van Kerkwijk, M. Brett, A. Haldane, J. F. del Río, M. Wiebe, P. Peterson, P. Gérard-Marchant, K. Sheppard, T. Reddy, W. Weckesser, H. Abbasi, C. Gohlke and T. E. Oliphant, Array programming with NumPy. *Nature* **2020**, 585 (7825), 357-362.
268. J. Reback, McKinney, W., Pandas: powerful Python data analysis toolkit, DOI: 10.5281/zenodo.13819579).
269. J. D. Hunter, Matplotlib: A 2D graphics environment. *Comput Sci Eng* **2007**, 9 (3), 90-95.
270. P. Virtanen, R. Gommers, T. E. Oliphant, M. Haberland, T. Reddy, D. Cournapeau, E. Burovski, P. Peterson, W. Weckesser, J. Bright, S. J. van der Walt, M. Brett, J. Wilson, K. J. Millman, N. Mayorov, A. R. J. Nelson, E. Jones, R. Kern, E. Larson, C. J. Carey, I. Polat, Y. Feng, E. W. Moore, J. VanderPlas, D. Laxalde, J. Perktold, R. Cimrman, I. Henriksen, E. A. Quintero, C. R. Harris, A. M. Archibald, A. N. H. Ribeiro, F. Pedregosa, P. van Mulbregt and S. Contributors, SciPy 1.0: fundamental algorithms for scientific computing in Python (vol 33, pg 219, 2020). *Nat Methods* **2020**, 17 (3), 352-352.
271. L. H. Alvarez, A. A. Rudov, R. A. Gumerov, P. Lenssen, U. Simon, I. I. Potemkin and D. Wöll, Controlling microgel deformation via deposition method and surface functionalization of solid supports. *Phys Chem Chem Phys* **2021**, 23 (8), 4927-4934.